INAUGURAL-DISSERTATION

zur
Erlangung der Doktorwürde
der
Naturwissenschaftlich-Mathematischen Gesamtfakultät
der
Ruprecht-Karls-Universität
Heidelberg

vorgelegt von

Dipl.-Math. Christian Reinhold Goll

aus Bingen am Rhein

Tag der mündlichen Prüfung:

_____

Design of Numerical Methods for Simulating Models of a Solid Oxide Fuel Cell

Betreuer

Prof. Dr. Dr. h. c. Rolf Rannacher

Contents

Abstract

The performance of fuel cells is significantly affected by “loss mechanisms”. This work is devoted to developing concepts for the efficient numerical computation of the diffusion polarization in the porous anode of a solid oxide fuel cell (*SOFC*). The following topics were covered:

The first part of this work is focused on the numerical verification of coupling conditions for effective viscous flows over a porous medium. It is generally accepted that the “Beavers-Joseph-Saffman slip law” holds true for a main flow direction which is tangential to the interface. However, the interface law for the effective stress has been a subject of controversy. We provide a confirmation of the “pressure jump law”, which has been recently derived by Marciniak-Czochra and Mikelić, for a range of configurations using a direct numerical simulation of the flow at the microscopic level.

The second part of this work is about the derivation of a goal-oriented, a posteriori error estimator for the finite element approximation of elliptic homogenization problems based on the “Dual Weighted Residual method” of Becker and Rannacher. In general, the solution of the macroscopic equation in the homogenized model depends on effective coefficients which in turn depend on the solutions of some additional auxiliary equations. Therefore, the accuracy of the physical goal functional is influenced by the discretization error of the macroscopic and the auxiliary solutions. By employing the error estimator developed in this work we can estimate the contribution of the discretization of each sub-problem (effective model and auxiliary problems) onto the overall error. These contributions are then balanced within a successive refinement cycle to set up an efficient discretization. Local error indicators are used to steer an adaptive mesh refinement for the macroscopic problem as well as the auxiliary problems.

We demonstrate the functionality of this algorithm on some prototypical homogenization problems and on an effective model developed in this work to simulate the gas transport in the anode of an SOFC. In the latter, the diffusion polarization is the quantity of interest. For a given accuracy, the application of the local mesh refinement based on the adaptive algorithm in this context decreases the number of degrees of freedom and computation time significantly compared to the global mesh refinement.

Zusammenfassung

Die Leistung von Brennstoffzellen wird maßgeblich von Verlustmechanismen beeinflusst. Gegenstand der vorliegenden Arbeit ist die Entwicklung von Konzepten, um die Gasdiffusionspolarisation in der porösen Anode einer Festoxidbrennstoffzelle numerisch effizient zu berechnen. Hierbei wurden folgende Themenfelder behandelt:

Der erste Schwerpunkt der Arbeit liegt auf der numerischen Verifikation von Kopplungsbedingungen effektiver viskoser Strömungen über ein poröses Medium. Im Falle einer Hauptflussrichtung parallel zur Grenzfläche des porösen Materials ist die Gültigkeit der „Beavers-Joseph-Saffmann-Bedingung“ akzeptiert. Uneinigkeit hingegen herrscht darüber, welche Bedingungen an den effektiven Spannungstensor zu stellen sind. Wir weisen mithilfe einer direkten Finite Elemente Simulation im Porenraum die Gültigkeit des kürzlich bewiesenen „Pressure Jump Laws“ von Marciniak-Czochra und Mikelić für verschiedene Konfigurationen nach.

Im zweiten großen Themenkomplex entwickeln wir, auf der Basis der „Dual Weighted Residual Methode“ von Becker und Rannacher, einen zielorienten a posteriori Fehlerschätzer für die Finite Elemente Approximation von elliptischen Homogenisierungsproblemen. Im Allgemeinen hängen die makroskopischen Gleichungen im homogenisierten Modell von effektiven Parametern ab, die mittels der Lösung sogenannter Hilfsprobleme berechnet werden. Der Diskretisierungsfehler bzgl. einer gegebenen physikalischen Zielgröße hängt von der Diskretisierung des effektiven Modells und der Hilfsprobleme ab. Mithilfe des von uns entwickelten Fehlerschätzers lässt sich der Beitrag der Diskretisierung eines jeden Teilproblems (effektives Modell, Hilfsprobleme) zum Gesamtfehler schätzen. In einem sukzessiven Gitterverfeinerungszyklus werden die Fehleranteile balanciert, um den Approximationsprozess effizient zu gestalten. Mittels lokaler Fehlerindikatoren können die Gitter jeweils lokal adaptiert werden.

Wir zeigen die Wirksamkeit dieses Algorithmus an generischen Homogenisierungsbeispielen sowie anhand eines von uns entwickelten effektiven Modells zur Simulation des Gastransports in der Anode einer Festoxidbrennstoffzelle. In letzterem Beispiel dient die Gasdiffusionspolarisation als Zielgröße. Die Anwendung des adaptiven Algorithmus in diesem Kontext führt im Vergleich mit globaler Gitterverfeinerung bei gleichbleibender Genauigkeit zu erheblichen Einsparungen bzgl. der Anzahl der Freiheitsgrade sowie der benötigten Rechenzeit.

1. Introduction

This thesis is dedicated to numerically simulating the negative electrode of a solid oxide fuel cell (*SOFC*). We conduct a systematic investigation of the modelling of the gas transport in the cell and develop a numerical algorithm which allows for an efficient simulation of aforementioned model. This work is part of a cooperation with the "Institut für Werkstoffe der Elektrotechnik" (*IWE*) at the Karlsruher Institut für Technologie (*KIT*).

The range of topics touched in this thesis is broad and includes: coupling conditions for the Stokes-Darcy problem (Chapter 3), numerical error control of homogenization problems (Chapter 4) and fuel cell modelling (Chapter 5). This introduction highlights the common thread of the different chapters. For a more thorough introduction to the specific topics we refer to Chapter 2 as well as the introductory parts of the chapters.

The motivation behind this thesis as well as a brief discussion of the problems addressed is presented in Section 1.1. An overview of the thesis can be found in Section 1.2.

1.1. Motivation and Goals

This introduction begins with a brief explanation of what a fuel cell is and how it works. Afterward, we elaborate on the objectives of the thesis: What are the goals and how do we achieve them?

1.1.1. What Is a Fuel Cell?

A fuel cell is an electrochemical device which converts the chemical energy of a fuel directly into electrical energy through a reaction with an oxidizing agent. In most types of fuel cells, the driving reaction is that of hydrogen (the fuel) with oxygen (the oxidizing agent) producing water and an electrical current, i.e. the overall reaction of the cell is

$$2\,H_2 + O_2 \longrightarrow 2\,H_2O + 4\,e^-.$$

However, it is not mandatory to use pure hydrogen as fuel. Other possibilities include natural gas, methanol and methane, see Lucia [97]. The advantages of using hydrocarbons as fuel are their availability and the lower production cost than pure hydrogen , see Cook [47]. The downside is that the cell then produces not only water but also carbon dioxide, which may accelerate global warming, see Cox et al. [48]. Hydrogen is not naturally available to us in pure form, but rather in chemical compounds like water or biomass. The environmentally-friendly and simultaneously cheap production of pure hydrogen is one of the big challenges of undergoing researches, see Kalamaras and Efstathiou [83].

Even though a broad range of fuel cell-types exists, in general, a fuel cell consist of **gas channels**, which transport fuel, the oxidant as well as products of the reaction, e.g. water, and two **electrodes** (anode and cathode), which are separated by an **electrolyte**, see Figure 1.1.1 for a scheme of an SOFC. The classification of fuel cells depends on the material used for the electrolyte. In this work we will focus on solid oxide fuel cells which use a solid ceramic material for the electrolyte.

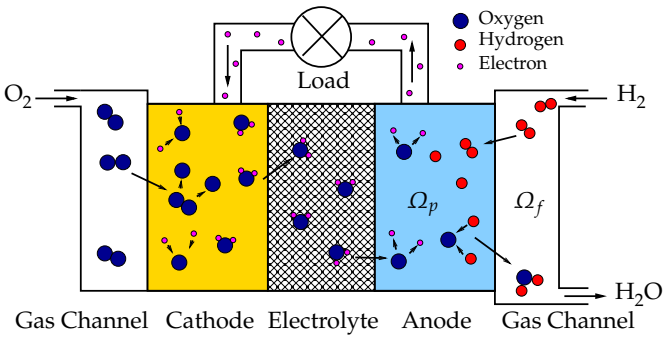

Figure 1.1.1.: Scheme of a solid oxide fuel cell – not true to scale.

We briefly discuss the **working principle** of an SOFC. Oxygen, in the form of O_2, flows through the gas channel on the left hand side in Figure 1.1.1 into the porous cathode. There the oxygen molecules are split and each atom is enriched with two electrons. The newly formed oxygen ions travel through the electrolyte, which acts as a barrier and allows passage only for these negatively charged ions, to the porous anode. On the anode side of the fuel cell H_2 is fed in the gas channel. These molecules split into positive hydrogen ions in the anode. Near the electrolyte/anode interface, the hydrogen ions react with the oxygen ions to produce water and emit electrons. These electrons flow through the external load back to the cathode and produce thus the electrical current (remember that the way through the electrolyte is "blocked" for the electrons).

The main areas of applications are transport and distributed power generation, especially as a combined heat and power source (see Andújar and Se-

gura [12], Kirubakaran et al. [86]). The main advantages of fuel cells compared to conventional combustion-based energy-generators, apart from the fact that the supply of fossil fuel is limited, are (see e.g. Cook [47], Kirubakaran et al. [86], Stambouli and Traversa [123]):

- Fuel cells have a potentially **higher conversion efficiency** (i.e. extracting a higher percentage out of the energy stored in the fuel fed to the cell) than conventional heat engines (such as diesel-engines or turbines). The reason is that the conventional engines translate the chemical energy of the fuel via combustion into mechanical energy (and heat), which is then converted to electrical energy. This detour greatly decreases the efficiency potential.
- Fuel cells are able to operate at a significantly **lower level of noise-emission**, also due to the lack of mechanical, moving parts.
- If hydrogen is used as fuel, there are no pollutant emissions, as water is the only product of the reaction, so fuel cells are "**cleaner**". To make the whole process of electricity generation with fuel cells environmentally-friendly, one has to ensure that the production process of the utilized hydrogen uses renewable energy sources. See also Cook [47, Figure 1] where the author reports that the amount of hydrogen in used fuels has been increasing over time.

Although fuel cells look promising as an efficient and environmentally-friendly way to generate electricity, there are still obstacles which prevent the use of fuel cells on a grand scale (even though the fuel cell business is constantly growing, see Fuel Cell Today [61]). We do not want to conceal that there is criticism which challenges the whole idea of hydrogen-based power generation, see Bossel [25].

Apart from problems like the need for a fuel-delivering infrastructure or safety issues related to the storage of hydrogen, a big obstacle is that electricity produced by fuel cells is too expensive. In the construction of fuel cells, expensive materials (like platinum) are used, and the durability of the cells is, due to degradation of the electrodes, relatively poor, see e.g. Cook [47], Kornely et al. [88]. However, to make the cell more cost-efficient, one could also try to raise the power output. The performance of a fuel cell is highly influenced by its layout as well as the material used for the electrodes, see Kornely et al. [87], Yang et al. [137].

Thus, there is still room for improvement in the development of fuel cells. One could, for example, try to reduce the thickness of the electrode to save material costs or optimize the design of the cell to increase cell voltage (which is directly related to electrical efficiency). However, the processes in the fuel cell are complex and not yet fully understood, and conducting experiments is expensive and time consuming (Yang et al. [137]).

The Role of Numerical Simulations

The use of a mathematical model, i.e. some mathematical formulas or (partial) differential equations, is a great tool in further understanding and developing fuel cells. The two main approaches to modelling are black- and white-box modelling, see Wang et al. [134]. A black-box model is derived by an empirical evaluation of experimental data, whereas the white-box models are based on physical principles, most often represented by a partial differential equation.

Running a simulation, i.e. approximating the solution to the aforementioned model with some numerical scheme, is usually much cheaper than conducting an experiment. Furthermore, a numerical simulation allows for the implementation of an optimization algorithm and for the decoupling of specific phenomena for a better understanding of complex processes. Another advantage is that measurements within such a simulation are easy (compared to the laboratory) and one can observe quantities that can not be measured by experiments in the laboratory at all. The downside is that the models are only an approximation of reality and may not reproduce every if any physical effect one is interested in.

The choice of a specific model is most often a trade-off of accuracy vs. (computational) cost. With increasing model-complexity (e.g. using partial differential equations instead of heuristic formulas, taking more physical effects into account, using a 3-d model) and thus more realistic results, the numerical effort of the simulation rises. This is the reason why even today 0-d or 1-d fuel cell models are widespread, see for example Wang et al. [134].

This work is focused on the **gas transport** (of fuel and reaction-products) in the anode and the overlying gas channel in a 2-d setting. The chemical reactions in the anode are taking place in the so called "three phase boundary" (*TPB*), which is located near the interface of the electrolyte and the anode. Thus, it is of importance that the transportation of fuel to (and water away from) the TPB is fast enough. Otherwise, the theoretical performance is hampered by an undersupply of fuel at the TPB – this loss mechanism is called **concentration loss**. The model we use should be able to accurately determine the concentration loss of a specific fuel cell configuration. So the performance of the fuel cell depends heavily on the distribution of fuel and exhaust in the anode (as well as the gas channel). The difficulty is that the anode is composed of a porous material which, along with the geometry of the cell, heavily influences the fuel-distribution.

Our work contributes to the goal of an accurate and efficient fuel cell simulation in two ways.

- Firstly, a systematic investigation of the part of the model responsible for the gas transport is undertaken (see also Section 1.1.2).

- Secondly, an advanced numerical algorithm to reduce the computational costs of solving the mathematical model is developed. This algorithm allows for the use of more complex models and, moreover, due to the reduction of computational time, it allows for the application of an optimization algorithm, which has higher numerical costs than a mere simulation.

1.1.2. Mathematical Model, Homogenization and Numerical Approximation

The model we consider and which describes the gas transport in the anode and the gas channel (of a mixture of N different species, where N is in the range of two to ten) looks (neglecting boundary conditions) as follows in a stationary configuration :

$$-\mu^\varepsilon \Delta \mathbf{v}^\varepsilon + \nabla p^\varepsilon = 0, \tag{1.1.1a}$$

$$\nabla \cdot (\rho^\varepsilon \mathbf{v}^\varepsilon) = 0, \tag{1.1.1b}$$

$$\nabla \cdot (\rho^\varepsilon y_i^\varepsilon \mathbf{v}^\varepsilon) + \nabla \cdot \mathfrak{F}_i^\varepsilon = 0, \qquad i = 1 \dots N, \tag{1.1.1c}$$

$$\sum_{i=1}^{N} y_i^\varepsilon = 1, \tag{1.1.1d}$$

where μ^ε is the dynamic viscosity of the mixture, ρ^ε its the density, $\mathbf{v}^\varepsilon$ its velocity, p^ε the pressure, y_i^ε the mass fraction of species i, and $\mathfrak{F}_i^\varepsilon$ the corresponding mass diffusion flux.

Note that when developing fuel cells one is in general not interested in the flow field or the distribution of the species per se, but rather their *impact on the actual performance* of the device. This performance depends heavily on the aforementioned **concentration loss**, which is caused by an undersupply of fuel at the anode/electrolyte-interface. So, the goal of the simulation therefore is to provide a precise value $\eta_{\text{conc}}^{\text{A}} = \eta_{\text{conc}}^{\text{A}}(\mathbf{v}^\varepsilon, p^\varepsilon, y_i^\varepsilon)$, i.e. the concentration loss of the anode, as our *quantity of interest*.

When running a simulation of (1.1.1), we have to *discretize* the problem, i.e. approximate the solution by some numerical scheme (we opt for the finite element method but the following discussion is also applicable to other discretization methods, such as finite volume discretizations). This approach also allows to calculate an approximation of $\eta_{\text{conc}}^{\text{A}}$. However, the discretization introduces a defect, the so called *discretization error*. To make sure that our results are meaningful, we must control this discretization error somehow, i.e. we have to evaluate: *What is the impact of using the FE-approximation of* (1.1.1) *in the computation of the concentration loss?*

Additionally, we compute this quantity of interest efficiently to obtain a good approximation by employing a **goal-oriented a posteriori error estimator**, see Becker and Rannacher [20]. This estimator not only measures how precise the approximation of the quantity of interest is, but also provides a set of *local error indicators*. These indicate which cells of the triangulation carry the major part of the discretization error and should consequently be refined. So, the indicators allow the use of an adaptive algorithm, which ensures the efficient allocation of (computational) effort. The development of such an estimator for the situation at hand is one of the main achievements of this thesis.

The set of PDEs (1.1.1) hold true in the pores of the anode-material and the overlying gas channel. Thus, when we want to compute an approximation of the model, our triangulation (subdivision of the domain into small polygons, called *cells*) should resolve the porous structure of the anode. Typically the pore-diameter is in the order of $\sim 10^{-6}$ m and the length and width of the anode are in the range of $\sim 10^{-3}$–10^{-2} m, see e.g. Tseronis et al. [131], Zhu et al. [140]. Note that we consider 2d-models of the fuel cell in this work. Consider an anode with a length of 1 cm and a width of 1 mm. A triangulation that would be able to resolve this structure thus needs approximately 10^7 cells. And this is only in 2-d; the problem is much more severe if 3-d simulations are considered.

Thus, it is not feasible to resolve the pore structure of the anode with a triangulation needed for a numerical approximation. We choose to overcome this problem by applying **homogenization theory** (see Cioranescu and Donato [43], Hornung [73], Tartar [127] or Section 2.2): From the *microscopic problem* (i.e. the aforementioned PDEs in the pore-space) we extract some effective behaviour which describes the (physical) process on a (much) larger scale. This means that instead of (1.1.1) on the perforated pore space, we consider a set of *effective* (or *macroscopic* or *homogenized*) equations on a plain domain. The (eligible) hope is that this set of equations still describes the crucial effects of the process on a macroscopic scale (in our case: the anode). One can think of the homogenization process as a kind of averaging; it is a transfer from the microscopic to the macroscopic level, catching the macroscopically important phenomena and neglecting fine scale oscillations.

We therefore use the homogenized version of equation (1.1.1) as our fuel cell model, which we approximate by a finite element scheme. Approximating the effective equation is generally cheaper than solving the microscopic problem directly, as the homogenized problem is defined on a domain without perforations. However, the macroscopic model additionally needs the solution of some auxiliary equations, which we must discretize too.

Figure 1.1.2 shows a sketch of the situation at hand: $\Omega_{\mathrm{f}}^{\varepsilon}$ represents the gas channel and $\Omega_{\mathrm{p}}^{\varepsilon}$ the anode on the microscopic level. The macroscopic model holds true

on a homogenized domain consisting of the gas channel Ω_f and (homogenized) anode Ω_p, compare also with Figure 1.1.1.

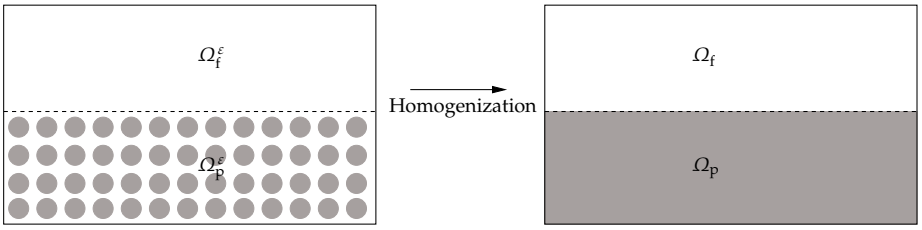

Figure 1.1.2.: Sketch of the transition from pore-space (left hand) to a homogenized domain (right hand) via homogenization.

1.1.3. Goals of the Thesis

The above consideration leads to the following two problems which are approached in this thesis:

(i) We are interested in the solution of our fuel cell model in the anode and the corresponding gas channel. Consider only the Stokes part ((1.1.1a) and (1.1.1b)) of our model. It is known that the type of the homogenized equation depends on whether we are in the gas channel or the anode, even though on the microscopic level we have Stokes equations in the whole domain. In the gas channel the homogenized model is still Stokes system, but in the porous anode the effective equation is Darcy's law. Stokes equations are a set of second order PDEs for the velocity and first order for the pressure, whereas Darcy's law is of second order for the pressure and first order for the velocity. Thus, the following problem arises naturally: *How should we couple these two equations across the interface separating the gas channel from the anode?*

This question has caused a lot of discussion in the scientific community, see Chapter 3 for an overview. We follow Marciniak-Czochra and Mikelić [98], who have analytically proven a set of coupling conditions in this context. In Chapter 3 we present numerical proof of these interface laws, based on a **direct simulation on the pore-scale level**. This study requires very high precision of the numerical approximations and is, to our knowledge, the first comparison of the aforementioned coupling conditions with pore-scale simulations.

(ii) Let us consider an approximation of a quantity of interest, which depends on the solution of a generic homogenization problem (see the introduction

of Chapter 4 for a more precise definition). Parts of the effective equations that emerge from the homogenization process are effective parameters, which in turn depend on the solution of additional auxiliary problems. Thus, when approximating the homogenized system (i.e. auxiliary problems and macroscopic equation), the discretization error introduced to the auxiliary problems carries over to the macroscopic level. The question is: *How should we distribute the available resources (i.e. degrees of freedom) between the macroscopic problem and the auxiliary problems?* How do we ensure that we do not waste precious computing time on computing the effective coefficients when in fact the bulk of the error stems from the macroscopic level (or vice versa)?

In Chapter 4 we apply the *Dual Weighted Residual (DWR) method* of Becker and Rannacher [20] to this kind of problem. This leads us to a **goal-oriented a posteriori error estimator**, which accounts for the coupling between the two levels and separates the discretization error into macroscopic and auxiliary error-contributions. Thus, we are able to efficiently allocate our computing power with locally adapted grids (for both macroscopic problem and auxiliary problems), tailored especially to minimize the error in the given (physical) quantity of interest.

These are the two main achievements of this thesis; please see the introductions of Chapters 3 and 4 for a more in-depth presentation of the respective problems.

Finally, we assemble the algorithms and models, systematically developed in chapter 3 and 4, and use them on our fuel cell model in Chapter 5. Whereas, in the previous chapters, we present our findings by means of some exemplary model problems, in this chapter they are tested in a more realistic scenario: We incorporate the correct coupling conditions for the Stokes-Darcy problem and show, with the resulting model, that the concentration loss of the anode can be efficiently approximated by applying the goal-oriented a posteriori error estimator of Chapter 4. The model considered in this chapter was developed in cooperation with the IWE at KIT.

1.2. Overview

In **Chapter 2** we set the notation used throughout the thesis and give a short introduction to periodic homogenization.

Chapter 3 presents the coupling conditions on the interface between Stokes and Darcy equation. This scenario is the outcome of a homogenization process of Stokes equations in a domain with a perforated part and a part where the

fluid can flow unhindered. We present the framework of this problem and give a numerical confirmation of the interface laws proposed by Marciniak-Czochra and Mikelić [98] by a direct numerical simulation on the microscopic level. Most of the chapter is concerned with a flow configuration where the main flow direction is tangential to the interface. We also present the justification of an interface law that deals with flows that are forced *through* the porous domain, i.e. flows which are normal to the interface.

After setting the coupling conditions, **Chapter 4** is concerned with goal-oriented a posteriori error estimation in the context of homogenization problems. We apply the DWR-method by Becker and Rannacher [20] on the homogenization problems, i.e. a number of PDEs, separated into macroscopic and auxiliary problems. The goal functionals in this framework depend on macroscopic quantities in most scenarios. It is of special interest to estimate the impact of the approximation of the auxiliary problems on the macroscopic *goal functional* (i.e. the quantity of interest). We present the results of our algorithm applied to some typical homogenization problems. The algorithm is able to separate and balance the influence of the discretizations of the various sub-problems on a given goal functional. This balancing process is coupled with local mesh refinement and allows for substantial savings when compared to global mesh refinement, as shown by the numerical tests.

Finally, in **Chapter 5**, we apply the methods developed in the previous chapters to the fuel cell simulation (focusing on the anode and the overlying gas channel). We start by giving a short introduction into fuel cells. Afterward, a model for the gas transport in the anode and the overlying gas channel of an SOFC is presented on the microscopic level. We proceed by deriving an effective equation where we incorporate the findings of Chapter 3. This formally homogenized problem is verified by some direct numerical simulations on the microscopic level. After the model is complete, we apply the algorithm developed in Chapter 4 to this set of PDEs and show with two numerical examples that we can efficiently compute the concentration loss of the anode. The chapter is closed by a more realistic test case where the application of the adaptive algorithm speeds up the solving process considerably when compared to global refinement.

The thesis is closed by **Chapter 6**. We summarize the presented results and discuss possible extensions for future work.

2. Basic Concepts

In this section we set the basic notation for the thesis in Section 2.1. Afterwards, we give a brief introductions into the theory of homogenization (Section 2.2). This section is for the benefit of readers unfamiliar with homogenization theory.

2.1. Notation

Let in the following $m, n \in \mathbb{N}^+$ and $k \in \mathbb{N}$. We consider only $\mathbb{R}^n$-valued functions in this thesis.

2.1.1. Vector Valued Functions

In general, vectors and vector valued functions are typeset in **bold**. We use '$\cdot$' as an abbreviation of the euclidian scalar product, i.e. for $\mathbf{a}, \mathbf{b} \in \mathbb{R}^n$ it holds

$$\mathbf{a} \cdot \mathbf{b} = \sum_{i=1}^{n} a_i b_i. \tag{2.1.1}$$

The euclidian norm is denoted by $|\cdot|$, i.e.

$$|\mathbf{a}| = \sqrt{\mathbf{a} \cdot \mathbf{a}}. \tag{2.1.2}$$

Let $\boldsymbol{\alpha} \in \mathbb{N}^n$ be a multi-index, $\mathbf{x} \in \mathbb{R}^n$. We use the following notation:

$$|\boldsymbol{\alpha}|_1 := \sum_{i=1}^{n} |\alpha_i|, \tag{2.1.3}$$

$$\mathrm{D}^{\boldsymbol{\alpha}} := \frac{\partial^{|\boldsymbol{\alpha}|_1}}{\partial x_1^{\alpha_1} \dots \partial x_n^{\alpha_n}}, \tag{2.1.4}$$

$$\mathbf{x}^{\boldsymbol{\alpha}} := \prod_{i=1}^{n} x_i^{\alpha_i}. \tag{2.1.5}$$

Definition 2.1.1. *By $\mathbf{e}_i \in \mathbb{R}^n$, $1 \leq i \leq n$, we denote the **Cartesian unit vectors**, i.e.*

$$\mathbf{e}_i := (\delta_{ij})_{j=1}^n, \tag{2.1.6}$$

with the Kronecker delta δ_{ij}.

Remark 2.1.2 (Arguments)**.** *We do not apply bold setting to arguments of functions, e.g.. we would write $f(x)$ instead of $f(\mathbf{x})$ for $x \in \mathbb{R}^2$.*

2.1.2. Function Spaces

In this section we assume $\Omega \subset \mathbb{R}^n$ to be an open domain with Lipschitz boundary. For an introduction into Sobolev spaces we refer to standard text books, e.g. Adams and Fournier [6] or Wloka [135], where one can also find the exact definition of a Lipschitz boundary.

Definition 2.1.3 (Continuously Differentiable Functions)**.** *As usual we denote the space of $\mathbb{R}$-valued, k-times **continuously differentiable functions** on Ω by $C^k(\Omega)$. The set of smooth functions on Ω is denoted by $C^\infty(\Omega)$. If all the functions have additionally compact support in Ω, we call the space $C_0^\infty(\Omega)$.*

We use standard notation in the context of Lebesgue- and Sobolev spaces, i.e. $L^p(\Omega)$ with $1 \leq p \leq \infty$ is the usual **Lebesgue-space** of order p and by $H^s(\Omega)$ is the **Sobolev-space** of order s with $s \in \mathbb{R}, s \geq 0$ and $L^2(\Omega) = H^0(\Omega)$.

- Let $1 \leq p < \infty$. $L^p(\Omega)$ is the set of all measurable functions $f : \Omega \to \mathbb{R}^n$ s.t. for the norm $\|\cdot\|_{L^p(\Omega)} = \|\cdot\|_{L^p}$ there holds

$$\|f\|_{L^p(\Omega)}^p := \int_\Omega |f(x)|^p \, \mathrm{d}x < \infty. \tag{2.1.7}$$

  $L^2(\Omega)$ is a Hilbert-space if we consider the scalar product

$$(f, g)_{L^2(\Omega)} := \int_\Omega f(x) g(x) \, \mathrm{d}x \qquad f, g \in L^2(\Omega). \tag{2.1.8}$$

- Let $p = \infty$. $L^\infty(\Omega)$ is the set of all essentially bounded functions, i.e. for the norm $\|\cdot\|_{L^\infty(\Omega)} = \|\cdot\|_{L^\infty}$ there holds

$$\|f\|_{L^\infty(\Omega)} := \inf\{\mathcal{C} \in \mathbb{R} \,|\, |f(x)| \leq \mathcal{C} \text{ a. e. in } \Omega\}. \tag{2.1.9}$$

- For $\varphi \in C^\infty(\Omega)$ we define the norms $\|\cdot\|_{H^k(\Omega)} = \|\cdot\|_{H^k}$ by

$$\|\varphi\|^2_{H^k(\Omega)} := \sum_{\substack{\boldsymbol{\alpha}\in\mathbb{N}^n \\ |\boldsymbol{\alpha}|_1 \le k}} \int_\Omega \left|\mathrm{D}^\alpha \varphi(x)\right|^2 \,\mathrm{d}x. \tag{2.1.10}$$

  The space $H^k(\Omega)$ is now defined as the completion of $C^\infty(\Omega)$ w.r.t. aforementioned norm:

$$H^k(\Omega) := \overline{C^\infty\Omega}^{\|\cdot\|_{H^k}}. \tag{2.1.11}$$

  Let $\Gamma \subset \partial\Omega$. We denote the space of Sobolev functions with zero trace on Γ by $H^k_\Gamma(\Omega)$, i.e.

$$H^k_\Gamma(\Omega) = \{\varphi \in H^k(\Omega) \mid \varphi|_\Gamma = 0\}. \tag{2.1.12}$$

A short remark regarding the scalar product and norm on the product spaces of L^2: For two functions $\mathbf{f}, \mathbf{g} \in L^2(\Omega)^m$ with $m \in \mathbb{N} \setminus \{0\}$. We use the following notation for the corresponding scalar product

$$(\mathbf{f}, \mathbf{g})_\Omega = \int_\Omega \mathbf{f}(x) \cdot \mathbf{g}(x) \,\mathrm{d}x \tag{2.1.13}$$

respective norm

$$\|\mathbf{f}\|^2_\Omega = \int_\Omega \left|\mathbf{f}(x)\right|^2 \,\mathrm{d}x. \tag{2.1.14}$$

If the domain of integration is clear from context, we omit the subscript in both cases.

Spaces of Periodic Functions

Let us describe how we denote periodicity. Let $f : \mathbb{R}^n \to \mathbb{R}$, $l > 0$.

Definition 2.1.4 (Periodicity in One Direction)**.** *We say f* is l-periodic w.r.t. *x_i if there holds*

$$f(x) = f(x + \mathbf{e}_i l). \tag{2.1.15}$$

Definition 2.1.5. *Let $\mathbf{l} \in \left(\mathbb{R}^+\right)^n$. We define the rectangle $Y \subset \mathbb{R}^n$ by $Y := \bigtimes_{i=1}^n (0, l_i)$. We say a function $f : \mathbb{R}^n \to \mathbb{R}$ is* Y-periodic*, if it is l_i-periodic w.r.t. x_i for all $1 \le i \le n$,*

i.e. there holds

$$f(x) = f(x + l_i \mathbf{e}_i) \qquad \forall 1 \leq i \leq n. \tag{2.1.16}$$

With the above definition of Y-periodicity, we define the function space of smooth, Y-periodic functions by

$$C^\infty_{\text{per}}(Y) := \{\varphi \in C^\infty(\mathbb{R}^n) \mid \varphi \text{ is } Y\text{-periodic}\}. \tag{2.1.17}$$

Definition 2.1.6. *We call the closure of this function space w.r.t. the $H^k(Y)$-norm $H^k_{\text{per}}(Y)$, i.e.*

$$H^k_{\text{per}}(Y) := \overline{C^\infty_{\text{per}}(Y)}^{\|\cdot\|_{H^k(Y)}}. \tag{2.1.18}$$

Remark 2.1.7. *Note the domain of integration of the norm in the completion of $H^k_{\text{per}}(Y)$ is Y, not $\mathbb{R}^n$.*

2.1.3. Theorems

We cite the following theorem from Cioranescu and Paulin [44]:

Theorem 2.1.8 (Mean Value Property of Periodic Functions)**.** *Let $\Omega \subset \mathbb{R}^n$ be a bounded open set and $Y := \bigtimes_{i=1}^n [0, l_i]$ and $l_i > 0$. Let f be a Y-periodic function s.t. $f \in L^p(Y)$ with $1 \leq p \leq \infty$. Define*

$$f^\varepsilon(x) = f(\tfrac{x}{\varepsilon}) \qquad \text{a.e. for} x \in \mathbb{R}^n. \tag{2.1.19}$$

Then, as $\varepsilon \to 0$,

$$f^\varepsilon \rightharpoonup \frac{1}{|Y|} \int_Y f(x)\,\mathrm{d}x \quad \text{in } L^p(\Omega), \tag{2.1.20}$$

if $p < \infty$. The convergence is weak- in $L^\infty(\mathbb{R}^n)$.*

2.1.4. Multicomponent Flows

We settle the notation for the multicomponent flows in Chapter 5. We consider a chemical mixture of $N_{\text{sp}} \in \mathbb{N}, N_{\text{sp}} \geq 2$ different species. Let $1 \leq i \leq N_{\text{sp}}$. Let the **molar mass** of species i be m_i, its **dynamic viscosity** is denoted by μ_i.

Definition 2.1.9 (Species Molar Fraction)**.** *The **molar fraction** of species i in the considered mixture, x_i, is the ratio of the number of moles of species i, n_i, and the total number of moles in the mixture, n:*

$$x_i := \frac{n_i}{n}. \tag{2.1.21}$$

There holds by definition

$$\sum_{i=1}^{N_{\text{sp}}} x_i = 1. \tag{2.1.22}$$

Definition 2.1.10 (Molecular Mass of the Mixture)**.** *The molecular weight of the mixture, $\overline{m}$, is the weighted harmonic mean of the molecular weights given by*

$$\overline{m} := \sum_{i=1}^{N_{\text{sp}}} x_i m_i. \tag{2.1.23}$$

We can now define another method to describe the composition of the mixture.

Definition 2.1.11 (Species Mass Fraction)**.** *Let x_i be the molar fraction of species i.Its* mass fraction *in the considered mixture, y_i, is defined by*

$$y_i := \frac{x_i m_i}{\overline{m}}. \tag{2.1.24}$$

There holds

$$\sum_{i=1}^{N_{\text{sp}}} y_i = 1. \tag{2.1.25}$$

Definition 2.1.12 (Universal Gas Constant)**.** *The **universal gas constant** R is*

$$R := 8.314\,462\,1\,\text{J/mol K}, \tag{2.1.26}$$

with a relative uncertainty of $9.1 \cdot 10^{-7}$.

Definition 2.1.13 (Faraday Constant)**.** *The **Faraday constant** F is defined as the product of the Avogadro constant and the elementary charge. Its value is*

$$F := 96\,485.3365\,\text{A s/mol}, \tag{2.1.27}$$

with a relative uncertainty of $2.2 \cdot 10^{-8}$.

Definition 2.1.14 (Perfect Gas Law)**.** *Let a pressure p, temperature T and and mass fractions y_k for $1 \leq k \leq N_{\text{sp}}$ be given. Under the assumption that the mixture behaves*

as an ideal gas*, its density* ρ *is given by*

$$\rho = \frac{p\overline{m}}{\overline{RT}}, \tag{2.1.28}$$

where R *is the* universal gas constant.

2.2. Introduction to Periodic Homogenization

We give in this section a brief introduction into the goals and methods of the mathematical homogenization of PDEs in a periodic context. For a broader presentation of the topic, we refer the reader to standard textbooks such as Bensoussan et al. [22], E [54], Tartar [127], Zhikov et al. [139] or Cioranescu and Donato [43].

Homogenization is a mathematical tool that allows us to make the *upscaling process* of a partial differential equation rigorous and can be understood as a kind of "averaging"-process. It takes a microscopic description of a (physical) process and transfers it to the macroscopic level. Examples for such a transfer from the micro- to the macro-level can be found in mathematical models from a lot of different areas of research (solid mechanics, fluid mechanics, gas dynamics). However, not all have bridged this step by an homogenization technique – instead, an empirical ansatz (using linearization, symmetry arguments or invariance properties) is often employed. Consider for example mathematical fluid mechanics, where we model Newtonian fluids (and property of fluids such as viscosity) as a continuum, even though on a very fine scale the fluid consists not of one homogeneous mass but single, distinct molecules. On the microscopic scale, the fluid is modelled by some molecular dynamics, but if the domain in which we consider this fluid is large enough, we can describe most quantities in a satisfactory manner by the solution of the Navier-Stokes equation.

Now the basic idea of homogenization is the following. Consider a family of partial differential equations which solutions v^ε have typically variations in the scale of $\varepsilon > 0$ (the **microscopic level**). The question is now, does a function v exist s.t.

$$v = \lim_{\varepsilon \to 0} v^\varepsilon \tag{2.2.1}$$

holds? If yes, what is the differential equation that v fulfills? This is then what we consider as the **macroscopic model**. The sense in which (2.2.1) is to be understood will be specified later in this chapter.

In the next section, we explain at an example how homogenization uses microscopic information to generate an appropriate model on the macroscopic level.

Introductory Example

We will show how homogenization transfers a microscopic description to the macroscopic level by a descriptive 1-d example.

Consider the function

$$\begin{array}{rccl} a & : & \mathbb{R} & \longrightarrow & \mathbb{R} \\ & & x & \longmapsto & 2 + 2\sin(2\pi x), \end{array} \tag{2.2.2}$$

and for $\varepsilon > 0$

$$\begin{array}{rccl} a^\varepsilon & : & \mathbb{R} & \longrightarrow & \mathbb{R} \\ & & x & \longmapsto & a(\frac{x}{\varepsilon}). \end{array} \tag{2.2.3}$$

Problem 2.2.1. *Find a solution v^ε s.t.*

$$-(a^\varepsilon v^{\varepsilon\prime})' = 1 \qquad \text{in } (0,1), \tag{2.2.4a}$$

$$v^\varepsilon = 0 \qquad \text{on } \{0,1\}. \tag{2.2.4b}$$

See Figure 2.2.1 where the solutions to this microscopic problem are depicted for $\varepsilon \in \{1/4, 1/8, 1/16, 1/32\}$. We observe that the oscillations get smaller with ε and that v^ε approaches a quadratic function. The question is, how is the series of solutions $(v^\varepsilon)_\varepsilon$ behaving for $\varepsilon \to 0$?

Consider the weak formulation of Problem 2.2.1. It can be shown by standard arguments that $(v^\varepsilon)_\varepsilon$ and $(v^{\varepsilon\prime})_\varepsilon$ are both bounded in $L^2(\Omega)$ (see e.g. Zhikov et al. [139]). Thus, there exists a function $v \in H_0^1(\Omega)$ s.t.

$$\left.\begin{array}{l} v^\varepsilon \to v \\ v^{\varepsilon\prime} \rightharpoonup v' \end{array}\right\} \text{ in } L^2(\Omega). \tag{2.2.5}$$

How can we determine v? Is there a PDE which v satisfies? Indeed there is such an equation. But let us first remark why we can not simply take advantage of (2.2.5) by passing to the limit in the microscopic equation.

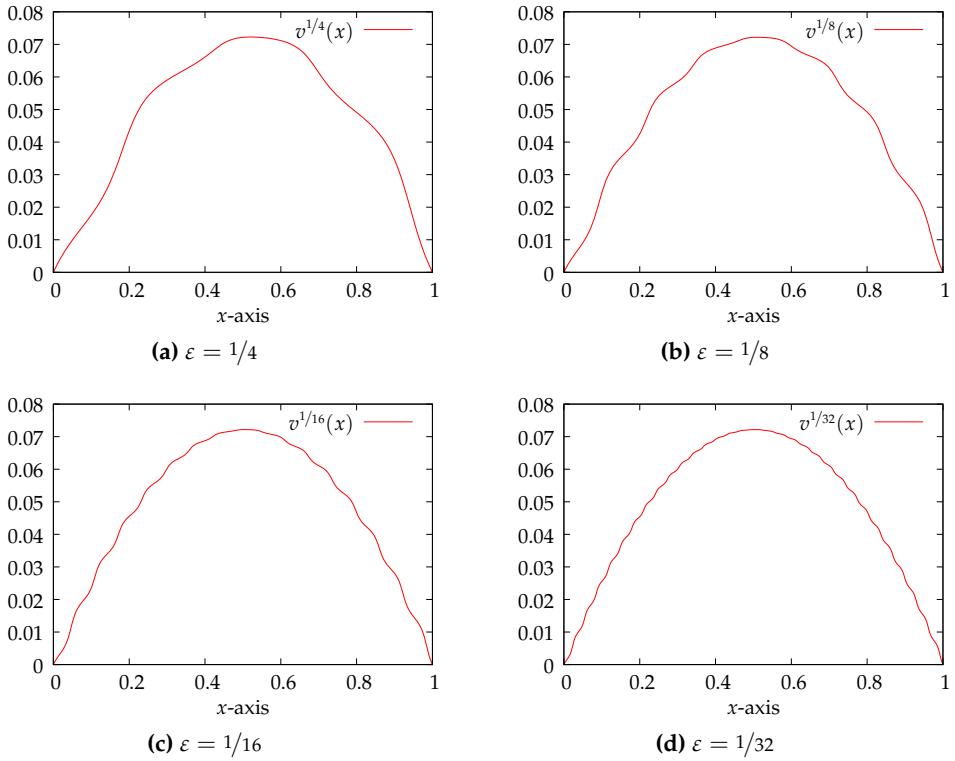

(a) $\varepsilon = 1/4$ **(b)** $\varepsilon = 1/8$

(c) $\varepsilon = 1/16$ **(d)** $\varepsilon = 1/32$

Figure 2.2.1.: Solutions of Problem 2.2.1 for different ε-values.

Remark 2.2.2 (Naive Approach)**.** *Note that due to the periodicity of a^ε and Theorem 2.1.8 it holds*

$$a^\varepsilon \rightharpoonup \bar{a} := \int_0^1 a(x)\,\mathrm{d}x. \tag{2.2.6}$$

Consider the variational formulation of Problem 2.2.1:

$$(a^\varepsilon v^{\varepsilon\prime}, \varphi') = (1, \varphi) \qquad \text{for all } \varphi \in H_0^1(\Omega). \tag{2.2.7}$$

So we could assume that v satisfies

$$(\bar{a}v', \varphi') = (1, \varphi) \qquad \text{for all } \varphi \in H_0^1(\Omega) \tag{2.2.8}$$

However, this is not true as the product of two weakly convergent functions is in general not the product of the limits, i.e.

$$\lim_{\varepsilon \to \inf} a^\varepsilon v^\varepsilon \neq \bar{a}v. \tag{2.2.9}$$

The challenge in the homogenization process is to determine the correct limit in (2.2.9).

The function v satisfies the following **homogenized** (or *effective* or *macroscopic*) equation:

Problem 2.2.3. *Find a solution v s.t.*

$$-(a^0 v')' = 1 \qquad \text{in } (0,1), \tag{2.2.10a}$$
$$v = 0 \qquad \text{on } \{0,1\}. \tag{2.2.10b}$$

The effective coefficient a^0 *is defined as*

$$a^0 = \frac{1}{\int_0^1 \frac{1}{a(x)}\,\mathrm{d}x} = \frac{1}{\sqrt{3}}. \tag{2.2.11}$$

Remark 2.2.4. *Note that in general*

$$a^0 = \frac{1}{\int_0^1 \frac{1}{a(x)}\,\mathrm{d}x} \neq \int_0^1 a(x)\,\mathrm{d}x = \bar{a}. \tag{2.2.12}$$

In Table 2.2.1 the convergence of the *homogenization error* $v - v^\varepsilon$ in the $L^2(\Omega)$ and $H_0^1(\Omega)$-norm is shown. We see that we have first order convergence in the $L^2(\Omega)$-norm, whereas the gradients do not converge to zero. In Figure 2.2.2 we show the gradients of v^ε for different ε-values and we see that we can not expect a strong convergence towards v', but only a weak convergence (see (2.2.5)). It is possible to enhance the convergence properties with the help of so called *correctors*, defined by some auxiliary equations. See the next section for an example.

ε	$\|v - v^\varepsilon\|$	$\|v' - v^{\varepsilon\prime}\|$
$1/4$	$4.2 \cdot 10^{-3}$	$6.4 \cdot 10^{-2}$
$1/8$	$2.1 \cdot 10^{-3}$	$6.5 \cdot 10^{-2}$
$1/16$	$1.1 \cdot 10^{-3}$	$6.5 \cdot 10^{-2}$
$1/32$	$5.4 \cdot 10^{-4}$	$6.5 \cdot 10^{-2}$

Table 2.2.1.: Homogenization error of Problem 2.2.1.

This 1-d example highlights the basic properties of homogenization and allows for a nice visualization, but some properties do not carry over to the multi-dimensional case. We will see that in general we can no longer describe the effective coefficient by an explicit formula as done in (2.2.11). We need the help of some auxiliary problems in this case, see next section.

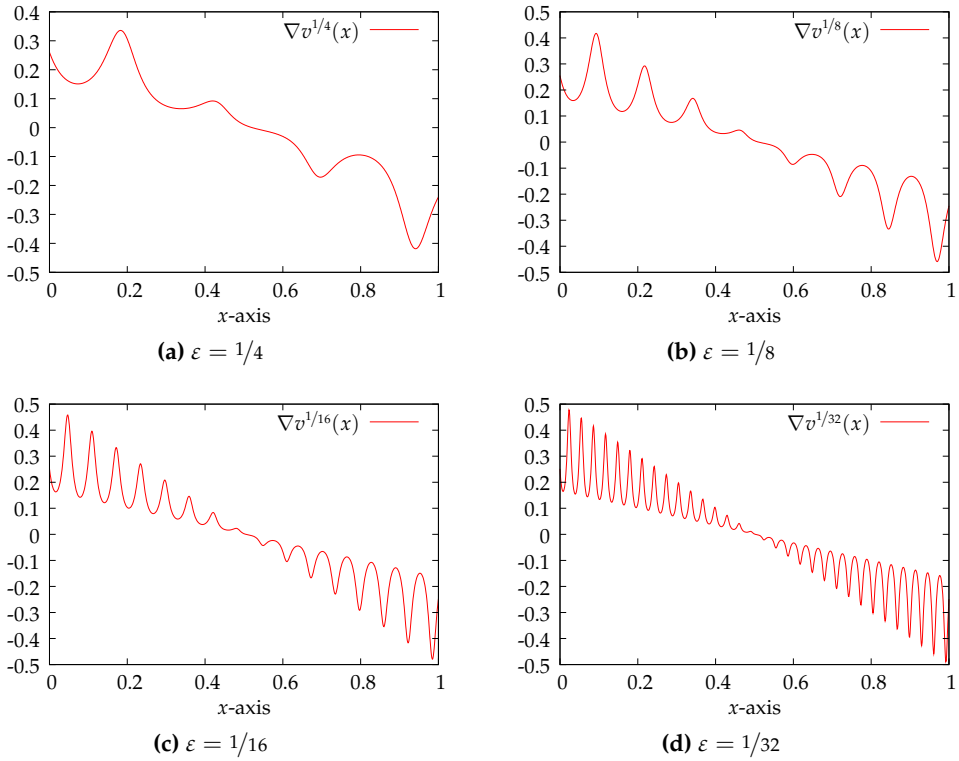

(a) $\varepsilon = 1/4$ **(b)** $\varepsilon = 1/8$

(c) $\varepsilon = 1/16$ **(d)** $\varepsilon = 1/32$

Figure 2.2.2.: Gradients of the solutions of Problem 2.2.1 for different ε-values.

Remark 2.2.5. *From the mathematical point of view we have a series of microscopic solutions which converge towards the macroscopic solution v, i.e. the v^ε approximate v. Further, when we want to model a physical process (like gas-transport in an SOFC) we are interested in one specific v^ε for a given epsilon, and we use the macroscopic solution as an approximation of this v^ε.*

We also adopt the latter viewpoint in this thesis. This means that the homogenization error *$v - v^\varepsilon$ is given for our model and we can not improve it by making ε small, as it is given (in our case by the geometry of the anode).*

2.2.1. Asymptotic Expansion

The 1-d example in the previous section has a microscopic problem with a periodically oscillating coefficient. We will focus in this section on 2-d microscopic problems whose oscillations are caused by the fact that the problems are studied in perforated domains with a periodic arrangement of the obstacles. We present

the **formal asymptotic two-scale expansion** at the well known model problem of a linear diffusion process. But first we define periodically perforated domains.

Definition 2.2.6 (Periodically Perforated Domains)**.** *A periodically perforated domain Ω^ε is defined as follows.*

Let (ε) be a series of small parameters s. t.

$$\frac{1}{\varepsilon} \in \mathbb{N} \tag{2.2.13}$$

and let $Y = [0,1]^2$ be the unit cell from which we cut out an obstacle Y_s, which does not have to be connected. We assume Y_s is closed, ∂Y_s is piecewise smooth and $Y_s \subset Y$. Let $Y_f = Y \setminus Y_s$.

We define the set O^ε as all obstacles homothetic to Y_s with a ratio of ε,

$$O^\varepsilon = \bigcup_{k\in\mathbb{Z}^2} \varepsilon\Big(k + Y_s\Big). \tag{2.2.14}$$

Given a bounded domain $\Omega \subset \mathbb{R}^2$ with

$$\partial\Omega \cap \partial O^\varepsilon = \emptyset \quad \forall \left\{ \varepsilon \,\middle|\, \frac{1}{\varepsilon} \in \mathbb{N} \right\}, \tag{2.2.15}$$

we define the perforated domain by

$$\Omega^\varepsilon = \Omega \setminus O^\varepsilon. \tag{2.2.16}$$

Remark 2.2.7. *In Definition 2.2.6 the restrictions* (2.2.13) *and* (2.2.15) *are stated to ensure a piecewise smooth outer boundary of the microscopic domain Ω^ε. One can drop these assumptions, see for example Zhikov et al. [139].*

Consider the simple model problem on a periodically perforated domain Ω^ε.

Problem 2.2.8. *We use the assumptions and notation of Definition 2.2.6 regarding the perforated domain Ω^ε. Let $f \in L^2(\Omega^\varepsilon)$. Consider the symmetric, Y-periodic diffusion tensor*

$$\mathbf{A} : \mathbb{R}^2 \setminus \bigcup_{z\in\mathbb{Z}^2} \Big(z + Y_s\Big) \to \mathbb{R} \tag{2.2.17}$$

(and $A_{ij} \in L^\infty(\mathbb{R}^n)$) which we assume to be elliptic, i.e. there exists $\alpha, \beta > 0$ s.t.

$$\alpha|\xi|^2 \le \sum_{i,j=1}^{2} A_{ij}(y)\xi_i\xi_j \le \beta|\xi|^2 \qquad \forall \xi \in \mathbb{R}^2, y \in Y_f. \tag{2.2.18}$$

We define the oscillating coefficient $\mathbf{A}^\varepsilon : \Omega \to \mathbb{R}^2$ *by*

$$\mathbf{A}^\varepsilon(x) = \mathbf{A}(\tfrac{x}{\varepsilon}). \tag{2.2.19}$$

The microscopic problem *reads:*

Find v^ε *s.t.*

$$-\nabla \cdot (\mathbf{A}^\varepsilon \nabla v^\varepsilon) = f \qquad \text{in } \Omega^\varepsilon \tag{2.2.20a}$$

$$v^\varepsilon = 0 \qquad \text{on } \partial\Omega^\varepsilon \setminus \partial O^\varepsilon, \tag{2.2.20b}$$

$$\mathbf{n} \cdot (\mathbf{A}^\varepsilon \nabla v^\varepsilon) = 0 \qquad \text{on } \partial O^\varepsilon. \tag{2.2.20c}$$

Again, we are interested in the behaviour of v^ε as $\varepsilon \to 0$, see Figure 2.2.3.

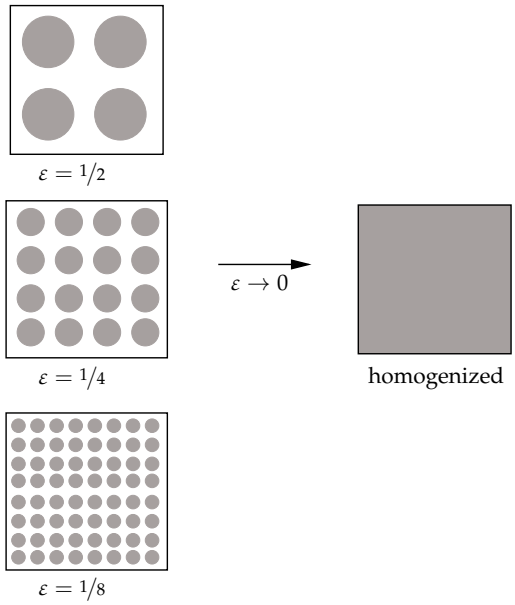

Figure 2.2.3.: Sketch of homogenization process of periodically perforated domains.

Before we proceed to get a result similar to (2.2.5), we have to address a point that makes the homogenization process in the context of perforated domains slightly more complex than in the case of oscillating coefficients. The basic reasoning is the same as in the previous 1-d example, see Section 2.2. However, we can not establish in the same way the boundedness of the series $(v^\varepsilon)_\varepsilon$ and $(v^{\varepsilon\prime})_\varepsilon$ in $L^2(\Omega^\varepsilon)$, as the microscopic problems are defined on a series of varying domains Ω^ε. To state the convergence results in some fixed Sobolev spaces defined on the

homogenized domain Ω, we need to extend v^ε to Ω, i.e. find a function

$$\tilde{v}^\varepsilon : \Omega \to \mathbb{R} \tag{2.2.21}$$

s.t.

$$\tilde{v}^\varepsilon\Big|_{\Omega^\varepsilon} = v^\varepsilon \quad \text{and} \quad \|\tilde{v}^\varepsilon\|_{H^1(\Omega)} \leq \mathcal{C}\|v^\varepsilon\|_{H^1(\Omega^\varepsilon)} \tag{2.2.22}$$

with a constant $\mathcal{C} > 0$ independent of ε. After this expansion is established the usual arguments lead to the existence of a function v s.t.

$$\left.\begin{array}{l} \tilde{v}^\varepsilon \to v \\ \tilde{v}^{\varepsilon,\prime} \rightharpoonup v' \end{array}\right\} \text{ in } L^2(\Omega). \tag{2.2.23}$$

How do we determine the macroscopic equation which v satisfies? There are various possibilities, we use the **formal asymptotic two-scale expansion**.

Formal Asymptotic Expansion

The ansatz utilizes an asymptotic expansion with a splitting into two different scales (i.e. "slow" and "fast" variables x and x/ε), see Bakhvalov and Panasenko [13], Bensoussan et al. [22], Sánchez-Palencia [119]. The slow variable x describes macroscopic changes and the fast variable y measures the microscopic behaviour. It is purely a formal method to determine the homogenized equations, the justification of the obtained formulas needs the use of other methods.

We take the ansatz that the microscopic solution allows for an expansion of the form

$$v^\varepsilon(x) = \sum_{i=1}^{\infty} \varepsilon^i v_i(x, \tfrac{x}{\varepsilon}), \tag{2.2.24}$$

where the functions

$$\begin{array}{rccc} v_i & : & \Omega \times \mathbb{R}^n \setminus O^\varepsilon & \longrightarrow & \mathbb{R} \\ & & (x, y) & \longmapsto & v_i(x, y), \end{array} \tag{2.2.25}$$

are assumed to be Y-periodic w.r.t. y for all $x \in \Omega$. For small ε, the value x/ε changes much more rapidly than x and allows us to exploit scale separation, i.e. treat x and $y = x/\varepsilon$ as *independent variables*.

Remark 2.2.9. *The ansatz* (2.2.24) *neglects information about the (outer) boundary conditions. This is the source of some serious technical difficulties when we try to justify*

the result of the method later on. One tool to correct this is the use of boundary layers, see, e.g., Bensoussan et al. [22].

The basic idea is to plug (2.2.24) into the microscopic equation (2.2.20a). Note that differentiating a function of type $\varphi^\varepsilon(x) := \varphi(x, x/\varepsilon)$ w.r.t. x leads to

$$\nabla\varphi^\varepsilon(x) = \nabla_x \varphi(x,y)\Big|_{y=x/\varepsilon} + \frac{1}{\varepsilon}\nabla_y \varphi(x,y)\Big|_{y=x/\varepsilon}. \tag{2.2.26}$$

Bearing this in mind, we express the application of the microscopic differential operator

$$\mathcal{A}^\varepsilon\varphi^\varepsilon := -\nabla\cdot(\mathbf{A}^\varepsilon\nabla\varphi^\varepsilon), \tag{2.2.27}$$

by

$$\mathcal{A}^\varepsilon\varphi^\varepsilon = \left(\varepsilon^{-2}\mathcal{A}_1 + \varepsilon^{-1}\mathcal{A}_2 + \varepsilon^0\mathcal{A}_3\right)\varphi, \tag{2.2.28}$$

where

$$\mathcal{A}_1 = -\nabla_y\cdot\left(\mathbf{A}(y)\nabla_y\right), \tag{2.2.29}$$

$$\mathcal{A}_2 = -\nabla_y\cdot\left(\mathbf{A}(y)\nabla_x\right) - \nabla_x\cdot\left(\mathbf{A}(y)\nabla_y\right), \tag{2.2.30}$$

$$\mathcal{A}_3 = -\nabla_x\cdot\left(\mathbf{A}(y)\nabla_x\right). \tag{2.2.31}$$

Inserting (2.2.24) and (2.2.28) into (2.2.20a) leads to a cascade of equations. Sorting by powers of epsilon and neglecting the terms of order ε leads to the following equations:

$$\mathcal{O}(\varepsilon^{-2}): \quad \mathcal{A}_1 v_0 = 0 \quad \text{in } \Omega\times Y_\mathrm{f}, \tag{2.2.32a}$$

$$\mathcal{O}(\varepsilon^{-1}): \quad \mathcal{A}_1 v_1 + \mathcal{A}_2 v_0 = 0 \quad \text{in } \Omega\times Y_\mathrm{f}, \tag{2.2.32b}$$

$$\mathcal{O}(\varepsilon^{0}): \quad \mathcal{A}_1 v_2 + \mathcal{A}_2 v_1 + \mathcal{A}_3 v_0 = f \quad \text{in } \Omega\times Y_\mathrm{f}. \tag{2.2.32c}$$

We deduce in the same way the following equations for $y \in \partial Y_\mathrm{s}$, the only difference is that we neglect only the equations corresponding to $\mathcal{O}(\varepsilon^2$ and higher):

$$\mathcal{O}(\varepsilon^{-1}): \quad \mathbf{n}\cdot\left(\mathbf{A}\nabla_y v_0\right) = 0 \quad \text{on } \Omega\times\partial Y_\mathrm{s}, \tag{2.2.33a}$$

$$\mathcal{O}(\varepsilon^{0}): \quad \mathbf{n}\cdot\left(\mathbf{A}\nabla_y v_1\right) + \mathbf{n}\cdot\left(\mathbf{A}\nabla_x v_0\right) = 0 \quad \text{on } \Omega\times\partial Y_\mathrm{s}, \tag{2.2.33b}$$

$$\mathcal{O}(\varepsilon^{1}): \quad \mathbf{n}\cdot\left(\mathbf{A}\nabla_y v_2\right) + \mathbf{n}\cdot\left(\mathbf{A}\nabla_x v_1\right) = 0 \quad \text{on } \Omega\times\partial Y_\mathrm{s}. \tag{2.2.33c}$$

Here denotes $\mathbf{n}$ the normal on ∂Y_s.

Consider (2.2.32a) together with the boundary condition (2.2.33a):

Problem 2.2.10. *Find v_0 Y-periodic s.t.*

$$-\nabla_y \cdot \Big(\mathbf{A}(\cdot)\nabla_y\Big) v_0(x,\cdot) = 0 \qquad \text{in } Y_f, \tag{2.2.34a}$$

$$\mathbf{n} \cdot \Big(\mathbf{A}(\cdot)\nabla_y v_0(x,\cdot)\Big) = 0 \qquad \text{on } \partial Y_s. \tag{2.2.34b}$$

The variable x acts as a parameter in this equation. Problem 2.2.10 is uniquely solvable in the function space

$$\frac{H^1_{\text{per}}(Y_f)}{\mathbb{R}} \tag{2.2.35}$$

(see, e.g., Cioranescu and Paulin [44]) and thus independent of y, i.e.

$$v_0(x,y) = v_0(x). \tag{2.2.36}$$

Now we consider (2.2.32b) together with (2.2.33b) and take (2.2.36) into account, we end up with

Problem 2.2.11. *Find v_1 Y-periodic s.t.*

$$-\nabla_y \cdot \Big(\mathbf{A}(\cdot)\nabla_y v_1(x,\cdot)\Big) = \nabla_y \cdot \big(\mathbf{A}(\cdot)\nabla_x v_0(x)\big) \qquad \text{on } Y_f, \tag{2.2.37a}$$

$$\mathbf{n} \cdot \Big(\mathbf{A}(\cdot)\nabla_y v_1(x,\cdot)\Big) = -\mathbf{n} \cdot \big(\mathbf{A}(\cdot)\nabla_x v_0(x)\big) \qquad \text{on } \partial Y_s. \tag{2.2.37b}$$

Due to the separation of x and y in the right hand side of equation (2.2.37) we take the following ansatz

$$v_1(x,y) = -\sum_{i=1}^{n} w_i(y)\partial_{x_i} v_0(x) + \tilde{v}_1(x), \tag{2.2.38}$$

where w_i are the solutions of the following **cell problems**:

Problem 2.2.12 (Cell Problem)**.** *We use the notation and assumptions of Problem 2.2.8 Let $1 \le i \le n$. Find w_j Y-periodic s.t. it fulfils the* cell problem

$$-\nabla_y \cdot \Big(\mathbf{A}\nabla_y w_j\Big) = \nabla_y \cdot \mathbf{A}\mathbf{e}_j \qquad \text{in } Y_f, \tag{2.2.39}$$

$$\mathbf{n} \cdot \Big(\mathbf{A}\nabla_y w_j\Big) = \mathbf{n} \cdot \mathbf{A}\mathbf{e}_j \qquad \text{on } \partial Y_s. \tag{2.2.40}$$

It is a simple calculation to check that (2.2.38) fulfills Problem 2.2.11. The constant $\tilde{v}_1(x)$ is somewhat irrelevant as only the gradient of v_1 is needed in the homogenized equation that follows.

Last, we consider (2.2.32c) together with (2.2.33b). After we integrate (2.2.32c) over Y_f and take the periodicity of the v_1 w.r.t. y, equation (2.2.36) and ansatz (2.2.38) into account, we end up with the following homogenized equation.

Problem 2.2.13 (Homogenized Equation)**.** *We use the notation and assumptions of Problem 2.2.8. The* homogenized problem *reads:*

Find $v = v_0$ s.t.

$$-\nabla \cdot \left(\mathbf{A}^{\mathrm{hom}} \nabla v \right) = |Y_\mathrm{f}| \, f \qquad \text{in } \Omega, \tag{2.2.41a}$$

$$v = 0 \qquad \text{on } \partial\Omega. \tag{2.2.41b}$$

Hereby is $\mathbf{A}^{\mathrm{hom}}$ the homogenized *or* effective *diffusion tensor. Its entries are defined by*

$$\mathbf{A}_{ij}^{\mathrm{hom}} := \int_{Y_\mathrm{f}} \left(\mathbf{A}(y) \nabla_y w_j \right) \cdot \mathbf{e}_i + A_{ij}(y) \, \mathrm{d}y \qquad 1 \le i, j \le n, \tag{2.2.42}$$

where $\{ w_1, \ldots, w_n \}$ are the solutions of the cell problems 2.2.12.

Remark 2.2.14. *The homogenized diffusion tensor* (2.2.42) *is again elliptic, see Bensoussan et al. [22].*

The presented method is not mathematically rigorous. It delivers (at least in this example) the correct homogenized limit, but it gives no proof of the convergence. Nevertheless it is a valuable tool to get an idea of how the effective equation looks like. We refer to the next section regarding the justification of the homogenization process.

Theorem 2.2.15. *There holds*

$$\| v^\varepsilon - v \|_{\Omega^\varepsilon} \to 0 \tag{2.2.43}$$

Proof. See, e.g., Cioranescu and Paulin [44]. □

Justification of the Homogenization Process

We present in this section briefly three methods (out of many more) which allow to justify the formal homogenization process of the previous section. We do not go into detail and refer the interested reader to the stated references.

- The **energy method** or **method of oscillating test functions** by Murat and Tartar [102], Tartar [126], see also Tartar [127]. The method is not restricted to the periodic case. The main idea of this method is to use in (2.2.6) a series of specially designed test functions φ^ε that allow in the end for a passing to the limit in the equation, even though the product of weakly convergent functions appears. The construction of the the series $(\varphi^\varepsilon)_\varepsilon$ of the so called oscillating test functions requires the solution of *dual cell problems*.
- The method of **two-scale convergence** was introduced in Nguetseng [105] and further developed in Allaire [8]. The method is only applicable to periodic homogenization problem. However, it is self-contained in the respect that we do not need to know the form of the homogenized equation before, as it comes out of the homogenization process with this method. The method relies on the definition of a new type of convergence (the eponymous two-scale convergence) and the choice of clever test functions. It leads to a (system of) partial differential equations in x and y, the *two-scale homogenized problem*. In some cases it is possible to decouple the two-scale homogenized problem into a macroscopic equation in x and some cell problems in y.
- The **periodic unfolding method** was introduced by Cioranescu et al. [45] for the study of classical periodic homogenization and applied to homogenization problems in periodically perforated domains in Cioranescu et al. [46]. This method relies on a so called unfolding operator and decomposition of macroscopic and microscopic scales. The main advantage is that due to the unfolding operator this method does not rely on any extension operators and can thus be applied to a broader range of inclusions (like snow-flake type inclusions). It is also only applicable in the periodic context.

3. Stokes-Darcy Interface Coupling

The application we have in mind is the description of mass transport in the anode-part of an SOFC. The focus of the present chapter lies on the description of the flow field in the anode and the overlying gas channel, i.e. the mathematical description of slow incompressible viscous flow (i.e. Stokes flow) over a porous bed. We note that in general the coupling of Stokes flow and Darcy flow is a problem with a wide range of applications and by no means restricted to fuel cell simulations. Examples are simulation of groundwater flow [33, 53], flow of blood through arterial vessels [49] or industrial filters [69].

For the main part of this chapter we are concerned about the situation we face in the fuel cell simulation, i.e. a main flow direction which is tangential to the interface of free flow domain and porous medium. In Section 3.4 we consider the case where we force the flow to enter the perforated domain, i.e. a main flow direction that is normal to the interface.

Lets focus on the tangential case first. As we have explained previously in Section 2.2, we have to use homogenized models as we can not resolve the porous structure of the anode with our discretization. Thus, we have to upscale the Stokes equation in the porous medium and replace it by its well known homogenization limit, Darcy's law. This homogenization process leads to the appearance of an artificial interface at the boundary between the perforated domain and the unconstrained flow domain. The question which arises then naturally is: *What are the correct coupling conditions on this interface?*

The answer to this question can be found in Marciniak-Czochra and Mikelić [98] (see also Jäger and Mikelić [77], Jäger et al. [80]), where the authors have (in the context of mathematical homogenization) rigorously proven a set of coupling conditions consisting of the famous Beavers-Joseph-Saffman (*BJS*, see Beavers and Joseph [19], Saffman [117]) condition as well as a so called **pressure jump law**. Whereas the BJS-condition is generally accepted, interface laws for the effective stress have been a subject of controversy.

We give a numerical confirmation of the aforementioned interface laws by a direct numerical simulation of the flow on the microscopic level. To this end we look at the "homogenization error" between the solution of the microscopic problems and the homogenized (or *effective*) solution. The numerical challenge

is that we have to make sure that the discretization error is smaller than the error stemming from the homogenization process, which leads to the necessity of high accuracy in our computations. We handle this difficulty by (goal-oriented) adaptive mesh refinement.

Most of the results presented in this chapter are already published in Carraro, Goll, Marciniak-Czochra, and Mikelič [36] and [37].

The structure of this chapter is as follows. We first present the problem in the tangential flow configuration on the microscopic level and recapitulate the effective equations (and more importantly the effective interface laws) on the macroscopic level in Section 3.1. Afterwards, we describe in Section 3.2 how we approximate the equations defined previously. In Section 3.3, we confirm the interface conditions (especially the pressure jump law) by a comparison between the microscopic problem and the effective one for two different flow configurations. Section 3.2 and Section 3.3 contain thus the main result of this chapter as well as the authors contribution to Carraro, Goll, Marciniak-Czochra, and Mikelič [36]. The chapter is completed by Section 3.4 which is concerned with the Stokes-Darcy interface coupling in the case of a forced infiltration into a porous medium. We present the correct conditions in this case and give, as before, a numerical confirmation by computations on the microscopic level. This part is the authors contribution to Carraro, Goll, Marciniak-Czochra, and Mikelić [37].

3.1. Statement of the Problem and Effective Equations

In the model we assume a slow incompressible viscous flow through an unconfined region

$$\Omega_{\mathrm{f}} := (0, L) \times (0, H_{\mathrm{u}}) \tag{3.1.1}$$

and the pores $\Omega_{\mathrm{p}}^{\varepsilon}$ (see (3.1.6)) of a porous medium

$$\Omega_{\mathrm{p}} := (0, L) \times (-H_{\mathrm{l}}, 0)\,, \tag{3.1.2}$$

where $L, H_{\mathrm{u}}, H_{\mathrm{l}} > 0$ are positive numbers denoting the length and the height of the domain above and below zero. We denote the line separating Ω_{f} and Ω_{p} by

$$\Gamma := (0, L) \times \{\, 0 \,\}\,. \tag{3.1.3}$$

Note that we consider in this chapter flows with main flow direction tangential to Γ, i.e. we assume no-slip conditions on the the part of the boundary which is parallel to the interface. The same holds true for the boundaries of the inclusions, as they model a rigid structure.

As we rely on analytically derived effective equations and interface conditions, the porous medium is assumed to be periodic, i.e. it is made up of the periodic repetition of a re-scaled unit cell, see the next Section 3.1.1, where we give a proper definition of the geometry and the equations on the microscopic level. After the formulation of the problem is settled, we present the homogenization results of Marciniak-Czochra and Mikelić [98], especially the interface laws on Γ, see Section 3.3.

3.1.1. The Microscopic Level

The flow on the microscopic level is modelled by the steady Stokes equation, which will be presented after the discussion of the pore-geometry. For a derivation of Stokes equation, we refer to standard textbooks on fluid dynamics, for example Temam [129].

Definition of the Geometry

The geometry of the microscopic problem is sketched in Figure 3.1.1b and, more precisely, the periodic structure of the perforated domain Ω_p is defined as follows.

Definition 3.1.1 (Unit Cell). *Let the so called* unit cell $Y := [0,1]^2$ *contain a closed solid obstacle* $Y_s \neq \emptyset$ *with a* $C^{0,1}$*-boundary* ∂Y_s *and a positive measure. The complement of* Y_s *in* Y *defines the pore, or the* fluid part

$$Y_f := Y \setminus Y_s. \tag{3.1.4}$$

We assume further, that Y_f is connected, i.e. the fluid can flow freely through the perforated domain and does not get trapped inside the solid structure, see Figure 3.1.1a for a sketch.

To make things easy, we assume the *characteristic pore size* $\varepsilon > 0$ (which we assume to be "small") to be such that there holds $L/\varepsilon, H_u/\varepsilon, H_l/\varepsilon \in \mathbb{N}$. We consider

a periodic repetition of the obstacle, scaled by ε, and build so the "skeleton" S_p of the porous bed. In formulas:

$$S_\mathrm{p} := \Omega_\mathrm{p} \cap \sum_{(i,j)\in\mathbb{Z}^2} \varepsilon \left(Y_\mathrm{s} + (i,j) \right) \tag{3.1.5}$$

Subsequently the pore-space of the perforated domain Ω_p is defined by

$$\Omega_\mathrm{p}^\varepsilon := \Omega_\mathrm{p} \setminus S_\mathrm{p}. \tag{3.1.6}$$

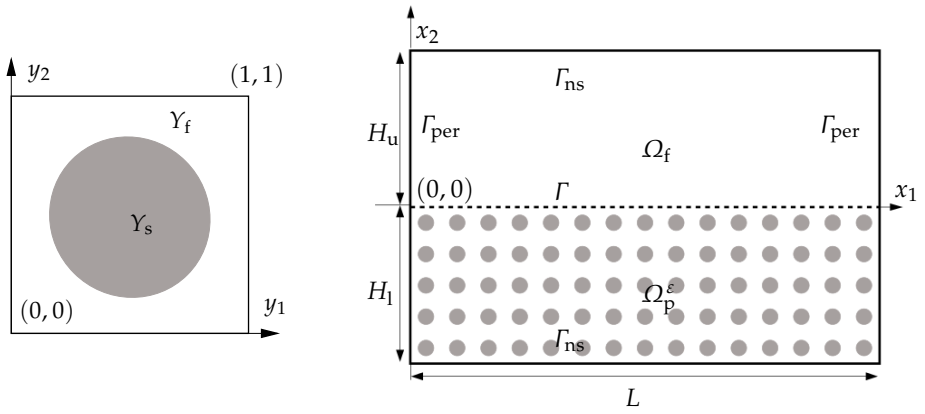

(a) Unit cell Y.

(b) Flow region Ω^ε.

Figure 3.1.1.: Sketch of the (microscopic) geometry.

Definition 3.1.2 (Microscopic Flow Domain)**.** *We define the microscopic flow domain by*

$$\Omega^\varepsilon := \Omega_\mathrm{f} \dot\cup \Gamma \dot\cup \Omega_\mathrm{p}^\varepsilon. \tag{3.1.7}$$

We split the boundary of Ω^ε into the two disjunct parts Γ_per and $\Gamma_\mathrm{ns}^\varepsilon$,

$$\partial\Omega^\varepsilon = \Gamma_\mathrm{per} \dot\cup \Gamma_\mathrm{ns}^\varepsilon, \tag{3.1.8}$$

where

$$\Gamma_\mathrm{per} := \{\, 0, L \,\} \times (-H_\mathrm{l}, H_\mathrm{u}), \tag{3.1.9}$$

$$\Gamma_\mathrm{ns}^\varepsilon := [0,L] \times \{\, -H_\mathrm{l}, H_\mathrm{u} \,\} \cup \left(\sum_{(i,j)\in\mathbb{Z}^2} \varepsilon \left(\partial Y_\mathrm{s} + (i,j) \right) \cap \Omega_\mathrm{p} \right). \tag{3.1.10}$$

Additionally, we name the following part of the boundary Γ_{ns}:

$$\Gamma_{\text{ns}} := [0, L] \times \{ -H_{\text{l}}, H_{\text{u}} \} . \tag{3.1.11}$$

Microscopic Model

As already stated, we impose no-slip boundary conditions on $\Gamma_{\text{ns}}^{\varepsilon}$, whereas we require the velocity and the pressure to be periodic on Γ_{per}. By this, we get rid of additional boundary layer effects near these boundaries. The driving force of the flow in this setting is a nontrivial right hand side $\mathbf{f}$, see equations (3.3.12) and (3.3.13) for an example.

Bringing everything together, the flow on the microscopic level is described by the following non-dimensional steady Stokes system.

Problem 3.1.3 (Microscopic Flow Problem)**.** *Let a force* $\mathbf{f}$ *be given. Find the velocity* $\mathbf{v}^{\varepsilon}$ *and pressure* p^{ε}*, both L-periodic in* x_1*-direction, such that there holds*

$$-\Delta \mathbf{v}^{\varepsilon} + \nabla p^{\varepsilon} = \mathbf{f} \qquad \text{in } \Omega^{\varepsilon} \tag{3.1.12a}$$
$$\nabla \cdot \mathbf{v}^{\varepsilon} = 0 \qquad \text{in } \Omega^{\varepsilon}, \tag{3.1.12b}$$
$$\mathbf{v}^{\varepsilon} = 0 \qquad \text{on } \Gamma_{\text{ns}}^{\varepsilon}, \tag{3.1.12c}$$

together with the normalization condition $\int_{\Omega_{\text{f}}} p^{\varepsilon} \, \mathrm{d}x = 0$.

Remark 3.1.4. *We present in this chapter the non-dimensional versions of the flow equations. See Section B.1.2 for the formulation with units.*

Remark 3.1.5. *We present all the equations in this thesis in strong from. However, we understand them in the usual weak sense. The strong form is chosen only to allow for better readability.*

For this example we present the weak formulation as well so that the incorporation of the periodic boundary conditions in the weak formulation becomes clear. The weak formulation related to Problem 3.1.3 reads

Problem 3.1.6 (Microscopic Flow Problem, Weak Formulation)**.** *Let a force* $\mathbf{f} \in L^2(\Omega)^2$ *be given. Find the velocity* $\mathbf{v}^{\varepsilon} \in H^1_{\Gamma_{\text{ns}}^{\varepsilon},\text{per}_1}(\Omega^{\varepsilon})^2$ *and pressure* $p^{\varepsilon} \in L^2(\Omega^{\varepsilon})$*, such that there holds*

$$(\nabla \mathbf{v}^{\varepsilon}, \nabla \boldsymbol{\varphi})_{\Omega^{\varepsilon}} - (p^{\varepsilon}, \nabla \cdot \boldsymbol{\varphi})_{\Omega^{\varepsilon}} = (\mathbf{f}, \boldsymbol{\varphi})_{\Omega^{\varepsilon}} \qquad \forall \boldsymbol{\varphi} \in H^1_{\Gamma_{\text{ns}},\text{per}_1}(\Omega^{\varepsilon})^2, \tag{3.1.13a}$$
$$(\nabla \cdot \mathbf{v}^{\varepsilon}, \xi)_{\Omega^{\varepsilon}} = 0 \qquad \forall \xi \in L^2(\Omega^{\varepsilon}). \tag{3.1.13b}$$

Additionally, we require the normalization condition $\int_{\Omega_{\text{f}}} p^{\varepsilon} \, \mathrm{d}x = 0$.

3.1.2. Macroscopic Level

In this section, we are interested in the equations that describe Problem 3.1.6 on the macroscopic level, i.e. we look for an effective equation on the *macroscopic flow domain* Ω, see Definition 3.1.7, that is valid for $\mathbf{v}^\varepsilon$ and p^ε in the limit $\varepsilon \to 0$.

Definition 3.1.7 (Macroscopic Flow Domain)**.** *We define the macroscopic flow domain by*

$$\Omega := \Omega_\mathrm{f} \dot\cup \Gamma \dot\cup \Omega_\mathrm{p}. \tag{3.1.14}$$

If we let ε tend to zero nothing happens in Ω_f so we obtain a Stokes flow after the upscaling process. This means that the effective velocity $\mathbf{v}_\mathrm{f}$ and the effective pressure p_f on the unconstrained flow domain Ω_f fulfill

$$-\Delta \mathbf{v}_\mathrm{f} + \nabla p_\mathrm{f} = \mathbf{f} \qquad \text{in } \Omega_\mathrm{f}, \tag{3.1.15a}$$
$$\nabla \cdot \mathbf{v}_\mathrm{f} = 0 \qquad \text{in } \Omega_\mathrm{f}. \tag{3.1.15b}$$

The situation is fundamentally different in the perforated domain $\Omega_\mathrm{p}^\varepsilon$. In such a medium, the flow on the macroscopic level is described by Darcy's law (3.1.16). Darcy's law for the effective pressure p_p and velocity $\mathbf{v}_\mathrm{p}$ in Ω_p reads

$$\nabla \cdot \mathbf{v}_\mathrm{p} = 0, \tag{3.1.16a}$$
$$\mathbf{v}_\mathrm{p} = \mathbf{K}(\mathbf{f} - \nabla p_\mathrm{p}), \tag{3.1.16b}$$

where $\mathbf{K} \in \mathbb{R}^{2\times 2}$ is the so called *re-scaled permeability Tensor*, which is constant, symmetric, and positive definite. Its value depends on the shape of the microstructure Y_s, see Definition 3.1.20 for the exact definition.

Remark 3.1.8. *Inserting* (3.1.16b) *into* (3.1.16a) *results in a second order elliptic PDE for the pressure* p_p*:*

$$\nabla \cdot \Big(\mathbf{K}(\mathbf{f} - \nabla p_\mathrm{p})\Big) = 0. \tag{3.1.17}$$

Interface Laws

The effective equations in the interior of Ω_f and Ω_p are known. However, the situation on the interface Γ is not so clear. We want to emphasize that this is not a physical interface but merely a consequence of the mathematical homogenization process, see Carraro, Goll, Marciniak-Czochra, and Mikelič [36]. The difficulty in defining correct coupling conditions across Γ is due to the fact that the differential

operators acting on Ω_f and Ω_p are quite different. Whereas the Stokes-operator (3.1.15) is of second order for the velocity and of first order for the pressure, the Darcy-operator (3.1.17) is of second order for the pressure.

To get rid of the latter problem, some authors prefer the *one-domain approach* (as opposed to the *two-domain approach* we employ, see also Goyeau et al. [67] for an overview) by using the Brinkman equation, see Brinkman [32],

$$\nabla p - \mu_{eff} \Delta \mathbf{v} + \chi_{\Omega_p} \mathbf{K}^{-1} \mathbf{v} = \mathbf{f}, \tag{3.1.18a}$$

$$\nabla \cdot \mathbf{v} = 0, \tag{3.1.18b}$$

in both domains, as this equation is of the same type as the Stokes equation, see for example Bars and Worster [17], Neale and Nader [104]. For this case, Ochoa-Tapia and Whitaker [107, 108] developed a set of coupling conditions involving the continuity of the velocity together with a stress jump. However, Nield [106] criticizes that the Brinkman model is semi-empirical and the value of the viscosity μ_{eff} in the porous medium is unclear. The Brinkman equation can also be derived by a homogenization process from the Stokes flow in a porous medium, but in a context where the solid obstacles are much smaller than the characteristic pore size ε described in the previous section, see Allaire [9].

The coupling of Darcy and Stokes equation is of great interest and thus there are a great number of publications concerned with this question, both from a mathematical, see [58, 77, 78, 80, 94, 98, 106], and computational point of view, see [33, 34, 42, 52, 84, 93, 115, 115, 132].

Two interface conditions are widely used and accepted: The first is a *continuity of the normal velocities*, i.e. if we denote the outer normal vector on $\partial\Omega_f$ by $\mathbf{n}_f$, it should hold

$$\mathbf{v}_f \cdot \mathbf{n}_f = \mathbf{v}_p \cdot \mathbf{n}_f \qquad \text{on } \Gamma. \tag{3.1.19}$$

This is due to the fact that the upscaled velocity remains incompressible. The incompressibility on Ω as well as on Ω_f and Ω_p together with the divergence theorem leads to equation (3.1.19).

The second interface law was found experimentally by Beavers and Joseph [19], it is a slip law and reads

$$-\boldsymbol{\tau}_f \cdot \nabla \mathbf{v}_f \cdot \mathbf{n}_f = \frac{\alpha_{BJ}}{\sqrt{k^\varepsilon}} \left(\mathbf{v}_f - \mathbf{v}_p \right) \cdot \boldsymbol{\tau}_f \qquad \text{on } \Gamma, \tag{3.1.20}$$

where α_{BJ} is a dimensionless parameter depending on the spatial structure of the pore-space (which has to be fitted by experiments), k^ε is the scalar permeability, cf. Remark 3.1.9, and $\boldsymbol{\tau}_f$ is the tangential vector on $\partial\Omega_f$.

Remark 3.1.9. *Beavers and Joseph [19] considered an isotropic porous medium and thus used a scalar permeability k^ε in the Darcy's law. This ties in with our definition of a rescaled permeability tensor, see Definition 3.1.20, by setting*

$$\mathbf{K} = \frac{k^\varepsilon}{\varepsilon^2}\,\mathrm{id}\,. \tag{3.1.21}$$

Saffman [117] noted that the magnitude of $\mathbf{v}_\mathrm{p}$ is much smaller than the order of $\mathbf{v}_\mathrm{f}$, and could thus be neglected in (3.1.20). This gave rise to the **Beavers-Joseph-Saffman** law:

$$-\boldsymbol{\tau}_\mathrm{f}\cdot\nabla\mathbf{v}_\mathrm{f}\cdot\mathbf{n}_\mathrm{f} = \frac{\alpha_{BJ}}{\sqrt{k^\varepsilon}}\mathbf{v}_\mathrm{f}\cdot\boldsymbol{\tau}_\mathrm{f} \qquad \text{on } \Gamma. \tag{3.1.22}$$

In the setting of the experiment of Beavers and Joseph [19] (i.e. a flow driven by a pressure drop), Jäger and Mikelić [77] rigorously justified the Saffman version of the interface law (3.1.22) in the form

$$\varepsilon C_1^{\mathrm{bl}}\boldsymbol{\tau}_\mathrm{f}\cdot\nabla\mathbf{v}_\mathrm{f}\cdot\mathbf{n}_\mathrm{f} = \mathbf{v}_\mathrm{f}\cdot\boldsymbol{\tau}_\mathrm{f} \qquad \text{on } \Gamma, \tag{3.1.23}$$

where C_1^{bl} is an effective constant derived by an additional auxiliary problem. Thus, they were able to confirm the form (3.1.22) and determine the value of the dimensionless parameter,

$$\alpha_{BJ} = -\frac{\sqrt{k^\varepsilon}}{\varepsilon C_1^{\mathrm{bl}}}, \tag{3.1.24}$$

see (3.1.51) for more details on the coefficient C_1^{bl}. Marciniak-Czochra and Mikelić [98] confirmed Saffmans' form (3.1.23) in the slightly more general context where the driving force of the flow on the microscopic level is given by a general right hand side and not necessarily a pressure drop, cf. Problem 3.1.3.

Jäger and Mikelić [77] showed that, in agreement with Ene and Sánchez-Palencia [58], the following orders of magnitude hold true for the effective variables:

$$\mathbf{v}_\mathrm{f} = \mathcal{O}(1), \quad \mathbf{v}_\mathrm{p} = \mathcal{O}(\varepsilon^2), \quad p_\mathrm{f} = \mathcal{O}(1) = p_\mathrm{p}. \tag{3.1.25}$$

Thus, they dropped the effective Darcy velocity also from (3.1.19), using

$$\mathbf{v}_\mathrm{f}\cdot\mathbf{n}_\mathrm{f} = 0 \qquad \text{on } \Gamma. \tag{3.1.26}$$

Remark 3.1.10. *We want to remark that Ene and Sánchez-Palencia [58] strongly advertised a continuity of the pressure instead of the Beavers-Joseph-Saffman condition. Bernardi et al. [23] also promote a continuity of the pressure.*

Summarizing, we obtain at the interface the continuity of the normal velocity, either in the form (3.1.19) or (3.1.26), together with the slip law of Beavers and Joseph or a variant thereof. However, this is not enough to uniquely determine the effective quantities, a third condition is required.

A widely used condition (see [52, 93, 115, 130, 132] and many more) to close the system of equations is *continuity of normal forces* across Γ, i.e.

$$p_{\mathrm{f}} - \mathbf{n}_{\mathrm{f}} \cdot \nabla \mathbf{v}_{\mathrm{f}} \cdot \mathbf{n}_{\mathrm{f}} = p_{\mathrm{p}}. \tag{3.1.27}$$

This condition is physically motivated and has the advantage that it fits nicely into a weak formulation of the effective equations. However, it is not clear at all if the physical conditions that hold true on the microscopic level should be lifted to the upscaled formulation.

An alternative is given in Jäger et al. [80]. The authors advocate to use a law of the form (called **pressure jump law**)

$$p_{\mathrm{f}} - C_{\omega}^{\mathrm{bl}} \boldsymbol{\tau}_{\mathrm{f}} \cdot \nabla \mathbf{v}_{\mathrm{f}} \cdot \mathbf{n}_{\mathrm{f}} = p_{\mathrm{p}}, \tag{3.1.28}$$

where the effective constant C_{ω}^{bl} depends solely on the structure on the porous medium. In Marciniak-Czochra and Mikelić [98], the authors were able to prove (B.1.9c) analytically. They showed that there holds $C_{\omega}^{\mathrm{bl}} = 0$ for isotropic porous media, leading to a continuous pressure in these cases. In general this is not true (see also Remark 3.1.10) as for $C_{\omega}^{\mathrm{bl}} \neq 0$, equation (B.1.9c) describes a jump of the effective pressures across the interface which is related to $\boldsymbol{\tau}_{\mathrm{f}} \cdot \nabla \mathbf{v}_{\mathrm{f}} \cdot \mathbf{n}_{\mathrm{f}}$ (instead of $\mathbf{n}_{\mathrm{f}} \cdot \nabla \mathbf{v}_{\mathrm{f}} \cdot \mathbf{n}_{\mathrm{f}}$ as in (3.1.27)).

We will thus use the following conditions on Γ, see also Jäger and Mikelić [77], Marciniak-Czochra and Mikelić [98]:

- the no-slip condition (3.1.26) for $\mathbf{v}_{\mathrm{f}}$,
- the Saffman version of the Beavers-Joseph condition (3.1.23) as well as the
- the pressure jump law (B.1.9c).

Remark 3.1.11. *The conditions* (3.1.26) *and* (B.1.9c) *will be incorporated into the formulation of the problem as Dirichlet boundary conditions, whereas* (3.1.23) *is a kind of Robin condition, emerging naturally in the weak formulation of the effective flow in* Ω_{f}.

Effective Equations

We give now a proper presentation of the effective equations and the interface laws together (following Carraro et al. [36], Marciniak-Czochra and Mikelić [98]). The auxiliary problems needed to define the effective constants used in this paragraph can be found in the next section.

The effective flow in Ω_f is given by the following problem which we present in strong formulation.

Problem 3.1.12 (Effective Flow in Ω_f)**.** *Let $\mathbf{f} \in L^2(\Omega)^2$ be the force given by Problem 3.1.3, restricted to Ω_f. Find a velocity field $\mathbf{v}_\mathrm{f}$ and a pressure field p_f, both L-periodic in x_1-direction, such that there holds*

$$-\Delta \mathbf{v}_\mathrm{f} + \nabla p_\mathrm{f} = \mathbf{f} \qquad \text{in } \Omega_\mathrm{f} \tag{3.1.29a}$$
$$\nabla \cdot \mathbf{v}_\mathrm{f} = 0 \qquad \text{in } \Omega_\mathrm{f}, \tag{3.1.29b}$$

together with the boundary conditions

$$\mathbf{v}_\mathrm{f} = 0 \qquad \text{on } \Gamma_\mathrm{ns}, \tag{3.1.29c}$$
$$v_{\mathrm{f},2} = 0 \qquad \text{on } \Gamma, \tag{3.1.29d}$$
$$v_{\mathrm{f},1} + \varepsilon C_1^\mathrm{bl} \tfrac{\partial v_{\mathrm{f},1}}{\partial x_2} = 0 \qquad \text{on } \Gamma \tag{3.1.29e}$$

and the normalization condition $\int_{\Omega_\mathrm{f}} p_\mathrm{f} \,\mathrm{d}x = 0$. The constant C_1^bl is given by (3.1.51)*.*

Let the mass flows M^ε and M^{eff} be given by

$$M^\varepsilon := \int_{\Omega_\mathrm{f}} v_1^\varepsilon \,\mathrm{d}x, \quad M^{eff} := \int_{\Omega_\mathrm{f}} v_{\mathrm{f},1} \,\mathrm{d}x. \tag{3.1.30}$$

The following error estimates from Marciniak-Czochra and Mikelić [98, Theorem 2] hold true

Theorem 3.1.13 (Convergence Results in Ω_f)**.** *Let $\mathbf{v}_\mathrm{f}$ and p_f be the solution to Problem 3.1.12 with $\mathbf{f} \in C^\infty_\mathrm{per}(\overline{\Omega})$. The following estimates hold true:*

$$\|\mathbf{v}^\varepsilon - \mathbf{v}_\mathrm{f}\|_{L^2(\Omega_\mathrm{f})} = \mathcal{O}(\varepsilon^{3/2}), \tag{3.1.31a}$$
$$|M^\varepsilon - M^{eff}| = \mathcal{O}(\varepsilon^{3/2}) \tag{3.1.31b}$$
$$\|p^\varepsilon - p_\mathrm{f}\|_{L^1(\Omega_\mathrm{f})} = \mathcal{O}(\varepsilon), \tag{3.1.31c}$$
$$\|\nabla(\mathbf{v}^\varepsilon - \mathbf{v}_\mathrm{f})\|_{L^1(\Omega_\mathrm{f})} = \mathcal{O}(\varepsilon), \tag{3.1.31d}$$

Proof. See Marciniak-Czochra and Mikelić [98, Theorem 2]. □

These estimates will be verified by a direct numerical simulation in Section 3.3.

As noted in the introduction of this section, the effective flow in the porous bed Ω_p is given by Darcy equation, which reads, together with the pressure jump law, as follows:

Problem 3.1.14 (Darcy's Law with Pressure Jump Law)**.** *Let* $\mathbf{f}$ *be the force given by Problem 3.1.3, restricted to* Ω_p*,* p_f *and* $\mathbf{v}_\mathrm{f}$ *be the solution of Problem 3.1.12.*

Find p_p*, L-periodic with respect to* x_1*, such that*

$$-\nabla \cdot \Big(\mathbf{K}(\mathbf{f} - \nabla p_\mathrm{p})\Big) = 0 \qquad \text{in } \Omega_\mathrm{p}, \tag{3.1.32a}$$

$$\mathbf{K}(\mathbf{f} - \nabla p_\mathrm{p}) \cdot \mathbf{e}^2 = 0 \qquad \text{on } \Gamma_\mathrm{ns}, \tag{3.1.32b}$$

$$p_\mathrm{p} = p_\mathrm{f} + C_\omega^\mathrm{bl} \tfrac{\partial v_{\mathrm{f},1}}{\partial x_2} \qquad \text{on } \Gamma. \tag{3.1.32c}$$

The rescaled permeability tensor $\mathbf{K}$ *is given by Definition 3.1.20, the interface constant* C_ω^bl *by* (3.1.52)*.*

We remark that the microscopic quantities are defined on the perforated domain Ω^ε. On the other hand, the effective quantities live on Ω. If we want to quantify the quality of the approximation, we must be able to compare those quantities. One possibility to do so is the extension of the microscopic quantities to Ω, see the following Remark 3.1.15.

Remark 3.1.15 (Extension of Velocity and Pressure)**.** *The microscopic fluid velocity* $\mathbf{v}^\varepsilon$ *is extended by zero to the solid part* $\Omega_\mathrm{p} \setminus \overline{\Omega_\mathrm{p}^\varepsilon}$ *of the porous medium* Ω_p*.*

Regarding the extension of the pressure: Let $(i,j) \in \mathbb{Z}^2$ *and* $x \in \varepsilon\left(Y + (i,j)\right)$*, then the extension of the pressure field* p^ε *to the corresponding solid part* $\varepsilon\left(Y_\mathrm{s} + (i,j)\right)$*, denoted by* $\widetilde{p^\varepsilon}$*, is given by*

$$\widetilde{p^\varepsilon}(x) = \begin{cases} p^\varepsilon(x), & x \in \varepsilon\left(Y_\mathrm{f} + (i,j)\right), \\ \frac{1}{\left|\varepsilon\left(Y_\mathrm{f}+(i,j)\right)\right|} \int_{\varepsilon\left(Y_\mathrm{f}+(i,j)\right)} p^\varepsilon, & x \in \varepsilon\left(Y_\mathrm{s} + (i,j)\right), \end{cases} \tag{3.1.33}$$

where $\left|\varepsilon\left(Y_\mathrm{f} + (i,j)\right)\right|$ *denotes the volume of* $\varepsilon\left(Y_\mathrm{f} + (i,j)\right)$*. The pressure extension* (3.1.33) *is the extension of Lipton and Avellaneda [96] and comes out from Tartar's construction, see Allaire [9] for more details.*

In the following, we abuse notation and name the extensions also by $\mathbf{v}^\varepsilon$ *and* p^ε*.*

Then, p_p is an effective quantity with respect to p^ε in Ω_p in the following sense.

Theorem 3.1.16 (Convergence Results in Ω_p, pt. 1)**.** *Let p_p be the solution to Problem 3.1.14 with $\mathbf{f} \in C^\infty_{per}(\overline{\Omega})$ and let $\mathbf{v}_p$ be defined by* (3.1.16b)*. There holds:*

$$\|p^\varepsilon - p_p\|_{L^2(\Omega_p)} = o(1), \tag{3.1.34a}$$

$$\|p^\varepsilon - p_p\|_{H^{-1/2}(\Gamma)} = \mathcal{O}(\varepsilon^{1/2}), \tag{3.1.34b}$$

$$\frac{1}{\varepsilon^2}\mathbf{v}^\varepsilon - \mathbf{v}_p \rightharpoonup 0 \qquad \text{in } L^2(\Omega_p^\delta) \text{ as } \varepsilon \to 0, \tag{3.1.34c}$$

where for all δ with $H_1 > \delta > 0$ we define

$$\Omega_p^\delta := (0, L) \times (-H_1, -\delta). \tag{3.1.35}$$

Proof. See Marciniak-Czochra and Mikelić [98, Theorem 3]. □

We have a few remarks concerning these homogenization error estimates.

Remark 3.1.17. *We want to comment on two things.*

- *Firstly, mind that $\varepsilon^2\mathbf{v}_p$ is an approximation of $\mathbf{v}^\varepsilon$, not $\mathbf{v}_p$.*
- *Secondly, note that in equation* (3.1.34c) *we have to exclude a small vicinity of Σ to gain the convergence results. If we want to get the weak convergence in all of Ω_p, a corrector is needed, see Theorem 3.1.18.*

Theorem 3.1.18. *We use the premises and notation of Theorem 3.1.16. There holds*

$$\frac{1}{\varepsilon^2}\mathbf{v}^\varepsilon - \mathbf{v}_p + \frac{1}{\varepsilon}\boldsymbol{\beta}^{bl}\left(\tfrac{\cdot}{\varepsilon}\right)\tfrac{\partial v_{f,1}}{\partial x_2} \circ \Pi_1 \rightharpoonup 0 \qquad \text{in } L^2(\Omega_p) \qquad \text{for } \varepsilon \to 0, \tag{3.1.36}$$

where Π_1 is a projection on Γ, i.e.

$$\begin{array}{rccc} \Pi_1 & : & \Omega_p & \longrightarrow & \Gamma \\ & & (x_1, x_2) & \longmapsto & (x_1, 0) \end{array} \tag{3.1.37}$$

and $\boldsymbol{\beta}^{bl}$ is the solution of the boundary layer problem Problem 3.1.25.

Proof. See Marciniak-Czochra and Mikelić [98, Remark 4]. □

We want to remark on the norm in equation (3.1.34b). The estimate for the homogenization error on the interface Γ is in the $H^{-1/2}$-norm only. This norm is relatively weak and allows for oscillations of $p^\varepsilon - p_p$. We will examine in Section 3.3 if the numerical computations provide an indication that at least a convergence in the $L^1(\Gamma)$-norm is possible. We will see that this is not true.

3.1.3. Auxiliary Equations

We give a brief overview of the auxiliary equations required to define the effective constants C_1^{bl}, C_ω^{bl}, and $\mathbf{K}$ used in the previous section.

Cell Problems

The (rescaled) permeability tensor $\mathbf{K}$ depends on the shape of the inclusions Y_s and for its definition, the solutions of additional auxiliary problems are necessary.

Problem 3.1.19 (Cell Problem)**.** *Let $i \in \{1, 2\}$.*

Find a velocity field $\mathbf{w}^i$ and pressure π^i with $\int_{Y_\mathrm{f}} \pi^i = 0$, both Y-periodic, s.t.

$$-\Delta \mathbf{w}^i + \nabla \pi^i = \mathbf{e}_i \qquad \text{in } Y_\mathrm{f}, \tag{3.1.38a}$$

$$\nabla \cdot \mathbf{w}^i = 0 \qquad \text{in } Y_\mathrm{f}, \tag{3.1.38b}$$

$$\mathbf{w}^i = 0 \qquad \text{on } \partial Y_\mathrm{s}. \tag{3.1.38c}$$

Definition 3.1.20 (Rescaled Permeability Tensor)**.** *Let $\mathbf{w}^i$ be the solution of Problem 3.1.19. The* rescaled permeability tensor $\mathbf{K} = \left(K_{ij}\right)_{i,j=1}^2$ *is defined by*

$$K_{ij} := \int_{Y_\mathrm{f}} w_j^i, \qquad 1 \le i, j \le 2. \tag{3.1.39}$$

Remark 3.1.21. *One may find in the literature also a definition of $\mathbf{K}$ like*

$$K_{ij} := \int_{Y_\mathrm{f}} \nabla w_j^i \cdot \nabla w_i^j, \qquad 1 \le i, j \le 2. \tag{3.1.40}$$

The equivalence of (3.1.39) *and* (3.1.40) *follows directly by testing the weak form of* (3.1.38a) *with $\mathbf{w}^j$.*

We cite the following result regarding $\mathbf{K}$.

Theorem 3.1.22. *The rescaled permeability tensor defined by Definition 3.1.20 is symmetric and positive definite.*

Proof. A proof of this theorem can be found in most articles containing the derivation of Darcy's law by homogenization, see for instance Allaire [9]. □

Note that we talk about a *rescaled* permeability tensor all the time. This is due to the fact that the leading order of the homogenization limit of $\mathbf{v}^\varepsilon$ in Ω_p is ε^2, see also Remark 3.1.17. Thus, we have to scale $\mathbf{K}$ by ε^2 if we want to talk about the physical (but nonetheless dimensionless) permeability. Not that the physical permeability (see Definition B.1.4) has the unit m^2. It is not to be mixed up with the *hydraulic conductivity*, which is often used in soil-sciences and has the unit $\mathrm{m/s}$.

One last remark regarding diagonal permeability tensors.

Remark 3.1.23 (Diagonal Permeability Tensor)**.** *If we assume the mirror symmetry of the solid obstacle Y_s with respect to y_1, then it is easy to prove that w_1^2 is uneven in y_1 with respect to the line $\{y_1 = 1/2\}$, and w_2^2 and π^2 are even. We obtain $K_{12} = K_{21} = 0$ and the permeability tensor $\mathbf{K}$ is diagonal.*

Navier Boundary Layer

We still have to define the effective constants C_1^bl and C_ω^bl used in the interface laws on Γ, see (B.1.8e) and (B.1.9c), as well as the function $\boldsymbol{\beta}^\mathrm{bl}$ which appears in (3.1.36). To this end, we introduce the boundary layer in Problem 3.1.25, called **Navier boundary layer** (*NBL*). It was first derived in Jäger and Mikelić [77] and numerically solved in Jäger et al. [80].

The solution to the Navier boundary layer $\boldsymbol{\beta}^\mathrm{bl}, \omega^\mathrm{bl}$ is calculated in a semi-porous column given by Definition 3.1.24, see also Figure 3.1.2 for a sketch of the domain.

Definition 3.1.24 (Boundary Layer Domain)**.** *The* boundary layer domain Z^bl *is defined by*

$$Z^\mathrm{bl} := Z^+ \cup \Sigma \cup Z^-, \tag{3.1.41}$$

with the interface

$$\Sigma := (0,1) \times \{\, 0 \,\} \tag{3.1.42}$$

and the two semi-infinite slabs

$$Z^+ := (0,1) \times (0, +\infty), \tag{3.1.43}$$

$$Z^- := \bigcup_{k=1}^{\infty} \left(Y_\mathrm{f} - \{\, 0, k \,\} \right). \tag{3.1.44}$$

The boundary of the inclusions in Z^+ is given by

$$\Gamma_{ns}^{\mathrm{bl}} := \bigcup_{k=1}^{\infty} \left(\partial Y_{\mathrm{s}} - \{\, 0, k \,\} \right). \tag{3.1.45}$$

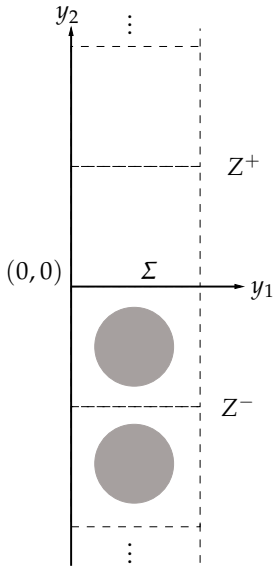

Figure 3.1.2.: Domain of the Navier boundary layer problem.

In this geometry, $\boldsymbol{\beta}^{\mathrm{bl}}$ and ω^{bl} are the solution of the following problem.

Problem 3.1.25 (Navier Boundary Layer)**.** *Find $\boldsymbol{\beta}^{\mathrm{bl}}$ and ω^{bl}, both 1-periodic in y_1-direction, such that*

$$-\Delta \boldsymbol{\beta}^{\mathrm{bl}} + \nabla \omega^{\mathrm{bl}} = 0 \qquad \text{in } Z^+ \cup Z^-, \tag{3.1.46a}$$

$$\nabla \cdot \boldsymbol{\beta}^{\mathrm{bl}} = 0 \qquad \text{in } Z^+ \cup Z^-, \tag{3.1.46b}$$

$$\left[\boldsymbol{\beta}^{\mathrm{bl}} \right]_{\Sigma} = 0 \qquad \text{on } \Sigma, \tag{3.1.46c}$$

$$\left[\{\, \nabla \boldsymbol{\beta}^{\mathrm{bl}} - \omega^{\mathrm{bl}} \,\mathrm{id}\, \} \, \mathbf{e}_2 \right]_{\Sigma} = \mathbf{e}_1 \qquad \text{on } \Sigma, \tag{3.1.46d}$$

$$\boldsymbol{\beta}^{bl} = 0 \qquad \text{on } \Gamma_{ns}^{\mathrm{bl}}. \tag{3.1.46e}$$

Further, to make ω^{bl} unique, we require

$$\omega^{\mathrm{bl}}(y) \to 0 \quad (y_2 \to -\infty). \tag{3.1.46f}$$

The solution of Problem 3.1.25 is a *boundary layer*, i.e. changes in $\boldsymbol{\beta}^{\mathrm{bl}}$ and ω^{bl}

are mostly concentrated around the (boundary-layer) interface Σ, and vanish fast with increasing distance from said interface. This was shown in Jäger and Mikelić [78], see the following theorem.

Theorem 3.1.26. *Let $\boldsymbol{\beta}^{\mathrm{bl}}$, ω^{bl} be the solution of Problem 3.1.25. Then there exists constants $C_1^{\mathrm{bl}} \in \mathbb{R}^-$, $C_\omega^{\mathrm{bl}} \in \mathbb{R}$ s.t.*

- *for all $0 < \delta < 2\pi$ exists $\mathcal{C} > 0$ with*

$$\left|\boldsymbol{\beta}^{\mathrm{bl}}(y_1, y_2) - \left(C_1^{\mathrm{bl}}, 0\right)\right| \leq \mathcal{C} e^{-\delta y_2} \qquad \forall y \in Z^+, \tag{3.1.47}$$

- *exists $\mathcal{C} > 0$ with*

$$\left|\omega^{\mathrm{bl}}(y_1, y_2) - C_\omega^{\mathrm{bl}}\right| \leq \mathcal{C} e^{-2\pi y_2} \qquad \forall y \in Z^+, \tag{3.1.48}$$

- *it exists $\mathcal{C}, \gamma > 0$ with*

$$\left|\boldsymbol{\beta}^{\mathrm{bl}}(y_1, y_2)\right| + \left|\nabla \boldsymbol{\beta}^{\mathrm{bl}}(y_1, y_2)\right| \leq \mathcal{C} e^{-\gamma |y_2|} \qquad \forall y \in Z^-, \tag{3.1.49}$$

- *it exists $\mathcal{C}, \gamma > 0$ with*

$$\left|\omega^{\mathrm{bl}}(y_1, y_2)\right| \leq \mathcal{C} e^{-\gamma |y_2|} \qquad \forall y \in Z^-. \tag{3.1.50}$$

We can compute the constants C_1^{bl} and C_ω^{bl} with the help of the solution of Problem 3.1.25, see also Jäger and Mikelić [78]:

Definition 3.1.27 (Effective Interface Constants)**.** *Let $\boldsymbol{\beta}^{\mathrm{bl}}$, ω^{bl} be the solution of Problem 3.1.25. For the constants C_1^{bl} and C_ω^{bl} from Theorem 3.1.26 there holds for all $a \geq 0$*

$$C_1^{\mathrm{bl}} = \int_0^1 \beta_1^{\mathrm{bl}}(s, 0)\, \mathrm{d}s = \int_0^1 \beta_1^{\mathrm{bl}}(s, a)\, \mathrm{d}s, \tag{3.1.51}$$

$$C_\omega^{\mathrm{bl}} = \int_0^1 \omega^{\mathrm{bl}}(s, 0)\, \mathrm{d}s = \int_0^1 \omega^{\mathrm{bl}}(s, a)\, \mathrm{d}s. \tag{3.1.52}$$

Remark 3.1.28. *If the geometry of Y_{f} is axisymmetric with respect to the line*

$$\{y \in Y \mid y_1 = 1/2\}, \tag{3.1.53}$$

then the constant C_ω^{bl} from Definition 3.1.27 is zero, and (B.1.9c) *describes thus a continuity of the effective pressures across the interface Γ. See Jäger et al. [80] for a proof.*

3.2. Numerical Treatment

In Section 3.3 the two interface conditions (B.1.8e) and (B.1.9c) are numerically confirmed by a direct simulation. To numerically verify the theoretical results we have to solve the following equations (or rather, their discretized versions):

- the microscopic Problem 3.1.6,
- the effective flow in Ω_f, see Problem 3.1.12,
- the Darcy's law in Ω_p, see Problem 3.1.14,
- the cell problems, see Problem 3.1.19, to compute the rescaled permeability $\mathbf{K}$,
- and the boundary layer, see Problem 3.1.25.

All these problems will be solved for two different kinds of inclusions to account for the qualitatively different behaviour of the effective pressure with regard to the shape of the inclusions, see Remark 3.1.28. The solution of the microscopic problem will also be computed for different boundary conditions, a periodic configuration and a flow with a pressure drop condition, see Sections 3.3.1 and 3.3.2. The case with periodic boundary condition is the one presented in the previous sections and the interface conditions have been presented in this setting. We consider the second configuration as it is the one we will use in our fuel cell simulation and thus are interested in the examination of the influence of outer boundary layers to the interface laws.

Particular attention has to be given to the calculation of the constants C_1^{bl} and C_ω^{bl} used in the interface conditions for the effective equations, since we are going to show converge results with $\varepsilon \to 0$ in Section 3.3. Thus, we have to ensure that the discretization error is smaller than the homogenization error, which reaches in some of our computations the scale of 10^{-10}. For this reason we adopt a goal-oriented adaptive scheme for the grid refinement that allows for reducing of the computational costs to obtain a precise evaluation of a given functional, in particular to compute the two constants C_1^{bl} and C_ω^{bl}.

We choose the (continuous) finite element method (*FEM*) as our means of discretization. For an introduction we refer to standard text-books such as Ciarlet [41] or Brenner and Scott [30]. In the following, we present the discretization of the microscopic equation in Section 3.2.1 and explain how we compute C_1^{bl} and C_ω^{bl} in Section 3.2.2 and $\mathbf{K}$ in Section 3.2.3. We present also the results of our computations of the effective constants which will be used in Section 3.3 in these two sections.

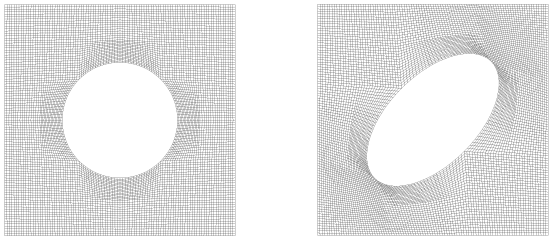

(a) Circle **(b)** Ellipse

Figure 3.2.1.: Triangulation of the fluid part of the unit cell for the two types of inclusions: circles ((a)) and ellipses ((b)).

All computations in this chapter are done using the toolkit `DOpElib` (Goll, Wick, and Wollner [65]) based upon the C++-library `deal.II` (Bangerth et al. [15, 16]). The author is one of the three maintainers of the software package `DOpElib`.

3.2.1. Finite Element Formulation of the Microscopic Problem

As explained in the introduction we consider in our computations two different kinds of inclusions in the porous part, *circles* and *ellipses*, see also Figure 3.2.1.

Definition 3.2.1 (Shape of the Inclusions)**.** *We consider the following two configurations of the unit cells* $Y = [0.1]^2$*:*

(i) the solid part of the cell Y_s *is formed by a circle with radius* 0.25 *and center* $(0.5, 0.5)$.

(ii) Y_s *consists of an ellipse with center* $(0.5, 0.5)$ *and semi-axes* $a = 0.357142857$ *and* $b = 0.192307692$*, which are rotated anti-clockwise by* 45°.

The circular geometry is a case of axis symmetric geometry with respect to the line

$$\{y \in Y \,|\, y_2 = 0.5\}, \tag{3.2.1}$$

for which we expect from the theory that $C_\omega^{\mathrm{bl}} = 0$, see Remark 3.1.28.

As stated before, we use the FEM to solve the problems numerically and we present here the discretization of the Stokes flow in the microscopic level. The natural setting of the finite element approximation of the problem is its weak formulation, see Problem 3.1.6.

For the discretization we consider a shape regular triangulation $\mathcal{T}_h$ of the domain Ω^ε with cells K, i.e. $\mathcal{T}_h = \{ K \}$. The transformations from the reference-cell $\hat{K}$ to the actual cells K we use are *bi-quadratic*. We define the computational domain

$$\Omega_h^\varepsilon := \text{interior} \left(\bigcup_{K \in \mathcal{T}_h} K \right), \tag{3.2.2}$$

with the two type of inclusions described above. Remember that, as Ω^ε has curved (i.e. non-polygonal) boundaries, there holds in general

$$\Omega^\varepsilon \neq \Omega_h^\varepsilon. \tag{3.2.3}$$

Let $s \in \mathbb{N}, s \geq 1$, and $\mathcal{S}_h^s(\Omega_h^\varepsilon) \subset H^1(\Omega_h^\varepsilon)$ be the *isoparametric* finite element spaces of order s. For the discretization of the Stokes system we use the *Taylor-Hood* element, see Taylor and Hood [128], adapted to the boundary conditions at hand, i.e. the ansatz space

$$V_h(\Omega_h^\varepsilon) := \left(\mathcal{S}_h^2(\Omega_h^\varepsilon) \right)^2 \cap H^1_{\Gamma_{\text{ns}}, \text{per}_1}(\Omega_h^\varepsilon)^2 \tag{3.2.4}$$

for the velocity and

$$L_h(\Omega_h^\varepsilon) := \mathcal{S}_h^1(\Omega_h^\varepsilon) \tag{3.2.5}$$

for the pressure. This pair of finite dimensional spaces is *inf-sup stable* (cf. Brezzi and Fortin [31], Girault and Raviart [64]), i.e. they fulfill

$$\exists \gamma \in \mathbb{R} \text{ s.t. } \inf_{\xi_h \in L_h(\Omega_h^\varepsilon)} \sup_{\boldsymbol{\varphi}_h \in V_h(\Omega_h^\varepsilon)} \frac{(\xi_h, \nabla \cdot \boldsymbol{\varphi}_h)}{\|\xi_h\| \|\nabla \boldsymbol{\varphi}_h\|} \geq \gamma > 0, \tag{3.2.6}$$

so there is no need for stabilization terms to solve the saddle point problem corresponding to the Stokes system.

The *finite element approximation* of the microscopic problem is obtained by replacing the function spaces $H^1_{\Gamma_{\text{ns}}, \text{per}_1}(\Omega^\varepsilon)^2$ and $L^2(\Omega^\varepsilon)$ in Problem 3.1.6 by their discretized counterparts $V_h(\Omega_h^\varepsilon)$ and $L_h(\Omega_h^\varepsilon)$.

Problem 3.2.2 (Finite Element Approximation of Microscopic Problem)**.** *Find a pair* $(\mathbf{v}_h^\varepsilon, p^\varepsilon) \in V_h(\Omega_h^\varepsilon) \times L_h(\Omega_h^\varepsilon)$*, such that*

$$(\nabla \mathbf{v}_h^\varepsilon, \nabla \boldsymbol{\varphi}_h)_{\Omega_h^\varepsilon} - (p_h^\varepsilon, \nabla \cdot \boldsymbol{\varphi}_h)_{\Omega_h^\varepsilon} = (\mathbf{f}, \boldsymbol{\varphi}_h)_{\Omega_h^\varepsilon} \qquad \forall \boldsymbol{\varphi}_h \in V_h(\Omega_h^\varepsilon), \tag{3.2.7}$$

$$(\nabla \cdot \mathbf{v}_h^\varepsilon, \xi_h)_{\Omega_h^\varepsilon} = 0 \qquad \forall \xi_h \in L_h(\Omega_h^\varepsilon). \tag{3.2.8}$$

and $\int_{\Omega_h^\varepsilon} p_h^\varepsilon \, \mathrm{d}x = 0$.

3.2.2. Approximation of the NBL on a Finite Domain

The Navier boundary layer Problem 3.1.25 is defined on the unbounded domain Z^{bl}. As we can not triangulate infinitely large domains with finitely many mesh-cells, we consider a cut-off domain for numerical calculations. Following Jäger et al. [80], we choose $k, l \in \mathbb{Z}^+$ and define the finite slab

$$Z_l^k := Z^{\mathrm{bl}} \cap (0,1) \times (-l, k). \tag{3.2.9}$$

The distance of the cut-off from the interface, determined by k and l, has to be taken large enough, taking into account the exponential decay of $\boldsymbol{\beta}^{\mathrm{bl}}$ and ω^{bl}, see Theorem 3.1.26, to reduce the approximation error introduced by cutting the domain.

At the newly introduced parts of the boundary, namely

$$\Gamma_k = (0,1) \times \{k\} \text{ and } \Gamma_l = (0,1) \times \{-l\}, \tag{3.2.10}$$

we have to set some appropriate boundary conditions. We follow Jäger et al. [80] and put a no-slip condition for the velocity on Γ_l, while on Γ_k a zero Dirichlet condition for the vertical component as well as zero normal flux of the first velocity component is imposed. This choice of boundary conditions is motivated by the asymptotic behaviour of the solution variables, see Theorem 3.1.26.

We introduce the function space

$$\widetilde{V}^{\mathrm{bl}}(Z_l^k) := \{\boldsymbol{\varphi} \in H^1_{\mathrm{per}_1}(Z_l^k)^2 \mid \boldsymbol{\varphi}\Big|_{\Gamma_l} = 0, \varphi_2\Big|_{\Gamma_k} = 0, \boldsymbol{\varphi}\Big|_{\Gamma_{ns}^{\mathrm{bl}} \cap \partial Z_l^k} = 0\}, \tag{3.2.11}$$

and formulate the problem on the truncated domain.

Problem 3.2.3 (Cut-off Navier Boundary Layer)**.** *Find $\boldsymbol{\beta}_{k,l}^{\mathrm{bl}} \in \widetilde{V}^{\mathrm{bl}}(Z_l^k)$ and $\omega_{k,l}^{\mathrm{bl}} \in L^2(Z_l^k)$, such that*

$$\left(\nabla \boldsymbol{\beta}_{k,l}^{\mathrm{bl}}, \nabla \boldsymbol{\varphi}\right)_{Z_l^k} - \left(\omega_{k,l}^{\mathrm{bl}}, \nabla \cdot \boldsymbol{\varphi}\right)_{Z_l^k} = -\left(\mathbf{e}_1, \boldsymbol{\varphi}\right)_{\Sigma} \qquad \forall \boldsymbol{\varphi} \in \widetilde{V}^{\mathrm{bl}}(Z_l^k), \tag{3.2.12}$$

$$\left(\nabla \cdot \boldsymbol{\beta}_{k,l}^{\mathrm{bl}}, \psi\right)_{Z_l^k} = 0 \qquad \forall \psi \in L^2(Z_l^k), \tag{3.2.13}$$

together with the normalization condition $\int_{Y_{\mathrm{f}}+(0,k)} \omega_{k,l}^{\mathrm{bl}} \,\mathrm{d}x = 0$

We refer to Jäger et al. [80] for the details of the approximation properties of $\boldsymbol{\beta}_{k,l}^{\mathrm{bl}}$

and $\omega_{k,l}^{\mathrm{bl}}$ w. r. t. $\boldsymbol{\beta}^{\mathrm{bl}}$ and ω^{bl}. Let us note here just briefly, that the quantities

$$\left\|\nabla\left(\boldsymbol{\beta}_{k,l}^{\mathrm{bl}}-\boldsymbol{\beta}^{\mathrm{bl}}\right)\right\|_{Z_l^k} \quad \text{and} \quad \left\|\omega_{k,l}^{\mathrm{bl}}-\omega^{\mathrm{bl}}\right\|_{Z_l^k} \tag{3.2.14}$$

decay exponentially fast with $k, l \to \infty$.

Our focus is in the approximation of the interface constants C_1^{bl} and C_ω^{bl}, which are defined as follows.

Definition 3.2.4. *Let $\boldsymbol{\beta}_{k,l}^{\mathrm{bl}}$, $\omega_{k,l}^{\mathrm{bl}}$ be the solution of Problem 3.2.3. We define for $0 \leq a \leq k$*

$$C_{1,k,l}^{bl} = \int_0^1 \beta_{k,l,1}^{\mathrm{bl}}(s,0)\,\mathrm{d}s, \tag{3.2.15a}$$

$$C_{\omega,k,l}^{bl} = \int_0^1 \omega_{k,l}^{\mathrm{bl}}(s,0)\,\mathrm{d}s = \int_0^1 \omega_{k,l}^{\mathrm{bl}}(s,a)\,\mathrm{d}s. \tag{3.2.15b}$$

The question is: *How good are the approximation properties of these constants*? The following theorem answers that question.

Theorem 3.2.5. *Given the notation and requirements of Definition 3.2.4, there exist constants $\mathcal{C}_1, \mathcal{C}_\omega > 0$ s.t.*

$$\left|C_1^{\mathrm{bl}} - C_{1,k,l}^{bl}\right| = \mathcal{O}\left(e^{-\mathcal{C}_1 \min(k,l)}\right) \tag{3.2.16}$$

$$\left|C_\omega^{\mathrm{bl}} - C_{\omega,k,l}^{bl}\right| = \mathcal{O}\left(e^{-\mathcal{C}_\omega \min(k,l)}\right) \tag{3.2.17}$$

Proof. See Jäger et al. [80]. □

We will verify the stated exponential decay with our numerical computations, see Section 3.3.

Finite Element Formulation

In the following we give the finite element approximation of the cut-off Navier boundary layer Problem 3.2.3. The general method has already been laid out, see Section 3.2.1, we also use a Taylor-Hood element together with a bi-quadratic mapping for the triangulation of Z_l^k, and thus end up with a computational

domain $Z_{l,h}^k \neq Z_l^k$. We adapt the velocity ansatz space to the boundary conditions at hand,

$$\widetilde{V}_h^{\mathrm{bl}}(Z_{l,h}^k) := \Big\{ \boldsymbol{\varphi} \in H^1_{\mathrm{per}_1}(Z_{l,h}^k)^2 \cap \mathcal{S}_h^2(Z_{l,h}^k) \;\Big|\; \boldsymbol{\varphi}\Big|_{\Gamma_l} = 0, \\ \varphi_2\Big|_{\Gamma_k} = 0, \boldsymbol{\varphi}\Big|_{\Gamma_{ns,h}^{\mathrm{bl}} \cap \partial Z_{l,h}^k} = 0 \Big\}, \quad (3.2.18)$$

where $\Gamma_{ns,h}^{\mathrm{bl}}$ denotes the boundary of the inclusions in $Z_{l,h}^k$ (which differs from $\Gamma_{ns}^{\mathrm{bl}}$ due to the presence of curved boundaries), and use, as before, the space of bilinear functions for the pressure. The finite element approximation of Problem 3.2.3 thus reads

Problem 3.2.6. *Find $\boldsymbol{\beta}_h^{\mathrm{bl}} \in \widetilde{V}_h^{\mathrm{bl}}(Z_{l,h}^k)$ and $\omega_h^{\mathrm{bl}} \in L_h(Z_l^k)$, such that*

$$\left(\nabla \boldsymbol{\beta}_h^{\mathrm{bl}}, \nabla \boldsymbol{\varphi}_h\right)_{Z_{l,h}^k} - \left(\omega_h^{bl}, \nabla \cdot \boldsymbol{\varphi}_h\right)_{Z_{l,h}^k} = -\left(\mathbf{e}_1, \boldsymbol{\varphi}_h\right)_{\Sigma}, \qquad \forall \boldsymbol{\varphi}_h \in \widetilde{V}_h^{\mathrm{bl}}(Z_{l,h}^k), \quad (3.2.19a)$$

$$\left(\nabla \cdot \boldsymbol{\beta}_h^{\mathrm{bl}}, \psi_h\right)_{Z_{l,h}^k} = 0, \qquad \forall \psi_h \in L_h(Z_{l,h}^k), \quad (3.2.19b)$$

together with the normalization condition $\int_{\Gamma_l} \omega_h^{bl} \,\mathrm{d}y = 0$.

Remark 3.2.7. *To declutter the notation and enhance readability, we dropped the indices k and l in our finite element approximation on the cut-off Navier boundary layer.*

Approximation of the Effective Interface Constants

We are interested in the constants C_1^{bl} and C_ω^{bl}. An approximation is gained by truncating the domain and approximating the solution on this domain by a FE solution. This is done for both the considered shapes of the inclusions (see Definition 3.2.1). The approximations $C_{1,h}^{\mathrm{bl}}$ and $C_{\omega,h}^{\mathrm{bl}}$ are calculated using this FE approximations in the following way:

$C_{1,h}^{\mathrm{bl}}$ is computed by swapping $\boldsymbol{\beta}_{k,l}^{\mathrm{bl}}$ in Definition 3.2.4 by the discretized counterpart, as it is expected. However, regarding the approximation $C_{\omega,h}^{\mathrm{bl}}$, we would like to draw the attention to the following remark.

Remark 3.2.8. *Due to* (3.1.52) *it actually holds for any $0 \leq a < b$:*

$$C_\omega^{\mathrm{bl}} = \frac{1}{b-a} \int_{[0,1]\times[a,b]} \omega^{\mathrm{bl}}(y) \,\mathrm{d}y, \quad (3.2.20)$$

and for similar reasons ($0 \leq a < b \leq k$)

$$C^{bl}_{\omega,k,l} = \frac{1}{b-a} \int_{[0,1]\times[a,b]} \omega^{\mathrm{bl}}_{k,l}(y)\, \mathrm{d}y, \tag{3.2.21}$$

So for $C^{\mathrm{bl}}_{\omega,h}$, we interchange $\omega^{\mathrm{bl}}_{k,l}$ by ω^{bl}_{h} in (3.2.21).

We observe that to enhance the numerical approximation of C^{bl}_{ω} in (3.2.15b) it is beneficial to calculate the mean of the pressure on a domain far enough from the interface. We calculate the integral in (3.2.21) for $a = 1, b = k$, i.e. along the domain $\{y \in Z^{\mathrm{bl}} \,|\, a \leq y_2 \leq b\}$.

Definition 3.2.9 (Approximation of Interface Constants)**.** *Let $\boldsymbol{\beta}^{\mathrm{bl}}_{h}$, ω^{bl}_{h} be the solution of Problem 3.2.6 with $k > 1$. The approximations of C^{bl}_{1} and C^{bl}_{ω} are defined by*

$$C^{\mathrm{bl}}_{1,h} := \int_0^1 \beta^{\mathrm{bl}}_{h,1}(s,0)\, \mathrm{d}s, \tag{3.2.22a}$$

$$C^{\mathrm{bl}}_{\omega,h} := \frac{1}{k-1} \int_{[0,1]\times[1,k]} \omega^{bl}_{h}(s,1)\, \mathrm{d}s. \tag{3.2.22b}$$

Remark 3.2.10. *As usual, the index h in $C^{\mathrm{bl}}_{1,h}$ and $C^{\mathrm{bl}}_{\omega,h}$ indicates the approximation due to discretization, but in this case also gives the information that the FE-solution was computed on the truncated domain, see also Remark 3.2.7.*

The approximation of C^{bl}_{1} and C^{bl}_{ω} by $C^{\mathrm{bl}}_{1,h}$ and $C^{\mathrm{bl}}_{\omega,h}$ introduces two different sources of error: the **cut-off errors**,

$$e^{co}_{1} := C^{\mathrm{bl}}_{1} - C^{bl}_{1,k,l} \quad \text{and} \quad e^{co}_{\omega} := C^{\mathrm{bl}}_{\omega} - C^{bl}_{\omega,k,l}, \tag{3.2.23}$$

and the **discretization errors**

$$e_{1} := C^{bl}_{1,k,l} - C^{\mathrm{bl}}_{1,h} \quad \text{and} \quad e_{\omega} := C^{bl}_{\omega,k,l} - C^{\mathrm{bl}}_{\omega,h}. \tag{3.2.24}$$

To obtain the convergence results in Section 3.3 with respect to ε, it is important to control both error sources, the cut-off and discretization errors, and balance them to reduce the computational costs. To achieve this we should cut the domain in a way that the magnitude of the cut-off error equals that of the discretization error. We will discuss both influences separately in the next two paragraphs.

Discretization Error We need to control the discretization error by a reliable estimation. To this end, we employ the **Dual Weighted Residual** (*DWR*) method from Becker and Rannacher [20] which gives an estimation of the discretization

error with respect to a given functional exploiting the solution of a proper adjoint equation.

Remark 3.2.11. *We refer to Chapter 4 where we present the DWR method in more detail.*

To set us in a context where the DWR-method is applicable, we have to represent our quantity of interest, i.e. the interface constants, by an evaluation of a functional. Thus, we define for $\boldsymbol{\varphi} \in H^1((0,1)\times(0,k))$ and $\xi \in L^2((0,1)\times(0,k))$:

$$J_1(\boldsymbol{\varphi}) := \int_0^1 \varphi_1(s,0)\,\mathrm{d}s, \quad J_\omega(\xi) := \int_{[0,1]\times[1,k]} \xi(y)\,\mathrm{d}y. \tag{3.2.25}$$

This enables us to rewrite the discretization-errors (3.2.24) by

$$e_1 = J_1(\boldsymbol{\beta}^{\mathrm{bl}}) - J_1(\boldsymbol{\beta}_h^{\mathrm{bl}}), \quad e_\omega = J_\omega(\omega^{\mathrm{bl}}) - J_\omega(\omega_h^{bl}). \tag{3.2.26}$$

The DWR method provides us with error estimators

$$\eta(C_1^{\mathrm{bl}}) \approx e_1, \quad \eta(C_\omega^{\mathrm{bl}}) \approx e_\omega, \tag{3.2.27}$$

as well as *local error indicators* to control the local mesh refinement. The triangulation of the truncated domain is then adaptively refined until the estimated discretization error is smaller than a given tolerance.

The reliability of this estimator has been shown in different applications in the context of flow problems as well as many other areas, a small selection is Becker and Rannacher [20], Braack and Richter [29], Rannacher [111, 112]. Nevertheless, we perform an additional check to assure that the method works. The tests verify that

- the solution on the locally refined grid actually converges and that
- the order of the error is indeed the one estimated.

To check the convergence with respect to the grid-width h we do not have the exact solution at hand, but we can rely on the best approximation property of Galerkin approximations on quasi-uniform meshes to perform the following verification.

On a series of uniformly refined grids we compute the approximations $C_{1,h}^{\mathrm{bl,unif}}$ and $C_{\omega,h}^{\mathrm{bl,unif}}$ and compare them with reference values $C_{1,h}^{\mathrm{bl,ref}}$ and $C_{\omega,h}^{\mathrm{bl,ref}}$ computed on a (very fine) locally refined mesh. Additionally, we evaluate the error estimator

η on the uniformly refined grids and compare it with the following approximated errors:

$$C_{1,h}^{\mathrm{bl,ref}} - C_{1,h}^{\mathrm{bl,unif}}, \quad C_{\omega,h}^{\mathrm{bl,ref}} - C_{\omega,h}^{\mathrm{bl,unif}}. \tag{3.2.28}$$

The results of this test show the expected reliability of the error estimator, since (cf. Table 3.2.1) the solution on uniform meshes converges towards our reference solution and the error estimator is of the same order as the one given by the reference value, aside from the big hiccup in the third line for C_{ω}^{bl}. We have used grids with up to around 3.9 millions of degrees of freedom (DoF) for the verification with uniformly refined meshes. Table 3.2.1 shows the efficiency of the error estimator, i.e.

$$I_{eff}(C_1^{\mathrm{bl}}) = \frac{\eta(C_1^{\mathrm{bl}})}{C_{1,h}^{\mathrm{bl,ref}} - C_{1,h}^{\mathrm{bl,unif}}}, \quad I_{eff}(C_{\omega}^{\mathrm{bl}}) = \frac{\eta(C_{\omega}^{\mathrm{bl}})}{C_{\omega,h}^{\mathrm{bl,ref}} - C_{\omega,h}^{\mathrm{bl,unif}}},$$

which describes how good our guess η of the error in the quantity of interest is.

# DoF	$C_{1,h}^{\mathrm{bl,ref}} - C_{1,h}^{\mathrm{bl,unif}}$	$\eta(C_1^{\mathrm{bl}})$	$I_{eff}(C_1^{\mathrm{bl}})$
1,096	$-4.52 \cdot 10^{-04}$	$-2.54 \cdot 10^{-03}$	5.61
4,142	$-7.49 \cdot 10^{-05}$	$-2.75 \cdot 10^{-04}$	3.67
16,066	$-1.10 \cdot 10^{-05}$	$-1.87 \cdot 10^{-05}$	1.71
63,242	$-9.60 \cdot 10^{-07}$	$-1.11 \cdot 10^{-06}$	1.15
250,906	$-6.83 \cdot 10^{-08}$	$-7.60 \cdot 10^{-08}$	1.11
999,482	$-4.54 \cdot 10^{-09}$	$-5.36 \cdot 10^{-09}$	1.18
3,989,626	$-2.90 \cdot 10^{-10}$	$-3.82 \cdot 10^{-10}$	1.32
# DoF	$C_{\omega,h}^{\mathrm{bl,ref}} - C_{\omega,h}^{\mathrm{bl,unif}}$	$\eta(C_{\omega}^{\mathrm{bl}})$	$I_{eff}(C_{\omega}^{\mathrm{bl}})$
1,096	$2.94 \cdot 10^{-02}$	$-8.53 \cdot 10^{-03}$	-0.29
4,142	$-1.63 \cdot 10^{-04}$	$-8.79 \cdot 10^{-04}$	5.39
16,066	$-6.49 \cdot 10^{-07}$	$-5.59 \cdot 10^{-05}$	86.11
63,242	$-1.03 \cdot 10^{-06}$	$-1.86 \cdot 10^{-06}$	1.80
250,906	$-9.64 \cdot 10^{-08}$	$-1.04 \cdot 10^{-07}$	1.07
999,482	$-7.12 \cdot 10^{-09}$	$-7.04 \cdot 10^{-09}$	0.99
3,989,626	$-4.99 \cdot 10^{-10}$	$-4.77 \cdot 10^{-10}$	0.96

Table 3.2.1.: Results of the approximation of the constants C_1^{bl} and C_{ω}^{bl} by uniform mesh refinement with $k = l = 3$ and ellipses as inclusions. The first column gives the number of degrees of freedom (DoF).

In Figure 3.2.2a an example of a mesh generated by the error estimator for the computation of $C_{\omega,h}^{\mathrm{bl}}$ with $k = l = 5$ is shown. We want to emphasize that the

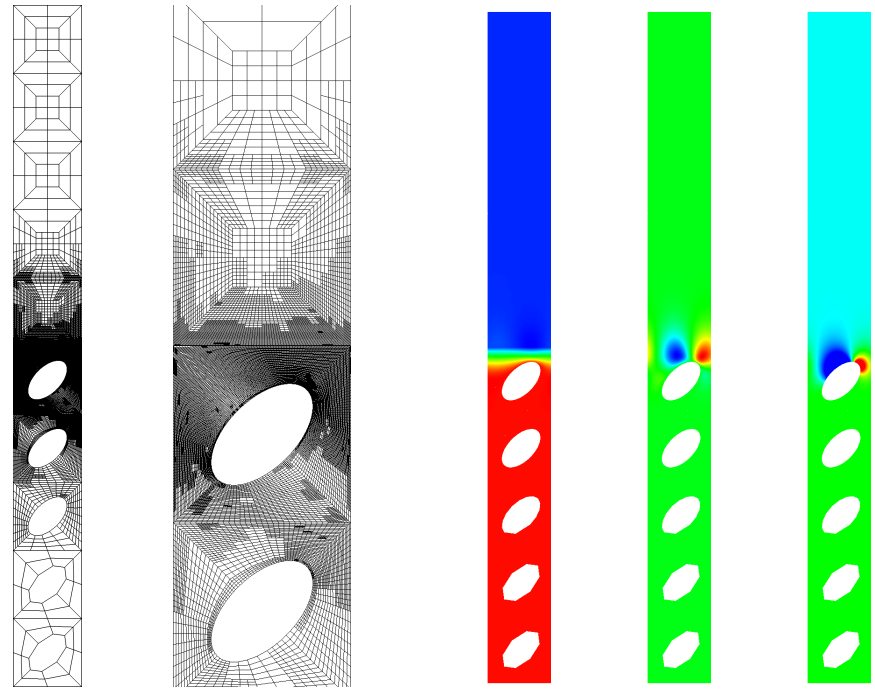

(a) Grid **(b)** Close-up **(c)** $\beta_{h,1}^{\mathrm{bl}}$ **(d)** $\beta_{h,2}^{\mathrm{bl}}$ **(e)** ω_h^{bl}

Figure 3.2.2.: Example of a locally refined grid for the adaptive computation of C_ω^{bl} with $k = l = 5$ in the NBL problem. The whole mesh is shown in ((a)), whereas ((b)) shows a close-up around the interface. In ((c)), ((d)) and ((e)), the associated solution is shown.

DWR method is a *goal-oriented* and *residual based* error estimator. This means the value of the local error indicators are mainly determined by two factors:

(i) It takes into account whether or not the FE solution locally violates the PDE it approximates (the residual-part), and

(ii) it takes into account the influence of the aforementioned error to the given goal functional.

The locally refined mesh in Figure 3.2.2a illustrates this behaviour nicely. A strong refinement can be observed in the neighbourhood of the line $\{y \in Z^{\mathrm{bl}} \mid y_2 = 1\}$. This is the lower boundary of the domain on which ω_h is evaluated to compute $C_{\omega,h}^{\mathrm{bl}}$. Strong refinement occurs also in the vicinity of the first inclusion, see also Figure 3.2.2b for a close-up of this region. In this part of the domain, the associated solution has large gradients, see Figures 3.2.2c, 3.2.2d and 3.2.2e for an illustration of the solution components.

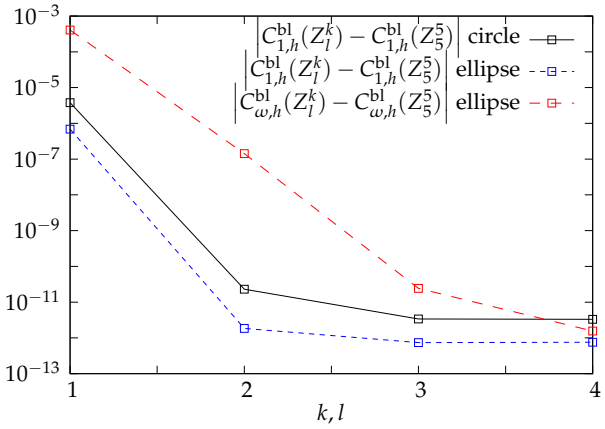

Figure 3.2.3.: Difference between the computed constants on domains with increasing length and $C^{\mathrm{bl}}_{1,h}(Z^5_5)$ resp. $C^{\mathrm{bl}}_{\omega,h}(Z^5_5)$.

Cut-off Error In the previous paragraph we explained how we estimate the discretization error (and gain simultaneously local error indicators for the local mesh refinement). Now we take a look on the error due to the truncation of the domain.

We set $k = l$ and compute the solution of Problem 3.2.6 for $1 \leq k \leq 5$ on a family of hierarchic adaptively refined meshes. The goal is to get an approximation of the constants on each domain with a discretization error below the preset tolerance $TOL = 10^{-11}$. On each domain, we run two computations, starting from a very coarse mesh. One uses the DWR-method with J_1 as goal functional, the second one does the same with J_ω. Each computation refines the grid adaptively as long as the error estimator says that the discretization error is above our preset tolerance TOL. The values of $C^{\mathrm{bl}}_{1,h}$ and $C^{\mathrm{bl}}_{\omega,h}$ obtained by these computations are listed in Table 3.2.2, together with the estimation of the related discretization error. Note that no entries for $C^{\mathrm{bl}}_{\omega,h}$ in the case of circular inclusion are shown, as we know a priori that the value is zero. The numerical computations confirm this in the sense that the result is not zero but lies in the order of the machine precision.

To find the optimal cut-off level l, k we perform a convergence check w.r.t. k, taking as reference value the constants computed on Z^5_5, i.e. $C^{\mathrm{bl}}_{1,h}(Z^5_5)$ resp. $C^{\mathrm{bl}}_{\omega,h}(Z^5_5)$. Figure 3.2.3 shows the error between the constants computed on Z^k_l with $k = l = 1, \ldots, 4$ and the reference values computed on Z^5_5. Remember, we expect an exponential decay of the cut-off error for increasing k, see Theorem 3.2.5.

The exponential decay of the cut-off error with the distance from interface can

k,l	$C_{1,h}^{\mathrm{bl}}$	$\left\lvert\eta(C_1^{\mathrm{bl}})\right\rvert$	$C_{\omega,h}^{\mathrm{bl}}$	$\left\lvert\eta(C_\omega^{\mathrm{bl}})\right\rvert$
	circular inclusions			
1	-0.3038181652339	$1.9 \cdot 10^{-12}$	-	
2	-0.3038219423526	$2.0 \cdot 10^{-12}$	-	
3	-0.3038219423790	$2.0 \cdot 10^{-12}$	-	
4	-0.3038219423789	$2.0 \cdot 10^{-12}$	-	
5	-0.3038219423756	$8.9 \cdot 10^{-13}$	-	
	oval inclusions			
1	-0.2694539064491	$4.3 \cdot 10^{-12}$	-0.2413211012145	$2.1 \cdot 10^{-11}$
2	-0.2694545953967	$1.4 \cdot 10^{-12}$	-0.2409146886571	$7.3 \cdot 10^{-12}$
3	-0.2694545953993	$3.1 \cdot 10^{-12}$	-0.2409148310717	$7.2 \cdot 10^{-12}$
4	-0.2694545953993	$2.1 \cdot 10^{-12}$	-0.2409148310975	$8.5 \cdot 10^{-12}$
5	-0.2694545953985	$2.0 \cdot 10^{-12}$	-0.2409148310959	$8.6 \cdot 10^{-12}$

Table 3.2.2.: Results of the approximation of the constants C_1^{bl} and C_ω^{bl} as well as the estimated discretization error η for different domain-lengths.

be observed for both approximations. Furthermore, it can be observed that the error $|C_{1,h}^{\mathrm{bl}}(Z_k^l) - C_{1,h}^{\mathrm{bl}}(Z_5^5)|$ is of the order of the discretization error, i.e. 10^{-12}, for $k, l \geq 3$ for C_1^{bl} and $k, l \geq 4$ for C_ω^{bl}.

Reference Values For the computations in Section 3.3, we use the approximations

$$C_{1,h}^{\mathrm{bl,circ}} = -0.3038219423756, \quad C_{\omega,h}^{\mathrm{bl,circ}} = 0, \tag{3.2.29}$$

$$C_{1,h}^{\mathrm{bl,ell}} = -0.2694545953985, \quad C_{\omega,h}^{\mathrm{bl,ell}} = -0.2409148310959, \tag{3.2.30}$$

which have been computed on Z_5^5 with the adaptive algorithm described in the previous section, see also Table 3.2.2. Note that $C_{\omega,h}^{\mathrm{bl,circ}} = 0$ is not an approximation but the true value of this constant, see Remark 3.1.28.

3.2.3. Cell Problem and Determination of the Permeability

For a numerical confirmation of the interface laws we need the solution of the appropriate cell problems 3.1.19 to calculate the rescaled permeability $\mathbf{K}$, see Definition 3.1.20.

By and large, we use the same methods as in the previous sections. This means we use bi-quadratic transformations in our triangulation of Y_f, leading to a domain $Y_{\mathrm{f},h} \neq Y_\mathrm{f}$ due to the curved boundary ∂Y_s, and call $Y \setminus Y_{\mathrm{f},h} =: Y_{\mathrm{s},h}$. We also use Taylor-Hood-type elements, adapted to the boundary conditions of the cell problems, so we define the ansatz space for the velocity

$$V_h^c(Y_{\mathrm{f},h}) := \left(\mathcal{S}_h^2(Y_{\mathrm{f},h})\right)^2 \cap H^1_{\partial Y_{\mathrm{s},h},per}(Y_{\mathrm{f},h})^2. \tag{3.2.31}$$

The finite element formulation reads:

Problem 3.2.12 (Finite Element Approximation of Cell Problems)**.** *Let $i, j = 1, 2$. Find a velocity field $\mathbf{w}_h^i \in V_h^c(Y_{\mathrm{f},h})$ and a pressure $\pi_h^i \in L_h(Y_{\mathrm{f},h})$, such that,*

$$\left(\nabla \mathbf{w}_h^i, \nabla \boldsymbol{\varphi}_h\right)_{Y_{\mathrm{f},h}} - \left(\pi_h^i, \nabla \cdot \boldsymbol{\varphi}_h\right)_{Y_{\mathrm{f},h}} = (\mathbf{e}_i, \boldsymbol{\varphi}_h)_{Y_{\mathrm{f},h}}, \quad \forall \boldsymbol{\varphi}_h \in V_h^c(Y_{\mathrm{f},h}), \tag{3.2.32}$$

$$\left(\nabla \cdot \mathbf{w}_h^i, \psi_h\right)_{Y_{\mathrm{f},h}} = 0, \qquad \forall \psi_h \in L_h(Y_{\mathrm{f},h}), \tag{3.2.33}$$

together with the normalization condition $\int_{Y_{\mathrm{f},h}} \psi_h = 0$.

We also use an adaptive algorithm based on the DWR method to compute precisely the reference values for the permeability matrix $\mathbf{K}$. Both cell problems are solved by a tailored grid refinement considering as goal functional for the a posteriori error estimation the components of $\mathbf{K}$.

Reference Values The computed reference values for the circles are

$$\mathbf{K}_h^{circ} = k_h^{circ}\,\mathrm{id} \approx 0.01990143534975\,\mathrm{id} \tag{3.2.34}$$

with an estimated discretization error of $1.38\ 10^{-11}$. For the case with ellipses as inclusions the following values have been calculated

$$\mathbf{K}_h^{oval} = \begin{pmatrix} K_{h,11} & K_{h,12} \\ K_{h,12} & K_{h,22} \end{pmatrix} \approx \begin{pmatrix} 0.0159787174788 & 0.00303449804138 \\ 0.00303449804138 & 0.0159787174788 \end{pmatrix}.$$

The estimated discretization errors are $2.76\ 10^{-12}$ for $K_{h,11}$ and $1.10\ 10^{-13}$ for $K_{h,12}$.

In the next section we use the reference values of $C_{1,h}^{\mathrm{bl}}$, $C_{\omega,h}^{\mathrm{bl}}$ and $\mathbf{K}_h$ to present a numerical confirmation of the interface law.

3.3. Numerical Confirmation of the Interface Law

In the context of the coupling between Stokes and Darcy, the slip condition for the velocity of the free flow (B.1.8e) has been established numerically for example in Kaviany [85], Sahraoui and Kaviany [118], and Larson and Higdon [91, 92]. In addition, the numerical calculation of the constants C_1^{bl} and C_ω^{bl} has been performed by the finite element method in Jäger et al. [80]. Nevertheless, numerical results on the evidence of the pressure relation (B.1.9c) based on a comparison between the microscopic and the homogenized flow have not yet been shown. This is the goal of this section.

Note that Kaviany [85], Sahraoui and Kaviany [118] always deal with isotropic geometries and, consequently, they do not observe the pressure jump but rather continuity of the pressure across Γ. This ties in with the condition (B.1.9c), as for isotropic mediums there holds $C_\omega^{\mathrm{bl}} = 0$, see Remark 3.1.28.

Specifically, we show numerical evidence based on the following consideration. As will be clear from the results of this section, in the microscopic model the pressure values, which converge to p_{p} on Ω_{p} and to p_{f} on Ω_{f}, oscillate due to the inclusions. Approaching the interface, the amplitude of the microscopic pressure oscillations do not vanish with ε. Indeed, it has been shown in Marciniak-Czochra and Mikelić [98] that the pressure of the microscopic model on the interface converges to (the non-oscillatory pressure) p_{p} in the sense of $H^{-1/2}$ that allows such oscillations for the difference p^ε-p_{p}. We give a numerical justification of the interface laws for the pressure and shear stress averages over the pore faces at the interface as explained in more detail in Section 3.3.1.

We focus first on the validation of the theoretical results from Theorem 3.1.13 and (3.1.34a) in Section 3.3.1. Remember that the microscopic problem Problem 3.1.6 in this context has periodic boundary conditions in x_1-direction. Section 3.3.2 examines the influence of non-periodic boundary conditions onto the effective interface laws. There, instead of periodic boundary conditions, we situate ourselves in the original experiment by Beavers and Joseph, i.e. we describe a pressure drop along the channel.

In what follows the reference values for $C_{1,h}^{\mathrm{bl}}$, $C_{\omega,h}^{\mathrm{bl}}$ and $\mathbf{K}_h$ computed in the previous section are used.

3.3.1. Case I: Periodic Case

In this part we present the *periodic case* for which the theory was developed in Marciniak-Czochra and Mikelić [98], i.e. we consider periodic boundary condi-

tions in x_1-direction for the microscopic problem, as stated in Problem 3.1.6.

To show convergence results w.r.t. epsilon without the predominance of the discretization errors, we compute the solutions of the microscopic Problem 3.2.2 for

$$\varepsilon \in \left\{ 1, 1/3, 1/10, 1/31, 1/100, 1/316, 1/1000, 1/3162 \right\}.$$

For smaller values of epsilon, our computational power allows only for approximations for which the discretization error dominates the value we are interested in, namely the homogenization error. This is actually the reason why we are interested in homogenized models. If a direct method would be applicable, we would not have such a need.

Data of the Example

We prescribe an inhomogeneous right hand side to drive the flow $\mathbf{f} = (1, 0)$, and choose the following parameters for the geometry: $L = 1$, $H_\mathrm{l} = 1$, $H_\mathrm{u} = 1$. As rigid inclusions in the porous part we consider the two cases presented in Definition 3.2.1.

With the given data we can exploit the fact that the solutions on the microscopic level $\mathbf{u}^\varepsilon = (\mathbf{v}^\varepsilon, p^\varepsilon)$ are not only L-periodic, but, due to the constant right hand side, also ε-periodic in x_1-direction. To strongly reduce computational costs we compute the approximations $\tilde{\mathbf{u}}_h^\varepsilon$ on a domain with length ε instead of L. We employ then the ε-periodicity to reconstruct the solution $\mathbf{u}_h^\varepsilon = (\mathbf{v}_h^\varepsilon, p_h^\varepsilon)$ on the whole domain with length L. The computational grids are obtained by global refinement.

To show the convergence with ε in Theorem 3.1.13 and (3.1.34a), we need the solution of the microscopic problem, the constants C_1^{bl} and C_ω^{bl}, the permeability $\mathbf{K}$ and the solution of the effective equations.

- For the microscopic solution, we use the FE-approximation presented here.
- The approximations of C_1^{bl}, C_ω^{bl}, and $\mathbf{K}$ have been computed in Section 3.2.
- Regarding the effective solutions: In this simple example, there exist closed formulas for $\mathbf{v}_\mathrm{f}$, p_f and p_p. The analytical solution for the effective problems 3.1.12 and 3.1.14 is (for $x \in \Omega_\mathrm{f}$) given by

$$v_{\mathrm{f},1}(x) = \frac{1 - x_2}{2} \frac{x_2(1 - \varepsilon C_1^{\mathrm{bl}}) - \varepsilon C_1^{\mathrm{bl}}}{1 - \varepsilon C_1^{\mathrm{bl}}}, \tag{3.3.1}$$

$$v_{\mathrm{f},2}(x) = 0 \quad \text{and} \quad p^{\mathit{eff}}(x) = 0. \tag{3.3.2}$$

It follows

$$M^{eff} = \frac{1}{12}\frac{1-4\varepsilon C_1^{\mathrm{bl}}}{1-\varepsilon C_1^{\mathrm{bl}}}. \tag{3.3.3}$$

We have then for $x \in \Omega_{\mathrm{p}}$

$$p_{\mathrm{p}}(x) = \frac{C_\omega^{\mathrm{bl}}}{2(1-\varepsilon C_1^{\mathrm{bl}})} + \frac{K_{12}}{K_{22}}x_2 = \frac{C_\omega^{\mathrm{bl}}}{2} + \frac{K_{12}}{K_{22}}x_2 + O(\varepsilon). \tag{3.3.4}$$

The analytical solutions are evaluated using the reference values $C_{1,h}^{\mathrm{bl}}$, $C_{\omega,h}^{\mathrm{bl}}$ as well as the permeability $\mathbf{K}_h$ computed in the previous Section 3.2 with a discretization error in the order of 10^{-12} or below. A discretization error is thus included in the calculation of $v_{\mathrm{f},1}$ and p_{p}, but it is negligible in comparison with the error in ε for the values considered in our convergence tests.To ease notation, we do not distinguish between the analytical solutions $\mathbf{v}_{\mathrm{f}}$, p_{f} and p_{p} and their approximations due to discretization errors of the constants used in the expressions.

We have now everything at hand to compute the error estimates between the solutions of the microscopic problems and the solutions of the effective/macroscopic problems. Direct simulations confirm the order of convergence in Theorem 3.1.13. This can be seen in Table 3.3.1 or Figure 3.3.1. These show the results of our approximations of the various homogenization errors presented in Theorem 3.1.13, i.e.

$$e_2^2(\mathbf{v}^\varepsilon, \Omega_{\mathrm{f}}) := \left\| \mathbf{v}_h^\varepsilon - \frac{1-x_2}{2}\frac{x_2(1-\varepsilon C_1^{\mathrm{bl}}) - \varepsilon C_1^{\mathrm{bl}}}{1-\varepsilon C_1^{\mathrm{bl}}}\mathbf{e}_1 \right\|_{\Omega_{\mathrm{f}}}^2 = \mathcal{O}(\varepsilon^3), \tag{3.3.5a}$$

$$e_M^2 := \left| M_h^\varepsilon - \frac{1}{12}\frac{1-4\varepsilon C_1^{\mathrm{bl}}}{1-\varepsilon C_1^{\mathrm{bl}}} \right|^2 = \mathcal{O}(\varepsilon^3), \tag{3.3.5b}$$

and the estimates

$$e_1(p^\varepsilon, \Omega_{\mathrm{f}}) := \left\| p_h^\varepsilon \right\|_{L^1(\Omega_{\mathrm{f}})} = \mathcal{O}(\varepsilon), \tag{3.3.6a}$$

$$e_1(\nabla \mathbf{v}^\varepsilon, \Omega_{\mathrm{f}}) := \left\| \nabla \mathbf{v}_h^\varepsilon - \left(\frac{1}{2(1-\varepsilon C_1^{\mathrm{bl}})} - x_2 \right) \begin{pmatrix} 0 & 1 \\ 0 & 0 \end{pmatrix} \right\|_{L^1(\Omega_{\mathrm{f}})} = \mathcal{O}(\varepsilon). \tag{3.3.6b}$$

Direct simulations in the porous medium confirm additionally equation (3.1.34a)

$$e_2(p^\varepsilon, \Omega_{\mathrm{p}}) := \left\| p_h^\varepsilon - \frac{C_\omega^{\mathrm{bl}}}{2} - \frac{K_{12}}{K_{22}}x_2 \right\|_{\Omega_{\mathrm{p}}}^2 = o(1), \tag{3.3.7}$$

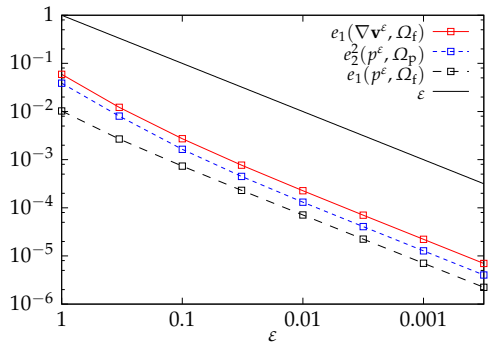

(a) Confirmation of (3.3.6) and (3.3.7), circles as inclusions.

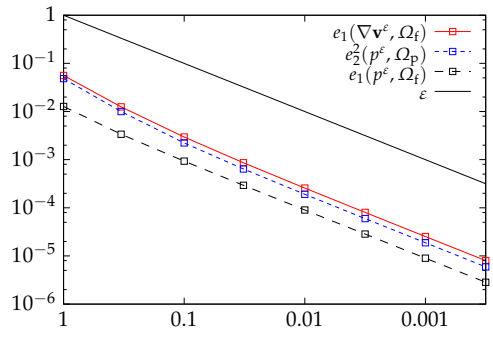

(b) Confirmation of (3.3.6) and (3.3.7), ovals as inclusions.

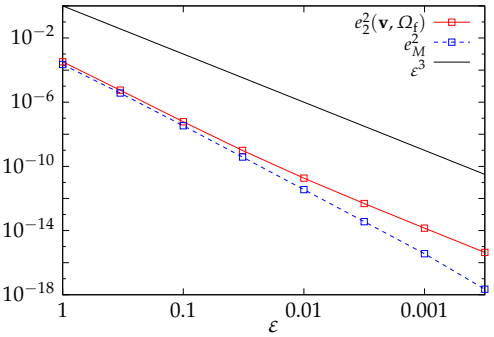

(c) Confirmation of (3.3.5), circles as inclusions.

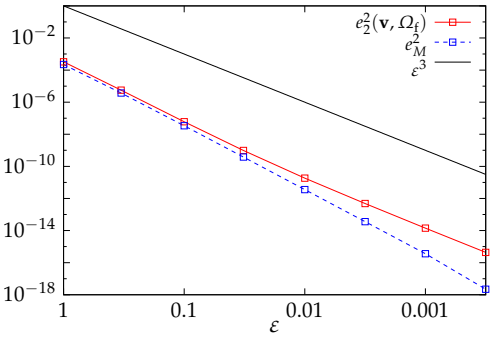

(d) Confirmation of (3.3.5), ovals as inclusions.

Figure 3.3.1.: Confirmation of the estimates (3.3.5), (3.3.6) and (3.3.7) for oval (right column) and circular (left column) inclusions. Notice the different logarithmic scaling in the two rows.

see the last column in Table 3.3.1 as well as Figure 3.3.1a and 3.3.1b.

We plot the homogenization errors vs. ε for the case with circular inclusions (left column) and elliptic inclusions (right column) in Figure 3.3.1. Note that both axes are scaled logarithmically. The drawn out black lines act as a guide for the eyes and picture the expected convergence rates. These are met almost perfectly, showing that we succeeded in making the discretization (and cut-off) errors smaller than the homogenization error. Note that the homogenization error reaches the order of 10^{-9}. The numbers depicted in Figure 3.3.1 are fleshed out in Table 3.3.1. Note that a priori only mere convergence without a given rate w.r.t. ε was given in (3.3.7). In the present case, a convergence of order $\mathcal{O}(\varepsilon)$ can be observed.

The main incentive of this section is the verification of the pressure jump law, so let us take a look at the pressure on the microscopic level. In Figure 3.3.2 the microscopic pressure is depicted for $\varepsilon = 0.1$ and both types of inclusions. There

ε	$\|\mathbf{v}^\varepsilon - \mathbf{v}_\mathrm{f}\|^2_{\Omega_\mathrm{f}}$	$\left\|M^\varepsilon - M^{eff}\right\|$	$\|p^\varepsilon - p_\mathrm{f}\|_{\Omega_\mathrm{f}}$	$\|\nabla(\mathbf{v}^\varepsilon - \mathbf{v}_\mathrm{f})\|_{L^1(\Omega_\mathrm{f})}$	$\|p^\varepsilon - p_\mathrm{p}\|^2_{\Omega_\mathrm{p}}$
	circular inclusions				
1	$4.7 \cdot 10^{-04}$	$1.8 \cdot 10^{-2}$	$1.0 \cdot 10^{-2}$	$5.9 \cdot 10^{-2}$	$3.9 \cdot 10^{-2}$
$\frac{1}{3}$	$8.2 \cdot 10^{-06}$	$2.4 \cdot 10^{-3}$	$2.7 \cdot 10^{-03}$	$1.2 \cdot 10^{-02}$	$8.1 \cdot 10^{-3}$
0.1	$8.3 \cdot 10^{-08}$	$2.3 \cdot 10^{-4}$	$7.4 \cdot 10^{-4}$	$2.7 \cdot 10^{-3}$	$1.6 \cdot 10^{-3}$
$\frac{1}{31}$	$1.2 \cdot 10^{-09}$	$2.5 \cdot 10^{-5}$	$2.3 \cdot 10^{-04}$	$7.7 \cdot 10^{-04}$	$4.5 \cdot 10^{-04}$
0.01	$1.8 \cdot 10^{-11}$	$2.4 \cdot 10^{-6}$	$7.1 \cdot 10^{-5}$	$2.3 \cdot 10^{-4}$	$1.3 \cdot 10^{-4}$
$\frac{1}{316}$	$4.1 \cdot 10^{-13}$	$2.4 \cdot 10^{-7}$	$2.2 \cdot 10^{-05}$	$7.0 \cdot 10^{-05}$	$4.1 \cdot 10^{-05}$
0.001	$1.1 \cdot 10^{-14}$	$2.4 \cdot 10^{-8}$	$7.1 \cdot 10^{-6}$	$2.2 \cdot 10^{-5}$	$1.3 \cdot 10^{-5}$
$\frac{1}{3162}$	$3.4 \cdot 10^{-16}$	$1.8 \cdot 10^{-9}$	$2.3 \cdot 10^{-06}$	$7.0 \cdot 10^{-06}$	$4.0 \cdot 10^{-06}$
	oval inclusions				
1	$3.3 \cdot 10^{-04}$	$1.5 \cdot 10^{-2}$	$1.3 \cdot 10^{-2}$	$5.6 \cdot 10^{-2}$	$4.8 \cdot 10^{-2}$
$\frac{1}{3}$	$5.6 \cdot 10^{-06}$	$1.9 \cdot 10^{-3}$	$3.4 \cdot 10^{-3}$	$1.3 \cdot 10^{-2}$	$1.0 \cdot 10^{-2}$
0.1	$6.0 \cdot 10^{-08}$	$1.9 \cdot 10^{-4}$	$9.3 \cdot 10^{-4}$	$3.0 \cdot 10^{-3}$	$2.2 \cdot 10^{-3}$
$\frac{1}{31}$	$9.8 \cdot 10^{-10}$	$2.0 \cdot 10^{-5}$	$2.9 \cdot 10^{-4}$	$8.6 \cdot 10^{-4}$	$6.4 \cdot 10^{-4}$
0.01	$1.9 \cdot 10^{-11}$	$1.9 \cdot 10^{-6}$	$9.0 \cdot 10^{-5}$	$2.6 \cdot 10^{-4}$	$1.9 \cdot 10^{-4}$
$\frac{1}{316}$	$4.8 \cdot 10^{-13}$	$1.9 \cdot 10^{-7}$	$2.9 \cdot 10^{-5}$	$8.1 \cdot 10^{-5}$	$6.0 \cdot 10^{-5}$
0.001	$1.4 \cdot 10^{-14}$	$1.9 \cdot 10^{-8}$	$9.0 \cdot 10^{-6}$	$2.5 \cdot 10^{-5}$	$1.9 \cdot 10^{-5}$
$\frac{1}{3162}$	$4.4 \cdot 10^{-16}$	$1.1 \cdot 10^{-9}$	$2.9 \cdot 10^{-6}$	$8.0 \cdot 10^{-6}$	$6.0 \cdot 10^{-6}$

Table 3.3.1.: Confirmation of the estimates (3.3.5), (3.3.6) and (3.3.7) for oval and circular inclusions.

are two things which catch the eye immediately.

- Visible "pressure jump" in Figure 3.3.2b, whereas no such thing occurs in Figure 3.3.2a.
- Notable oscillations on the interface. The z-axis has the same scaling as the other axes.

Pressure Oscillations Firstly, we want to comment on these oscillations and clear up that these are not numerical artefacts. The pressure in the top layer inclusions of the porous domain oscillates due to the inclusions. In particular, we see in Figure 3.3.2 that the pressure at the boundary of each inclusion adjacent to the interface has two prominent peaks, one positive and one negative. To visualize it better, we refer to Figure 3.3.3, where we show the microscopic pressure for $\varepsilon = 1$. It can be clearly seen that the solution is smooth and bounded and the maximum and minimum values are on the boundary, as expected by the

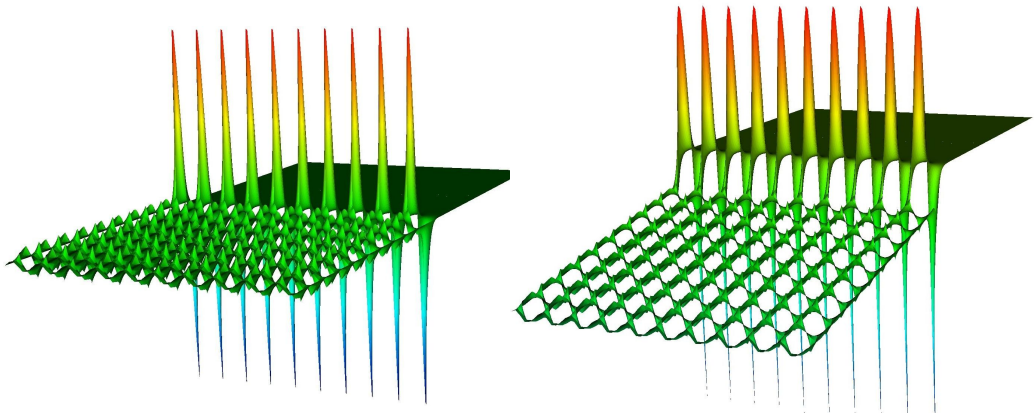

(a) Circles as inclusions.

(b) Ellipses as inclusions.

Figure 3.3.2.: Visualization of the pressure p^ε with $\varepsilon = 10^{-1}$ and periodic boundary conditions.

maximum principle (the pressure is a harmonic function in this example). Thus, the numerical approximation looks satisfying.

Keep in mind that in this example $p_\mathrm{f} = 0$, so the microscopic pressure is essentially the homogenization error $p^\varepsilon - p_\mathrm{f}$. We observe that the amplitude of the pressure oscillations on the interface is of order $\mathcal{O}(1)$ with respect to ε. Figure 3.3.4 clearly shows this behaviour. The microscopic pressure on the interface $p^\varepsilon \,|_\Gamma$ is depicted in this figure for three different ε-values. The x_1-axis is scaled by ε for comparison purposes (i.e. we pick one period of the oscillation). We have an a priori estimate of $p^\varepsilon - p_\mathrm{f}$ on Γ in the $H^{-1/2}(\Gamma)$-norm only, and the observed behaviour of the pressure on said interface indicates that no "better" estimate (i.e. in a stronger norm which does not allow for oscillations, like a $L^p(\Gamma)$-norm) is possible without a corrector of the pressure.

Pressure Jump As can be observed in Figure 3.3.2, there appears a "pressure jump" in the vicinity of the interface if we consider ellipses as inclusions. No such thing is observed for the circular inclusions. The quotation marks are put there because the microscopic pressure p^ε is naturally continuous. Rather, we see a drop of the pressure across the first row of inclusions (this behaviour is the same for all our computations, independent of ε.). So the pictures verify, at least qualitatively, the expected behaviour of the pressure at the interface. Note that if we consider ellipses that are rotated anti-clockwise by 135° the pressure actually increases over the first lines of inclusions in Ω_p. This is reflected in the fact that C_ω^bl can be positive or negative, depending on the form of the inclusions.

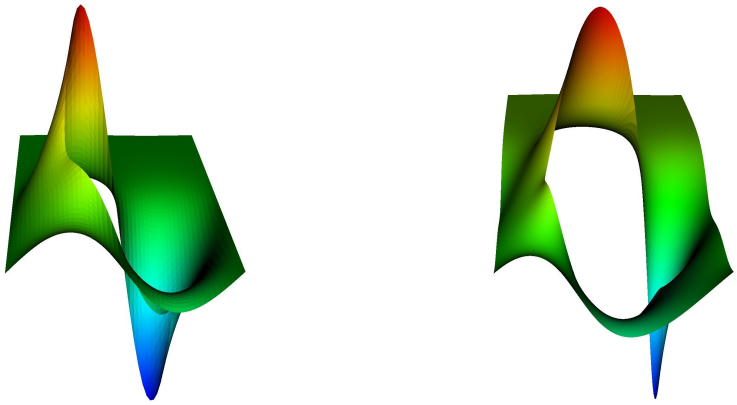

(a) Circles as inclusions.

(b) Ellipses as inclusions.

Figure 3.3.3.: Plot of the pressure values with $\varepsilon = 1$ and periodic boundary conditions.

Interface-Law Indicators

In the periodic case we have been looking at so far the interface law has been rigorously confirmed by the convergence rates of Table 3.3.1. Nevertheless, in the following we give an insightful illustration of the jump behaviour on the interface. The goal is to have an indicator on the microscopic level which quantifies somehow how well the interface laws (B.1.8e) and (B.1.9c) are satisfied by the solution on the microscopic level. This procedure is tested in the periodic case, which is supported by theoretical results, and is applied in Section 3.3.2 to a more general flow condition.

The idea which emerges naturally is the (local) averaging of the microscopic quantities. We have observed that the average value of p^ε over one ε-period converges towards zero, which is the value of p_f in the given example. As a consequence of this observation we introduce cell-wise averaged quantities on Γ denoted with a bar over it (i.e. $\bar{p}^\varepsilon$ for the averaged microscopic pressure on Γ), see also Figure 3.3.5 for a sketch.

Definition 3.3.1 (Cell-Wise Averages)**.** *Let $\mathbf{v}^\varepsilon$ and p^ε be the solution of Problem 3.1.6, $x \in \Gamma$, $m \in \mathbb{N}$ with $m\varepsilon < x < (m+1)\varepsilon$, . The* cell average *of $\partial_2 v_1^\varepsilon$ is defined by*

$$\overline{\partial_2 v_1^\varepsilon}(x) = \frac{1}{\varepsilon} \int_{m\varepsilon}^{(m+1)\varepsilon} \partial_2 v_1^\varepsilon(s,0)\ \mathrm{d}s. \tag{3.3.8}$$

The values $\overline{v_1^\varepsilon}$ and $\overline{p^\varepsilon}$ are defined analogously.

Our indicators are now defined by inserting these (locally) averaged values into

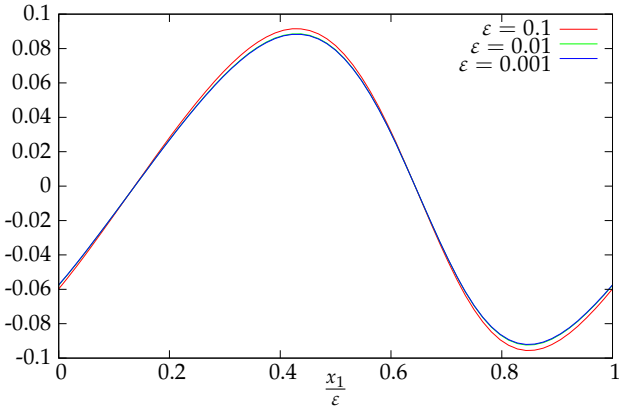

Figure 3.3.4.: Values of the pressure p^ε on the interface Γ for different ε. The horizontal axis is scaled by ε, i.e. the plot shows $p^\varepsilon(x_1/\varepsilon, 0)$ for $x_1 \in [0, \varepsilon]$.

the residual of the interface laws (B.1.8e) and (B.1.9c), taking the L^2-norm and check if this quantity vanishes with $\varepsilon \to 0$. This means, the indicator for the Beavers-Joseph-Condition is given by

$$\text{BJS} := \left\| \frac{\overline{v_1^\varepsilon}}{\varepsilon} + C_1^{\text{bl}} \overline{\partial_2 v_1^\varepsilon} \right\|_\Gamma . \tag{3.3.9}$$

This reasoning can not be applied directly to the pressure jump law, as the microscopic pressure is continuous and subsequently there is no "jump". Therefore, the pressure jump for the microscopic pressure is measured by taking the difference between the cell average of p^ε on Γ and the cell average p_{p}^ε on a parallel line below Γ. The distance of this line from the interface is heuristically motivated by the following consideration. In view of the continuity of p^ε, the "*pressure from below*" has to be taken away from the interface. In addition, since the pressure in Ω_{p} converges to an affine function (cf. (3.3.4)), the line below must not be too far from the interface to define the jump. Hence, we define $\overline{p_{\text{p}}^\varepsilon}$ as follows.

Definition 3.3.2. *Given the notation of Definition 3.3.1, we define the* pressure from below *by*

$$\overline{p_{\text{p}}^\varepsilon}(x) = \frac{1}{\varepsilon} \int_{m\varepsilon}^{(m+1)\varepsilon} p^\varepsilon(s, -2\varepsilon) \, \mathrm{d}s. \tag{3.3.10}$$

With this the indicator for the pressure jump law is defined by

$$\text{PJL} := \| \overline{p_{\text{p}}^\varepsilon} - \overline{p^\varepsilon} - C_\omega^{\text{bl}} \overline{\partial_2 v_1^\varepsilon} \|_\Gamma . \tag{3.3.11}$$

Remark 3.3.3. *As a remark, calculations have been done for the pressure taken at a*

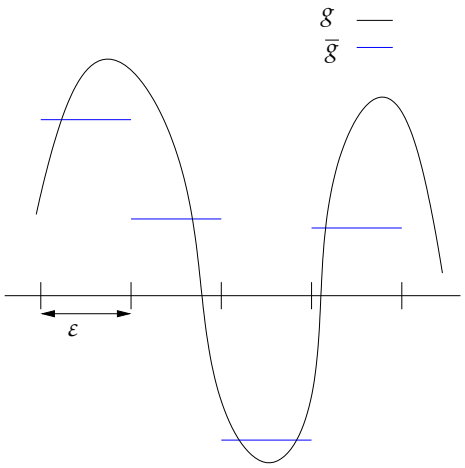

Figure 3.3.5.: Cell-wise average $\overline{g}$ of function g on Γ.

distance ε, 2ε and 3ε from the interface in the porous part. In these three tests we observed convergence in epsilon, but only the distance 2ε, in this specific case, gives the perfect convergence rate as can be observed in Figure 3.3.6.

In Figure 3.3.6 the values of the previously defined indicators are shown. We observe convergence of order $O(\varepsilon)$ for both, the Beavers-Joseph- and jump-law-indicator, except for the jump-law-indicator for the circular inclusions. Due to symmetry the indicator stays in the order of the machine precision, i.e. it is numerically zero (and thus not shown in the picture). We use this heuristic definition of the indicators also in the next section for the verification of the interface laws in a more general case.

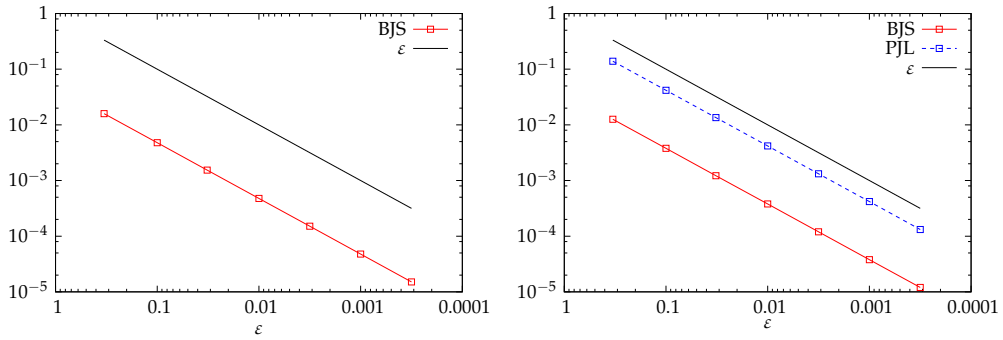

(a) Circles as inclusions.

(b) Ellipses as inclusions.

Figure 3.3.6.: Values of the indicators BJS and PJL in the case of periodic boundary conditions.

3.3.2. Case II: Beavers-Joseph Case

In this case we investigate the behaviour of the microscopic solutions on the interface for a set of boundary conditions corresponding to the original experiment of Beavers and Joseph [19]. Are the interface laws still valid in this context, or is the perturbation due to the boundary conditions too big?

Data of the Example

The length of the domain is set to $L = 2$. In contrast to the periodic case, we assume a zero right-hand side and a constant pressure drop in x_1-direction, i.e. $p^\varepsilon = p_l$ at $x_1 = 0$ and $p^\varepsilon = p_r$ at $x_1 = L$. Additionally, the vertical velocity component is set to zero on Γ_{per}. On the same part of the boundary, due to the divergence free condition, there holds $\partial_1 v_1^\varepsilon = 0$. We transform these non-homogeneous Dirichlet boundary conditions for the pressure into homogeneous ones with a nonzero right hand side $\mathbf{f}$ by setting

$$p_{zr}^\varepsilon(x) = p^\varepsilon(x) - p_l - (p_r - p_l)\frac{x_1}{L}. \tag{3.3.12}$$

It follows that p_{zr}^ε solves the microscopic equation with $p_{zr}^\varepsilon\Big|_{\Gamma_{per}} = 0$ and right hand side

$$\mathbf{f} = \frac{p_l - p_r}{L}\,\mathbf{e}_1. \tag{3.3.13}$$

Remark 3.3.4. *This setting with the pressure drop is also of importance for us because these are the boundary conditions we will employ for the simulation of the fuel cell.*

As opposed to Section 3.3.1, we can not exploit additional ε-periodicity of $\mathbf{v}^\varepsilon$ and p^ε. Therefore, we limit computations in this section to

$$\varepsilon \in \left\{ 1, 1/3, 1/10, 1/31, 1/100 \right\}.$$

This range is nevertheless sufficient to show the convergence results. We use, as before, the reference values of C_1^{bl} and C_ω^{bl} computed in Section 3.2.2.

Validity of the Interface Laws

The non-periodic boundary conditions introduce a pollution effect in comparison with the theoretical results valid for the periodic case, due to the appearance

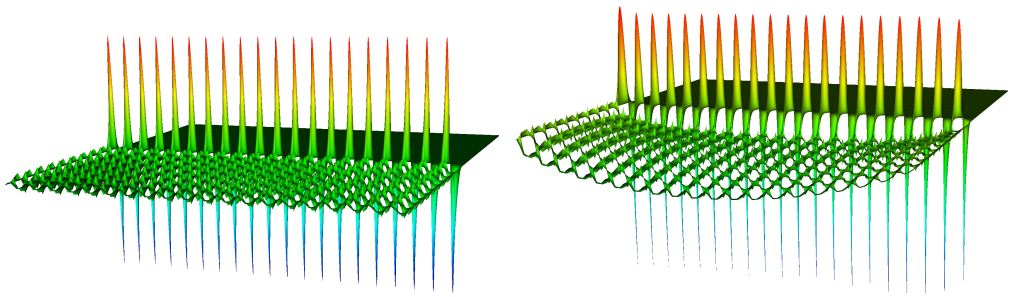

(a) Circles as inclusions. **(b)** Ellipses as inclusions.

Figure 3.3.7.: Visualization of the pressure with $\varepsilon = 10^{-1}$.

of an outer boundary layer. However, let us take a look at Figure 3.3.7, where the microscopic pressure with $\varepsilon = 0.1$ for circular and elliptical inclusions is depicted. We see for both inclusions in the interior of the domain qualitatively the same behaviour as in the previous section, i.e. pressure continuity for circles and a "jump" for ellipses.

We are now interested to quantify somehow the pollution of the interface laws. To this end, we employ the quantities BJS and PJL (see (3.3.9) and (3.3.11)), where $\mathbf{v}^\varepsilon$ and p^ε are the microscopic solutions to the Stokes problems with the boundary conditions described above. The results can be seen in Figure 3.3.8. In Figure 3.3.8a one sees the first order convergence of the indicator for the Beavers-Joseph-Saffman condition for circles as inclusions. The indicator PJL is missing in this case, as its values are again numerically zero.

Figure 3.3.8b shows the results for the elliptical inclusions. We observe that the pressure interface condition (B.1.9c) is not fulfilled by the cell-wise average quantities, while the Beavers-Joseph condition (B.1.8e) is satisfied (in the sense that the indicator goes to zero with ε). We observe thus that the pollution effect on the interface condition mainly concerns the pressure and outer boundary layer effects appear, see Jäger et al. [80]. It is also by no means surprising that this behaviour appears, as the pressure-jump on the interface is not compatible with the zero pressure condition on the left- and right hand side boundaries.

To get rid of this effect we consider the averaged quantities only over part of the interface away from the boundary, i.e. the integral is taken over $\widehat{\Gamma} := (0.2, 1.8) \times \{ 0 \}$ instead of $\Gamma = (0, 2) \times \{ 0 \}$. In this case, as observed in Figure 3.3.8d, both interface laws are fulfilled, i.e. a convergence with order ε is shown. So for this relatively big values of ε, we have to restrict our analysis only to the inner 80% of the domain. We want to remark that the influence of the outer boundary layers gets smaller with ε.

This shows firstly, that the influence of the boundary conditions to the interface laws in this flow configuration is not too big and secondly, we gain an additional confirmation of the validity of our computations of the effective interface constants $C^{\mathrm{bl}}_{1,h}$ and $C^{\mathrm{bl}}_{\omega,h}$, using purely information on the microscopic level.

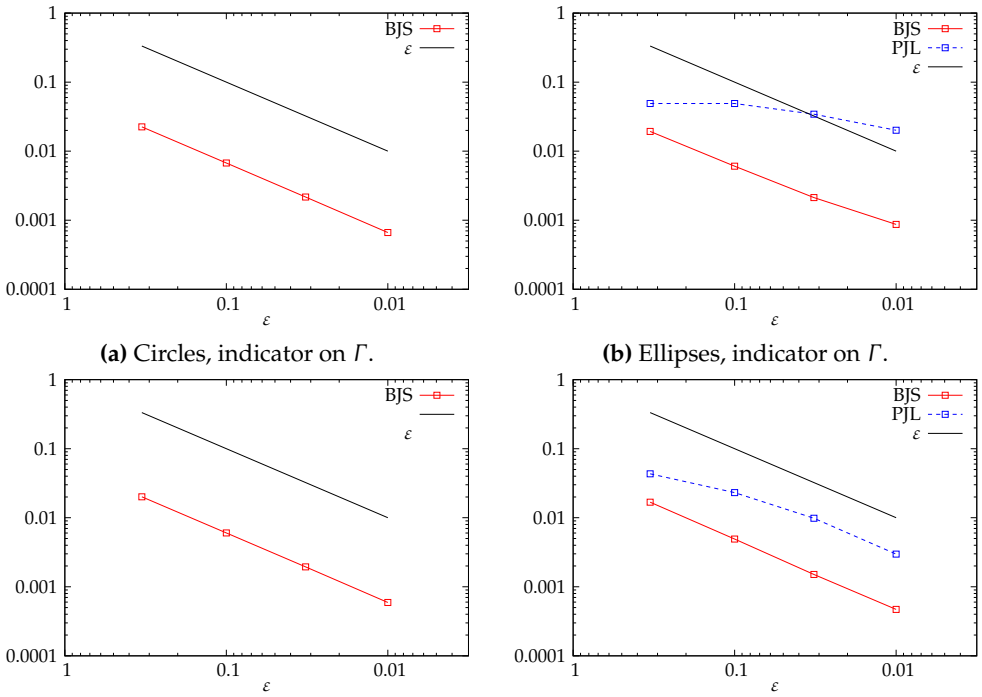

(a) Circles, indicator on Γ.

(b) Ellipses, indicator on Γ.

(c) Circles, indicator on $\hat{\Gamma}$.

(d) Ellipses, indicator on $\hat{\Gamma}$.

Figure 3.3.8.: Values of the indicators BJS and PJL in the case of pressure drop boundary conditions. First row: Indicator applied to whole Γ. Second row: Indicator applied only to $\hat{\Gamma}$.

3.4. Forced Infiltration

We consider in this section also the problem of coupling a free flow with a flow through a porous domain on the macroscopic level, but in a different configuration than before. On the microscopic level, instead of a flow profile mainly tangential to the interface Γ between the free flow domain and the porous medium, we look at a flow which is *forced* through the perforated domain. This leads to a main flow direction that is orthogonal to Γ.

In Carraro et al. [37], Marciniak-Czochra and Mikelić prove analytically that the interface laws for the effective flow in this case are

(i) the continuity of the normal effective velocities,

(ii) zero Darcy's pressure and

(iii) a given slip velocity for the tangential component of the effective velocity.

The goal of this section is to give an independent confirmation of these analytical results using a direct numerical simulation of the flow at the microscopic level.

Even though the setup described above is not the situation we face in our application, the simulation of a fuel cell model, the problem is closely related to the first part of this chapter and quite interesting in itself. However, we will keep the presentation short, as the direct link to the fuel cell simulation is lacking.

The rest of this section is organized as follow: We give a short introduction into the topic in Section 3.4.1. Subsequently, we present the equations on the microscopic and macroscopic level as well as the auxiliary systems we need for the computation of some effective parameters in Section 3.4.2. We describe the discretizations of all these equations and present the results of our computations in 3.4.3.

3.4.1. Introduction

We start from an incompressible 2-d flow of a Newtonian fluid penetrating a periodically perforated domain. At the pore scale, the flow is described by the stationary Stokes system in the unconstrained fluid part as well as in the pore space. Upscaling of the Stokes system in a porous medium yields Darcy's law as the effective momentum equation, valid at every point of the porous medium. The two models, Stokes system and the Darcy equation, are PDEs of different order and need to be coupled across the (artificial) interface Γ of the fluid and the porous medium.

After Marciniak-Czochra and Mikelić, the resulting interface conditions have the following form.

(i) Let $\mathbf{v}_\mathrm{p}$ and p_p be the Darcy velocity and the Darcy pressure, $\mathbf{v}_\mathrm{f}$ the unconfined fluid velocity and $\mathbf{n}$ a normal vector on Γ. The first part of the coupling conditions looks like

$$\mathbf{v}_\mathrm{f} \cdot \mathbf{n} = \mathbf{v}_\mathrm{p} \cdot \mathbf{n} \quad \text{and} \quad p_\mathrm{p} = 0 \quad \text{on } \Gamma. \tag{3.4.1}$$

(ii) Let $C^{2,bl}_{1,\mathrm{fi}}$ be a boundary layer stabilization constant $\boldsymbol{\tau}$ the tangential vector on Γ. There holds

$$\mathbf{v}_\mathrm{f} \cdot \boldsymbol{\tau} = C^{2,bl}_{1,\mathrm{fi}} \nabla p_\mathrm{p} \cdot \mathbf{n} \quad \text{on } \Gamma. \tag{3.4.2}$$

Note that in general $C^{2,bl}_{1,\mathrm{fi}} \neq K_{12}$ and there is a jump of the effective tangential velocities, see Remark 3.4.13.

The constant $C^{2,bl}_{1,\mathrm{fi}}$ is calculated from a boundary layer similar to the one presented in Section 3.1 and depends only on the pore geometry.

Remark 3.4.1. *Note that we assume a homogeneous right hand side on the microscopic level, thus* $\mathbf{v}_\mathrm{p} = \mathbf{K}\nabla p_\mathrm{p}$ *instead of* $\mathbf{v}_\mathrm{p} = \mathbf{K}(\mathbf{f} - \nabla p_\mathrm{p})$.

Interface Conditions for Forced Infiltration

There is vast literature on modeling interface conditions between a free flow and a porous medium. Most of the references focus on flows which are tangential to the porous medium. In such a situation, the free fluid velocity is much larger than the Darcy velocity in the porous medium. For more information on this case, we refer to the other sections of this chapter.

Infiltration into a porous medium corresponds to a different situation, in which the free fluid velocity and the Darcy velocity are of the same order, see the article by Levy and Sánchez-Palencia [94]. They classify the situation as "Case B: The pressure gradient on the side of the porous body at the interface is normal to it". In that case, the pressure gradient in the porous medium is much larger than in the free fluid. Using an order-of-magnitude analysis, they concluded that the effective interface conditions have to satisfy the conditions stated in (3.4.1). In order to close the system, one more condition is needed. In Levy and Sánchez-Palencia [94], zero tangential velocity was assumed. However, as we will see later in Remark 3.4.7, this is only true if the porous medium is isotropic in the direction tangential to the interface. In general, we have a slip velocity.

We note that in a number of articles devoted to numerical simulations, the porous part was modeled using the Brinkman-extended Darcy law. We refer to Discacciati et al. [53], Hanspal et al. [70], Iliev and Laptev [76], Nassehi et al. [103], Yu et al. [138] and references therein. In such settings, the authors used general interface conditions introduced in Ochoa-Tapia and Whitaker [107], consisting of the *continuity* of the velocity and some jump relations for the stresses. The latter contain some parameters which have to be fitted to the problem at hand. However, we recall that the effective viscosity in the Brinkman equation is not known and the use of it seems to be justified only in the case of a high porosity

(see the discussion in Nield [106]). Note that a similar procedure was proposed by several authors for the case of tangential flow, see Section 3.1.

A rigorous mathematical study of the interface conditions between a free fluid and a porous medium was initiated in Jäger and Mikelić [78]. The analytical work of Marciniak-Czochra and Mikelić presented in Carraro et al. [37] builds upon the boundary layers introduced there. Our numerical computations in 3.4.3 confirm these coupling conditions.

Remark 3.4.2. *Note that we discuss here only low Reynolds number flows. Darcy-Navier-Stokes coupling yields also interesting numerical problems, see Layton et al. [93], Rivière and Yotov [115], and Discacciati and Quarteroni [52] as well as the references therein.*

Computational Aspects

We use the finite element method to obtain a numerical confirmation of the conditions (3.4.1) and (3.4.2). Numerical study of the homogenization error is a challenging task. The first difficulty is to find a numerical solution of the microscopic problem used as a reference because the geometry of the porous part has to be resolved in great detail. In addition, the tangential velocity component of the microscopic solution has large gradients in the vicinity of the surface of the porous medium that result in a discontinuity across Γ on the macroscopic level. The accuracy needed by the resolution of the interface and porous part requires a lot of computational effort.

Let us assume that Γ is parallel to the x_1-direction. In our test cases, we reduce the computational costs by considering a problem with data (boundary conditions, prescribed inflow, etc.) which is constant in the direction tangential to Γ. As we have a ε-periodic geometry, the whole problem is ε-periodic in the x_1 direction. Therefore, we reduce the computations to one column of inclusions in the porous part. Nevertheless, even in the simplified example problem, all the computations must be performed with high accuracy.

The reason is that the **homogenization errors**, especially in the estimates based on correction terms, are small in comparison with numerical errors even for simulations with millions of degrees of freedom. A further difficulty is that to check the estimates numerically, we have to solve several coupled auxiliary problems. Therefore the numerical precision of one problem influences the precision of the others. We apply the Dual Weighted Residual method by Becker and Rannacher [20] to calculate some constants needed for the estimates, increasing the overall accuracy of our numerical tests.

3.4.2. Problem Setting and Effective Equations

We start by defining the geometry on the microscopic level. In this setting, it is basically the same as in the case of mainly tangential flow, so we will carry over the notation and definitions of Section 3.1.1 for the domains Y, Y_f, Y_s, Ω_f, Ω_p and Ω^ε as well as the interface Γ. We only change the notations for the boundaries to reflect the difference in the boundary conditions directly in the naming of the respective parts.

Given the microscopic flow domain Ω^ε as defined in Definition 3.1.2, we split its boundary $\partial\Omega^\varepsilon$ into the following disjunct parts

$$\partial\Omega^\varepsilon = \Gamma_{ns}^\varepsilon \dot\cup \Gamma_{in} \dot\cup \Gamma_{out} \dot\cup \Gamma_{per}, \tag{3.4.3}$$

where

$$\Gamma_{ns}^\varepsilon := \Omega_p \cap \sum_{(i,j)\in\mathbb{Z}^2} \varepsilon\left(\partial Y_s + (i,j)\right), \tag{3.4.4}$$

$$\Gamma_{in} := [0,L] \times \{ H_u \}, \tag{3.4.5}$$

$$\Gamma_{out} := [0,L] \times \{ -H_l \}, \tag{3.4.6}$$

$$\Gamma_{per} := \{ 0, L \} \times (-H_l, H_u). \tag{3.4.7}$$

We refer to Figure 3.4.1 for a sketch of the geometry.

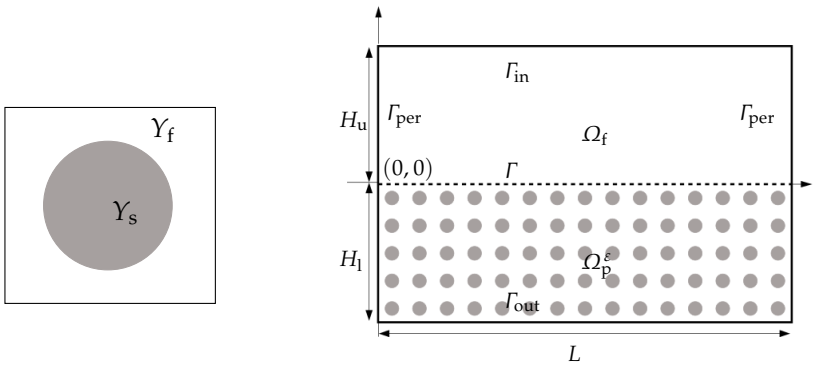

(a) Unit cell Y. **(b)** Flow region Ω^ε.

Figure 3.4.1.: Sketch of the microscopic geometry for the case of forced infiltration.

Remark 3.4.3 (Flow Direction)**.** *We talk about an injection at Γ_{in} and an outflow at Γ_{out}, but of course the reverse situation is also covered by the following discussion.*

The Microscopic Model

Having defined the geometrical structure of the porous medium, we specify the flow problem. We consider the slow viscous incompressible flow of a single fluid through a porous medium. The flow is caused by the *fluid injection* at the boundary Γ_{in}. We assume the no-slip condition at the boundaries of the pores $\Gamma_{\text{ns}}^{\varepsilon}$ (i.e. the filtration through a rigid porous medium). In Ω^{ε}, the flow is described by the following non-dimensional steady Stokes system.

Problem 3.4.4 (Microscopic Flow Problem)**.** *Let an inflow* $\mathbf{v}^{\text{in}}$ *and an outflow* g *be given s.t. they fulfill the compatibility condition*

$$\int_{\Gamma_{\text{out}}} g = \int_{\Gamma_{\text{in}}} v_2^{\text{in}}. \tag{3.4.8}$$

Find the velocity $\mathbf{v}^{\varepsilon}$ *and pressure* p^{ε}*, both L-periodic in* x_1*-direction, such that there holds*

$$-\Delta \mathbf{v}^{\varepsilon} + \nabla p^{\varepsilon} = 0 \qquad \text{in } \Omega^{\varepsilon}, \tag{3.4.9a}$$

$$\nabla \cdot \mathbf{v}^{\varepsilon} = 0 \qquad \text{in } \Omega^{\varepsilon}, \tag{3.4.9b}$$

together with the boundary conditions

$$\mathbf{v}^{\varepsilon} = 0 \quad \text{on } \Gamma_{\text{ns}}^{\varepsilon}, \qquad \mathbf{v}^{\varepsilon} = \mathbf{v}^{\text{in}} \quad \text{on } \Gamma_{\text{in}}, \tag{3.4.9c}$$

$$v_2^{\varepsilon} = g \quad \text{on } \Gamma_{\text{out}}, \qquad \nabla v_1^{\varepsilon} \cdot \mathbf{n} = 0 \quad \text{on } \Gamma_{\text{out}}, \tag{3.4.9d}$$

and the normalization condition $\int_{\Omega_{\text{f}}} p^{\varepsilon} \, \mathrm{d}x = 0$.

Note that we have not only an inflow at Γ_{in}, but a prescribed outflow at Γ_{out} too. This forces the flow through the porous medium.

The Boundary Layer

We are interested in the behavior of solutions to Problem 3.4.4 when $\varepsilon \to 0$. In such a limit the equations in Ω_{f} remain unchanged and the Stokes system in $\Omega_{\text{p}}^{\varepsilon}$ is upscaled to Darcy's equation posed in Ω_{p}. The interesting part is how these two PDEs are linked across the interface Γ.

We will present the results from Carraro et al. [37]. In order to formulate the coupling conditions we need the viscous boundary layer problem connecting free fluid flow and a porous medium flow.

Let Z^{bl} be the boundary layer domain defined in Definition 3.1.24, see also Figure 3.1.2. The domains Z^+, Z^- as well as the boundary layer interface Σ and the no slip boundary $\Gamma_{ns}^{\mathrm{bl}}$ are also defined in Definition 3.1.24.

Problem 3.4.5. *Let $j = 1, 2$ and $\mathbf{w}^i$, π^i be the solution of Problem 3.1.19, and let $\mathbf{K}$ be the corresponding permeability tensor, defined by Definition 3.1.20.*

Find $\boldsymbol{\beta}^{j,\mathrm{bl}}$, $\omega^{j,\mathrm{bl}}$ satisfying

$$-\Delta\boldsymbol{\beta}^{j,\mathrm{bl}} + \nabla\omega^{j,\mathrm{bl}} = 0 \qquad \text{in } Z^+ \cup Z^-, \tag{3.4.10a}$$

$$\nabla \cdot \boldsymbol{\beta}^{j,\mathrm{bl}} = 0 \qquad \text{in } Z^+ \cup Z^-, \tag{3.4.10b}$$

$$\left[\boldsymbol{\beta}^{j,\mathrm{bl}}\right]_{\Sigma} = K_{2j}\mathbf{e}_2 - \mathbf{w}^j \qquad \text{on } \Sigma, \tag{3.4.10c}$$

$$\left[\{\nabla\boldsymbol{\beta}^{j,\mathrm{bl}} - \omega^{j,\mathrm{bl}}\,\mathrm{id}\}\,\mathbf{e}_2\right]_{\Sigma} = -\{\nabla\mathbf{w}^j - \pi^i\,\mathrm{id}\} \qquad \text{on } \Sigma, \tag{3.4.10d}$$

$$\boldsymbol{\beta}^{j,\mathrm{bl}} = 0 \qquad \text{on } \Gamma_{ns}^{\mathrm{bl}}. \tag{3.4.10e}$$

After the results from Jäger and Mikelić [78], the system in Problem 3.4.5 describes a boundary layer, i.e. $\boldsymbol{\beta}^{j,\mathrm{bl}}$ and $\omega^{j,\mathrm{bl}}$ stabilize exponentially towards constants, when $|y_2| \to \infty$:

Theorem 3.4.6. *Let $j = 1, 2$. There exists $\gamma_0 > 0$ and constants $C_{1,\mathrm{fi}}^{j,bl}$ and $C_{\omega,\mathrm{fi}}^{j,bl}$ such that*

$$\left|\boldsymbol{\beta}^{j,\mathrm{bl}} - \left((C_{1,\mathrm{fi}}^{j,bl}, 0\right)\right| + \left|\omega^{j,\mathrm{bl}} - C_{\omega,\mathrm{fi}}^{j,bl}\right| \leq \mathcal{C}e^{-\gamma_0 y_2} \qquad \forall y \in Z^+, \tag{3.4.11}$$

$$e^{-\gamma_0 y_2}\nabla\boldsymbol{\beta}^{j,\mathrm{bl}}, \quad e^{-\gamma_0 y_2}\boldsymbol{\beta}^{j,\mathrm{bl}}, \quad e^{-\gamma_0 y_2}\omega^{j,\mathrm{bl}} \in L^2(Z^-). \tag{3.4.12}$$

The stabilization constants are defined by

$$C_{1,\mathrm{fi}}^{j,bl} = \int_0^1 \lim_{\varepsilon\downarrow 0} \beta_1^{j,\mathrm{bl}}(s,\varepsilon)\,\mathrm{d}s, \tag{3.4.13}$$

$$C_{\omega,\mathrm{fi}}^{j,bl} = \int_0^1 \lim_{\varepsilon\downarrow 0} \omega^{j,\mathrm{bl}}(s,\varepsilon)\,\mathrm{d}s. \tag{3.4.14}$$

The constant $C_{1,\mathrm{fi}}^{2,bl}$ plays an important role in the jump of the tangential effective velocity at the interface. Because of this we add a short remark regarding isotropic porous media.

Remark 3.4.7. *In the case of mirror symmetry of the solid obstacle Y_{s} with respect to y_1, the function w_1^2 is uneven in y_1 with respect to the line $\{y_1 = 1/2\}$, and w_2^2 and π^2 are even (see Remark 3.1.23). This means that $\beta_1^{2,\mathrm{bl}}$ is uneven in y_1 with respect to this line, and $\beta_2^{2,\mathrm{bl}}$ and $\omega^{2,\mathrm{bl}}$ are even. Using formula (3.4.13) yields $C_{1,\mathrm{fi}}^{2,bl} = 0$ in the case of the mirror symmetry of the solid obstacle Y_{s} w.r.t. y_1.*

The Macroscopic Model

We introduce the effective problem in Ω. It consists of two subproblems, which are to be solved sequentially. Let g and $\mathbf{v}^{\text{in}}$ be given as in Problem 3.4.4.

The first problem is posed in Ω_{p} and reads:

Problem 3.4.8. *Find a pressure field p_{p}, L-periodic with respect to x_1, such that there holds*

$$-\nabla \cdot \Big(\mathbf{K}(\nabla p_{\text{p}})\Big) = 0 \qquad \text{in } \Omega_{\text{p}}, \tag{3.4.15a}$$

$$\mathbf{K}(\nabla p_{\text{p}}) \cdot \mathbf{n} = g \qquad \text{on } \Gamma_{\text{out}}, \tag{3.4.15b}$$

$$p_{\text{p}} = 0 \qquad \text{on } \Gamma. \tag{3.4.15c}$$

The rescaled permeability tensor $\mathbf{K}$ is given by Definition 3.1.20.

Next, we present the situation in the unconfined fluid domain Ω_{f}:

Problem 3.4.9. *Find a velocity field $\mathbf{v}_{\text{f}}$ and a pressure field p_{f}, both L-periodic w.r.t. x_1, such that*

$$-\Delta \mathbf{v}_{\text{f}} + \nabla p_{\text{f}} = 0 \qquad \text{in } \Omega_{\text{f}}, \tag{3.4.16a}$$

$$\nabla \cdot \mathbf{v}_{\text{f}} = 0 \qquad \text{in } \Omega_{\text{f}}, \tag{3.4.16b}$$

together with the boundary conditions

$$\mathbf{v}_{\text{f}} = \mathbf{v}^{\text{in}} \qquad \text{on } \Gamma_{\text{in}}, \tag{3.4.16c}$$

$$v_{\text{f},1} = C^{2,bl}_{1,\text{fi}} \nabla p_{\text{p}} \cdot \mathbf{n} \qquad \text{on } \Gamma, \tag{3.4.16d}$$

$$v_{\text{f},2} = -\mathbf{K}\nabla p_{\text{p}} \cdot \mathbf{n} = -K_{22} \frac{\partial p_{\text{p}}}{\partial x_2} \qquad \text{on } \Gamma, \tag{3.4.16e}$$

and the normalization condition $\int_{\Omega_{\text{f}}} p_{\text{f}} \, \mathrm{d}x = 0$. The constant $C^{2,bl}_{1,\text{fi}}$ is given by (3.4.13).

We note that the value $p_{\text{p}}|_{\Sigma}$ of the pressure field at the interface Σ is equal to zero and thus $\frac{\partial p_{\text{p}}}{\partial x_1}\Big|_{\Gamma} = 0$.

Convergence Results

After settling the effective equations in the previous section, we cite now the results regarding the quality of the approximation of the microscopic quantities by the macroscopic ones. We present only the relevant estimates of the homogenization errors, for a derivation we refer to Carraro et al. [37].

Remark 3.4.10 (Extension)**.** *In what follows we assume the microscopic velocity and pressure to be extended from Ω^ε to Ω as described in Remark 3.1.15.*

Theorem 3.4.11. *Let $\mathcal{O}$ be a neighborhood of Γ_{out}, and $\Pi_j : \mathbb{R}^2 \to \mathbb{R}^2, x \mapsto x \cdot \mathbf{e}_j$ the projection onto the j-th component, $j = 1, 2$. The superscript '+' indicates as usual the limit from above. $H : \mathbb{R} \to \mathbb{R}$ is the Heaviside function. We use the abbreviation*

$$\psi := \frac{\partial p_{\text{p}}}{\partial x_2}\Big|_{\Gamma}. \tag{3.4.17}$$

Under the assumption of smooth geometry and data there holds

$$\|\mathbf{v}^\varepsilon - \mathbf{v}_{\text{f}}\|_{L^2(\Omega_{\text{f}})} \leq C\sqrt{\varepsilon} \tag{3.4.18}$$

$$\left\|\mathbf{v}^\varepsilon + \psi\left(K_{22}\mathbf{e}_2 - \boldsymbol{\beta}^{2,\text{bl}}(\frac{\Pi_1}{\varepsilon})^+\right)\right\|_{L^2(\Gamma)} \leq C\varepsilon \tag{3.4.19}$$

$$\left\|\mathbf{v}^\varepsilon + \sum_{k=1}^{2}\frac{\partial p_{\text{p}}}{\partial x_k}\mathbf{w}^k(\tfrac{\cdot}{\varepsilon}) - \psi\boldsymbol{\beta}^{2,\text{bl}}(\tfrac{\cdot}{\varepsilon})\right\|_{L^2(\Omega_{\text{p}}\setminus\mathcal{O})} \leq C\varepsilon \tag{3.4.20}$$

$$\|p^\varepsilon - H(-x_2)\varepsilon^{-2}p_{\text{p}}\|_{L^2(\Omega)} \leq \frac{C}{\varepsilon}. \tag{3.4.21}$$

It is possible to improve these estimates by taking more terms into account.

Theorem 3.4.12. *Under the same assumptions as in Theorem 3.4.11 there holds*

$$\left\|\mathbf{v}^\varepsilon - \mathbf{v}_{\text{f}} + C^{j,bl}_{1,\text{fi}}\psi\mathbf{e}_1 - \psi\boldsymbol{\beta}^{2,\text{bl}}(\tfrac{\cdot}{\varepsilon})\right\|_{L^2(\Omega_{\text{f}})} \leq C\varepsilon \tag{3.4.22}$$

$$\left\|p^\varepsilon - H(-\Pi_2)(\varepsilon^{-2}p_{\text{p}} - \varepsilon^{-1}\left(C^{j,bl}_{\omega,\text{fi}}\psi + \sum_{j=1}^{2}\pi^j(\tfrac{\cdot}{\varepsilon})\frac{\partial p_{\text{p}}}{\partial x_j}\right)\right\|_{L^2(\Omega)} \leq \frac{C}{\sqrt{\varepsilon}}. \tag{3.4.23}$$

Remark 3.4.13. *Leaving the boundary layer corrections aside, the effective velocity at the interface Γ is*

$$\mathbf{v}_{\text{f}} = C^{j,bl}_{1,\text{fi}}\frac{\partial p_{\text{p}}}{\partial x_2}\mathbf{e}_1 - K_{22}\frac{\partial p_{\text{p}}}{\partial x_2}\mathbf{e}_2, \tag{3.4.24}$$

and from the porous media side

$$\mathbf{v}_{\text{p}} = -K_{12}\frac{\partial p_{\text{p}}}{\partial x_2}\mathbf{e}_1 - K_{22}\frac{\partial p_{\text{p}}}{\partial x_2}\mathbf{e}_2. \tag{3.4.25}$$

This means that there is an effective tangential velocity jump *at the interface.*

3.4.3. Numerical Confirmation

This part is dedicated to the numerical confirmation of the convergence results shown in Theorem 3.4.11 and Theorem 3.4.12. We solve the problems needed to numerically compare the microscopic with the macroscopic problem by the finite element method. We keep the presentation short to avoid tiresome repetitions, please see Section 3.2 for more on FE discretizations.

For the discretization of the Stokes system we use the (generalized) Taylor-Hood element. In particular, since the **homogenization error** in some of the proposed estimates is small in comparison with the **discretization error** even for meshes with a number of elements in the order of millions, we have used higher order finite elements (polynomial of third degree for the velocity components and of second degree for the pressure) to reduce the discretization error. The smoothness of the solutions allows for this procedure.

The flow properties depend on the geometry of the pores. In particular there is a substantial difference between the case with symmetric inclusions with respect to the axis orthogonal to the interface and the case with asymmetric inclusions, see Remark 3.4.7 and Remark 3.1.23. We use in the examples therefore two different types of inclusion in the porous part, *circles* and rotated *ellipses*, i.e. ellipses with the major principal axis non parallel to the flow. The increased accuracy using higher order finite elements in the numerical solutions was necessary, as shown later, especially for the case with symmetric inclusions. The geometries of the unit cells $Y = (0.1)^2$, see Figure 3.4.2, for these two cases are as follows:

(i) the solid part of the cell Y_s is formed by a circle with radius 0.25 and center $(0.5, 0.5)$.

(ii) Y_s consists of an ellipse with center $(0.5, 0.5)$ and semi-axes $a = 0.4$ and $b = 0.2$, which are rotated anti-clockwise by 45°.

In addition, since the considered domains have curved boundaries we use cells of the FEM mesh with curved boundaries (a mapping with polynomial of second degree was used for the geometry) to obtain a better approximation.

All computations are done using the toolkit `DOpElib` (Goll et al. [65]) based upon the C++-library `deal.II` (Bangerth et al. [15, 16]).

Numerical Setting

In this section we describe the setting for the numerical test. To confirm the estimates of Theorem 3.4.11 and 3.4.12 we have to solve the microscopic problem (4.2.1) to get $\mathbf{v}^\varepsilon$ and p^ε, the macroscopic problems 3.4.8 and 3.4.9 to get $\mathbf{v}_f$, p_f and

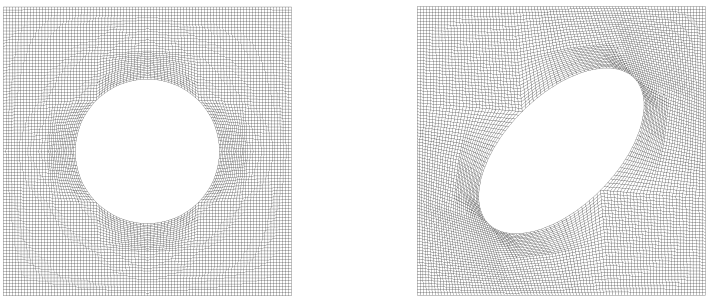

(a) Circle **(b)** Ellipse

Figure 3.4.2.: Mesh of the fluid part of the unit cell for the two types of inclusions: circles and ellipses

p_{p}, the cell problems 3.1.19 to calculate the permeability tensor $\mathbf{K}$, the velocity vector $\mathbf{w}^j$ and pressure π^j, and the boundary layers 3.4.5 for the velocities $\boldsymbol{\beta}^{j,\mathrm{bl}}$ and pressures $\omega^{j,\mathrm{bl}}$, $j = 1, 2$.

To reduce the discretization errors we consider a test case, described below, for which it is easy to derive the exact form of the macroscopic solution. As we will show below, the analytical solution of the macroscopic problem can be expressed in terms of the solution of the cell and boundary layer problems. The discretization error of the macroscopic problem in this case depends on the discretization error of the cell and boundary layer problems and does not imply, therefore, an additional discretization error.

We consider the domains

$$\Omega = [0, 1] \times [-1, 1] \tag{3.4.26}$$

and

$$\Omega^\varepsilon = \Omega \setminus \text{‘the obstacles’}, \tag{3.4.27}$$

where the obstacles are either circles or ellipses as described in the section above. In our example we consider the in- and outflow condition

$$\mathbf{v}^{\mathrm{in}} = (0, -1) \text{ and } g = -1 \tag{3.4.28}$$

in the microscopic problem (4.2.1)

The macroscopic solution in this setting is

$$v_{\mathrm{f},1}(x) = \frac{C^{2,bl}_{1,\mathrm{fi}}}{K_{22}}(1 - x_2), \qquad x \in \Omega_{\mathrm{f}}, \tag{3.4.29a}$$

$$v_{\mathrm{f},2}(x) = -1, \qquad x \in \Omega_{\mathrm{f}}, \tag{3.4.29b}$$

$$p_{\mathrm{f}}(x) = 0, \qquad x \in \Omega_{\mathrm{f}}, \tag{3.4.29c}$$

$$p_{\mathrm{p}}(x) = \frac{1}{K_{22}}x_2, \qquad x \in \Omega_{\mathrm{p}}. \tag{3.4.29d}$$

The macroscopic solution is linked to the solutions of the cell problems through the permeability $\mathbf{K}$, see expressions (3.4.29a) and (3.4.29d). Furthermore it depends on the solution of the boundary layer though the constant $C^{2,bl}_{1,\mathrm{fi}}$.

The microscopic problem (4.2.1) is solved with around 10–15 million degrees of freedom, the cell problem uses around 7 million degrees of freedom. The permeability constant has been precisely calculated using the goal-oriented strategy for mesh adaptivity described in Section 3.2.2.

In the boundary layer problem, due to the interface condition (3.4.10c), the velocity as well as the pressure are discontinuous on the interface Σ. Since with the H^1 conform finite elements chosen for the discretization the discontinuity cannot be properly approximated, we have decided to transform the problem so that the solution variables are continuous across Σ. The values of $\boldsymbol{\beta}^{j,\mathrm{bl}}$ and $\omega^{j,\mathrm{bl}}$ needed to check the estimates are recovered by post-processing.

For the numerical solution, as explained in detail in Section 3.2.2, we use a cut-off domain. That procedure is justified by the exponential decay of the boundary layer solution. The solution of the boundary layer problem is obtained with a mesh of around 4 million degrees of freedom and the constants $C^{j,bl}_{1,\mathrm{fi}}$ and $C^{j,bl}_{\omega,\mathrm{fi}}$ are calculated by the goal-oriented strategy for mesh adaptivity described in Section 3.2.2 where we have made sure that the cut-off error is smaller than the discretization error. We note that in the computation of $C^{j,bl}_{\omega,\mathrm{fi}}$ we do not use the formula given in (3.4.14) but the equivalent one

$$C^{j,bl}_{\omega,\mathrm{fi}} = \int_0^1 \omega^{j,\mathrm{bl}}(y_1, 1)\, dy_1 \tag{3.4.30}$$

as this proved to be advantageous numerically.

In Table 3.4.1 the computed constants $K, C^{j,bl}_{1,\mathrm{fi}}$ and $C^{j,bl}_{\omega,\mathrm{fi}}$ for the two different inclusions are listed. As there holds for the permeability tensor $\mathbf{K}$ in these cases $K_{11} = K_{22}$ and $K_{12} = K_{21}$, we state only K_{11} and K_{12}. Additionally, we give an estimation of the discretization error.

	circular inclusions	**oval inclusions**
K_{11}	0.0199014353519271 $\pm 2 \cdot 10^{-12}$	0.0122773324576884 $\pm 2 \cdot 10^{-13}$
K_{12}	0	0.00268891986291451 $\pm 2 \cdot 10^{-13}$
$C^{j,bl}_{1,\mathrm{fi}}$	0	-0.003336740001686 $\pm 4 \cdot 10^{-10}$
$C^{j,bl}_{\omega,\mathrm{fi}}$	0.025777570627281 $\pm 3 \cdot 10^{-8}$	-0.004429782196436 $\pm 1 \cdot 10^{-8}$

Table 3.4.1.: Computed constants for the computations in the example.

Numerical Results

In this section we present the numerical confirmation of the convergence rates of the homogenization errors (3.4.18–3.4.21) and (3.4.22–3.4.23).

For our test we set $\Omega_\mathrm{p} \setminus \mathcal{O} = [0,1] \times [-0.6, 0]$, and use a computation of the boundary layer on a cut-off domain ranging from -4 to 4. This means that to compute the norms we evaluate the terms involving the boundary layer only for $x \in \Omega$ with $-4\varepsilon < x_2 < 4\varepsilon$. Outside of this region we assume the difference between the boundary layer components and their respective asymptotic values to be sufficiently small.

In the case of inclusions symmetric in the sense explained above, e.g. circles, the homogenization errors are much smaller than the numerical error even for large epsilon such as 0.1 as can be observed in Figure 3.4.3. The lines with markers represent the results of the computations for

$$\varepsilon \in \left\{ 1, 1/3, 1/10, 1/31, 1/100 \right\}, \tag{3.4.31}$$

the solid lines are reference values for various convergence rates and are plotted only to compare the respective slopes.

The case of circles is shown in Figure 3.4.3. For the velocity in the fluid part of the domain the estimate (3.4.18) can be verified. For the better estimate (3.4.22), that uses correction terms to improve the estimation, the homogenization error is so small that the curve shows only the numerical error. In Figure 3.4.3b we can confirm (3.4.20) only for values of epsilon not bigger than $1/31$, for $\varepsilon = 0.01$ the numerical error dominates the homogenization error. Regarding the estimates for the velocity on the interface with circular inclusions (Figure 3.4.3c) we can observe only the numerical error for the same reason explained above.

Notice that the error for circles shown in Figure 3.4.3 is much smaller than the error for ellipses shown in Figure 3.4.4. In addition, we could verify both

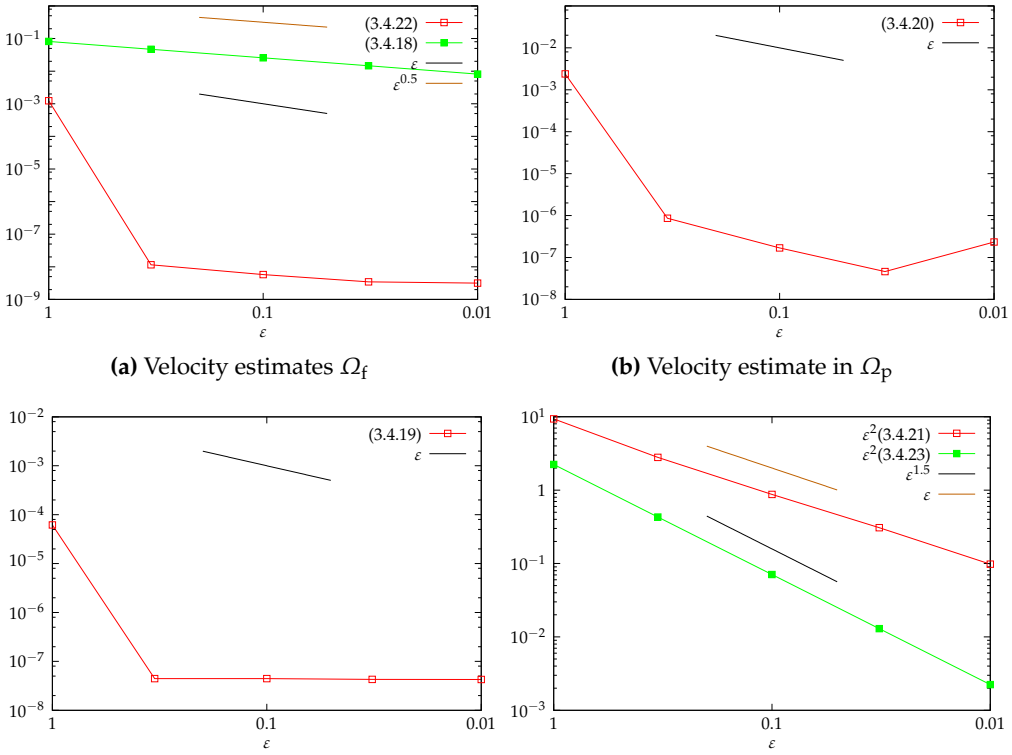

(a) Velocity estimates Ω_f

(b) Velocity estimate in Ω_p

(c) Velocity on Σ

(d) Pressure estimates multiplied by ε^2

Figure 3.4.3.: Convergence results for circular inclusions.

estimates for the pressure (3.4.21) and (3.4.23) as shown in Figure 3.4.3d. Note that the pressure estimates have been scaled by multiplying by ε^2.

The case of ellipses is shown in Figure 3.4.4. As it can be observed, all estimates could be numerically verified, since the discretization error in this case was smaller than the homogenization error. The pressure estimates in this case have been also scaled by ε^2. Note, that we observe for the velocity in the porous domain a convergence rate of 1.5 instead of the predicted first order convergence, see Figure 3.4.4b.

In conclusion, we show in Figure 3.4.5 and Figure 3.4.6 pictures of the flow for the case $\varepsilon = 1/3$. Since we use periodic boundary conditions in the x_1-direction, constant in- and outflow data as well as a periodic geometry, the computations have been performed on a stripe of one column of inclusions to reduce the computational effort. In Figure 3.4.5a and 3.4.5c we see streamline plots of the velocity, Figure 3.4.5b and 3.4.5d show the corresponding pressures. Both pressures are nearly constant in the fluid part and show then a linear descent to

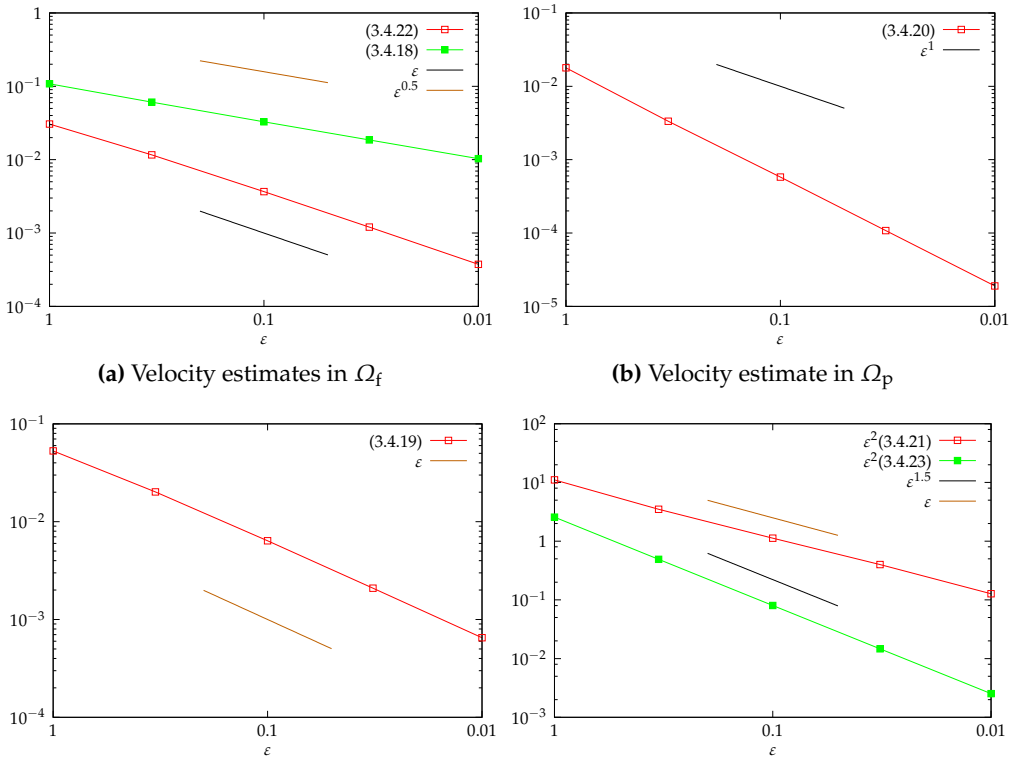

(a) Velocity estimates in Ω_f

(b) Velocity estimate in Ω_p

(c) Velocity on Σ

(d) Pressure estimates multiplied by ε^2

Figure 3.4.4.: Convergence results for elliptical inclusions.

the outflow boundary, similar to the effective pressure (3.4.29c) and (3.4.29d).

Figure 3.4.6 shows only the values of the tangential velocity component. In the case of circular inclusions (Figure 3.4.6a), the velocity is nearly zero throughout the fluid region and shows some oscillations around the mean value zero on the position of the interface. Note that the effective model prescribes here a no slip condition because there holds $C_{1,\mathrm{fi}}^{j,bl} = 0$. In Figure 3.4.6b) we see the corresponding solution for oval inclusions. We notice a linear descent from the inflow boundary (which lies in this picture on the left hand side) to the interface, which leads to the slip condition for the tangential velocity component of the effective flow in this case. Both behaviors are predicted from the effective interface condition for this velocity component, see (3.4.16d).

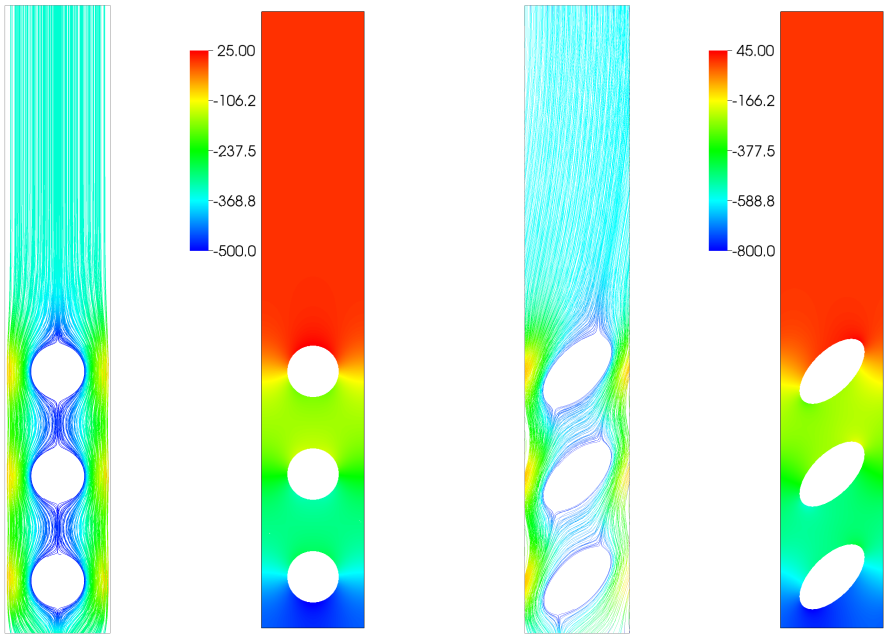

(a) Streamlines of v^ε **(b)** p^ε **(c)** Streamlines of v^ε **(d)** p^ε

Figure 3.4.5.: Visualization of the solution to the microscopic problem for $\varepsilon = 1/3$. Subfigures (a) and (b) show the results for circular inclusions, (c) and (d) for elliptical inclusions.

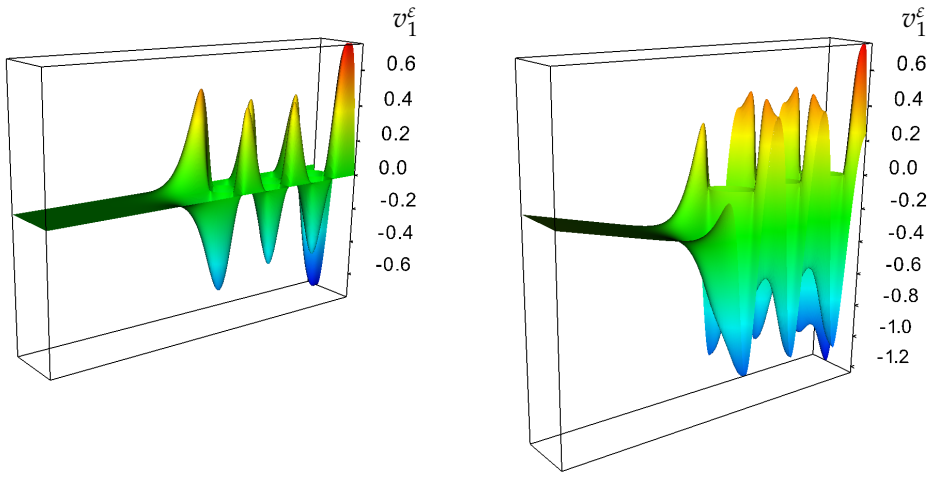

(a) Circular inclusions. **(b)** Elliptical inclusions.

Figure 3.4.6.: Visualization of v_1^ε for $\varepsilon = 1/3$.

4. DWR for Homogenization Problems

The formulation of the macroscopic model in Section 5.2.3 contains effective parameters like the interface constants C_1^{bl} or the effective diffusion coefficient $\mathbf{A}^{\mathrm{hom}}$. These depend on the solutions of some auxiliary problems (the Navier Boundary Layer and the cell problems), so before we can solve the discretized macroscopic model, an approximation of these effective quantities has to be computed. It is clear that the quality of the approximation of the effective constants has an impact on the approximation error on the macroscopic level. The question is: *Are we able to quantify and estimate this effect?*

This section is about the derivation of an a posteriori error estimator which is able to separate the influence on the overall discretization error of a homogenized problem into the following parts

- The part stemming from the discretization of the **macroscopic problem** and
- the parts coming from the approximation of an effective constant through the discretization of the corresponding **auxiliary problem**.

We develop the algorithm in the general context of homogenization problems and apply it later on to our problem at hand, see Chapter 5.

The chapter is organized in the following way. We give a more thorough introduction in Section 4.1, define the abstract problem setting in Section 4.2, introduce the error estimator and the adaptive algorithm in Section 4.3 and show by three examples that the previously developed algorithm works in Section 4.4.

4.1. Introduction

In this section we consider a goal-oriented adaptive finite element method for homogenization problems. A microscopic quantity is therefore approximated by an effective quantity that is obtained by solving a homogenized problem, see e.g. Allaire [8], Bensoussan et al. [22], Cioranescu and Donato [43], Tartar [127], Zhikov et al. [139] as well as Section 2.2 for an introduction into homogenization theory.

More in detail, the effective parameters and correction terms used in the macroscopic problem, which is somehow the limit of the microscopic equations, are derived by the solutions of some auxiliary problems. Using a discretization by finite elements for the macroscopic problem and the auxiliary equations the total approximation error comprehends the **model error** due to homogenization and the **discretization error** of the effective problem and the auxiliary problems.

In this work we do not focus on the model error due to homogenization. We rather consider available a priori estimates of it, see e.g. Abdulle [1] for the case of periodic diffusion tensor, Fatima et al. [59] for a case of a perforated domain and Marciniak-Czochra and Mikelić [98] (as well as Chapter 3) for a priori estimates in the context of Stokes-Darcy coupling.

We are interested in *estimating* and *reducing* the discretization error in a *goal functional* representing a (physical) *quantity of interest*. Essential ingredients in reducing the discretization error are

- firstly, the choice of a proper locally refined mesh for both the macroscopic problem and the auxiliary problems, to reach a given error tolerance in the prescribed goal functional and
- secondly, **the separation of the discretization error into macroscopic and auxiliary error-shares**.

With this last information we are able to balance the influence of the discretizations of the different PDEs bundled in the homogenized problem to the total discretization error. We are interested in a posteriori error estimates which allow for a splitting into the various error-parts and possible strategies for local mesh refinement based on local indicators.

Literature Overview

There are several numerical methods designed to approximate a multiscale problem like the variational multiscale method, see Hughes et al. [75], the multiscale finite element method (MsFEM), see Hou and Wu [74] or the heterogeneous multiscale method (FE-HMM), see Abdulle et al. [5]. In particular the heterogeneous multiscale finite element method (see E and Engquist [55]) has won increasing interest in the last years and several works have been done to derive discretization error estimates in this context. A priori error estimates are available for elliptic (Abdulle [1], E et al. [56]) and parabolic (Ming and Zhang [101]) homogenization problems using FE-HMM, see also references therein.

The first a posteriori error estimates for the discretization of homogenization problems by FE-HMM has been derived by Ohlberger [110]. His method relies on

a reformulation of the numerical method in the two-scale framework (see Allaire [8]) and the a posteriori error estimates are obtained in terms of the two-scale norm. The advantage of this error analysis is that the error estimation is split in a contribution from the macroscale and one from the microscale. Additionally, this method provides also cell-wise error indicators that can be used to steer local mesh refinement for the macroscopic problem and for the microscopic cell problems at the same time. The limitation of this work is that the estimates are not given in physically meaningful quantities, but the rather abstract two-scale norm.

A residual based a posteriori error estimation for the FE-HMM discretization in the general non-periodic case have been first shown in Abdulle and Nonnenmacher [2] and rigorously derived in Abdulle and Nonnenmacher [3]. These results regard the error in the energy norm. The main difference between Ohlberger [110] and Abdulle and Nonnenmacher [3] is the validity of the two formulations. In particular, it has been pointed out that the derivation in Ohlberger [110] does not allow in a straightforward way estimations in the physical domain. A further difference is that the mesh for the microscopic problem in Abdulle and Nonnenmacher [3] is refined only proportionally to the macroscopic mesh. Besides these aspects, from the practical point of view the error in some global norms is often less useful than the error with respect to a specific functional of the solution. The first work on a posteriori error estimation in a quantity of interest for the heterogeneous multiscale finite element method has been done by Abdulle and Nonnenmacher [4].

Application of the DWR Method to Homogenization Problems

The contribution of this work is the derivation of a *goal-oriented* error estimator for homogenization problems that identifies the error of the macroscopic problem and of the auxiliary problems with respect to a physical quantity of interest and allows for a *splitting of the influence of the discretization of the auxiliary problems and the macroscopic problem*. This allows for the systematic discretization of the different meshes independently while still maintaining an estimation of the influence of the respective discretization errors to the goal functional at hand. Note that we require that the number of auxiliary problems is a priori known and somehow "small", in the sense that it is efficient to approximate all of the auxiliary problems. Examples for this type of homogenization problems are presented in Section 4.4.

The error estimator derived in this chapter is based on the **Dual Weighted Residual** method (see Becker and Rannacher [20]) as in Abdulle and Nonnenmacher [4]. Our approach is nevertheless different because we use a different dual

problem that allows defining error indicators for both the macroscopic and microscopic mesh while in Abdulle and Nonnenmacher [4] the microscopic mesh size is statically coupled to the macroscopic one. Even though we consider only *periodic* homogenization problems and do not treat the more general non-periodic case, there is a broad range of applications (see below) in which the adaptive algorithm developed here can be of assistance. The prototypical problems treated in Section 4.4, where we present the viability of our algorithm, have a wide practical relevance in different applications such as diffusion in porous media, heat transport in composite materials, and Darcy flow in subsurface formations.

Applications

To explain the practical relevance of this work apart from the performance estimation of an SOFC that is the focus of this thesis we briefly describe a problem from practice that can be solved with the method presented here. A problem that we have in mind is the simulation of porous electrodes in electrochemical applications as e.g. Lithium-ion batteries Carraro et al. [35], Ender et al. [57], Joos et al. [81]. This is a prototypical problem in which the cell problems can be three dimensional (3-d) microstructures reconstructed by tomography and made periodic by reflections around the main axes, cf. Remark 5.2.3. The mesh derived by the reconstruction is typically voxel-based and has a large number of degrees of freedom needed to optically resolve the porous microstructure. Therefore, the calculation of effective parameters is computationally intensive. This can be disproportionate to obtain a given tolerance of the error in the macroscopic goal functional, e.g. a flux over a boundary. In case of reconstructions with a higher than needed resolution, one could reduce the computational costs by error-based local mesh adaptivity.

A further motivation to locally refine/coarse the cell problems is the non-convexity of the resolved porous structure. In this case, the discretization with finite elements may introduce corner singularities. It is not possible hence to define a priori to which extent these singularities must be resolved to obtain a given tolerance for the macroscopic discretization error. Our approach will lead to an adaptive refinement of the cell problems independently of the macroscopic discretization. Additionally, it is possible to balance the error contribution of the two parts, as shown in our test cases.

A further problem that we have in mind is the coupling between a gas channel and a porous bed. The corresponding effective problem is given by the coupling between the Stokes problem in the gas channel and the Darcy law in the porous part. In this case cell problems have to be solved for the upscaling of the permeability tensor and a boundary layer problem has to be solved to determine

the coupling at the Stokes-Darcy interface in the effective problem Carraro et al. [36], Marciniak-Czochra and Mikelić [98]. Depending on the scale of the pores the coupling might be more or less severe implying that the auxiliary problems must be more or less precisely solved. This can be seen in the numerical tests that we have reported.

4.2. Problem Setting

We are interested in the value $J^\varepsilon(v^\varepsilon) \in \mathbb{R}$ where J^ε is a given (possibly nonlinear) functional and v^ε is the solution of a partial differential equation (PDE) based model (the microscopic problem, see 4.2.1) which is too expensive to be solved numerically. This can be, for example, due to the fact that it is defined on a very complex domain which we cannot afford to resolve by a computational mesh or because the PDE has coefficients that are highly oscillating. We suppose that the series of **microscopic solutions** $(v^\varepsilon)_\varepsilon$ converges (in some sense) to a **macroscopic solution** v that solves a homogenized problem.

Let us fix some notation. The microscopic problem in weak form for a given value of $\varepsilon >$ reads:

Problem 4.2.1 (Microscopic Problem)**.** *Let a Hilbert space U^ε, a linear functional $F^\varepsilon \in \mathcal{L}(U^\varepsilon, \mathbb{R})$ and an elliptic semi-linear form $a^\varepsilon : U^\varepsilon \times U^\varepsilon \to \mathbb{R}$, linear in the argument after the semicolon, be given. Find the microscopic solution $v^\varepsilon \in U^\varepsilon$ s.t.*

$$a^\varepsilon(v^\varepsilon; \varphi^\varepsilon) = F^\varepsilon(\varphi^\varepsilon) \qquad \forall \varphi^\varepsilon \in U^\varepsilon. \tag{4.2.1}$$

Suppose the macroscopic solution v is taken from the solution space U and fulfills the macroscopic equation represented by the **effective semi-linear form**

$$a : \mathcal{U} \times U \to \mathbb{R} \tag{4.2.2}$$

that depends on the solutions $w_j \in W_j$ of some *auxiliary problems*, $j = 1, \dots, M$, where W_j is an appropriate solution space and $M \in \mathbb{N} \setminus \{ 0 \}$ denotes the number of auxiliary equations. Hereby is

$$\mathcal{U} = U \times \bigtimes_{j=1}^{M} W_j. \tag{4.2.3}$$

We specify what we mean by "appropriate" and how to choose the functional spaces U, W_j, the linear functionals F^v, F^{w_j} and the forms a and b_j in Assumption 4.2.4.

Problem 4.2.2 (Homogenized Problem). *Let U, W_j be Hilbert spaces, let $F^v \in \mathcal{L}(U, \mathbb{R})$ and $F^{w_j} \in \mathcal{L}(W_j, \mathbb{R})$ and let $a : \mathcal{U} \times U \to \mathbb{R}$ be the* macroscopic equation *and $b_j : W_j \times W_j \to \mathbb{R}$ be some auxiliary problems.*

Find the macroscopic solution $v \in U$ and the cell solutions $\mathbf{w} \in W := \bigtimes_j^M W_j$ s.t.

$$a(v, \mathbf{w}; \varphi^v) = F^v(\varphi^v) \qquad \forall \varphi^v \in U. \tag{4.2.4}$$

The macroscopic problem depends on the solutions $\mathbf{w} = (w_j)_j$ of the auxiliary problems

$$b_j(w_j; \varphi^{w_j}) = F^{w_j}(\varphi^{w_j}) \qquad \forall \varphi^{w_j} \in W_j, \tag{4.2.5}$$

where $1 \leq j \leq M$.

Examples for the additional problems (4.2.5) are cell problems, which solutions define effective model coefficients (e.g. diffusion or permeability coefficients) or the Navier Boundary Layer required by the Stokes-Darcy coupling, see Carraro et al. [36] and Section 4.4.3.

Remark 4.2.3. *Let us assume that U^ε is a function space on a domain Ω^ε, U is a function space on a domain Ω and W_j is a function space on Z_j. Note that these domains, especially Ω and Ω^ε do not have to be identical and thus the models* (4.2.1) (4.2.4) *and* (4.2.5) *may be defined on different domains, see numerical examples in Section 4.4.*

Before we proceed with the description of the problem, we want to emphasize that we are not interested here in solution theory or the derivation of homogenized models. Rather, we are concerned with the balancing of the discretization error stemming form the FE-approximation of the macroscopic problem (4.2.4) with the discretization errors of the auxiliary problems (4.2.5). Thus, we assume the following.

Assumption 4.2.4.

(i) The Solution spaces U^ε, U, W_j, the semi-linear forms a^ε, a and b_j and the functionals $F^\varepsilon \in \mathcal{L}(U^\varepsilon, \mathbb{R})$, $F^v \in \mathcal{L}(U, \mathbb{R})$ and $F^{w_j} \in \mathcal{L}(W_j, \mathbb{R})$ are chosen s.t. there exist unique solutions to Problem 4.2.1 and Problem 4.2.2.

(ii) The number M in Problem 4.2.2 which describes the number of auxiliary problems is a priori known and "reasonably small", cf. Remark 4.2.5

(iii) Let v^ε be the solution to Problem 4.2.1 and $\{v, \mathbf{w}\}$ the solution of Problem 4.2.2. We assume that $J^\varepsilon(v^\varepsilon) \to J(v, \mathbf{w})$ as $\varepsilon \to 0$. Here, J^ε and J are given functionals, acting on the solution space of microscopic resp. the homogenized equation.

Remark 4.2.5. *A short note regarding the severeness of the Assumption 4.2.4 (ii). Linear PDEs with oscillating coefficients/on a perforated domain, where the oscillations/perforations do not depend on the macroscopic variable fulfil this assumption. The same does hold for semi- and quasi-linear PDEs, see 5.2.3.*

Let us turn back to the homogenized problem. Since the macroscopic model is derived from the microscopic model by homogenization, the underlying PDEs may differ (as in the case of Stokes equation, which becomes Darcy equation after the upscaling), the coefficients are replaced with upscaled versions and the boundary conditions may be different as well (as for example in the Stokes-Darcy coupling). A prototypical example for the situation described in Problem 4.2.2 is shown in Example 4.2.6, for more examples see Section 4.4. We will substantiate the abstract notation by the following, well established standard Example 4.2.6 of homogenization theory, see also Section 2.2.

Example 4.2.6 (Laplace Equation with Oscillating Coefficients)**.** *Let $Y = (0,1)^2$ be the unit cell, $\Omega \subset \mathbb{R}^2$ be a bounded domain, $f \in L^2(\Omega)$ and $\varepsilon > 0$ with $\varepsilon \ll \operatorname{diam}(\Omega)$. Consider the symmetric, Y-periodic diffusion tensor $\mathbf{A} = (A_{ij}) : \mathbb{R}^2 \to \mathbb{R}$ which we assume to be elliptic, i.e. there exists $\alpha, \beta > 0$ s.t. for $y \in Y$*

$$\alpha|\xi|^2 \leq \sum_{i,j=1}^{2} A_{ij}(y)\xi_i\xi_j \leq \beta|\xi|^2 \qquad \forall \xi \in \mathbb{R}^2. \tag{4.2.6}$$

We define the oscillating coefficient $\mathbf{A}^\varepsilon : \Omega \to \mathbb{R}^2$ by

$$\mathbf{A}^\varepsilon(x) = \mathbf{A}(\tfrac{x}{\varepsilon}). \tag{4.2.7}$$

The microscopic problem *in weak form reads:*

Find $v^\varepsilon \in H_0^1(\Omega)$ s.t.

$$(\mathbf{A}^\varepsilon \nabla v^\varepsilon, \nabla \varphi^\varepsilon)_\Omega = (f, \varphi^\varepsilon)_\Omega \qquad \forall \varphi^\varepsilon \in H_0^1(\Omega). \tag{4.2.8}$$

We are interested in the solution of the macroscopic problem*:*

Find $v \in H_0^1(\Omega)$ s.t.

$$(\mathbf{A}^{\hom}(\mathbf{w})\nabla v, \nabla \varphi^v)_\Omega = (f, \varphi^v)_\Omega \qquad \forall \varphi^v \in H_0^1(\Omega). \tag{4.2.9}$$

The (constant) homogenized tensor*, cf.* (2.2.42)

$$\mathbf{A}^{\hom}(\mathbf{w}) := \Big(\int_Y \mathbf{A}(y)\{\nabla w_j \cdot \mathbf{e}_i + \delta_{ij}\} dy \Big)_{ij} \tag{4.2.10}$$

depends on the solutions w_j, $j = 1, 2$ of the auxiliary problems *or* cell problems*:*

Find $w_j \in H^1_{\text{per}}(Y) \cap \left\{ \varphi^{w_j} \in H^1(Y) \,\middle|\, \int_Y \varphi^{w_j}(y)\,\mathrm{d}y = 0 \right\}$ *s.t.*

$$(\mathbf{A}\nabla w_j, \nabla \varphi^{w_j})_Y = -(\mathbf{A}\mathbf{e}_i, \nabla \varphi^{w_j})_Y \qquad \forall \varphi^{w_j} \in H^1_{\text{per}}(Y). \tag{4.2.11}$$

There holds then $v^\varepsilon \rightharpoonup v$ *in* $H^1_0(\Omega)$ *as* $\varepsilon \to 0$*, see for example Bensoussan et al. [22, Chapter I, Theorem 6.1].*

Keep in mind that we are interested in the functional value $J^\varepsilon(v^\varepsilon)$. Since the computation of $J^\varepsilon(v^\varepsilon)$ is too expensive, we want to approximate this quantity by $J(v, \mathbf{w})$ where J is a functional acting on the solution space of the homogenized problem. By substituting the microscopic solution v^ε with the pair $(v, \mathbf{w})$ we introduce a *model error*

$$J^\varepsilon(v^\varepsilon) - J(v, \mathbf{w}). \tag{4.2.12}$$

Typically, a priori error estimates in global norms for the model error are available (see references in the introduction), while error estimates in the quantity of interest are mostly not available. The estimation of the model error, especially in a quantity of interest, is of great importance in context of multiscale problems. We cite the work Oden et al. [109] in which a method to estimate the model error a posteriori is introduced. This approach allows for an adaptive modelling controlled by the error in a quantity of interest and needs the local computation of the microscopic problem. Nevertheless, we do not consider this aspect and rely on available a priori error estimates as done in Ohlberger [110] and Abdulle and Nonnenmacher [4] for example. Thus, we assume in the following:

Assumption 4.2.7. *We consider an ε-range for the microscopic problems such that the model error is small in comparison with the error introduced by the numerical approximations.*

Remark 4.2.8. *A short note on the Assumption 4.2.7. In mathematical homogenization the talk is often about the convergence of the microscopic solution towards the macroscopic one. So if we are looking at a convergence result for $\varepsilon \to 0$, why are we talking about an ε-range in the previous assumption?*

This is due to the reason that in real applications, one is generally interested in the solution of the microscopic equation for a given fixed value ε_0, which describes the features of, for example, some porous medium. Thus, the macroscopic solution is only an approximation of the model we are interested in. The model error *is preset by the application. The Assumption 4.2.7 is to be understood in this sense. We consider only applications which allow a "good" approximation by a homogenized problem.*

Our work is hence focused on the estimation of the **discretization error**

$$J(v, \mathbf{w}) - J(v_h, \mathbf{w}_h) \tag{4.2.13}$$

of a general nonlinear functional J, where $\{v_h, \mathbf{w}_h\}$ represents an FE-approximation of $\{v, \mathbf{w}\}$. This means we will derive an estimator η which approximates this discretization error. But more importantly, this chapter is focused on splitting this error estimator into a part η^{m}, which stems from the discretization of the **macroscopic problem** and parts η^{c_j}, $1 \leq j \leq M$, which measure the influence of the discretization of the **auxiliary problems**. Additionally, we gain local error indicators for the macroscopic mesh and the auxiliary-meshes. All these ingredients are then used in the derivation of an adaptive solution algorithm for the discretized homogenized problem.

4.3. Finite Element Approximation and Goal-Oriented Error Estimation

In this section we describe briefly the problem discretization with the finite element method in 4.3.1 and the representation of the consequently derived discretization error $J(v, \mathbf{w}) - J(v_h, \mathbf{w}_h)$ in 4.3.2. How to evaluate the error representation is explained in 4.3.3; an adaptive algorithm based on this evaluation is shown in 4.3.4.

4.3.1. Discretization with Finite Elements

We consider a discretization of Problems 4.2.1 and 4.2.2 using appropriate finite element spaces which will be specified later in the numerical examples. For an introduction on the finite element method we refer to standard text books as e.g. Brenner and Scott [30], Ciarlet [41]. We will give a brief summary here to make this chapter self-contained.

We are interested in the discretization error $J(v, \mathbf{w}) - J(v_h, \mathbf{w}_h)$, where $(v_h, \mathbf{w}_h)$ is the finite element approximation of the solution of Problem 4.2.2. The discrete counterpart of the macroscopic problem reads

Problem 4.3.1 (Discrete macroscopic problem)**.** *Let $U_h, W_{j,h}$ be appropriate finite element spaces.*

Find $v_h \in U_h$ and $\mathbf{w}_h \in W_h = \bigtimes_j W_{j,h}$ s.t.

$$a(v_h, \mathbf{w}_h; \varphi_h^v) = F^v(\varphi_h^v) \quad \forall \varphi_h^v \in U_h. \tag{4.3.1}$$

The solution components $\mathbf{w}_h = (w_{j,h})_j$ *are given by*

$$b_j(w_{j,h}; \overset{w_j}{\varphi_h}) = F^{w_j}(\overset{w_j}{\varphi_h}) \quad \forall \overset{w_j}{\varphi_h} \in W_{j,h}. \tag{4.3.2}$$

Equation (4.3.1) is defined on the *macroscopic domain* Ω and the equations (4.3.2) are defined on the *auxiliary domains* Z_j. We consider shape-regular triangulations of these domains given by a set of non-overlapping, non-degenerate open grid-cells $\{ K \}$ s.t. the union of the closure of the grid cells covers the whole domain. In our numerical example we use quadrilateral cells K^m resp. K^{c_j} and define the triangulations $\mathcal{T}_h^m = \{K^m\}$ and $\mathcal{T}_h^{c_j} = \{K^{c_j}\}$. We denote the union of aforementioned triangulations by $\mathcal{T}_h = \bigcup_j \mathcal{T}_h^{c_j} \cup \mathcal{T}_h^m = \{K\}$. The subscript h corresponds, as usual, to a mesh parameter which is defined respectively on the different domains as the piecewise constant function $h_{|K} = h_K$, where h_K is the cell diameter of the cell K.

One of the main goals of this work is to determine the triangulations $\mathcal{T}_h^m$ and $\mathcal{T}_h^{c_j}$ in an adaptive way such that the error with respect to a goal functional is minimized for a given number of cells. We consider independent adaptive meshes for all subproblems in 4.3.1. Local refinement is achieved by allowing the subdivision of one cell without varying the neighbours. This is obtained by introducing hanging nodes between a refined cell and its neighbours, see Rheinboldt and Mesztenyi [113]. We allow only one hanging node per edge, see also Figure 4.3.1. For practical purposes, we need also that all the involved meshes follow a so called *patch-structure*. This means that each grid $\mathcal{T}_h$ has a corresponding coarse grid $\mathcal{T}_{2h}$ such that $\mathcal{T}_h$ is made up of a global refinement of $\mathcal{T}_{2h}$, see again Figure 4.3.1 for an example of this.

Remark 4.3.2. *Note that no degrees of freedom are connected to the hanging nodes. These nodal values are eliminated from the linear system by interpolation s.t. the corresponding finite element space is still* H^1*-conform.*

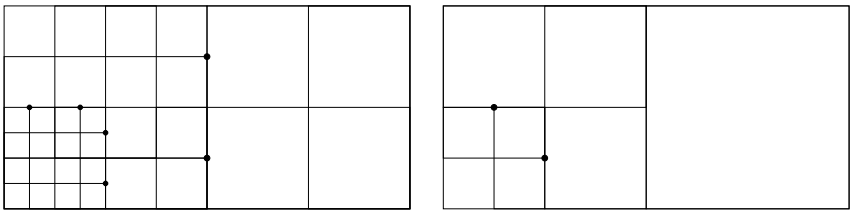

(a) Grid $\mathcal{T}_h$ **(b)** Coarse mesh $\mathcal{T}_{2h}$

Figure 4.3.1.: Example of a grid $\mathcal{T}_h$ with patch-structure (a) hanging nodes. The mesh $\mathcal{T}_{2h}$ in (b) is the result of a patch-wise coarsening of $\mathcal{T}_h$.

In general, the discretization errors of all subproblems in 4.3.1 contribute to the overall error in the goal functional. The question is, how big is the contribution? In the numerical example of Section 4.4.1 we present an extreme case in which the discretization of one auxiliary problem can be neglected completely. We derive a method in the next sections that not only allows for an estimation of the different sources of error separately, but takes also the coupling between the problems into account.

4.3.2. Error Representation

In this section, we derive an a posteriori error estimator for the error arising in the goal functional J due to the discretization of the macroscopic solution v and the auxiliary solutions $\mathbf{w}$ with the finite element method. We follow Becker and Rannacher [20] and employ the DWR method. First, we reformulate Problem 4.2.2 to apply a theorem of Becker and Rannacher [20] to gain the desired error estimator. Afterward, we translate the result back to the language of the homogenized problem.

Problem 4.3.3 (Homogenized Problem in Compact Form)**.** *We use the notation of Problem 4.2.2. Let $\mathcal{U} = U \times W$. We define the semi-linear form $\bar{a} : \mathcal{U} \times \mathcal{U} \to \mathbb{R}$ and the functional $F \in \mathcal{L}(U, \mathbb{R})$ for $\boldsymbol{\varphi} = (\varphi^v, \boldsymbol{\varphi}^w), \boldsymbol{\psi} = (\psi^v, \boldsymbol{\psi}^w) \in \mathcal{U}$ by*

$$\bar{a}(\boldsymbol{\psi}; \boldsymbol{\varphi}) = a(\psi^v, \boldsymbol{\psi}^w; \varphi^v) + \sum_{j=1}^{M} b_j(\psi^{w_j}; \varphi^{w_j}) \tag{4.3.3}$$

and

$$F(\boldsymbol{\varphi}) = F^v(\varphi^v) + \sum_{j=1}^{M} F^{w_j}(\varphi^{w_j}) \tag{4.3.4}$$

Problem 4.2.2 is then equivalent to: Find $\mathbf{u} \in \mathcal{U}$ with $\mathbf{u} = (v, \mathbf{w})$, s.t.

$$\bar{a}(\mathbf{u}; \boldsymbol{\varphi}) = F(\boldsymbol{\varphi}) \qquad \forall \boldsymbol{\varphi} \in \mathcal{U}. \tag{4.3.5}$$

The finite element discretization of Problem 4.3.3 described in Section 4.3.1, reads in compact form

Problem 4.3.4. *We use the notation of Problem 4.3.1. Let $\mathcal{U}_h = U_h \times W_h$. Find $\mathbf{u}_h \in \mathcal{U}_h$ s.t.*

$$\bar{a}(\mathbf{u}_h; \boldsymbol{\varphi}_h) = F(\boldsymbol{\varphi}_h) \qquad \forall \boldsymbol{\varphi}_h \in \mathcal{U}_h. \tag{4.3.6}$$

We keep in mind the goal of our computations.

Definition 4.3.5. *Let the* goal functional $J : \mathcal{U} \cup \mathcal{U}_h \to \mathbb{R}$ *be given. Our goal is the computation of the quantity* $J(\mathbf{u})$*, where* $\mathbf{u}$ *is the solution of Problem 4.3.3.*

Assumption 4.3.6. *We assume for the following that*

(i) Problems 4.3.3 and 4.3.4 have unique solutions and

(ii) $J(\mathbf{u}_h) \to J(\mathbf{u})$ *for* $h \to 0$*.*

(iii) Furthermore we assume the existence of Fréchet derivative of the functional J *and the semi-linear forms* a *and* b_j *up to the order three (w.r.t. their first argument).*

In the DWR method an error estimator is obtained by weighting the residual of the problem at hand with the solution of an appropriate *adjoint* (or *dual*) problem. For the DWR error representation we need the residual of Problem 4.3.4, $\rho(\mathbf{u}_h)(\cdot)$, which is defined by

$$\rho(\mathbf{u}_h)(\boldsymbol{\varphi}) = \underbrace{F^v(\varphi^v) - a(v_h, \mathbf{w}_h; \varphi^v)}_{=:\rho^v(\mathbf{u}_h)(\varphi^v)} + \sum_{j=1}^{M} \underbrace{F^{w_j}(\varphi^{w_j}) - b_j(w_{j,h}; \varphi^{w_j})}_{=:\rho^{w_j}(w_{j,h})(\varphi^{w_j})}, \quad \boldsymbol{\varphi} \in \mathcal{U}, \tag{4.3.7}$$

and can be split in the sum of the **macroscopic residual** $\rho^v(\mathbf{u}_h)(\cdot)$ and the **auxiliary residuals** $\rho^{w_j}(w_{j,h})(\cdot)$.

Furthermore, we need the adjoint of Problem 4.3.3 considering the chosen goal functional, which reads

Problem 4.3.7 (Dual Problem in Compact Form)**.** *Find* $\mathbf{z} \in \mathcal{U}$ *s.t.*

$$\bar{a}'(\mathbf{u}; \mathbf{z}, \boldsymbol{\psi}) = J'(\mathbf{u}; \boldsymbol{\psi}) \qquad \forall \boldsymbol{\psi} \in \mathcal{U}. \tag{4.3.8}$$

Its finite element discretization is

Problem 4.3.8. *Find* $\mathbf{z}_h \in \mathcal{U}_h$ *s.t.*

$$\bar{a}'(\mathbf{u}_h; \mathbf{z}_h, \boldsymbol{\psi}_h) = J'(\mathbf{u}_h; \boldsymbol{\psi}_h) \qquad \forall \boldsymbol{\psi}_h \in \mathcal{U}_h. \tag{4.3.9}$$

Equivalently to (4.3.7), the **adjoint residual** $\rho^*(\mathbf{u}_h, \mathbf{z}_h; \cdot)$ is defined as the sum of the **dual macroscopic residual** $\rho^{v,*}(\mathbf{u}_h, \mathbf{z}_h)(\cdot)$ and the **dual auxiliary residuals**

$\rho^{w_j,*}(\mathbf{u}_h, \mathbf{z}_h)(\cdot)$ which are defined by:

$$\rho^*(\mathbf{u}_h, \mathbf{z}_h)(\boldsymbol{\psi}) := \underbrace{\partial_v J(\mathbf{u}_h; \psi^v) - \partial_v \bar{a}(\mathbf{u}_h; \mathbf{z}_h, \psi^v)}_{=:\rho^{v,*}(\mathbf{u}_h,\mathbf{z}_h)(\psi^v)} + \sum_{j=1}^{M} \underbrace{\partial_{w_j} J(\mathbf{u}_h; \psi^{w_j}) - \partial_{w_j} \bar{a}(\mathbf{u}_h; \mathbf{z}_h, \psi^{w_j})}_{=:\rho^{w_j,*}(\mathbf{u}_h,\mathbf{z}_h)(\psi^{w_j})}, \quad \boldsymbol{\psi} \in \mathcal{U}. \tag{4.3.10}$$

With these definitions at hand, we recall Becker and Rannacher [20, Proposition 2.2.] (adapted to our notation):

Theorem 4.3.9. *Let* $\mathbf{u}$, $\mathbf{u}_h$ *be the solutions of Problem 4.3.3 and Problem 4.3.4 and let* $\mathbf{z}$, $\mathbf{z}_h$ *be the solutions of the respective adjoint problems 4.3.7 and 4.3.8. We have the a posteriori error representation*

$$J(\mathbf{u}) - J(\mathbf{u}_h) = \tfrac{1}{2} \min_{\boldsymbol{\psi}_h \in \mathcal{U}_h} \rho(\mathbf{u}_h)(\mathbf{z} - \boldsymbol{\varphi}_h) + \tfrac{1}{2} \min_{\boldsymbol{\varphi}_h \in \mathcal{U}_h} \rho^*(\mathbf{u}_h, \mathbf{z}_h)(\mathbf{u} - \boldsymbol{\psi}_h) + R \tag{4.3.11}$$

with the residual $\rho(\mathbf{u}_h)(\cdot)$ *defined in* (4.3.7) *and the adjoint residual* $\rho^*(\mathbf{z}_h)(\cdot)$ *defined in* (4.3.10). *The* remainder term R *is given by*

$$R = \tfrac{1}{2} \int_0^1 \big\{ J'''(\mathbf{u}_h + s\mathbf{e}; \mathbf{e}, \mathbf{e}, \mathbf{e}) - \bar{a}'''(\mathbf{u}_h + s\mathbf{e}; \mathbf{z}_h + s\mathbf{e}^*, \mathbf{e}, \mathbf{e}, \mathbf{e}) - 3\bar{a}''(\mathbf{u}_h + s\mathbf{e}; \mathbf{e}^*, \mathbf{e}, \mathbf{e}) \big\}\, s(s-1)\, ds, \tag{4.3.12}$$

where $\mathbf{e} := \mathbf{u} - \mathbf{u}_h$ *and* $\mathbf{e}^* := \mathbf{z} - \mathbf{z}_h$.

To translate the error representation (4.3.11) of the goal functional into the terms of Problem 4.2.2 we define the corresponding adjoint problem (see (4.3.8)) as follows

Problem 4.3.10. *Find* $(z^v, \mathbf{z}^w) \in U \times W$ *s.t.*

$$\partial_v a(v, \mathbf{w}; z^v, \psi^v) = \partial_v J(\mathbf{u}; \psi^v) \qquad \forall \psi^v \in U, \tag{4.3.13a}$$

$$\partial_{w_j} b_j(w_j; z^{w_j}, \psi^{w_j}) = \partial_{w_j} J(\mathbf{u}; \psi^{w_j}) - \partial_{w_j} a(v, \mathbf{w}; z^v, \psi^{w_j}) \qquad \forall \psi^{w_j} \in W_j. \tag{4.3.13b}$$

Thus, one has to solve first the macroscopic dual and then the dual auxiliaries. The highlighted part in (4.3.13b) takes the coupling of the auxiliary problems with the macroscopic equation into account.

We can also express the **dual macroscopic residual** $\rho^{v,*}(\mathbf{u}_h, \mathbf{z}_h)(\cdot)$ and the **dual auxiliary residuals** $\rho^{w_j,*}(\mathbf{u}_h, \mathbf{z}_h)(\cdot)$ in these terms (note that the dual macroscopic

residual does not depend on the solutions of the dual auxiliaries, i.e. there holds $\rho^{v,*}(\mathbf{u}_h, \mathbf{z}_h)(\cdot) = \rho^{v,*}(\mathbf{u}_h, z_h^v)(\cdot)$):

$$\rho^{v,*}(\mathbf{u}_h, z_h^v)(\psi^v) = \partial_v J(\mathbf{u}_h; \psi^v) - \partial_v a(v_h, \mathbf{w}_h; z_h^v, \psi^v), \qquad \psi^v \in U, \tag{4.3.14}$$

$$\begin{aligned}\rho^{w_j,*}(\mathbf{u}_h, \mathbf{z}_h)(\psi^{w_j}) = {} & \partial_{w_j} J(\mathbf{u}_h; \psi^{w_j}) - \partial_{w_j} a(v_h, \mathbf{w}_h; z_h^v, \psi^{w_j}) \\ & - \partial_{w_j} b_j(w_{j,h})(z_h^{w_j}, \psi^{w_j}), \qquad \psi^{w_j} \in W_j.\end{aligned} \tag{4.3.15}$$

Corollary 4.3.11. *Theorem 4.3.9 reads with the introduced notation:*

With $\psi_h^v, \varphi_h^v \in U_h$ and $\psi_h^{w_j}, \varphi_h^{w_j} \in W_{j,h}$ holds

$$J(\mathbf{u}) - J(\mathbf{u}_h) = \tfrac{1}{2}\left\{\rho^v(\mathbf{u}_h)(z^v - \varphi_h^v) + \rho^{v,*}(\mathbf{u}_h, z_h^v)(v - \psi_h^v)\right\} \tag{4.3.16a}$$

$$+ \sum_{j=1}^{M} \tfrac{1}{2}\left\{\rho^{w_j}(w_{j,h})(z^{w_j} - \varphi^{w_j}) + \rho^{w_j,*}(\mathbf{u}_h, \mathbf{z}_h)(w_j - \psi^{w_j})\right\} \tag{4.3.16b}$$

$$+ R. \tag{4.3.16c}$$

In Corollary 4.3.11 the error $J(\mathbf{u}) - J(\mathbf{u}_h)$ is split into two main components (neglecting the remainder),

- a **macroscopic part** (4.3.16a) and
- an **auxiliary part** (4.3.16b).

This splitting allows for balancing the error stemming from the discretization of macroscopic and auxiliary equations as shown in the examples in Section 4.4.

4.3.3. Practical Evaluation of the Error Estimator

The error representation (4.3.16) is not evaluable because the terms $\mathbf{u}$ and $\mathbf{z}$ are the analytical solutions of problems (4.3.5) and (4.3.8). We will discuss in this section how we make these terms computable to get an **error estimator**

$$\eta \approx J(\mathbf{u}) - J(\mathbf{u}_h). \tag{4.3.17}$$

Additionally, we explain how we localize the error estimator η to the cells K of our computational grid $\mathcal{T}_h$ to gain a set of local **error indicators**

$$\mathcal{E} := \{\, \eta_K \mid K \in \mathcal{T}_h \,\} \tag{4.3.18}$$

used to steer a local mesh refinement. As before, we follow the lines of Becker and Rannacher [20].

Typically the remainder term R in (4.3.16) can be neglected in η, since it is of higher order w.r.t. the errors $\mathbf{e}$ and $\mathbf{e}^*$. In case the remainder term is large, e.g. due to high non-linearities, and hence cannot be disregarded, we refer the reader to Becker and Rannacher [20, section 6.2].

We aim at substituting the continuous primal and adjoint solution from the error representation (4.3.16). There are various possibilities how to achieve this. One can for example employ a better approximation of $\mathbf{u}$ and $\mathbf{z}$ using a richer finite element space. This leads usually to good results, but it is mostly not worth to spend more work in estimating the error than in solving the original problem. In view of this consideration, we use here an approximation of the interpolation errors $\mathbf{z} - \boldsymbol{\psi}_h$ and $\mathbf{u} - \boldsymbol{\varphi}_h$ by a *patch-wise higher-order interpolation*. This means given the finite element approximations $\mathbf{u}_h$ and $\mathbf{z}_h$ we use component-wise interpolations $i_{2h}^+ \mathbf{u}_h$ and $i_{2h}^+ \mathbf{z}_h$ in a finite element space which is of higher order w.r.t. the polynomial degree using a coarser mesh $\mathcal{T}_{2h}$ obtained by combining four adjacent cells of $\mathcal{T}_h$ to one macro-cell (a so called *patch*). We replace then the expressions $\mathbf{z} - \boldsymbol{\psi}_h$ and $\mathbf{u} - \boldsymbol{\varphi}_h$ in the error representation by

$$\Pi_h \mathbf{z}_h := (i_{2h}^+ - \mathrm{id})\mathbf{z}_h \quad \text{and} \quad \Pi_h \mathbf{u}_h := (i_{2h}^+ - \mathrm{id})\mathbf{u}_h. \tag{4.3.19}$$

This approach is well established in the context of the DWR method and has been used with success, see, e.g. Bangerth and Rannacher [14], Becker et al. [21], Goll et al. [66] and the references therein. Also, for the scenario of uniformly refined meshes and smooth primal and dual solutions, a proof that this weight-approximation works can be found in Bangerth and Rannacher [14].

Taking all these modifications into account, we define the error estimator η by

$$\eta := \underbrace{\tfrac{1}{2}\left\{\rho^v(\mathbf{u}_h)(\Pi_h z_h^v) + \rho^{v,*}(\mathbf{u}_h, z_h^v)(\Pi_h v_h)\right\}}_{=:\eta^{\mathrm{m}}} \tag{4.3.20a}$$

$$+ \sum_{j=1}^{M} \underbrace{\tfrac{1}{2}\left\{\rho^{w_j}(w_{j,h})(\Pi_h z_h^{w_j}) + \rho^{w_j,*}(\mathbf{u}_h, \mathbf{z}_h)(\Pi_h w_{j,h})\right\}}_{=:\eta^{\mathrm{c}_j}}, \tag{4.3.20b}$$

with the the macroscopic part η^{m} and the auxiliary part $\eta^{\mathrm{c}} = \sum_{j=1}^{M} \eta^{\mathrm{c}_j}$.

Example 4.3.12 (Error Estimator for Example 4.2.6)**.** *How would the error estimator* (4.3.20) *look like for the approximation of Example 4.2.6? Assume that we are interested in the mean of v over Ω, i.e.*

$$J(\mathbf{u}) := \int_\Omega v(x)\, dx = (1, v). \tag{4.3.21}$$

We start off with the dual equations, the FE approximations are defined correspondingly.

The dual macroscopic problem is: Find $z^v \in H_0^1(\Omega)$ *s.t.*

$$(\mathbf{A}^{\hom}(\mathbf{w})^t \nabla z^v, \nabla \psi^v)_\Omega = (1, \psi^v)_\Omega \qquad \forall \psi^v \in H_0^1(\Omega).$$

The dual auxiliaries are: Find $z^{w_j} \in H^1_{\mathrm{per}}(Y) \cap \left\{ \psi^{w_j} \in H^1(Y) \,\middle|\, \int_Y \psi^{w_j}(y)\,\mathrm{d}y = 0 \right\}$ *s.t.*

$$(\mathbf{A}^t \nabla z^{w_j}, \nabla \psi^{w_j})_Y = -\left(\partial_{w_j} \mathbf{A}^{\hom}(\mathbf{w})(\psi^{w_j}) \nabla v, \nabla z^v\right)_\Omega \qquad \forall \psi^{w_j} \in H^1_{\mathrm{per}}(Y).$$

Back to the error estimator. Suppose we use of piecewise bi-linear approximations v_h *and* $\mathbf{w}_h$ *on a grid* $\mathcal{T}_h$ *of the solutions* v *and* $\mathbf{w}$ *of equations* (4.2.9) *and* (4.2.11) *in Example 4.2.6.*

In this case, we would use an interpolation i_{2h}^+ *into the space of piecewise bi-quadratic finite elements on* $\mathcal{T}_{2h}$*. The nine nodal values of a bi-linear finite element function on four neighbouring cells are used to define a bi-quadratic interpolation on the union of these four cells.*

The parts of the error estimator for this example reads as

$$\begin{aligned}\eta^{\mathrm{m}} = \tfrac{1}{2}\{&(f^v, \Pi_h z_h^v)_\Omega - (\mathbf{A}^{\hom}(\mathbf{w}_h)\nabla v_h, \nabla \Pi_h z_h^v)_\Omega \\ &+ (1, \Pi_h v_h)_\Omega - (\mathbf{A}^{\hom}(\mathbf{w}_h)^t \nabla z_h^v, \nabla \Pi_h v_h)_\Omega\}, \end{aligned} \tag{4.3.22a}$$

$$\begin{aligned}\eta^{\mathrm{c}_j} = \tfrac{1}{2}\{&-(\mathbf{A}\left\{\mathbf{e}_i + \nabla w_{j,h}\right\}, \nabla \Pi_h z_h^{w_j})_Y \\ &- (\partial_{w_j}\mathbf{A}^{\hom}(\mathbf{w}_h)(\Pi_h w_{j,h})\nabla v_h, \nabla z_h^v)_\Omega - (\mathbf{A}^t \nabla z_h^{w_j}, \nabla \Pi_h w_{j,h})_Y\}. \end{aligned} \tag{4.3.22b}$$

The last step is to split the various error parts of the error estimator (4.3.20) into a set of cell-wise contributions $\mathcal{E}$ to drive an adaptive mesh refinement. We will explain this at the Example 4.3.12.

A simple localization of (4.3.22), i.e. an evaluation of the involved integrals over the cells K, leads generally to bad local error indicators due to the oscillatory nature of the residuals see Carstensen and Verfurth [38]. We overcome this shortcoming by integrating the residuals cell-wise by parts. Afterward, we sum up the normal derivatives over inner cell-edges (the so called *jump* terms) and distribute them, scaled by $1/2$, onto the two neighbouring cells. We obtain

$$\eta^{\mathrm{m}} = \sum_{K^m \in \mathcal{T}_h^m} \tilde{\eta}_{K^m}^m \quad \text{and} \quad \eta^{\mathrm{c}_j} = \sum_{K^{c_j} \in \mathcal{T}_h^{\mathrm{c}_j}} \tilde{\eta}_{K^{c_j}}^{c_j} \tag{4.3.23}$$

with the local cell contributions $\tilde{\eta}^m_{K^m}$ and $\tilde{\eta}^{c_j}_{K^{c_j}}$ defined as

$$\begin{aligned}\tilde{\eta}^m_{K^m} = \tfrac{1}{2}\{&(f^v + \nabla\cdot\Big(\mathbf{A}^{\text{hom}}(\mathbf{w}_h)\nabla v_h\Big), \Pi_h\, z_h^v)_{K^m} \\ &+ \tfrac{1}{2}([\mathbf{n}\cdot\mathbf{A}^{\text{hom}}(\mathbf{w}_h)\nabla v_h], \Pi_h\, z_h^v)_{\partial K^m\setminus\partial\Omega} \\ &+ (1 + \nabla\cdot\Big(\mathbf{A}^{\text{hom}}(\mathbf{w}_h)^t\nabla z_h^v\Big), \Pi_h\, v_h)_{K^m} \\ &+ \tfrac{1}{2}([\mathbf{n}\cdot\mathbf{A}^{\text{hom}}(\mathbf{w}_h)^t\nabla z_h^v], \Pi_h\, v_h)_{\partial K^m\setminus\partial\Omega}\}\end{aligned}$$

and

$$\begin{aligned}\tilde{\eta}^{c_j}_{K^{c_j}} = \tfrac{1}{2}\{&-(\mathbf{A}\mathbf{e}_i, \nabla\,\Pi_h\, z_h^{w_j})_{K^{c_j}} + (\nabla\cdot\Big(\mathbf{A}\nabla w_{j,h}\Big), \Pi_h\, z_h^{w_j})_{K^{c_j}} \\ &+ \tfrac{1}{2}([\mathbf{n}\cdot\mathbf{A}\nabla w_{j,h}], \Pi_h\, z_h^{w_j})_{\partial K^{c_j}\setminus\partial Y} \\ &- (\partial_{w_j}\mathbf{A}^{\text{hom}}(\mathbf{w}_h)(\Pi_h\, w_{j,h})\Big|_{K^{c_j}}\nabla v_h, \nabla z_h^v)_\Omega \\ &+ (\nabla\cdot\Big(\mathbf{A}^t\nabla z_h^{w_j}\Big), \Pi_h\, w_{j,h})_{K^{c_j}} + \tfrac{1}{2}([\mathbf{n}\cdot\mathbf{A}^t\nabla z_h^{w_j}], \Pi_h\, w_{j,h})_{\partial K^{c_j}\setminus\partial Y}\}.\end{aligned}$$

Finally, local error indicators are gained by taking the absolute values:

$$\eta^{\text{m}}_{K^m} = |\tilde{\eta}^m_{K^m}| \qquad \forall K^m \in \mathcal{T}_h^m \tag{4.3.24}$$

$$\eta^{\text{c}_j}_{K^{c_j}} = \left|\tilde{\eta}^{c_j}_{K^{c_j}}\right| \qquad \forall K^{c_j} \in \mathcal{T}_h^{c_j} \tag{4.3.25}$$

Summing up all terms, we end up with a formula for the error estimator

$$\eta = \eta^{\text{m}} + \sum_{j=1}^{M}\eta^{\text{c}_j} \approx J(\mathbf{u}) - J(\mathbf{u}_h) \tag{4.3.26}$$

as well as sets of local error indicators for the macroscopic and the auxiliary problems,

$$\mathcal{E}^m = \{\eta^{\text{m}}_{K^m} | K^m \in \mathcal{T}_h^m\} \quad \text{and} \quad \mathcal{E}^{c_j} := \{\eta^{\text{c}_j}_{K^{c_j}} | K^{c_j} \in \mathcal{T}_h^{\text{c}_j}\}. \tag{4.3.27}$$

4.3.4. Adaptive Algorithm

The goal of the local adaption of the grids $\mathcal{T}_h^m$ and $\mathcal{T}_h^{\text{c}_j}$ is the efficient approximation of the goal quantity $J(\mathbf{u})$ up to a given tolerance $TOL > 0$

$$\left|J(\mathbf{u}) - J(\mathbf{u}_h)\right| < TOL. \tag{4.3.28}$$

We start our computation with relatively coarse grids and use then in every cycle the error estimator η to check if our approximation is already good enough. If this is not the case, we decide based on the ratio between η^{m} and η^{c_j}, which grids we refine. It is desirable to balance all the different parts of the error, i.e. to have

$$\eta^{\mathrm{m}} \approx \eta^{\mathrm{c}_1} \approx \cdots \approx \eta^{\mathrm{c}_M}$$

during all the refinement cycles, as this is the most efficient way of distributing the available resources, cf. Algorithm 4.3.1. We are free to set the parameters $\mathcal{C}_i$ in line 16 of the algorithm, their value depends on the assumed local convergence of the different error components.

If we have decided to refine a particular grid, we do this based on the given set of local error indicators $\mathcal{E}$. There are several ways which cells should be marked for refinement, refer once more to Becker and Rannacher [20] for an overview. In this chapter, we employ a refinement strategy based upon minimization of expected error and computational effort required for the solution on the new mesh, see Richter [114].

4.4. Numerical Examples

In this section we present the numerical results for three different problems obtained by the adaptive Algorithm 4.3.1 showing the reliability of the error estimator and local grid refinement.

As it is mostly done in a posteriori error estimation, we measure the quality of the error estimator with the help of the so called *effectivity index*

$$I_{eff} := \frac{\eta}{J(\mathbf{u}) - J(\mathbf{u}_h)}. \tag{4.4.1}$$

An effectivity index close to one is the desired result.

We present all the equations in the examples in strong form, we refer again to Remark 3.1.5.

All computations in this section are done using the toolkit `DOpElib` Goll et al. [65] based upon the C++-library `deal.II` Bangerth et al. [15, 16].

4.4.1. Simple Poisson Example

This is an introductory example similar to Example 4.2.6, the only difference is that we take non-homogeneous boundary conditions. To keep the golden thread,

Algorithm 4.3.1.: Adaptive refinement algorithm.

Choose $TOL > 0$
Choose initial meshes $\mathcal{T}_h^{m,1}$ and $\mathcal{T}_h^{c_j,1}$
Set $n = 1$, $\eta^0 = 2TOL$
while $\eta^{n-1} < TOL$ **do**
  Compute auxiliary solutions $w_{j,h}^n$
  Evaluate macroscopic semi-linear form $a(\cdot, \mathbf{w}^n)(\cdot)$
  Compute macroscopic solution v_h^n
  Evaluate functional $J(\mathbf{u}_h^n)$
  Compute macroscopic dual solution $z_h^{v,n}$
  Evaluate dual coupling term $\partial_{w_j} a(v_h^n, \mathbf{w}_h^n)(z_h^{v,n}, \cdot)$
  Compute auxiliary dual solutions $z_h^{w_j,n}$
  Evaluate $\eta^{m,n}$ and $\eta^{c_j,n}$, set $\eta^n = \eta^{m,n} + \sum_{j=1}^{M} \eta^{c_j,n}$
  Set $E = (\eta^{m,n}, \eta^{c_1,n}, \ldots, \eta^{c_M,n}, 0)$, sort E from large to small
  for $i = 1 : M + 1$ **do**
    Refine grid belonging to E_i adaptively
    if $E_i > C_i E_{i+1}$ **then**
      end for loop
    else
      continue for loop
    end if
  end for
  Set $n \to n + 1$.
end while

we will show the first results of the adaptive algorithm in the framework of this common example. The other examples in this section are more closely related to the fuel cell model we consider in this dissertation in Chapter 5.

Let $\Omega = (0,1)^2$. The microscopic problem in strong form reads:

Problem 4.4.1. *Find v^ε s.t.*

$$-\nabla \cdot \left(\mathbf{A}^\varepsilon \nabla v^\varepsilon \right) = 1 \qquad \text{in } \Omega, \tag{4.4.2}$$

$$v^\varepsilon = \tfrac{x_2}{2}(-x_2 + 11) \qquad \text{on } \partial\Omega, \tag{4.4.3}$$

with

$$\mathbf{A}^\varepsilon = \lambda^\varepsilon \, \mathrm{id}, \tag{4.4.4}$$

where $\lambda^\varepsilon(x) = \lambda(\frac{x}{\varepsilon})$ *and*

$$\lambda(y) = \tfrac{64}{9\sqrt{17}}(\sin(2\pi y_1) + \tfrac{9}{8})(\cos(2\pi y_2) + \tfrac{9}{8}), \quad \text{for } y \in Y = (0,1)^2. \tag{4.4.5}$$

We are interested in the quantity

$$J(v) = \int_\Omega v(x)\,dx. \tag{4.4.6}$$

v is the solution of the *macroscopic problem* belonging to Problem 4.4.1, which reads in strong form

Problem 4.4.2. *Find v s.t.*

$$-\nabla \cdot \left(\mathbf{A}^{\text{hom}} \nabla v\right) = 1 \qquad \text{in } \Omega, \tag{4.4.7}$$

$$v = \tfrac{x_2}{2}(-x_2 + 11) \qquad \text{on } \partial\Omega. \tag{4.4.8}$$

See Example 4.2.6 for the definition of $\mathbf{A}^{\text{hom}}$ *and the* cell problems.

Remark 4.4.3. *In the example at hand, the correct homogenization coefficient and macroscopic solution are known. For $x \in \Omega$ there holds*

$$\mathbf{A}^{\text{hom}} = \text{id} \quad \text{and} \quad v(x) = \tfrac{x_2}{2}(-x_2 + 11). \tag{4.4.9}$$

This means that the macroscopic solution is independent of x_1 and subsequently the cell problem related to this direction should not contribute to the solution. We will see that the adaptive algorithm picks up on this behaviour.

As the solution is smooth and the functional has no special local features, we do not expect to experience local refinement on the macroscopic level. This example highlights the fact that the algorithm can handle the estimation *and* separation *of the different error-shares.*

We discretize the macroscopic problem and the cell problems with bi-linear elements. The direct solver UMFPACK is employed for the solution of the emerging discrete equations, see Davis [50].

Independence of the different error parts Of special importance when splitting the overall discretization error into the different parts is the independence of the various error components of the refinement of the other parts. This is numerically justified in this paragraph.

In Table 4.4.1 we present the behaviour of the different parts of the error estimator for a fixed mesh under the refinement of the other parts of the discretization. Listed are

- the degrees of freedom (DoF) used in the discretization of the macroscopic problem, $\mathrm{DoF}^{\mathrm{m}}$,
- the DoF used in the discretization of the two cell problems, $\mathrm{DoF}^{\mathrm{c}_1}$ and $\mathrm{DoF}^{\mathrm{c}_2}$, and
- the value of the different parts of the error estimator, η^{m}, η^{c_1} and η^{c_2}.

For example, in the first big row, we keep $\mathrm{DoF}^{\mathrm{m}}$ constant whereas we refine the meshes of the cell problems globally. We see that the changes in η^{m} are negligible, i.e. the error estimator of the macroscopic problem is independent with respect to changes of the meshes of the cell problems. The same holds true for the other cases. This gives a numerical confirmation that the error estimators can be split into the decoupled terms η^{m}, η^{c_1} and η^{c_2} and justifies the balancing strategy presented in Algorithm 4.3.1.

$\mathrm{DoF}^{\mathrm{m}}$	$\mathrm{DoF}^{\mathrm{c}_1}$	$\mathrm{DoF}^{\mathrm{c}_2}$	η^{m}	η^{c_1}	η^{c_2}
1,089	81	81	$7.28 \cdot 10^{-5}$		
1,089	289	289	$7.94 \cdot 10^{-5}$		
1,089	1,089	1,089	$8.09 \cdot 10^{-5}$		
1,089	4,225	4,225	$8.13 \cdot 10^{-5}$		
1,089	16,641	16,641	$8.13 \cdot 10^{-5}$		
81	1,089	81		$5.35 \cdot 10^{-34}$	
289	1,089	289		$9.41 \cdot 10^{-35}$	
1,089	1,089	1,089		$1.25 \cdot 10^{-34}$	
4,225	1,089	4,225		$5.97 \cdot 10^{-35}$	
16,641	1,089	16,641		$2.89 \cdot 10^{-34}$	
81	81	1,089			$4.79 \cdot 10^{-4}$
289	289	1,089			$4.85 \cdot 10^{-4}$
1,089	1,089	1,089			$4.86 \cdot 10^{-4}$
4,225	4,225	1,089			$4.87 \cdot 10^{-4}$
16,641	16,641	1,089			$4.87 \cdot 10^{-4}$

Table 4.4.1.: Independence of the error estimators on the refinement of the other parts of the problem.

Results of the adaptive algorithm In Table 4.4.2 we apply the adaptive algorithm as explained in the previous chapter onto the problem at hand. Besides

the DoF and the various parts of the error estimator η, the error in the functional $J(e) := J(\mathbf{u}) - J(\mathbf{u}_h)$ and the quality measure I_{eff} are shown. We see that the effectivity index is close to one throughout the whole adaptive cycle, showing that the error estimator is able to estimate the overall discretization error.

Note also, that the correct macroscopic solution (4.4.9) is independent of x_1, and because of that, the entries A_{11}^{hom} and A_{21}^{hom} are irrelevant for the exact computation of $J(v)$. The error contribution from the first cell problem is therefore zero and our estimator η^{c_1} shows precisely this feature. Since our refinement strategy based on the presented error estimator takes into account only the necessary components, it does not refine the first cell problem at all.

We note in addition that even though we use adaptive mesh refinement, the macroscopic problem is refined globally. This is due to the fact that the discretization error is distributed evenly across all cells, so that our refinement Algorithm 4.3.1 selects all the cells of $\mathcal{T}_h^m$ to be refined, which is in fact the most efficient refinement strategy in this situation.

DoF^{m}	DoF^{c_1}	DoF^{c_2}	$J(e)$	η^{m}	η^{c_1}	η^{c_2}	I_{eff}
25	81	81	$1.3 \cdot 10^{-2}$	$4.7 \cdot 10^{-3}$	$-7.5 \cdot 10^{-35}$	$6.0 \cdot 10^{-3}$	0.79
81	81	189	$3.4 \cdot 10^{-3}$	$1.3 \cdot 10^{-3}$	$-2.1 \cdot 10^{-34}$	$2.2 \cdot 10^{-3}$	1.02
289	81	353	$1.3 \cdot 10^{-3}$	$3.2 \cdot 10^{-4}$	$-3.5 \cdot 10^{-34}$	$8.7 \cdot 10^{-4}$	0.92
1,089	81	1,313	$3.3 \cdot 10^{-4}$	$8.1 \cdot 10^{-5}$	$-8.5 \cdot 10^{-35}$	$2.4 \cdot 10^{-4}$	0.97
4,225	81	4,593	$8.8 \cdot 10^{-5}$	$2.0 \cdot 10^{-5}$	$1.7 \cdot 10^{-34}$	$6.6 \cdot 10^{-5}$	0.98
16,641	81	6,533	$5.1 \cdot 10^{-5}$	$5.1 \cdot 10^{-6}$	$2.4 \cdot 10^{-33}$	$4.5 \cdot 10^{-5}$	0.99
16,641	81	23,505	$1.7 \cdot 10^{-5}$	$5.1 \cdot 10^{-6}$	$1.7 \cdot 10^{-33}$	$1.2 \cdot 10^{-5}$	0.99
66,049	81	29,933	$1.2 \cdot 10^{-5}$	$1.3 \cdot 10^{-6}$	$-4.3 \cdot 10^{-33}$	$1.1 \cdot 10^{-5}$	0.99

Table 4.4.2.: Results of local mesh refinement applied to the simple Poisson example.

4.4.2. Nonlinear Multi-Cell Example

The first example in Section 4.4.1 showed merely a proof of concept, whereas this example corresponds to a more complex situation to present the advantages of our adaptive Algorithm 4.3.1. In comparison with the first example, we have now a non-constant macroscopic diffusion coefficient and a nonlinear equation. We consider a perforated domain on the microscopic level as opposed to the periodically oscillating coefficient in the previous example.

Let the macroscopic domain $\Omega = (0, 2)^2$ be split into the domains Ω_{m} and Ω_{b} and the separating lines Γ as shown in Figure 4.4.1a. The microscopic problem is defined on the periodically perforated domain Ω^ε (see Definition 2.2.6). The

shape of the inclusion depends on the position in the domain Ω^ε, i.e. all inclusions that lie in Ω_b are shaped as described Y^b and all inclusions that lie in Ω_m are shaped as described Y^m. The unit cell Y^m which describes the microscopic domain in the middle part Ω_m is a circle with radius 0.25 and center $(0.5, 0.5)$, see Figure 4.4.1c. In Figure 4.4.1b we see a sketch of Y^b, which shows the unit-cell correlated to the pore-space in the brown-sketched regions Ω_b.

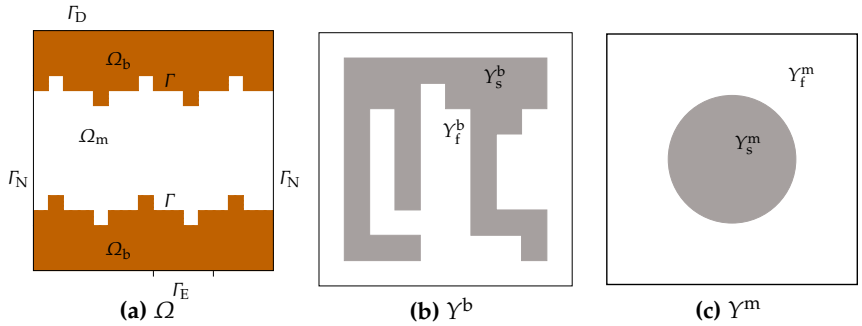

(a) Ω^ε **(b)** Y^b **(c)** Y^m

Figure 4.4.1.: Overview of the distribution of the two different inclusions in (a). In the brown parts Ω_b the microscopic domain is made up of repetitions of Y^b, see (b). In the white part Ω_m, the inclusions look as shown in the unit cell Y^m, see (c). The grey parts in the two unit cells represent the solid inclusions.

We split the boundary of Ω^ε into the disjunct parts Γ_D, Γ_N, Γ_E and Γ_O. Γ_O represents the boundary of the inclusions, the other parts of the boundary are defined as:

$$\Gamma_\mathrm{N} := \{0, 2\} \times (0, 2), \tag{4.4.10}$$
$$\Gamma_\mathrm{D} := (0, 2) \times \{0, 2\}, \tag{4.4.11}$$
$$\Gamma_\mathrm{E} := (1, 1.5) \times \{0\}. \tag{4.4.12}$$

The microscopic problem is a nonlinear PDE and reads as follows:

Problem 4.4.4. *Find v^ε s.t.*

$$-\nabla \cdot \left(\mathbf{A}^\varepsilon(1 + v^\varepsilon)\nabla v^\varepsilon\right) = 0 \qquad \text{in } \Omega^\varepsilon, \tag{4.4.13a}$$
$$v^\varepsilon = g_\mathrm{D} \qquad \text{on } \Gamma_\mathrm{D}, \tag{4.4.13b}$$
$$v^\varepsilon = 0 \qquad \text{on } \Gamma_\mathrm{O}, \tag{4.4.13c}$$
$$\mathbf{n} \cdot \left(\mathbf{A}^\varepsilon(1 + v^\varepsilon)\nabla v^\varepsilon\right) = g_\mathrm{N} \qquad \text{on } \Gamma_\mathrm{N}, \tag{4.4.13d}$$

with

$$\mathbf{A}^\varepsilon = \lambda^\varepsilon \,\mathrm{id}, \tag{4.4.14}$$

where,

$$\lambda^\varepsilon(x) = \lambda(x, \tfrac{x}{\varepsilon}) = \begin{cases} \lambda_{\mathrm{m}} := 0.1\chi_{Y_{\mathrm{f}}^{\mathrm{m}}}(\tfrac{x}{\varepsilon}), & x \in \Omega_{\mathrm{m}}, \\ \lambda_{\mathrm{b}} := \chi_{Y_{\mathrm{f}}^{\mathrm{b}}}(\tfrac{x}{\varepsilon}), & x \in \Omega_{\mathrm{b}}, \end{cases} \tag{4.4.15}$$

and the boundary data is

$$g_{\mathrm{D}} = \tfrac{1}{2}\exp\left((-20(x-0.5)^2\right) + 0.3, \tag{4.4.16}$$

$$g_{\mathrm{N}} = -0.08. \tag{4.4.17}$$

Remark 4.4.5. *This example is motivated by the mass-transport equation we model in the anode of the fuel-cell in Chapter 5. Given a distribution of some chemical species at the boundary between anode and gas channel Γ_{D} we are interested in the distribution of the species across the anode, which consist in this case of the compound of two different materials with specific diffusion properties and pore-shapes. The part of the boundary Γ denotes the interface between anode and electrolyte and thus we prescribe a negative flow of the species. Even if the given model is not actually the one we use in Chapter 5, we opted for a nonlinear PDE to show that our algorithm works in this case too. In the situation described here, the amount of the species at the boundary Γ_{E} is of special interest, see Chapter 5.*

The homogenization of this microscopic PDE leads to a nonlinear macroscopic equation and a homogenized diffusion coefficient which depends on four cell problems (see Chapter A for a formal derivation). These cell problems are given as follows.

Problem 4.4.6. *Find $w_{i,j}$, $i \in \{\mathrm{m}, \mathrm{b}\}$, $j \in \{1, 2\}$ s.t. $w_{i,j}$ is Y-periodic and*

$$\nabla \cdot (\lambda_i)\nabla w_{i,j} = -\nabla \cdot \lambda_i \mathbf{e}_j \qquad \text{in } Y_{\mathrm{f}}^i, \tag{4.4.18}$$

$$\mathbf{n} \cdot \lambda_i w_{i,j} = -\mathbf{n} \cdot \lambda_i \mathbf{e}_j \qquad \text{on } \partial Y_{\mathrm{s}}^i. \tag{4.4.19}$$

The macroscopic problem is defined on the square $\Omega = [0, 2]^2$ and reads in strong form

Problem 4.4.7. *Find v s.t.*

$$-\nabla \cdot \left(\mathbf{A}^{\mathrm{hom}}(1+v)\nabla v^\varepsilon\right) = 0 \qquad \text{in } \Omega^\varepsilon, \tag{4.4.20a}$$

$$v = g_D \qquad \text{on } \Gamma_{\mathrm{D}}, \tag{4.4.20b}$$

$$\mathbf{n} \cdot \left(\mathbf{A}^{\mathrm{hom}}(1+v^\varepsilon)\nabla v^\varepsilon\right) = g_N \qquad \text{on } \Gamma_N, \tag{4.4.20c}$$

Here $\mathbf{w} = (\mathbf{w}_\mathrm{m}, \mathbf{w}_\mathrm{b})$ *with* $\mathbf{w}_\mathrm{m}$ *and* $\mathbf{w}_\mathrm{b}$ *being the solutions of the cell problems 4.4.6. The homogenization tensor is defined as*

$$\mathbf{A}^{\mathrm{hom}}(\mathbf{w}, x) = \begin{cases} \mathbf{A}_\mathrm{m}^{\mathrm{hom}}(\mathbf{w}_\mathrm{m}), & x \in \Omega_\mathrm{m}, \\ \mathbf{A}_\mathrm{b}^{\mathrm{hom}}(\mathbf{w}_\mathrm{b}), & x \in \Omega_\mathrm{b}, \end{cases} \tag{4.4.21}$$

with

$$\mathbf{A}_{\mathrm{m/b}}^{\mathrm{hom}}(\mathbf{w}_{\mathrm{m/b}}) := \int_Y \lambda_{\mathrm{m/b}}(y)\{\nabla w_{\mathrm{m/b},j} \cdot \mathbf{e}_i + \delta_{ij}\}dy)_{ij}. \tag{4.4.22}$$

The quantity of interest in this example is given by

$$J(\mathbf{u}) = \int_\Gamma v(s)\, ds. \tag{4.4.23}$$

In Table 4.4.3 we see the results of our algorithm used to solve Problem 4.4.7. We use bi-linear finite elements for the discretization of all the involved problems. The notation in the table is analogous to the one described in Section 4.4.1. Table 4.4.3a shows the results for the macroscopic problem, whereas 4.4.3b and 4.4.3c show the DoF and error estimators for the four cell problems.

We see that our estimator is able to estimate the total error quite accurate (note that it is a nonlinear problem), as $0.5 \leq I_{eff} \leq 1$ throughout the computation. Moreover, the total error gets evenly distributed over the different cell problems and the macroscopic problem as expected by our error balancing strategy.

In the balancing procedure we note that the cell problem related to the x_1-direction Ω_m needs much less assigned degrees of freedom to get its error share into the same magnitude as the other parts. This behaviour shows that the diffusion in x_1-direction in this part of the domain has minor influence on the goal functional.

Lastly, our error estimator provides also meaningful local error indicators, as one can see in Figure 4.4.2. This figure shows the relative error in the target quantity plotted versus the sum of all DoF, i.e. the sum of DoF^m and the degrees of freedom used in the four cell problems. We see clearly the superiority of the algorithm using local grid refinement and balancing of different error parts in comparison with global refinement. The global refinement results in a convergence rate of approximately 1.5, whereas we achieve a convergence of order 2 with our algorithm (w.r.t. $\tilde{h} = \mathrm{DoF}^{-0.5}$).

In Figure 4.4.3 we see the resulting locally refined meshes after the fifth refinement cycle. The macroscopic domain is mostly refined in the vicinity of the boundary

$\mathrm{DoF}^{\mathrm{m}}$	$J(\mathbf{u})-J(\mathbf{u}_h)/J(\mathbf{u})$	$\eta/J(\mathbf{u})$	$\eta^{\mathrm{m}}/J(\mathbf{u})$	I_{eff}
1,089	$-7.7\cdot10^{-2}$	$-4.5\cdot10^{-2}$	$-1.6\cdot10^{-2}$	0.58
2,123	$-3.0\cdot10^{-2}$	$-1.7\cdot10^{-2}$	$-6.4\cdot10^{-3}$	0.58
5,115	$-1.2\cdot10^{-2}$	$-7.7\cdot10^{-3}$	$-2.7\cdot10^{-3}$	0.62
9,167	$-5.7\cdot10^{-3}$	$-3.9\cdot10^{-3}$	$-1.5\cdot10^{-3}$	0.69
25,249	$-2.2\cdot10^{-3}$	$-1.5\cdot10^{-3}$	$-4.9\cdot10^{-4}$	0.70
34,423	$-1.1\cdot10^{-3}$	$-8.1\cdot10^{-4}$	$-3.5\cdot10^{-4}$	0.77
118,717	$-3.6\cdot10^{-4}$	$-2.7\cdot10^{-4}$	$-9.4\cdot10^{-5}$	0.76
247,333	$-1.4\cdot10^{-4}$	$-1.1\cdot10^{-4}$	$-4.1\cdot10^{-5}$	0.82

(a) Data of the macroscopic problem.

$\mathrm{DoF}^{\mathrm{c_{m,1}}}$	$\mathrm{DoF}^{\mathrm{c_{m,2}}}$	$\eta^{\mathrm{c_{m,1}}}/J(\mathbf{u})$	$\eta^{\mathrm{c_{m,2}}}/J(\mathbf{u})$
288	288	$-2.3\cdot10^{-4}$	$-9.3\cdot10^{-3}$
288	1,088	$-2.3\cdot10^{-4}$	$-2.6\cdot10^{-3}$
288	3,924	$-2.3\cdot10^{-4}$	$-7.9\cdot10^{-4}$
1,088	5,680	$-6.4\cdot10^{-5}$	$-6.3\cdot10^{-4}$
1,088	21,108	$-6.4\cdot10^{-5}$	$-1.7\cdot10^{-4}$
4,008	37,120	$-1.8\cdot10^{-5}$	$-1.4\cdot10^{-4}$
6,592	135,308	$-1.5\cdot10^{-5}$	$-3.7\cdot10^{-5}$
14,000	420,424	$-1.0\cdot10^{-5}$	$-1.2\cdot10^{-5}$

(b) Data of Cell Problem on Y^{m}.

$\mathrm{DoF}^{\mathrm{c_{b,1}}}$	$\mathrm{DoF}^{\mathrm{c_{b,2}}}$	$\eta^{\mathrm{c}b,1}/J(\mathbf{u})$	$\eta^{\mathrm{c_b,2}}/J(\mathbf{u})$
358	358	$-4.5\cdot10^{-3}$	$-1.5\cdot10^{-2}$
784	758	$-1.9\cdot10^{-3}$	$-6.2\cdot10^{-3}$
1,350	1,362	$-9.7\cdot10^{-4}$	$-3.1\cdot10^{-3}$
4,132	3,198	$-3.8\cdot10^{-4}$	$-1.4\cdot10^{-3}$
10,208	7,260	$-1.8\cdot10^{-4}$	$-6.3\cdot10^{-4}$
32,682	23,338	$-6.7\cdot10^{-5}$	$-2.4\cdot10^{-4}$
102,900	68,044	$-2.7\cdot10^{-5}$	$-9.8\cdot10^{-5}$
292,408	209,814	$-1.1\cdot10^{-5}$	$-3.8\cdot10^{-5}$

(c) Data of cell Problem on Y^{b}.

Table 4.4.3.: Results of the adaptive algorithm applied to the multi-cell example.

Γ_{E} where the functional is evaluated. We also see refinement at the points where the interface Γ has kinks. Note that the effective diffusion coefficient has a jump across these faces and that the solution is thus not as smooth in theses points as it is in the rest of the domain. The small line of refined cells in the left half of the

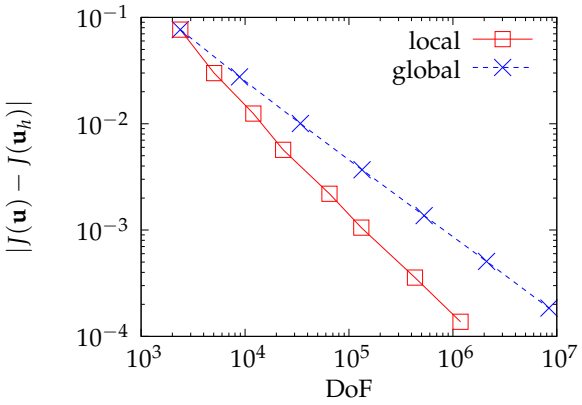

Figure 4.4.2.: Plot of error in target quantity vs. DoF for global and local refinement of multi-cell problem.

vicinity of Γ_D are due to the prescribed Dirichlet function which has relatively large gradients in this region.

The refinement of the cell problems on Y^{m}, i.e. 4.4.3b and 4.4.3c, depends solely on the smoothness of the solution. Note that, as the geometry and the data of the PDE are symmetric, so are the grids. The meshes on Y^{b} are mostly refined around the re-entrant corners.

4.4.3. Stokes Flow over a Porous Bed

With this example we extend our approach to problems in which an effective interface condition is derived by auxiliary problems. We consider the situation of Chapter 3, i.e. on the microscopic level, we are interested in a Stokes flow over a porous bed. An interface condition between the free flow and the porous part has to be imposed to calculate the effective velocity and pressure. This is the Beavers-Joseph-Saffman law, see Beavers and Joseph [19], Jäger and Mikelić [77], Saffman [117], which can be rigorously defined by solving an auxiliary problem, see Chapter 3. To make this chapter self contained and to adapt the problems to the notation in this chapter, we briefly repeat the equations from Chapter 3. However, we refer to the previous chapter and the references therein for a discussion of the homogenization process involved.

The setting for the microscopic problem is as follows: We assume a slow incompressible viscous flow around a fixed obstacle over a porous bed. The microscopic geometry consists of the unconstrained fluid domain containing an obstacle, which lies atop a periodically perforated porous flow domain, see Figure 4.4.4b and definition Definition 2.2.6.

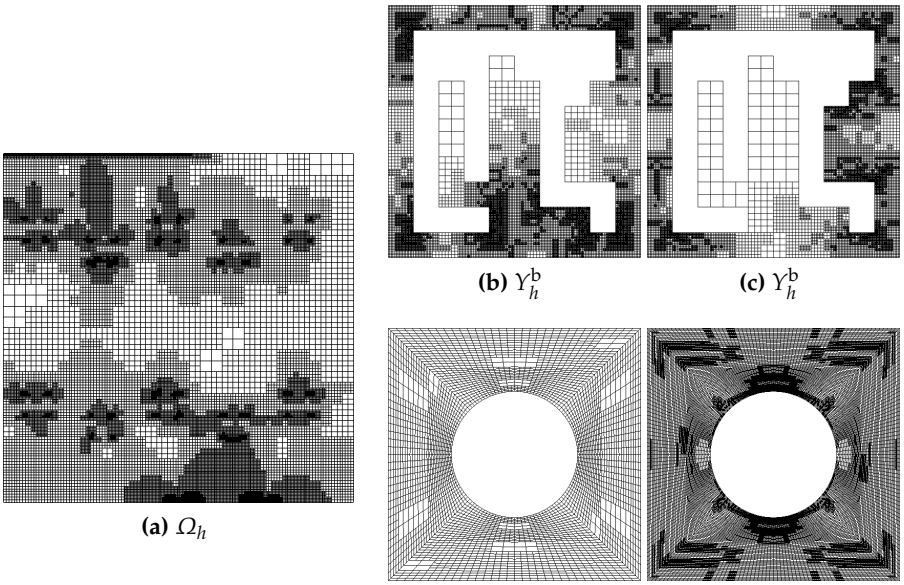

(a) Ω_h **(b)** Y_h^{b} **(c)** Y_h^{b} **(d)** Y_h^{m} **(e)** Y_h^{m}

Figure 4.4.3.: Locally refined meshes of multi-cell example after five refinement steps. We see the macroscopic triangulation $\mathcal{T}_h^m$ (a), the two grids of the cell problems on Y^{b}, (b) and (c), and the meshes connected to Y^{m}, (d) and (e). The grids in the left column belong to the cell problems connected to the x_1-direction, the grids in the right column belong to x_2-direction.

In our computations, we take an ellipsoid with center at $(0.5, 0.5)$, rotated by 45 degrees and with main axes with length 0.357142857 and 0.192307692 as the obstacle Y_{s} in the unit cell Y. The flow is modelled by the non-dimensional Stokes equation, driven by a pressure difference along the x_1-axis. Additionally, we assume no-slip conditions on the upper and lower boundary as well as on the boundaries of the inclusions.

We are only interested in the solution of the effective equation in the upper fluid domain, see Figure 4.4.5 for the specific configuration of this example. The geometry is taken from Schäfer and Turek [120]. As for the homogenized equations, we assume that the following holds (again, see Carraro et al. [36] or Chapter 3 for more details):

Problem 4.4.8. *Find an effective velocity* $\mathbf{v}$ *and effective pressure* p *s.t.*

$$-\Delta \mathbf{v} + \nabla p = 0, \qquad \text{in } \Omega \tag{4.4.24a}$$

$$\nabla \cdot \mathbf{v} = 0, \qquad \text{in } \Omega \tag{4.4.24b}$$

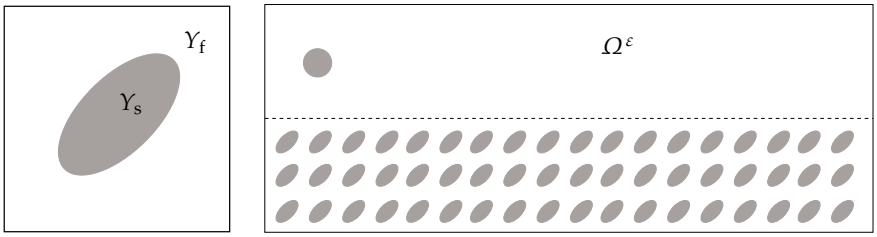

Figure 4.4.4.: Sketch of the microscopic geometry (b) and the corresponding unit cell (a) of the Stokes example.

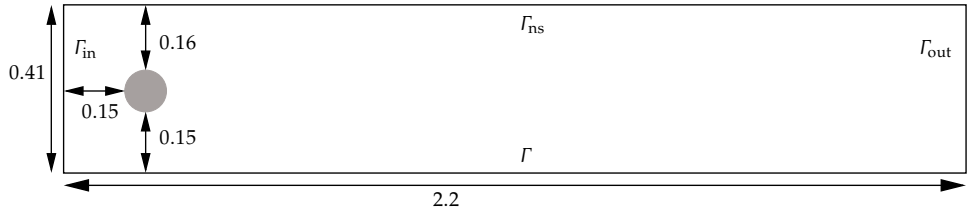

Figure 4.4.5.: Parameters of the macroscopic flow domain Ω of the Stokes example.

together with the boundary conditions

$$\mathbf{v} = 0 \quad \text{on } \Gamma_{\text{incl}} \cup \Gamma_{\text{ns}} \cup \Gamma, \qquad v_2 = 0 \quad \text{on } \Gamma_{\text{in}} \cup \Gamma_{\text{out}} \cup \Gamma, \tag{4.4.24c}$$

$$p = 19 \quad \text{on } \Gamma_{\text{in}}, \qquad p = 0 \quad \text{on } \Gamma_{\text{out}}, \tag{4.4.24d}$$

$$v_1 = \varepsilon C_1^{\text{bl}} \partial_2 v_2 \quad \text{on } \Gamma. \tag{4.4.24e}$$

The interface constant $C_1^{\text{bl}} = C_1^{\text{bl}}(\beta_1^{\text{bl}})$ is defined as

$$C_1^{\text{bl}}(\beta_1^{\text{bl}}) = \int_0^1 \beta_1^{\text{bl}}(y_1, 0)\, \mathrm{d}y_1 \tag{4.4.25}$$

where $\boldsymbol{\beta}^{\text{bl}}$ is part of the solution of an additional problem called Navier Boundary Layer (*NBL*), see Section 3.1.3 and especially Problem 3.1.25.

Remark 4.4.9. *In our numerical computations Problem 3.1.25 is solved on a cut-off domain with a length of ten unit cells (five above and below Σ, see also Figure 4.4.7), see Section 3.2.2 for more details on the numerical treatment.*

The quantity of interest in this example is the integral of the first velocity compo-

nent over the interface Γ.

$$J(\mathbf{v}, p) = \int_{\Gamma} v_2(s)\, \mathrm{d}s. \tag{4.4.26}$$

The results of the adaptive algorithm for $\varepsilon = 10^{-5}$ are reported in Table 4.4.4. $\mathrm{DoF}^{\mathrm{m}}$ and η^{m} describe the degrees of freedom and the calculated error estimator of the macroscopic flow domain, $\mathrm{DoF}^{\mathrm{c}}$ and η^{c} are the respective quantities for the NBL. Note the excellent effectivity index, which is close to one even for the relatively coarse grids after the first refinement step. The refinement strategy is able to balance the error between the macroscopic domain and the boundary layer problem quite well.

$\mathrm{DoF}^{\mathrm{m}}$	$\mathrm{DoF}^{\mathrm{c}}$	$J(e)/J(\mathbf{v},p)$	$\eta/J(\mathbf{v},p)$	$\eta^{\mathrm{m}}/J(\mathbf{v},p)$	$\eta^{\mathrm{c}}/J(\mathbf{v},p)$	I_{eff}
1,610	6,888	$4.2 \cdot 10^{-4}$	$1.1 \cdot 10^{-3}$	$1.8 \cdot 10^{-4}$	$9.1 \cdot 10^{-4}$	2.60
3,824	8,662	$4.9 \cdot 10^{-5}$	$6.2 \cdot 10^{-5}$	$1.8 \cdot 10^{-5}$	$4.4 \cdot 10^{-5}$	1.26
7,848	13,534	$4.7 \cdot 10^{-6}$	$5.9 \cdot 10^{-6}$	$3.2 \cdot 10^{-6}$	$2.7 \cdot 10^{-6}$	1.26
20,840	27,174	$8.7 \cdot 10^{-7}$	$9.0 \cdot 10^{-7}$	$4.3 \cdot 10^{-7}$	$4.7 \cdot 10^{-7}$	1.04
53,814	49,772	$2.1 \cdot 10^{-7}$	$2.2 \cdot 10^{-7}$	$7.0 \cdot 10^{-8}$	$1.5 \cdot 10^{-7}$	1.05
102,980	105,910	$3.3 \cdot 10^{-8}$	$3.3 \cdot 10^{-8}$	$1.2 \cdot 10^{-8}$	$2.1 \cdot 10^{-8}$	1.01

Table 4.4.4.: Results of the adaptive algorithm applied to the Stokes example with $\varepsilon = 10^{-5}$.

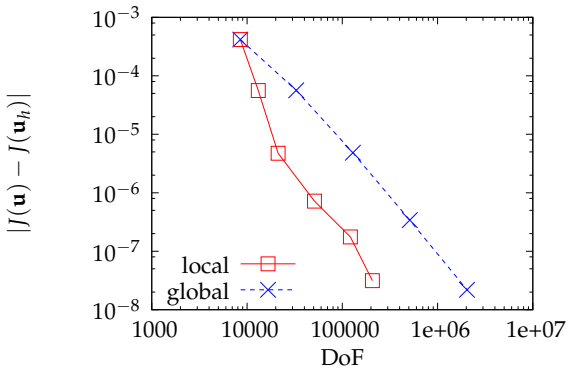

Figure 4.4.6.: Plot of error in target quantity vs. DoF for global and local refinement with $\varepsilon = 10^{-5}$.

Figure 4.4.6 shows a comparison of the sum of $\mathrm{DoF}^{\mathrm{c}}$ and $\mathrm{DoF}^{\mathrm{m}}$ for local and global refinement. Global refinement shows the expected convergence rate of four, the local refinement is clearly superior to the global refinement in terms of

degrees of freedom. After the first four refinement steps the error for the local mesh refinement lies nearly two orders of magnitude below the global refinement. This behaviour would be even more pronounced if the macroscopic- and cell-part of the error are not so well balanced from the beginning, see Table 4.4.4, because the ability of Algorithm 4.3.1 to balance the different parts of the error would allow us to save even more degrees of freedom.

In Figure 4.4.7 we see the locally refined meshes $\mathcal{T}_h^m$ and $\mathcal{T}_h^c$ after five refinement cycles. In the macroscopic domain, the refinement concentrates around the inclusion, where the gradients of the solution are relatively big, and the left hand side half of the interface Γ where the functional is evaluated. In the boundary layer the major refinement is taken around the interface Σ and the first inclusion, showing the influence region for the calculation of the interface constant.

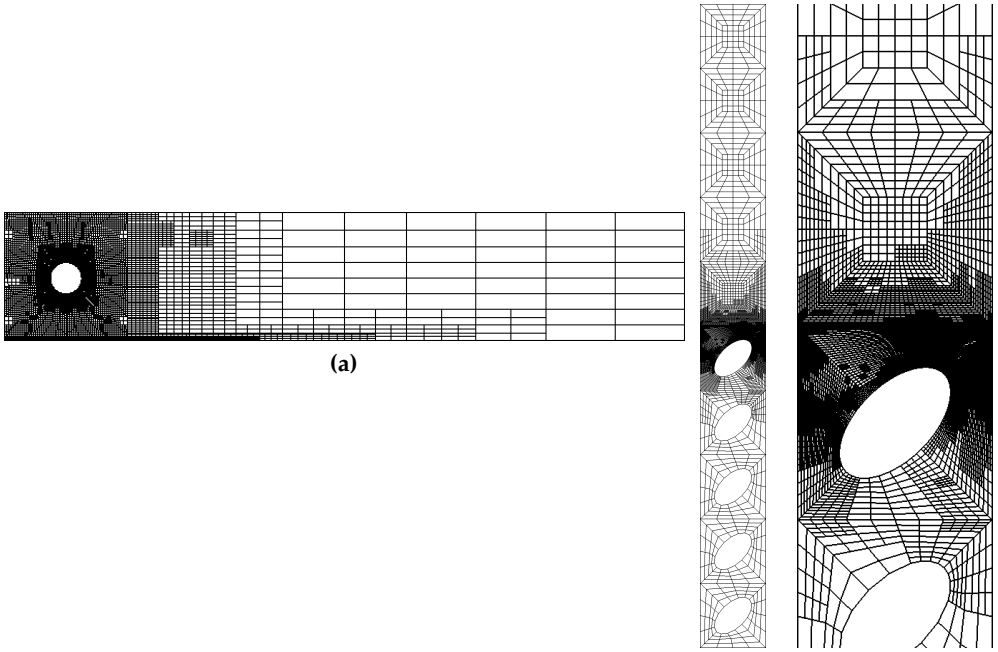

Figure 4.4.7.: Locally refined meshes of the Stokes example after five refinement steps. We see the macroscopic triangulation in (a), the mesh of the cut-off NBL domain (b) and a close up of this mesh around the interface Σ (c).

5. Simulation of Porous Anode of an SOFC

This chapter is devoted to develop and solve a model of the gas transport in the anode and the overlying gas channel of a solid oxide fuel cell using the algorithms and techniques developed in Chapter 3 and Chapter 4.

The chapter begins with a short introduction to the working principles and electrochemical mechanisms in a fuel cell in Section 5.1. We develop an effective model of the gas transport and present the results of the computations of this model in Section 5.2 and Section 5.3.

5.1. Motivation & Short Introduction to Fuel Cells

As stated in the introduction (see Chapter 1), fuel cells look promising as an efficient and environmentally-friendly energy conversion device in the near future. There exists a broad range of different fuel cell types such as proton exchange membrane fuel cells (*PEMFCs*) or alkaline fuel cells (*AFCs*), see e.g. Andújar and Segura [12], Cook [47], Kirubakaran et al. [86], Larminie and Dicks [90] for an overview. In this thesis we consider **solid oxide fuel cells** (*SOFCs*) whose main characteristic is that they use a a solid ceramic as the electrolyte and require a high operating temperature ($800 - 1000^{\circ}$C). The main advantage in comparison with other fuel cell types is that they have a higher electrical efficiency and run on a variety of hydrocarbons instead of only pure hydrogen, due to their capability of internal reforming. Their high operating temperature makes SOFCs also suitable for a combined heat and power generation which increases their efficiency even further, see Kirubakaran et al. [86], Stambouli and Traversa [122]. Drawbacks of the SOFCs are that they have a relatively slow start-up time and are build from cost-intensive materials. The latter is due to the fact that the electrodes/electrolyte/gas channels have to withstand the heat in the fuel cell.

SOFCs come in different designs, there are *planar* (anode, electrolyte and cathode are flat plates) and *tubular* (anode, electrolyte and cathode are coiled inside a

hollow cylinder) cells and they can be cathode-, electrolyte- or anode-supported, see Suwanwarangkul et al. [125]. In this work we focus on a **planar** and **anode-supported** SOFC.

There is still a need of improvement in fuel cell design; the energy produced by fuel cells is still too costly, see, e.g. Cook [47], Kornely et al. [87] and Chapter 1. The performance of a fuel cell highly depends on the materials used for electrodes and electrolyte. But not only the choice *which* material to use is important. The electrodes in a SOFC are build from **porous materials**, and the *form* of these microstructures (which influences parameters like tortuosity and porosity) have also a high impact on fuel cell efficacy, see DeCaluwe et al. [51].

Not all processes that occur in a fuel cell are yet fully understood. Thus, considerable effort is still required in developing and testing models that describe the physical processes accurately, see Bove and Ubertini [27]. Numerical simulations play an important role at this point as individual phenomena can be examined separately, the simulations reduce the amount of experiments needed in determine optimal parameters.

5.1.1. Working Principle

Fuel cells convert chemical energy into electrical energy (see Figure 1.1.1 for a sketch which explains the principle). At the cathode, O_2 gets reduced to O_2^--ions. The electrons needed for this process flow from the anode through the load and generate the electrical current. The oxygen ions travel through the electrolyte (which allows only these oxygen-ions to pass and acts as a barrier for other ions and electrons) to the anode where they react with H_2 and produce H_2O. During this latter reaction the aforementioned electrons are emitted.

5.1.2. Loss Mechanisms

The *reversible cell potential* (also *reversible cell voltage* or *open-circuit voltage*) V_{th} is the maximal electrical energy potential which can be obtained in a fuel cell. It depends on temperature, pressure and the composition fuel and oxidant. In an ideal fuel cell, V_{th} is the voltage of the fuel cell when no current is drawn. The open circuit voltage in real life situation, V_{oc}, is generally smaller than V_{th}. This is due to several issues such as partial conductivity of the electrolyte (i.e. a few electrons travel from the anode through the electrolyte to the cathode) or gas leaking in the fuel cell apparatus. When a current is applied, more so called **loss mechanisms** (also **overpotentials** or **polarizations**) can be observed, see Lucia [97], Yang et al. [137].

The three main loss mechanisms are *activation polarization* η_{act}, *ohmic polarization* η_{ohm} and *concentration polarization* η_{conc}.

Activation Overpotential This loss is due to the slowness of the electrochemical reactions in the three phase boundary (*TPB*, boundary of the electrodes where electrolyte, electrode and pores meet). Each reaction has a certain activation barrier that must be overcome before the reaction can actually take place. This overpotential is called activation polarization.

Ohmic Overpotential This voltage drop is caused by the electric and ionic resistance in the electrodes and the electrolyte.

Concentration Overpotential This polarization is due to an undersupply of fuel or an overaccumulation of products in the reaction area of anode and cathode, the TPBs. The transportation of the species to (or from) the TPB in this case is too slow, resulting in a voltage drop. The concentration overpotential splits into an anodic and cathodic part,

$$\eta_{\text{conc}} = \eta^{\text{A}}_{\text{conc}} + \eta^{\text{C}}_{\text{conc}}. \tag{5.1.1}$$

This leads us to the following (approximative) formula for the cell voltage V:

$$V = V_{\text{oc}} - \eta_{\text{act}} - \eta_{\text{ohm}} - \eta_{\text{conc}}. \tag{5.1.2}$$

In Figure 5.1.1 a characteristic plot of cell voltage vs. current density is shown for a generic fuel cell. The exact form depends on the individual cell configuration. Note the difference of V_{th} and V_{oc} due to small imperfections in the fuel cell.Then a steep initial drop in voltage due to activation overpotential is observed. This is followed by a less rapid, linear decrease caused by ohmic overpotential. At high currents, the voltage falls rapidly owing to concentration overpotential. It has been reported that the performance of an anode-supported SOFC at a high current density depends mostly on $\eta^{\text{A}}_{\text{conc}}$, see Chan et al. [40], Yakabe et al. [136].

5.1.3. Goal of this Chapter

The scope here is to compute the quantity $\eta^{\text{A}}_{\text{conc}}$ for a planar SOFC in a steady-state configuration. To this end, we develop a 2-d model for mass and momentum transport in the pore space Ω^ε of the anode and the overlying gas channel in Section 5.2. As it is computationally too expensive to solve this model in Ω^ε, we homogenize (formally) the aforementioned model for the case of a periodic pore space. In this process the coupling conditions examined in Chapter 3 enter the

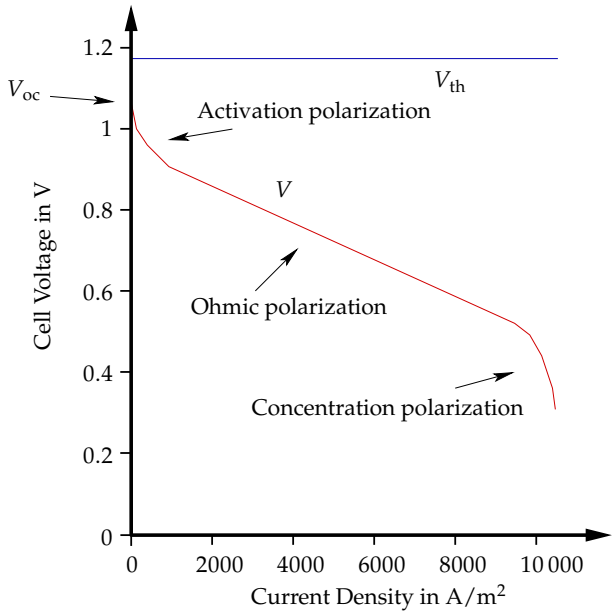

Figure 5.1.1.: Plot of actual theoretical cell voltage V_{th} (blue line) and cell voltage V (red line) vs. current density.

macroscopic model. Some effective parameters require the solution of several auxiliary equations. As we want to approximate $\eta^{\text{A}}_{\text{conc}}$ efficiently, we utilize the algorithms developed in Chapter 4 to balance the discretization errors of the auxiliary and macroscopic problem with respect to $\eta^{\text{A}}_{\text{conc}}$.

5.2. Full Model of the Anode Part

In this section we present the system of PDEs modelling gas transport in the anode and the overlying gas channel. There is a vast amount of literature regarding SOFC modelling, we only mention [10, 11, 24, 24, 27, 39, 68, 82, 95, 121, 131, 134]. Nearly all of aforementioned references use effective models with either fitted or heuristically determined effective coefficients. One example is the use of effective diffusivity constants in species mass transport models. Mostly an effective diffusivity constant is used which is defined as the normal diffusivity constant scaled by $\varepsilon^{\text{por}}/\tau$ with ε^{por} being the porosity and τ the tortuosity, see for example Veldsink et al. [133].

While this is a valid approach which leads to reasonably good agreement with experiments (see for example Tseronis et al. [131]), we consider a different path as this thesis focuses more on new numerical algorithms instead of state-of-the

art models for SOFCs. We look for a model which holds true in the (periodic) pore space of the anode (as well as in the corresponding gas channel) and then consider a homogenized version with effective coefficients computed via some auxiliary equations. Regarding the example above: As opposed to the scaling of the diffusion coefficient by ε/τ, we use in this circumstances the effective diffusion matrix as (2.2.42).

We are interested in a mixture of $N_{\mathrm{sp}} \in \mathbb{N}$ different chemical species in a *stationary, 2-d configuration*. The assumption of stationarity is valid in our scenario, as we are interested in the steady state behaviour of the fuel cell, which is reached by the cell under working conditions after an initial ramp up time, see Bove and Ubertini [27], Gemmen and Johnson [62], Tseronis et al. [131]. We list the basic assumptions from which we develop the model on the microscopic level in the next section.

Assumption 5.2.1. *We consider the following assumptions to hold true for the rest of this chapter. For a discussion on the validity of the assumptions (except the restrictions imposed on the geometry) we refer to Suwanwarangkul et al. [125], Yakabe et al. [136] and the references therein.*

Geometry *We model the equations in the two dimensional pore space Ω^ε which is composed by the gas channel Ω_{f}, the pore space of the anode, $\Omega_{\mathrm{p}}^\varepsilon$, and the planar interface Γ, which separates Ω_{f} and $\Omega_{\mathrm{p}}^\varepsilon$. We assume that $\Omega_{\mathrm{p}}^\varepsilon$ is a periodically perforated domain, see Definition 2.2.6.*

Steady State *We assume that the SOFC is in a steady state.*

TPB *The electrochemical conversion happens in the three phase boundary (*TPB*). We consider fuel cells where the width of the TBP is negligible in comparison with the width of the anode. Thus we assume that the electrochemical reactions happen on the anode-electrolyte boundary.*

Constant Current Density *The current density is constant on the anode/electrolyte interface Γ_{el}.*

Isothermal *We assume a constant temperature throughout the fuel cell.*

Isobar *We neglect the effects of pressure variations on mixture density and species mass transport, see also* (5.2.22).

Mixture Composition *We model a mixture of $N_{\mathrm{sp}} = 3$ different species: Hydrogen, steam and nitrogen. Hydrogen is the fuel and steam is a product of the reaction at the TPB. Nitrogen is used to dilute the mixture so that we can modify the hydrogen concentration in the fuel without perturbing the H_2-H_2O ratio. The latter is important to keep V_{oc} constant when comparing different SOFC configurations, see Yakabe et al. [136].*

Remark 5.2.2 (Characteristic Pore Size)**.** *We consider* dimensional- *as well as* non-dimensional *formulations in this chapter, so let us remark shortly on the characteristic pore size ε. In the previous chapters (esp. Chapter 3) we considered only adimensional equations, thus ε had no dimension. In this chapter, ε denotes the characteristic pore size in the physical space and is measured in* m*. Its nondimensional counterpart is ε^*, i.e. ε scaled by a characteristic length.*

*In general, in this chapter we mark adimensional quantities with the superscript *.*

Remark 5.2.3 (Geometry Assumptions)**.** *Note that we assume that the pore space is made up of a periodic repetition of a unit cell in 2-d where the inclusion does not touch the boundary of the unit cell. This has to be relaxed if we consider 3-d models in future work, as one has to ensure that both the pore-space Ω^ε as well as the structure $\Omega \setminus \Omega^\varepsilon$ are connected.*

Regarding the periodicity assumption. The next step would be to consider randomly perforated domains. There exists a procedure called "periodization": It is sometimes possible to to approximate the effective quantities in a scenario with randomly distributed holes by considering only a representative slab of the microstructure and extend this slab by periodicity on the domain. We are then back at the framework of periodic homogenization, see Alexanderian et al. [7], Bourgeat and Piatnitski [26], Sab and Nedjar [116].

Let us first define the (microscopic) geometry in a little more detail before we start with the model derivation.

5.2.1. Fuel Cell Layout

We consider two types of SOFC geometries in this chapter, called type A and type B. Both are sketched in Figure 5.2.1. Note that in both cases the anode Ω_p is a **periodically perforated domain** with the pore space $\Omega_\mathrm{p}^\varepsilon$, see Definition 2.2.6.

Type A Geometry

This microscopic domain is defined as in Definition 3.1.2 with the unconfined fluid domain Ω_f and the porous medium Ω_p. We assume $L, H_\mathrm{u}, H_\mathrm{l} > 0$ and

$$x_\mathrm{el}^\mathrm{l}, x_\mathrm{el}^\mathrm{r} \in \{x \in \partial\Omega_\mathrm{p} \,|\, 0 \leq x_1 \leq L \text{ and } x_2 = -H_\mathrm{l}\}, \tag{5.2.1}$$

with $x_{\mathrm{el},1}^\mathrm{l} < x_{\mathrm{el},1}^\mathrm{r}$, see also the sketch in Figure 5.2.1a.

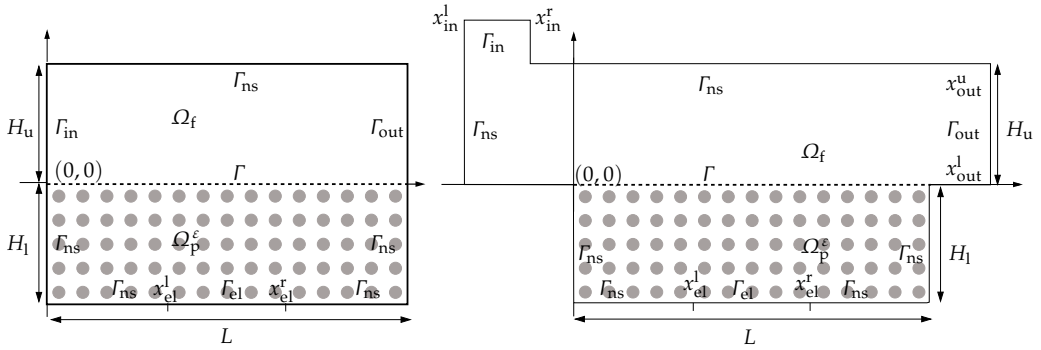

(a) Type A **(b)** Type B

Figure 5.2.1.: Sketch of the two considered SOFC geometries.

Let the macroscopic flow domain Ω be defined by Definition 3.1.7. The boundary $\partial\Omega^{\varepsilon}$ is split into the following parts:

$$\partial\Omega^{\varepsilon} = \Gamma_{\mathrm{in}} \dot{\cup} \Gamma_{\mathrm{out}} \dot{\cup} \Gamma_{\mathrm{el}} \dot{\cup} \Gamma^{\varepsilon}_{\mathrm{ns}}, \tag{5.2.2}$$

where

$$\Gamma_{\mathrm{in}} := \{\, 0 \,\} \times [0, H_{\mathrm{u}})\,, \quad \Gamma_{\mathrm{out}} := \{\, L \,\} \times [0, H_{\mathrm{u}})\,, \tag{5.2.3}$$

$$\Gamma_{\mathrm{el}} := \{x \in \partial\Omega \mid x = x^{\mathrm{l}}_{\mathrm{el}} + \lambda(x^{\mathrm{r}}_{\mathrm{el}} - x^{\mathrm{l}}_{\mathrm{el}}) \text{ for a } \lambda \in [0,1]\}, \tag{5.2.4}$$

and the no slip parts of the boundary are

$$\Gamma_{\mathrm{ns}} := \partial\Omega \setminus \{\, \Gamma_{\mathrm{el}} \cup \Gamma_{\mathrm{in}} \cup \Gamma_{\mathrm{out}} \,\}\,, \tag{5.2.5}$$

$$\Gamma^{\varepsilon}_{\mathrm{ns}} := \Gamma_{\mathrm{ns}} \cup \Big\{ \sum_{(i,j)\in\mathbb{Z}^2} \varepsilon \left(\partial Y_{\mathrm{s}} + (i,j)\right) \cap \Omega_{\mathrm{p}} \Big\}. \tag{5.2.6}$$

The latter part in (5.2.6) describes the boundary of the inclusions, see Section 3.1.1.

Type B Geometry

A sketch of this geometry can be seen in Figure 5.2.1b. When compared with type A, the difference lies in the fact that the gas channel Ω_{f} is lengthened and has a buckling on the inflow side.

Let $L, H_{\mathrm{u}}, H_{\mathrm{l}} > 0$ be the length of the anode, the height of the gas channel and

the height of the anode. Let $x^{\mathrm{l}}_{\mathrm{in}}, x^{\mathrm{r}}_{\mathrm{in}}, x^{\mathrm{l}}_{\mathrm{el}}, x^{\mathrm{r}}_{\mathrm{el}}, x^{\mathrm{u}}_{\mathrm{out}}, x^{\mathrm{l}}_{\mathrm{out}} \in \mathbb{R}^2$ be given such that

$$x^{\mathrm{l}}_{\mathrm{in},2} = x^{\mathrm{r}}_{\mathrm{in},2} \geq H_{\mathrm{u}}, \quad x^{\mathrm{l}}_{\mathrm{in},1} < x^{\mathrm{r}}_{\mathrm{in},1}, \quad x^{\mathrm{l}}_{\mathrm{el},1} < x^{\mathrm{r}}_{\mathrm{el},1}, \tag{5.2.7}$$

$$x^{\mathrm{l}}_{\mathrm{el}}, x^{\mathrm{r}}_{\mathrm{el}} \in \{x \in \partial\Omega_{\mathrm{p}} \,|\, 0 \leq x_1 \leq L \text{ and } x_2 = -H_{\mathrm{l}}\}, \tag{5.2.8}$$

$$x^{\mathrm{u}}_{\mathrm{out},1} = x^{\mathrm{l}}_{\mathrm{out},1} \geq L, \quad x^{\mathrm{u}}_{\mathrm{out},2} = H_{\mathrm{u}}, \quad x^{\mathrm{l}}_{\mathrm{out},2} = 0. \tag{5.2.9}$$

We define the gas channel Ω_{f} and the porous anode Ω_{p} by

$$\Omega_{\mathrm{f}} := (x^{\mathrm{l}}_{\mathrm{in},1}, x^{\mathrm{l}}_{\mathrm{out}1}) \times H_{\mathrm{u}} \cup (x^{\mathrm{l}}_{\mathrm{in},1}, x^{\mathrm{r}}_{\mathrm{in}1}) \times x^{\mathrm{l}}_{\mathrm{in}2} \tag{5.2.10}$$

$$\Omega_{\mathrm{p}} := (0, L) \times (-H_{\mathrm{l}}, 0). \tag{5.2.11}$$

The anodic pore space $\Omega^{\varepsilon}_{\mathrm{p}}$ is defined as Ω_{p} minus the obstacles, see (3.1.6). We define the microscopic domain Ω^{ε} by

$$\Omega^{\varepsilon} := \Omega_{\mathrm{f}} \cup \Gamma \cup \Omega^{\varepsilon}_{\mathrm{p}}, \tag{5.2.12}$$

and the macroscopic domain Ω is consequently

$$\Omega := \Omega_{\mathrm{f}} \cup \Gamma \cup \Omega_{\mathrm{p}}. \tag{5.2.13}$$

The interface Γ between the gas channel and the anode is defined as in (3.1.3).

The boundary of the domain is split into Γ_{in}, Γ_{out}, Γ_{el} and $\Gamma^{\varepsilon}_{\mathrm{ns}}$. Inflow, outflow and electrolyte-part of the boundary are defined as

$$\Gamma_{\mathrm{in}} := \{x \in \partial\Omega \,|\, x = x^{\mathrm{l}}_{\mathrm{in}} + \lambda(x^{\mathrm{r}}_{\mathrm{in}} - x^{\mathrm{l}}_{\mathrm{in}}) \text{ for a } \lambda \in [0,1]\}, \tag{5.2.14}$$

$$\Gamma_{\mathrm{out}} := \{x \in \partial\Omega \,|\, x = x^{\mathrm{u}}_{\mathrm{out}} + \lambda(x^{\mathrm{l}}_{\mathrm{out}} - x^{\mathrm{u}}_{\mathrm{out}}) \text{ for a } \lambda \in [0,1]\}, \tag{5.2.15}$$

$$\Gamma_{\mathrm{el}} := \{x \in \partial\Omega \,|\, x = x^{\mathrm{l}}_{\mathrm{el}} + \lambda(x^{\mathrm{r}}_{\mathrm{el}} - x^{\mathrm{l}}_{\mathrm{el}}) \text{ for a } \lambda \in [0,1]\}. \tag{5.2.16}$$

The rest of the boundary is impermeable and is defined as follows

$$\Gamma_{\mathrm{ns}} := \partial\Omega \setminus \{\, \Gamma_{\mathrm{in}} \cup \Gamma_{\mathrm{out}} \cup \Gamma_{\mathrm{el}} \,\}, \tag{5.2.17}$$

$$\Gamma^{\varepsilon}_{\mathrm{ns}} := \Gamma_{\mathrm{ns}} \dot{\cup} \Big\{ \sum_{(i,j)\in\mathbb{Z}^2} \varepsilon \left(\partial Y_{\mathrm{s}} + (i,j)\right) \cap \Omega_{\mathrm{p}} \Big\}. \tag{5.2.18}$$

Remark 5.2.4. *In both type of geometries Γ_{el} describes the electrolyte/anode interface.*

5.2.2. Microscopic Level

Our goal is to determine the distribution of the species in the anode and the gas channel for a given fuel cell configuration. This means that we are interested

in the **velocity field** $\mathbf{v}^\varepsilon$ and the **pressure** p^ε of the mixture as well as the **species mass fractions** y_i^ε with $i = 1 \dots N_{\text{sp}}$ (see Definition 2.1.11). Let T be the constant temperature in the fuel cell (see Assumption 5.2.1). We denote the molar mass of species i by m_i and its dynamic viscosity by μ_i.

Remark 5.2.5. *For the mass and mole fractions, we sometimes use chemical symbols instead of integers as indices. Let us assume that the first species in the mixture is hydrogen, then we use the notation y_1^ε and $y_{\text{H}_2}^\varepsilon$ for the hydrogen mass fraction interchangeably.*

Conservation Principles

In Ω^ε The solution variables $\mathbf{v}^\varepsilon$, p^ε and y_i^ε are subject to the following physical principles: *Conservation of momentum*, *conservation of total mass* and *conservation of species mass*. We present the PDEs modelling these conservation laws subsequently.

Conservation of Momentum Let the viscous stress tensor be given by

$$\pi_{\text{s}}^\varepsilon := \mu^\varepsilon(\nabla \mathbf{v}^\varepsilon + \nabla^t \mathbf{v}^\varepsilon) - \frac{2}{3}\nabla \cdot \mathbf{v}^\varepsilon \,\text{id}\,. \tag{5.2.19}$$

Conservation of momentum is described by the Navier Stokes equation

$$-\nabla \cdot \pi_{\text{s}}^\varepsilon + \rho^\varepsilon \mathbf{v}^\varepsilon \cdot \nabla \mathbf{v}^\varepsilon + \nabla p^\varepsilon = 0, \tag{5.2.20}$$

where μ^ε describes the **dynamic viscosity** of the mixture and ρ^ε its density. The dynamic viscosity of the mixture is modelled as in Bove and Ubertini [27] by

$$\mu^\varepsilon := \sum_{k=1}^{N_{\text{sp}}} y_k^\varepsilon \mu_k. \tag{5.2.21}$$

The density ρ^ε is modelled by the perfect gas law, see Definition 2.1.14, with the following modification:

The flow of the mixture in Fuel Cells is in general slow, so a low Mach number laminar flow is assumed, see Bove and Ubertini [27]. As a consequence, the total pressure p^ε is split into a constant thermodynamic pressure $p_{\text{th}}^\varepsilon$ and a spatially variable hydrodynamic part $p_{\text{hyd}}^\varepsilon$, i.e. there holds for $x \in \Omega^\varepsilon$

$$p^\varepsilon(x) = p_{\text{th}}^\varepsilon + p_{\text{hyd}}^\varepsilon(x), \tag{5.2.22}$$

see, e.g., Braack and Richter [28].

Because of the pressure splitting (5.2.22) and the fact that $p^\varepsilon_{\text{th}} \gg p^\varepsilon_{\text{hyd}}$ (see Braack and Richter [28]), in our model we use

$$\rho^\varepsilon = \frac{p^\varepsilon_{\text{th}} \overline{m}^\varepsilon}{RT} \tag{5.2.23}$$

instead of (2.1.28). $\overline{m}^\varepsilon$ describes the total molecular mass of the mixture as defined in Definition 2.1.10.

Let L_c be the characteristic length of the flow domain and v_c the characteristic velocity of the flow. Reynolds number on the microscopic level is defined by

$$Re^\varepsilon := \frac{\rho^\varepsilon v_c L_c}{\mu^\varepsilon}. \tag{5.2.24}$$

In a typical SOFC configuration we have $L_c \approx 0.001\,\text{m}$, $\mu^\varepsilon \approx 10^{-5}\,\text{kg/ms}$ and $\rho^\varepsilon \approx 0.01 - 0.1\,\text{kg/m}^3$. In the gas channel there holds $v_c \approx 1\,\text{m s}^{-1}$ and thus $Re^\varepsilon \approx 1 - 10$. However, the situation changes in the pore space of the anode. The velocity is much smaller, so we should adapt the Reynolds number there. There holds that the velocity in the pore space is of the order $\varepsilon^{*2}\,\text{m s}^{-1}$, see Remark 3.1.17. A typical fuel cell has pore diameter of around $10^{-6}\,\text{m}$, which means $\varepsilon^* \approx 10^{-3}$, note Remark 5.2.2. It follows that the Reynolds number in the pores is around 10^{-5}, which is in agreement with Haberman and Young [68].

We conclude that, at least in the pore space, inertia terms play a minor role in the conservation of momentum. We go one step further and neglect the term

$$\rho \mathbf{v}^\varepsilon \cdot \nabla \mathbf{v}^\varepsilon \tag{5.2.25}$$

also in the gas channel. Additionally, we use the following approximation of the viscous stress tensor,

$$\pi^\varepsilon_s := \mu^\varepsilon \nabla \mathbf{v}^\varepsilon \tag{5.2.26}$$

instead of (5.2.19). We have tested both these simplifications at representative examples and have seen that the changes in the results are negligible, at least in the configurations we consider in this thesis.

All in all, we use the following Stokes equation in our model

$$-\nabla \cdot (\mu^\varepsilon \nabla \mathbf{v}^\varepsilon) + \nabla p^\varepsilon = 0 \tag{5.2.27}$$

with the expression (5.2.21) for the viscosity.

Conservation of total mass The *continuity equation* for the stationary setting we consider is given by

$$\nabla \cdot (\rho^\varepsilon \mathbf{v}^\varepsilon) = 0. \tag{5.2.28}$$

The density is modelled as in (5.2.23).

Conservation of species mass Species mass conservation in the stationary setting is given by (see e.g. Giovangigli [63])

$$\nabla \cdot (\rho^\varepsilon y_i^\varepsilon \mathbf{v}^\varepsilon) + \nabla \cdot \mathfrak{F}_i^\varepsilon = 0, \qquad i = 1, \dots, N_{\text{sp}} \tag{5.2.29}$$

$$\sum_{i=1}^{N_{\text{sp}}} y_i^\varepsilon = 1, \tag{5.2.30}$$

with $\mathfrak{F}_i^\varepsilon$ being the **mass diffusion flux** of species i. Before we discuss the form of $\mathfrak{F}_i^\varepsilon$ we want to remark that due to the mass conservation constraints there holds

$$\sum_{i=1}^{N_{\text{sp}}} \mathfrak{F}_i^\varepsilon = 0. \tag{5.2.31}$$

Remark 5.2.6. *Note that if we sum equation* (5.2.29) *over i and consider* (5.2.30) *and* (5.2.31)*, we end up with the continuity equation* (5.2.28)*. The system of PDEs is thus over-determined. We solve that point by skipping one species equation in our final system, i.e. we discard* (5.2.30)*, evaluate* $y_{N_{\text{sp}}}^\varepsilon$ *by*

$$y_{N_{\text{sp}}}^\varepsilon = 1 - \sum_{i=1}^{N_{\text{sp}}-1} \tag{5.2.32}$$

and consider (5.2.29) *only for* $i = 1 \dots N_{\text{sp}} - 1$.

Assumption 5.2.7. *We choose to replace nitrogen in our computations, i.e. we set*

$$y_{\text{N}_2}^\varepsilon = 1 - y_{\text{H}_2}^\varepsilon - y_{\text{H}_2\text{O}}^\varepsilon. \tag{5.2.33}$$

There are several possibilities how to model $\mathfrak{F}_i^\varepsilon$. We mention the three most used in SOFC modelling: (extended) **Fick's model** (*FM*), **Dusty-Gas model** (*DGM*) and **Stefan-Maxwell model** (*SMM*), see Krishna and Wesselingh [89], Veldsink et al. [133] and references therein for an overview as well as Fick [60], Mason and Malinauskas [99], Maxwell [100], Stefan [124]. In Suwanwarangkul et al. [125] the authors compare anodic overpotentials computed with these three transport

models with experimental results. The DGM comes out on top, FM and SMM also give reasonable results, depending on the configuration (pore size, current density, mixture composition). Note that Suwanwarangkul et al. [125] restrict their computations to the anode, the gas channel is not modelled. Tseronis et al. [131], who incorporate the gas channel into the simulations, advertise a combination of SMM in the gas channel and DGM in the anode.

We use FM in our computations and describe it in more detail later on, but let us first discuss the reasoning behind this decision. We want to develop a model that holds true in the pore space and allows for a upscaling process. The DGM incorporates so called *Knudsen diffusion*, which accounts for molecule-wall interactions. The Knudsen diffusion coefficient depends on the pore geometry as well as the gas-surface scattering law of the involved molecules, see Mason and Malinauskas [99]. Consequently, the computation of the Knudsen diffusion coefficient directly from the pore geometry is a complicated and difficult task and lies not in the scope of this work. Most authors that incorporate the Knudsen term use either experimentally determined values or assume the pores to be long, circular tubes, see Mason and Malinauskas [99]. For the reasons explained above we dismiss the DGM.

That leaves us with a choice between FM and SMM. We choose FM over SMM because Fick's model allows for an explicit representation of the diffusive flux which helps us to derive the effective equation more easily, see Section 5.2.3 and Chapter A. A (formal) homogenization process of SMM would be lengthy and would at the same time contribute only in a minor way to this work as the focus of this thesis lies on the design of numerical methods.

Remark 5.2.8. *Fick's Law was originally derived to model the diffusion in a binary mixture. However, there exists a modification called* extended Fick's law *which is used to model multi-species diffusion.*

As discussed above, we use the **extended Fick's law** for the mass diffusion flux, which looks for species i:

$$\mathfrak{F}_i^{\mathrm{F},\varepsilon} := -\rho^\varepsilon D_i^\varepsilon \frac{y_i^\varepsilon}{x_i^\varepsilon} \nabla x_i^\varepsilon \tag{5.2.34}$$

with the diffusion coefficients

$$D_i^\varepsilon := \frac{1 - y_i^\varepsilon}{\sum_{l \neq i} \frac{x_l^\varepsilon}{D_{il}^{\mathrm{bin}}}} = \frac{1}{\overline{m}^\varepsilon} \frac{1 - y_i^\varepsilon}{\sum_{l \neq i} \frac{y_l^\varepsilon}{m_l D_{il}^{\mathrm{bin}}}} \tag{5.2.35}$$

due to Hirschfelder and Curtiss [72]. D_{il}^{bin} is the binary diffusion coefficient for the species pair (i, l) and x_i^ε denotes the molar fractions on the microscopic level,

see Definition 2.1.9. There holds

$$\nabla x_i^\varepsilon = \nabla\left(\frac{\overline{m}^\varepsilon}{m_i} y_i^\varepsilon\right) = \nabla y_i^\varepsilon \frac{\overline{m}^\varepsilon}{m_i} + \nabla \overline{m}^\varepsilon \frac{y_i^\varepsilon}{m_i}, \quad \text{and} \quad \frac{y_i^\varepsilon}{x_i^\varepsilon} = \frac{m_i}{\overline{m}^\varepsilon}. \tag{5.2.36}$$

Together with the formula for the density (5.2.23) we can simplify the Fickian mass diffusion flux as follows

$$\mathfrak{F}_i^{\mathrm{F},\varepsilon} = -\frac{p_{\mathrm{th}}^\varepsilon \overline{m}^\varepsilon}{RT} \frac{1}{\overline{m}^\varepsilon} \frac{1 - y_i^\varepsilon}{\sum_{l\neq i} \frac{y_l^\varepsilon}{m_l D_{il}^{\mathrm{bin}}}} \frac{m_i}{\overline{m}^\varepsilon} \left(\nabla y_i^\varepsilon \frac{\overline{m}^\varepsilon}{m_i} + \nabla \overline{m}^\varepsilon \frac{y_i^\varepsilon}{m_i}\right), \tag{5.2.37}$$

$$= -\frac{p_{\mathrm{th}}^\varepsilon}{RT} \frac{1 - y_i^\varepsilon}{\sum_{l\neq i} \frac{y_l^\varepsilon}{m_l D_{il}^{\mathrm{bin}}}} \left(\nabla y_i^\varepsilon + \nabla \overline{m}^\varepsilon \frac{y_i^\varepsilon}{\overline{m}^\varepsilon}\right). \tag{5.2.38}$$

If we insert this expression into (5.2.29) we end up with the following expression of the species mass conservation equation

$$\nabla \cdot \left(\rho^\varepsilon y_k^\varepsilon \mathbf{v}^\varepsilon\right) - \nabla \cdot \left(\frac{p_{\mathrm{th}}^\varepsilon}{RT} \frac{1 - y_i^\varepsilon}{\sum_{l\neq i} \frac{y_l^\varepsilon}{m_l D_{il}^{\mathrm{bin}}}} \left(\nabla y_i^\varepsilon + \nabla \overline{m}^\varepsilon \frac{y_i^\varepsilon}{\overline{m}^\varepsilon}\right)\right) = 0. \tag{5.2.39}$$

Correction of Fluxes In general, overall mass conservation constraint demands that the sum of all the fluxes amounts to zero, see (5.2.31). As the FM does in general not obey this constraint, we correct the fluxes in the following way:

$$\mathfrak{F}_i^{\mathrm{F},\varepsilon,\mathrm{c}} := \mathfrak{F}_i^{\mathrm{F},\varepsilon} - y_i^\varepsilon \sum_{l=1}^{N_{\mathrm{sp}}} \mathfrak{F}_l^{\mathrm{F},\varepsilon}. \tag{5.2.40}$$

Remark 5.2.9. *To declutter notation we denote the corrected Fickian fluxes $\mathfrak{F}_i^{\mathrm{F},\varepsilon,\mathrm{c}}$ from now on simply by $\mathfrak{F}_i^\varepsilon$.*

Boundary Conditions

Having discussed the PDEs that hold true in Ω^ε in the previous section, we present here the boundary conditions in our model. By and large, the boundary conditions of Tseronis et al. [131] are used. The boundary $\partial\Omega^\varepsilon$ is split into the parts Γ_{in}, Γ_{out}, Γ_{el} and $\Gamma_{\mathrm{ns}}^\varepsilon$, see Section 5.2.1. We discuss the boundary conditions on each of them separately. To make the presentation clearer we define the *total mass flux* of species i as the sum of the corresponding diffusive and convective

fluxes:

$$\mathfrak{N}_i^\varepsilon := \mathfrak{F}_i^\varepsilon + \rho^\varepsilon y_i^\varepsilon \mathbf{v}^\varepsilon \tag{5.2.41}$$

Inflow Boundary We prescribe the inflow velocity $\mathbf{v}^{\text{in}}$ as well as the mass fractions y_i^{in} for $1 \leq i \leq N_{\text{sp}} - 1$.

Outflow Boundary We assume that the convective flux dominates the total flux on the outflow boundary, i.e. let $\mathbf{n}$ be the normal on Γ_{out}, there holds then

$$\mathfrak{F}_i^\varepsilon \cdot \mathbf{n} = 0, \qquad i = 1, \ldots, N_{\text{sp}} - 1. \tag{5.2.42}$$

Moreover, we do not allow for a tangential flow, so there holds with the tangential vector $\boldsymbol{\tau}$

$$\mathbf{v}^\varepsilon \cdot \boldsymbol{\tau} = 0. \tag{5.2.43}$$

Additionally, we use the condition

$$\mathbf{n} \cdot (\mu^\varepsilon \nabla \mathbf{v}^\varepsilon - p^\varepsilon \,\mathrm{id}) \cdot \mathbf{n} = 0, \tag{5.2.44}$$

see the pressure outflow condition of Barth and Carey [18] or the "do-nothing condition" of Heywood et al. [71]. For incompressible flows on planar boundaries, this last condition prescribes a mean pressure value. As we have only weak compressible effects (especially near the outflow), the same holds true in our examples.

Electrolyte Boundary Let a current density I_{C} be given. On the boundary Γ_{el}, which describes the electrode/anode interface, the electrochemical reaction takes place. The consumption of hydrogen and simultaneous production of steam is given by (see Bove and Ubertini [27], Zhu et al. [140])

$$\mathfrak{F}_{\text{H}_2}^\varepsilon \cdot \mathbf{n} = \frac{-I_{\text{C}} m_{\text{H}_2}}{2F}, \tag{5.2.45}$$

$$\mathfrak{F}_{\text{H}_2\text{O}}^\varepsilon \cdot \mathbf{n} = \frac{I_{\text{C}} m_{\text{H}_2\text{O}}}{2F}, \tag{5.2.46}$$

where F denotes the Faraday constant, see Definition 2.1.13. For the velocity, this is a no-slip boundary, so we set

$$\mathbf{v}^\varepsilon = 0. \tag{5.2.47}$$

Impermeable Boundary As the name suggests, nothing penetrates this part of

the boundary and we have subsequently

$$\mathfrak{N}_i^\varepsilon \cdot \mathbf{n} = 0, \qquad i = 1, \dots, N_{\text{sp}}, \tag{5.2.48}$$

$$\mathbf{v}^\varepsilon = 0. \tag{5.2.49}$$

The Microscopic Model

Before we proceed with the presentation of the effective equations, let us summarize the microscopic problem.

Problem 5.2.10. *Let inflow velocity $\mathbf{v}^{\text{in}}$, inflow mass fractions y_k^{in}, molar masses m_k and viscosities μ_k for $k \in \{ \text{H}_2, \text{H}_2\text{O}, \text{N}_2 \}$ as well as the current density I_{C} and the thermodynamic pressure $p_{\text{th}}^\varepsilon$ be given. Let Ω^ε be a SOFC geometry of either type A or type B as described in Section 5.2.1.*

Find ***velocity field*** $\mathbf{v}^\varepsilon$, ***pressure*** $p_{\text{hyd}}^\varepsilon$ *and* ***species mass fractions*** y_i^ε *s.t. for* $i \in \{ \text{H}_2, \text{H}_2\text{O} \}$ *there holds*

$$-\nabla \cdot (\mu^\varepsilon \nabla \mathbf{v}^\varepsilon) + \nabla p_{\text{hyd}}^\varepsilon = 0 \qquad \text{in } \Omega^\varepsilon, \tag{5.2.50a}$$

$$\nabla \cdot (\rho^\varepsilon \mathbf{v}^\varepsilon) = 0 \qquad \text{in } \Omega^\varepsilon, \tag{5.2.50b}$$

$$\nabla \cdot (\rho^\varepsilon y_i^\varepsilon \mathbf{v}^\varepsilon) + \nabla \cdot \mathfrak{F}_i^\varepsilon = 0 \qquad \text{in } \Omega^\varepsilon \tag{5.2.50c}$$

and on the boundaries

$$\mathbf{v}^\varepsilon = \mathbf{v}^{\text{in}} \qquad \text{on } \Gamma_{\text{in}}, \tag{5.2.50d}$$

$$\mathbf{v}^\varepsilon = 0 \qquad \text{on } \Gamma_{\text{ns}}^\varepsilon \cup \Gamma_{\text{el}}, \tag{5.2.50e}$$

$$\mathbf{n} \cdot (\mu^\varepsilon \nabla \mathbf{v}^\varepsilon - p_{\text{hyd}}^\varepsilon \,\text{id}) \cdot \mathbf{n} = 0 \qquad \text{on } \Gamma_{\text{out}}, \tag{5.2.50f}$$

(5.2.50g)

as well as

$$y_i^\varepsilon = y_i^{\text{in}} \qquad \text{on } \Gamma_{\text{in}}, \tag{5.2.50h}$$

$$\mathfrak{F}_i^\varepsilon \cdot \mathbf{n} = 0 \qquad \text{on } \Gamma_{\text{out}}, \tag{5.2.50i}$$

$$\mathfrak{N}_i^\varepsilon \cdot \mathbf{n} = 0 \qquad \text{on } \Gamma_{\text{ns}}^\varepsilon, \tag{5.2.50j}$$

$$\mathfrak{F}_{\text{H}_2}^\varepsilon \cdot \mathbf{n} = -I_{\text{C}} \frac{m_{\text{H}_2}}{2F} \qquad \text{on } \Gamma_{\text{el}}, \tag{5.2.50k}$$

$$\mathfrak{F}_{\text{H}_2\text{O}}^\varepsilon \cdot \mathbf{n} = I_{\text{C}} \frac{m_{\text{H}_2\text{O}}}{2F} \qquad \text{on } \Gamma_{\text{el}}. \tag{5.2.50l}$$

Hereby, $\mathfrak{F}_i^\varepsilon$ is given by (5.2.40), *$\mathfrak{N}_i^\varepsilon$ by* (5.2.41) *and the following relations hold true:*

$$y_{\mathrm{N}_2}^\varepsilon = 1 - y_{\mathrm{H}_2\mathrm{O}}^\varepsilon - y_{\mathrm{H}_2}^\varepsilon, \qquad \mu^\varepsilon = \sum_{i=1}^{N_{\mathrm{sp}}} y_i^\varepsilon \mu_i, \tag{5.2.51}$$

$$\overline{m}^\varepsilon = \frac{1}{\sum_{k=1}^{N_{\mathrm{sp}}} \frac{y_k^\varepsilon}{m_k}}, \qquad \rho^\varepsilon = \frac{p_{\mathrm{th}}^\varepsilon \overline{m}^\varepsilon}{RT}. \tag{5.2.52}$$

The anode overpotential $\eta_{\mathrm{conc}}^{\mathrm{A}}$ depends on the mass fractions of hydrogen and steam at the TPB as well as the inflow concentrations. As only mean values of the anode overpotential are experimentally accessible (Suwanwarangkul et al. [125], Tseronis et al. [131], Yakabe et al. [136]), we define the mean anodic overpotential functional J^{A} by:

Definition 5.2.11 (Mean Anodic Overpotential)**.** *Let φ_{H_2} and $\varphi_{\mathrm{H}_2\mathrm{O}}$ be the mass fractions of hydrogen and steam in a SOFC of type A or B. The functional representing the mean anodic overpotential is defined by*

$$\begin{aligned} J^{\mathrm{A}}(\varphi_{\mathrm{H}_2}, \varphi_{\mathrm{H}_2\mathrm{O}}) &:= \frac{1}{|\Gamma_{\mathrm{el}}|} \int_{\Gamma_{\mathrm{el}}} \eta_{\mathrm{conc}}^{\mathrm{A}}(s)\, \mathrm{d}s \\ &= \frac{RT}{2F|\Gamma_{\mathrm{el}}|} \int_{\Gamma_{\mathrm{el}}} \log\Big(\frac{\varphi_{\mathrm{H}_2}(s) y_{\mathrm{H}_2\mathrm{O}}^{\mathrm{in}}}{\varphi_{\mathrm{H}_2\mathrm{O}}(s) y_{\mathrm{H}_2}^{\mathrm{in}}}\Big)\, \mathrm{d}s \end{aligned} \tag{5.2.53}$$

$y_{\mathrm{H}_2}^{\mathrm{in}}$ and $y_{\mathrm{H}_2\mathrm{O}}^{\mathrm{in}}$ are the mass fractions at the inflow boundary.

We summarize molar weights, viscosities and the binary diffusion coefficients of hydrogen, steam and nitrogen in Table 5.2.1. Note that there holds $D_{ij}^{\mathrm{bin}} = D_{ji}^{\mathrm{bin}}$.

Adimensionalization

We present the non-dimensional version of Problem 5.2.10. To this end, we choose characteristic quantities as defined in Table 5.2.2.

Non-dimensional quantities are marked with the superscript $*$. We set

$$x = Lx^*, \qquad \mathbf{v}^\varepsilon = v_{\mathrm{c}} \mathbf{v}^{\varepsilon,*}, \quad p_{\mathrm{th}}^\varepsilon = p_{\mathrm{c}} p_{\mathrm{th}}^{\varepsilon,*}, \quad p_{\mathrm{hyd}}^\varepsilon = p_{\mathrm{c}} p_{\mathrm{hyd}}^{\varepsilon,*}, \tag{5.2.54a}$$

$$D_{ij}^{\mathrm{bin}} = D_{\mathrm{c}} D_{ij}^{\mathrm{bin},*}, \quad m_i = m_c m_i^*, \quad \mu_i = \mu_{\mathrm{c}} \mu_i^*, \quad \mathbf{v}^{\mathrm{in}} = v_{\mathrm{c}} \mathbf{v}^{\mathrm{in},*}. \tag{5.2.54b}$$

It follows $\nabla = \frac{1}{L}\nabla^*$ and we get the following adimensional formulation of Problem 5.2.10

Molar Weights in $10^{-3}\,\mathrm{kg/mol}$	
m_{H_2}	2.1588
$m_{\mathrm{H}_2\mathrm{O}}$	18.015 28
m_{N_2}	28.0134
Viscosities in $10^{-5}\,\mathrm{kg/m\,s}$	
μ_{H_2}	1.8770
$\mu_{\mathrm{H}_2\mathrm{O}}$	3.7585
μ_{N_2}	4.158 083
BDC in $10^{-4}\,\mathrm{m}^2/\mathrm{s}$	
$D^{\mathrm{bin}}_{\mathrm{H}_2,\mathrm{N}_2}$	6.2868
$D^{\mathrm{bin}}_{\mathrm{H}_2\mathrm{O},\mathrm{N}_2}$	2.21
$D^{\mathrm{bin}}_{\mathrm{H}_20,\mathrm{H}_2}$	7.535

Table 5.2.1.: Molar weights, viscosities and binary diffusion coefficients (*BDC*) for the considered species.

Problem 5.2.12 (Adimensional Microscopic Problem)**.** *Let inflow velocity* $\mathbf{v}^{\mathrm{in},*}$*, inflow mass fractions* y_k^{in}*, molar masses* m_k^* *and viscosities* μ_k^* *for* $k \in \{\mathrm{H}_2, \mathrm{H}_2\mathrm{O}, \mathrm{N}_2\}$ *as well as the current density* I_{C} *and the thermodynamic pressure* $p_{\mathrm{th}}^{\varepsilon}$ *be given. Let* Ω^{ε} *be a SOFC geometry of either type A or type B as described in Section 5.2.1. Let* $\Omega^{\varepsilon,*}$ *be* Ω^{ε} *scaled by* L_{c}*, the same holds true for the boundaries with superscript *.*

Find ***velocity field*** $\mathbf{v}^{\varepsilon,*}$*, the* ***pressure*** $p_{\mathrm{hyd}}^{\varepsilon,*}$ *and the* ***species mass fractions*** y_i^{ε} *s.t. for* $i \in \{\mathrm{H}_2, \mathrm{H}_2\mathrm{O}\}$ *there holds in* $\Omega^{\varepsilon,*}$

$$-\nabla^* \cdot (\mu^{\varepsilon,*} \nabla^* \mathbf{v}^{\varepsilon,*}) + \nabla^* p_{\mathrm{hyd}}^{\varepsilon,*} = 0, \qquad \text{in } \Omega^{\varepsilon,*} \tag{5.2.55a}$$

$$\nabla^* \cdot (\overline{m}^{\varepsilon,*} p_{\mathrm{th}}^* \mathbf{v}^{\varepsilon,*}) = 0, \qquad \text{in } \Omega^{\varepsilon,*} \tag{5.2.55b}$$

$$\nabla^* \cdot (\overline{m}^{\varepsilon,*} p_{\mathrm{th}}^* y_i^{\varepsilon} \mathbf{v}^{\varepsilon,*}) + \nabla^* \cdot \mathfrak{F}_i^{\varepsilon,*} = 0, \qquad \text{in } \Omega^{\varepsilon,*}, \tag{5.2.55c}$$

with

$$\mathfrak{F}_i^{\varepsilon,*} = \frac{RT}{p_{\mathrm{c}} v_{\mathrm{c}} m_c} \mathfrak{F}_i^{\varepsilon}. \tag{5.2.55d}$$

On the boundaries, there holds

$$\mathbf{v}^{\varepsilon,*} = \mathbf{v}^{\mathrm{in},*}, \qquad \text{on } \Gamma_{\mathrm{in}}^*, \tag{5.2.55e}$$

$$\mathbf{v}^{\varepsilon,*} = 0, \qquad \text{on } \Gamma_{\mathrm{ns}}^{\varepsilon,*} \cup \Gamma_{\mathrm{el}}^* \tag{5.2.55f}$$

Characteristic quantities		
Velocity	v_c	m/s
Length	L_c	m
Pressure	p_c	kg/m s^2
Diffusion coefficient	D_c	m^2/s
Molar mass	m_c	kg/mol
Viscosity	μ_c	kg/m s
Other constants		
Current density	I_C	A/m^2
Universal gas constant	R	J/mol K = kg m^2/s^{2}mol K
Faraday constant	F	A s/mol
Temperature	T	K

Table 5.2.2.: Constants overview.

and

$$\mathbf{n} \cdot (\mu^{\varepsilon,*} \nabla \mathbf{v}^{\varepsilon,*} - p_{\text{hyd}}^{\varepsilon,*} \,\mathrm{id}) \cdot \mathbf{n} = 0, \qquad \text{on } \Gamma_{\text{out}}^*, \tag{5.2.55g}$$

$$y_i^\varepsilon = y_i^{\text{in}}, \qquad \text{on } \Gamma_{\text{in}}^*, \tag{5.2.55h}$$

$$\mathfrak{F}_i^{\varepsilon,*} \cdot \mathbf{n} = 0, \qquad \text{on } \Gamma_{\text{out}}^*, \tag{5.2.55i}$$

$$\mathfrak{N}_i^{\varepsilon,*} \cdot \mathbf{n} = 0, \qquad \text{on } \Gamma_{\text{ns}}^{\varepsilon,*}, \tag{5.2.55j}$$

$$\mathfrak{F}_{\text{H}_2}^{\varepsilon,*} \cdot \mathbf{n} = -I_{\text{C}}^* \frac{m_{\text{H}_2}^*}{2}, \qquad \text{on } \Gamma_{\text{el}}^*, \tag{5.2.55k}$$

$$\mathfrak{F}_{\text{H}_2\text{O}}^{\varepsilon,*} \cdot \mathbf{n} = I_{\text{C}}^* \frac{m_{\text{H}_2\text{O}}^*}{2} \qquad \text{on } \Gamma_{\text{el}}^*. \tag{5.2.55l}$$

Hereby, $\mathfrak{F}_i^\varepsilon$ is given by (5.2.40), *$\mathfrak{N}_i^\varepsilon$ by* (5.2.41) *and the following relations hold true:*

$$y_{\text{N}_2}^\varepsilon = 1 - y_{\text{H}_2\text{O}}^\varepsilon - y_{\text{H}_2}^\varepsilon, \qquad \mu^{\varepsilon,*} = \sum_{i=1}^{N_{\text{sp}}} y_i^\varepsilon \mu_i^*, \tag{5.2.56}$$

$$\overline{m}^{\varepsilon,*} = \frac{1}{\sum_{k=1}^{N_{\text{sp}}} \frac{y_k^\varepsilon}{m_k^*}}, \qquad I_{\text{C}}^* = I_{\text{C}} \frac{RT}{F p_c v_c}. \tag{5.2.57}$$

5.2.3. Effective Equations

After setting the system of equations on the microscopic level in the previous section, we present here the system on the macroscopic level. A homogenization

procedure lies out of the scope of this work. Instead we present a candidate for the effective problem and discuss some heuristics why this might be the right choice. Afterward, we solve a number of microscopic problems as well as aforementioned effective equations for a test case and show that the microscopic solution converge under the anodic overpotential functional towards the effective solution.

We present the adimensional version, domains and boundaries with the superscript * are scaled by L_c in comparison with their non-superscript counterparts. Let Ω^* be a macroscopic SOFC geometry of either type A or type B as described in Section 5.2.1. If not stated otherwise, we use the notation and requirements of the previous section.

$\mathfrak{F}_i$, $\overline{m}$, ρ and μ, are defined exactly as $\mathfrak{F}_i^\varepsilon$ (cf. (5.2.40)), $\overline{m}^\varepsilon$ (cf. Definition 2.1.10), ρ^ε (cf. (5.2.23)) and μ^ε (cf. (5.2.21)), when we use the macroscopic quantities y_i, x_i, etc. instead of y_i^ε, x_i^ε in the respective definitions. The same holds true for the non-dimensional versions of these quantities.

Let the interface constant $C_1^{\mathrm{bl}} \in \mathbb{R}$ be given by Definition 3.1.27, and the matrix $\mathbf{A}^{\mathrm{hom}} \in \mathbb{R}^{2\times 2}$ by (A.1.36), see also (2.2.42). We define $\mathfrak{F}^{\mathrm{hom},*}$ for $x \in \Omega_{\mathrm{f}}^* \cup \Omega_{\mathrm{p}}^*$ by

$$\mathfrak{F}^{\mathrm{hom},*}(x) := \begin{cases} \mathfrak{F}^*, & x \in \Omega_{\mathrm{f}}^*, \\ \mathbf{A}^{\mathrm{hom}}\mathfrak{F}^*, & x \in \Omega_{\mathrm{p}}^*. \end{cases} \tag{5.2.58}$$

The effective equations in non-dimensional formulation reads as follows (see Chapter B for the dimensional formulation).

Problem 5.2.13. *Let inflow velocity $\mathbf{v}^{\mathrm{in},*}$, inflow mass fractions y_k^{in}, molar masses m_k^* and viscosities μ_k^* for $k \in \{ \mathrm{H}_2, \mathrm{H}_2\mathrm{O}, \mathrm{N}_2 \}$ as well as the current density I_{C} and the thermodynamic pressure p_{th}^* be given. Let $\varepsilon^* := \frac{\varepsilon}{L_c}$.*

*With the notation from above, find the **velocity field** $\mathbf{v}^*$, the **pressure** p_{hyd}^* and the **species mass fractions** y_i^ε s.t. for $i \in \{ \mathrm{H}_2, \mathrm{H}_2\mathrm{O} \}$ there holds*

$$-\nabla^* \cdot (\mu^* \nabla^* \mathbf{v}^*) + \nabla^* p_{\mathrm{hyd}}^* = 0 \qquad \text{in } \Omega_{\mathrm{f}}^* \tag{5.2.59a}$$

$$\nabla^* \cdot (\overline{m^*} p_{\mathrm{th}}^* \mathbf{v}^*) = 0 \qquad \text{in } \Omega_{\mathrm{f}}^* \tag{5.2.59b}$$

$$\nabla^* \cdot (\overline{m^*} p_{\mathrm{th}}^* \omega_i^* \mathbf{v}^*) + \nabla \cdot \mathfrak{F}_i^* = 0 \qquad \text{in } \Omega_{\mathrm{f}}^*, \tag{5.2.59c}$$

$$\nabla^* \cdot (\mathbf{A}^{\mathrm{hom}} \mathfrak{F}_i^*) = 0 \qquad \text{in } \Omega_{\mathrm{p}}^*. \tag{5.2.59d}$$

On the boundaries, there holds

$$\mathbf{v}^* = \mathbf{v}^{\mathrm{in},*} \qquad \text{on } \Gamma^*_{\mathrm{in}}, \tag{5.2.59e}$$
$$\mathbf{v}^* = 0 \qquad \text{on } \Gamma^*_{\mathrm{f,ns}}, \tag{5.2.59f}$$
$$\mathbf{n} \cdot (\mu^* \nabla \mathbf{v}^* - p^*_{\mathrm{hyd}}\,\mathrm{id}) \cdot \mathbf{n} = 0 \qquad \text{on } \Gamma^*_{\mathrm{out}} \tag{5.2.59g}$$

and

$$y_i = y_i^{\mathrm{in}} \qquad \text{on } \Gamma^*_{\mathrm{in}}, \tag{5.2.59h}$$
$$\mathfrak{F}^*_i \cdot \mathbf{n} = 0 \qquad \text{on } \Gamma^*_{\mathrm{out}}, \tag{5.2.59i}$$
$$\mathfrak{N}^*_i \cdot \mathbf{n} = 0 \qquad \text{on } \Gamma^*_{\mathrm{f,ns}}, \tag{5.2.59j}$$
$$\mathbf{A}^{\mathrm{hom}}\mathfrak{F}^*_i \cdot \mathbf{n} = 0 \qquad \text{on } \Gamma^*_{\mathrm{p,ns}}, \tag{5.2.59k}$$
$$\mathbf{A}^{\mathrm{hom}}\mathfrak{F}^*_{\mathrm{H}_2} \cdot \mathbf{n} = -I^*_{\mathrm{C}}\frac{m^*_{\mathrm{H}_2}}{2} \qquad \text{on } \Gamma^*_{\mathrm{el}}, \tag{5.2.59l}$$
$$\mathbf{A}^{\mathrm{hom}}\mathfrak{F}^*_{\mathrm{H}_2\mathrm{O}} \cdot \mathbf{n} = I^*_{\mathrm{C}}\frac{m^*_{\mathrm{H}_2\mathrm{O}}}{2} \qquad \text{on } \Gamma^*_{\mathrm{el}}. \tag{5.2.59m}$$

On the interface, the following coupling conditions hold true

$$[y_i] = 0 \qquad \text{on } \Gamma^*, \tag{5.2.59n}$$
$$[\mathfrak{F}^{\mathrm{hom},*}_i \cdot \mathbf{n}] = 0 \qquad \text{on } \Gamma^*, \tag{5.2.59o}$$
$$v^*_2 = 0, \qquad \text{on } \Gamma^* \tag{5.2.59p}$$
$$v^*_1 + \varepsilon^* C^{\mathrm{bl}}_1 \frac{\partial v^*_1}{\partial x^*_2} = 0 \qquad \text{on } \Gamma^*. \tag{5.2.59q}$$

In deriving the effective model we orient ourselves on the homogenized equations for the stokes flow (see Chapter 3) and the nonlinear diffusion equation (see Chapter A). Note that we only use the formal argument of asymptotic expansion in deriving the effective diffusion equation in Chapter A. Note also that the derivation of the homogenized problem in Chapter 3 was for an *incompressible* flow. However, computations of the compressible stokes flow on the microscopic level in a typical SOFC configuration show only weak compressibility effects. We also want to make clear that in general the product of two microscopic quantities does not converge towards the product of the effective quantities, see Section 2.2. We check the validity of the effective system by some numerical examples in the next section. However, this is no proof and more work is required to prove convergence w.r.t. ε.

In Chapter 3 the problem regarding the homogenization process of Stokes equation across an interface between a porous medium and an unconfined region

was discussed extensively. The main problem was due to the different type of effective PDEs in Ω_f and Ω_p. We do not expect this kinds of problems for the nonlinear diffusion as the effective PDEs are of the same type on both sides of the interfaces, see Jäger et al. [79] for a similar problem with the Laplace equation.

Note that we assume zero effective velocity in Ω_p. This is due to the a priori estimation of the effective velocity in Ω_p, which is of order ε^{*2}, see Theorem 3.1.16. For a typical SOFC configuration we assume ε^* to be in the order of 10^{-3} or 10^{-4}, so convective transport in the pores is negligible. This is in agreement with experiments, see Yakabe et al. [136].

Confirmation by Direct Numerical Simulation

We show at an explicit example that the mean anodic overpotential for a series of microscopic problems converge towards the macroscopic overpotential.

Input parameters	
T	$1000\,\mathrm{K}$
p_{hyd}	$101\,300\,\mathrm{kg/ms^2}$
I_C	$50\,\mathrm{A/m^2}$
$\mathbf{v}^{\mathrm{in}}$	$(x_1, x_2) \mapsto (2x_2(1-x_2), 0)\ \mathrm{m/s}$
$x^{\mathrm{in}}_{\mathrm{H_2}}$	0.3
$x^{\mathrm{in}}_{\mathrm{H_2O}}$	0.6
Geometry parameters	
Type	A
H_u	$1\,\mathrm{m}$
H_l	$1\,\mathrm{m}$
L	$1\,\mathrm{m}$
x^l_{el}	$(0,-1)$
x^r_{el}	$(1,-1)$

Table 5.2.3.: Parameters of the homogenization error example.

For the parameters specified in Table 5.2.3 (see also Table 5.2.1) we compute the solution of (the discretized versions of) the macroscopic Problem 5.2.13 and the microscopic Problem 5.2.12 for

$$\varepsilon \in \left\{ 1, \frac{1}{3}, \frac{1}{6}, \frac{1}{10}, \frac{1}{16}, \frac{1}{30} \right\}. \tag{5.2.60}$$

The domain is of type A and the *inclusions* are circles with midpoint $(0.5, 0.5)$ and diameter 0.25 in the unit cell.

In Figure 5.2.2 the homogenization error

$$e^\varepsilon = J^{\mathrm{A}}(y_{\mathrm{H}_2}, y_{\mathrm{H}_2\mathrm{O}}) - J^{\mathrm{A}}(y^\varepsilon_{\mathrm{H}_2}, y^\varepsilon_{\mathrm{H}_2\mathrm{O}}) \tag{5.2.61}$$

is shown. We observe a clear convergence (slightly faster than ε) of e^ε with $\varepsilon \to 0$. Note that we deal with relatively big values of ε^* ($\varepsilon^* = 1/30$ means here that we consider only 900 inclusions). Nevertheless, the (absolute) homogenization error is 10^{-4} and, as the functional values in this example are of order 10^{-2}, the relative homogenization error is around 10^{-2}. This shows that, at least for this example, the macroscopic problem is a meaningful approximation of the microscopic problems.

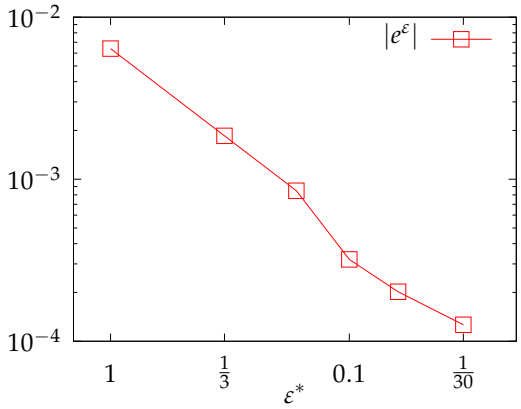

Figure 5.2.2.: Convergence of the homogenization error of the mean anode overpotential functional.

5.3. Numerical Results

We apply the adaptive refinement algorithm developed in Chapter 4 (see Algorithm 4.3.1) to the effective SOFC-model 5.2.13. The target quantity is the mean anodic overpotential J^{A} defined in Definition 5.2.11. We start by showing in Section 5.3.2 with two simple examples that the adaptive algorithm developed in Chapter 4 works for the SOFC model. In Section 5.3.3 we apply Algorithm 4.3.1 to a more realistic SOFC scenario.

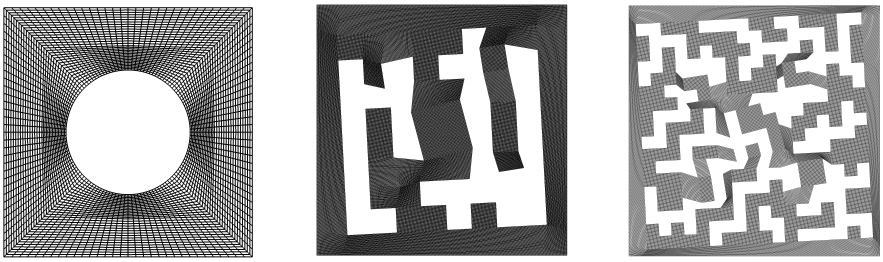

(a) Circular inclusion **(b)** Angular inclusion **(c)** Detailed inclusion

Figure 5.3.1.: Sketches of the unit cell geometries for the CIE(a), AIE(b) and DIE(c).

5.3.1. Discretization

We solve discretized versions of the macroscopic SOFC model (Problem 5.2.13), the cut-off boundary layer (Problem 3.2.3) as well as the two cell problems for the computation of $\mathbf{A}^{\text{hom}}$ (Problem 2.2.12, with $A = \text{id}$). All these problems are discretized with systems of **parametric finite elements**. We use triangulations of the domains based on quadrilateral cells which follow a patch-structure, see Section 4.3.1. All Stokes equations are discretized with the Taylor-Hood element, the other variables use a bilinear element. Curved boundaries are approximated with a bi-quadratic mapping.

For the solution of the nonlinear equations we utilize an inexact Newton method with line-search. The Newton matrix is updated only "when necessary", i.e. when the residual does not decrease fast enough. Linear systems are solved with a direct solver (UMFPACK, see Davis [50]). All computations are done with the software package `DOpElib`, see Goll et al. [65], which is based on `deal.II`, see Bangerth et al. [15, 16].

5.3.2. Test Cases

In this section we test if the adaptive Algorithm 4.3.1 is able to handle the SOFC model with two examples, called "circular inclusion example" (*CIE*) and "angular inclusion example" (*AIE*), which only differ in their microstructure. In Table 5.3.1 and Table 5.2.1 the SOFC configuration is shown. Note that we specify x_k^{in} instead of y_k^{in}. Of course, we can convert mole fractions into mass fractions. We choose the geometry labeled Type B with a parabolic inflow on Γ_{in}. The two different microstructures are shown in Figure 5.3.1. We describe their structure in the unit cell $Y = [0,1]^2$.

Input parameters	
T	$1000\,\mathrm{K}$
p_{th}	$101\,300\,\mathrm{kg/ms^2}$
I_{C}	$15\,000\,\mathrm{A/m^2}$
$\mathbf{v}^{\mathrm{in}}$	$(x_1, x_2) \mapsto -1.5(0, \frac{4}{\lvert\Gamma_{\mathrm{in}}\rvert}(x_1 - x^{\mathrm{l}}_{\mathrm{in},1})(1 - \frac{x_1 - x^{\mathrm{l}}_{\mathrm{in},1}}{\lvert\Gamma_{\mathrm{in}}\rvert}))\,\mathrm{m/s}$
$x^{\mathrm{in}}_{\mathrm{H_2}}$	0.6
$x^{\mathrm{in}}_{\mathrm{H_2O}}$	0.15
Geometry parameters	
Type	B
H_{u}	$0.001\,\mathrm{m}$
H_{l}	$0.002\,\mathrm{m}$
L	$0.01\,\mathrm{m}$
ε	$2 \cdot 10^{-5}\,\mathrm{m}$
$x^{\mathrm{l}}_{\mathrm{el}}$	$(0002, -0.002)$
$x^{\mathrm{r}}_{\mathrm{el}}$	$(0.008, -0.002)$
$x^{\mathrm{l}}_{\mathrm{in}}$	$(-0.002, 0.002)$
$x^{\mathrm{r}}_{\mathrm{in}}$	$(-0.001, 0.002)$

Table 5.3.1.: Parameters of test examples CIE and AIE.

CIE In this example the inclusion is a circle with midpoint at $(0.5, 0.5)$ and a diameter of 0.25, see Figure 5.3.1a.

AIE We do not give a precise definition of the angular microstructure in this example and refer to Figure 5.3.1b instead.

Parts of the effective SOFC model (see Problem 5.2.13) are

- the macroscopic equation (5.2.59) on Ω^*,
- the cut off Navier Boundary Layer Problem to compute C_1^{bl} on Z_l^k and
- two cell problems to compute $\mathbf{A}^{\mathrm{hom}}$ on Y_{f}.

We use the notation of Chapter 4. Let us explain how it applies to the situation at hand. The triangulation of Ω^* is called $\mathcal{T}_h^m$, the triangulation of Z_l^k is $\mathcal{T}_h^{\mathrm{bl}}$ and the triangulation of Y_{f} is (depending on which cell problem we consider) $\mathcal{T}_h^{\mathrm{c}_j}$ for $j = 1, 2$.

The total number of degrees of freedom, DoF, is defined by

$$\mathrm{DoF} = \mathrm{DoF}^{\mathrm{m}} + \mathrm{DoF}^{\mathrm{c}_1} + \mathrm{DoF}^{\mathrm{c}_2} + \mathrm{DoF}^{\mathrm{bl}}, \tag{5.3.1}$$

where $\mathrm{DoF}^{\mathrm{m}}$, $\mathrm{DoF}^{\mathrm{c}_j}$ and $\mathrm{DoF}^{\mathrm{bl}}$ are the number of unknowns on $\mathcal{T}_h^m$, $\mathcal{T}_h^{\mathrm{c}_j}$ and $\mathcal{T}_h^{\mathrm{bl}}$ respectively.

Circular Inclusion Example

In Table 5.3.2 we see the results of Algorithm 4.3.1 with $TOL = 1 \cdot 10^{-5}$ and $\mathcal{C}_i = 4$ for the circular inclusions.

$\mathrm{DoF}^{\mathrm{m}}$	$J^{\mathrm{A}}(\mathbf{y}_h)$	e^h	η	η^{m}	I_{eff}
1,513	0.01898	$1.6 \cdot 10^{-4}$	$1.6 \cdot 10^{-4}$	$1.1 \cdot 10^{-4}$	1.02
4,275	0.01908	$5.2 \cdot 10^{-5}$	$4.9 \cdot 10^{-5}$	$3.2 \cdot 10^{-5}$	0.95
5,513	0.01910	$3.2 \cdot 10^{-5}$	$2.9 \cdot 10^{-5}$	$2.2 \cdot 10^{-5}$	0.92
15,767	0.01912	$1.5 \cdot 10^{-5}$	$1.4 \cdot 10^{-5}$	$6.4 \cdot 10^{-6}$	0.94
48,601	0.01913	$3.9 \cdot 10^{-6}$	$4.0 \cdot 10^{-6}$	$1.9 \cdot 10^{-6}$	1.02

(a) Data of the macroscopic problem.

$\mathrm{DoF}^{\mathrm{c}_1}$	$\mathrm{DoF}^{\mathrm{c}_2}$	$\mathrm{DoF}^{\mathrm{bl}}$	η^{c_1}	η^{c_2}	η^{bl}
80	80	1,457	$3.4 \cdot 10^{-6}$	$4.8 \cdot 10^{-5}$	$-2.4 \cdot 10^{-8}$
80	288	1,457	$3.4 \cdot 10^{-6}$	$1.4 \cdot 10^{-5}$	$-2.4 \cdot 10^{-8}$
80	1,088	1,457	$3.4 \cdot 10^{-6}$	$3.8 \cdot 10^{-6}$	$-2.4 \cdot 10^{-8}$
80	1,088	1,457	$3.4 \cdot 10^{-6}$	$3.8 \cdot 10^{-6}$	$-2.5 \cdot 10^{-8}$
288	3,972	1,457	$9.9 \cdot 10^{-7}$	$1.1 \cdot 10^{-6}$	$-2.5 \cdot 10^{-8}$

(b) Data of auxiliary problems.

Table 5.3.2.: Results of the local mesh refinement applied to the test problem CIE.

e^h is the error in the functional J^{A}:

$$e^h := J^{\mathrm{A}}(\mathbf{y}) - J^{\mathrm{A}}(\mathbf{y}_h) \tag{5.3.2}$$

with $\mathbf{y}$ being the vector of mass fractions and $\mathbf{y}_h$ its discrete counterpart. As the solution to the macroscopic problem is of course unknown to us, we take a reference value computed on a very fine grid as $J^{\mathrm{A}}(\mathbf{y})$. η is the sum of the error estimators η^{m}, η^{c_1},η^{c_2}, η^{bl}, which describe the error due to the discretization of the macroscopic problem (η^{m}), the two cell problems (η^{c_j}) and the boundary layer problem (η^{bl}) as described in Section 4.3. The effectivity index is the ratio of η and e^h, see (4.4.1). Note that the error as well as the error estimators are signed.

We see that the algorithm works very well for this example. Throughout the refinement process there holds $0.92 \leq I_{eff} \leq 1.02$, so we estimate the error precisely. Moreover, the splitting of η into the macroscopic and auxiliary parts works also very well too. For the initial mesh there holds

$$\eta^{\mathrm{m}} > \eta^{\mathrm{c}_2} \gg \eta^{\mathrm{c}_1} \gg \eta^{\mathrm{bl}} \tag{5.3.3}$$

and consequently $\mathcal{T}_h^{\mathrm{c}_1}$ gets much less refined than $\mathcal{T}_h^{\mathrm{c}_2}$ and $\mathcal{T}_h^{m}$ during the adaptive cycle process. We see also that the impact of Naviers Boundary Layer discretization is very weak, and thus the $\mathcal{T}_h^{\mathrm{bl}}$ is not touched during the whole process. The goal of the adaptive algorithm is to refine the grids in a way that in the end all error-parts are balanced. We see that we achieve this in the example at hand. After the last refinement step there holds

$$\eta^{\mathrm{m}} \approx 2\eta^{\mathrm{c}_1} \approx 2\eta^{\mathrm{c}_2}, \tag{5.3.4}$$

whereas in the beginning these three errors were stretched across nearly two orders of magnitude.

Angular Inclusion Example

$\mathrm{DoF}^{\mathrm{m}}$	$J^{\mathrm{A}}(\mathbf{y}_h)$	e^h	η	η^{m}	I_{eff}
1,513	0.02611	$2.4 \cdot 10^{-4}$	$1.8 \cdot 10^{-4}$	$1.1 \cdot 10^{-4}$	0.73
4,157	0.02625	$9.7 \cdot 10^{-5}$	$6.4 \cdot 10^{-5}$	$3.4 \cdot 10^{-5}$	0.66
5,035	0.02629	$6.1 \cdot 10^{-5}$	$4.3 \cdot 10^{-5}$	$2.4 \cdot 10^{-5}$	0.71
16,077	0.02633	$2.0 \cdot 10^{-5}$	$1.4 \cdot 10^{-5}$	$6.3 \cdot 10^{-6}$	0.68
43,121	0.02634	$8.1 \cdot 10^{-6}$	$5.8 \cdot 10^{-6}$	$2.2 \cdot 10^{-6}$	0.72

(a) Data of the macroscopic problem.

$\mathrm{DoF}^{\mathrm{c}_1}$	$\mathrm{DoF}^{\mathrm{c}_2}$	$\mathrm{DoF}^{\mathrm{bl}}$	η^{c_1}	η^{c_2}	η^{bl}
1,287	1,287	19,741	$4.3 \cdot 10^{-6}$	$5.9 \cdot 10^{-5}$	$-3.0 \cdot 10^{-9}$
1,287	2,217	19,741	$4.4 \cdot 10^{-6}$	$2.6 \cdot 10^{-5}$	$-3.0 \cdot 10^{-9}$
1,287	3,739	19,741	$4.4 \cdot 10^{-6}$	$1.5 \cdot 10^{-5}$	$-3.0 \cdot 10^{-9}$
2,247	11,813	19,741	$2.1 \cdot 10^{-6}$	$5.4 \cdot 10^{-6}$	$-3.1 \cdot 10^{-9}$
5,147	25,939	19,741	$1.0 \cdot 10^{-6}$	$2.7 \cdot 10^{-6}$	$-3.1 \cdot 10^{-9}$

(b) Data of auxiliary problems.

Table 5.3.3.: Results of the local mesh refinement applied to the test problem AIE.

In Table 5.3.3 we see that the situation is basically the same for the example with

the angular inclusion (TOL and $\mathcal{C}_i$ are choose as before). The only difference is that the effectivity index is a bit worse in this example. This is due to the fact that we have a lower regularity due to the reentrant corners in the cell problems. As before, the Navier Boundary Layer has nearly no impact on J^{A}. However, we see that the cell problems are more important in this example than in CIE. On the finest level there holds for AIE

$$\mathrm{DoF}^{\mathrm{c}_1} + \mathrm{DoF}^{\mathrm{c}_2} \approx \mathrm{DoF}^{\mathrm{m}}, \tag{5.3.5}$$

whereas for the example with the circular inclusions there holds

$$10(\mathrm{DoF}^{\mathrm{c}_1} + \mathrm{DoF}^{\mathrm{c}_2}) \approx \mathrm{DoF}^{\mathrm{m}}. \tag{5.3.6}$$

For both problems, the second cell problem has a bigger impact on J^{A} than the first one. This is reasonable, since the second cell problem is connected with the macroscopic diffusion in x_2-direction, and the distribution of the species in this direction is more important for the determination of J^{A} than the distribution in x_1 direction.

Note that the anodic overpotential in the scenario with angular pores is more than 25% higher than in the previous case with the circular inclusions. We see that the microstructure has a significant influence on the overpotential.

5.3.3. More Detailed Microstructure Example

In this section we apply the adaptive algorithm to an example which is a little bit more representative for real problems in the respect that we choose a more detailed and complex inclusion in the unit cell which has more resemblance with real pore structures. We call it the "detailed inclusion example" (*DIE*). The configuration of the fuel cell model is shown in Table 5.3.4.

Regarding the inclusion in the unit cell, we choose the structure shown in Figure 5.3.1c, which is a more complicated version of the angular pores example in the previous section. Note that we reduced the amount of hydrogen and steam at the inlet in comparison with the previous examples. This corresponds to a higher fuel utilization which in turn results in higher concentration overpotential. In this scenario, a precise estimation of J^{A} is essential for an accurate estimation of fuel cell voltage, see Tseronis et al. [131].

In Table 5.3.5 the results of the adaptive algorithm for this example are shown. We have no reference values for this case, so no "true" error or effectivity indices are shown. We see in comparison with the previous examples that the cell problems have become more important in the sense that we need more degrees of

Input parameters	
T	1000 K
p_{th}	101 300 kg/ms^2
I_{C}	15 000 A/m^2
$\mathbf{v}^{\text{in}}$	$(x_1, x_2) \mapsto -1.5(0, \frac{4}{\lvert\Gamma_{\text{in}}\rvert}(x_1 - x^{\text{l}}_{\text{in},1})(1 - \frac{x_1 - x^{\text{l}}_{\text{in},1}}{\lvert\Gamma_{\text{in}}\rvert}))$ m/s
$x^{\text{in}}_{\text{H}_2}$	0.2
$x^{\text{in}}_{\text{H}_2\text{O}}$	0.05
Geometry parameters	
Type	B
H_{u}	0.001 m
H_{l}	0.002 m
L	0.01 m
ε	2e-5
x^{l}_{el}	$(0002, -0.002)$
x^{r}_{el}	$(0.008, -0.002)$
x^{l}_{in}	$(-0.002, 0.002)$
x^{r}_{in}	$(-0.001, 0.002)$

Table 5.3.4.: Parameters of the DIE.

freedom to achieve the same accuracy. As before, the discretization of the Navier Boundary Layer has a minor influence on the error in the anode overpotential.

This is a valuable information as it allows to save the effort of solving that problem. In Figure 5.3.2 we show a plot of the total degrees of freedom versus the relative value of the error estimator, i.e. the quantity

$$\frac{\eta}{J^{\text{A}}}, \tag{5.3.7}$$

for a global refinement, where in each refinement cycle we refine all triangulations globally and our adaptive algorithm. We see clearly that the adaptive refinement is superior in terms of degrees of freedom. In terms of runtime the global refinement is 20 times slower than the adaptive algorithm. The source of the savings is twofold.

- Firstly, we gain an advantage over global refinement by locally refining the triangulations. This is especially effective if the solution has some localized regions of reduced smoothness and/or the domain of dependence of the goal functional is highly localized.

$\mathrm{DoF}^{\mathrm{m}}$	$J^{\mathrm{A}}(\mathbf{y}_h)$	η	η^{m}
1,513	0.10069	$6.7 \cdot 10^{-4}$	$3.2 \cdot 10^{-4}$
4,383	0.10128	$2.9 \cdot 10^{-4}$	$1.0 \cdot 10^{-4}$
5,263	0.10154	$1.5 \cdot 10^{-4}$	$6.4 \cdot 10^{-5}$
17,315	0.10166	$6.5 \cdot 10^{-5}$	$1.8 \cdot 10^{-5}$
35,155	0.10172	$2.9 \cdot 10^{-5}$	$8.2 \cdot 10^{-6}$

(a) Data of the macroscopic problem.

$\mathrm{DoF}^{\mathrm{c}_1}$	$\mathrm{DoF}^{\mathrm{c}_2}$	$\mathrm{DoF}^{\mathrm{bl}}$	η^{c_1}	η^{c_2}	η^{bl}
4,741	4,741	101,219	$3.5 \cdot 10^{-5}$	$3.1 \cdot 10^{-4}$	$-2.7 \cdot 10^{-9}$
4,741	8,495	101,219	$3.5 \cdot 10^{-5}$	$1.6 \cdot 10^{-4}$	$-2.8 \cdot 10^{-9}$
10,319	21,659	101,219	$1.6 \cdot 10^{-5}$	$7.0 \cdot 10^{-5}$	$-2.8 \cdot 10^{-9}$
10,319	54,477	101,219	$1.6 \cdot 10^{-5}$	$3.2 \cdot 10^{-5}$	$-2.8 \cdot 10^{-9}$
22,423	158,589	101,219	$8.1 \cdot 10^{-6}$	$1.3 \cdot 10^{-5}$	$-2.8 \cdot 10^{-9}$

(b) Data of auxiliary problems.

Table 5.3.5.: Results of the local mesh refinement applied to detailed microstructure example.

How does this apply to the situation at hand? The cell problems in the DIE have (a lot of) reentrant corners (see Figure 5.3.1c), but the connection with the goal functional J^{A} is through the effective diffusion tensor $\mathbf{A}^{\mathrm{hom}}$, which has no local features in Y_{f}. On the macroscopic level, the solution is relatively smooth (see Figure 5.3.6). So the overall effect of the local refinement on each grid is visible, but not too big.

- Secondly, and more importantly in this scenario, we save degrees of freedom (and thus computation time) because we are able to evaluate (and thus balance) the contribution of the various problems to the overall discretization error: We refine the first cell problem only two times, whereas the second cell problem, as well as the macroscopic problem, is refined in every step. The Navier Boundary Layer does not get refined at all, see Table 5.3.5. This means that we do not "waste" any effort on problems which contributions to the overall discretization error are minor.

In Figure 5.3.3 and Figure 5.3.4 we see the grids resulting from the adaptive algorithm after the final refinement step. We see that most of the refinement in the macroscopic domain is near the points $x_{\mathrm{el}}^{\mathrm{l}}$ and $x_{\mathrm{el}}^{\mathrm{r}}$, as well as near reentrant corners, where the smoothness of the solution variables is reduced. We also see some refinement in the gas channel, presumably because the distribution of the species on Γ is important, as the diffusive transport in the anode is much slower

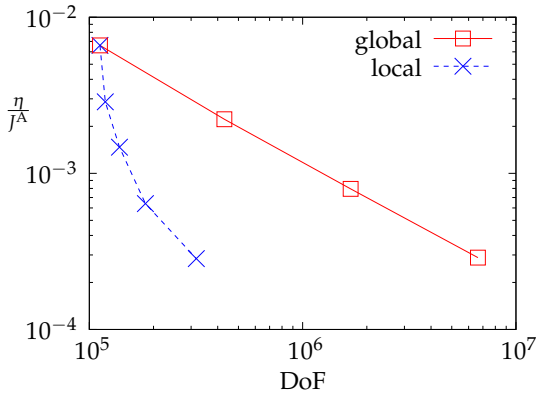

Figure 5.3.2.: Total number of dofs vs. relative error estimator in the mean anodic overpotential for global and local mesh refinement in the detailed microstructure example.

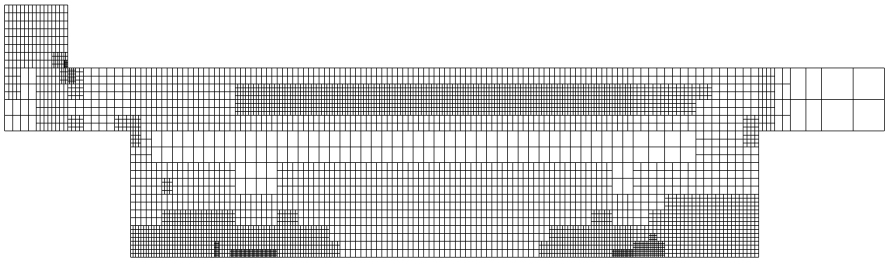

Figure 5.3.3.: Locally refined macroscopic domain for the detailed microstructure example on the final refinement level.

compared to the convective transport in the gas channel. Thus, the point of entry into the anode influences the species distribution on Γ_{el}. The outflow channel is not refined at all. The cell problems are mostly refined near reentrant corners where the regularity breaks down.

We see plots of the solution in Figure 5.3.6. The mass fractions of hydrogen and water as well as the hydrostatic pressure and the norm of the velocity are shown. Note that we do not solve for velocity and pressure in the anode, which is visualized by the figures by a constant 0. The artefacts of $|\mathbf{v}|$ at the outflow are due to the very coarse grid, see also Figure 5.3.3. We see that hydrogen is absorbed at Γ_{el}, and steam is produced at this site. We thus have a steep gradient in x_2 direction from Γ_{el} to Γ. Note that the distribution of species along Γ is not constant as sometimes assumed in computations, so the gas channel should not be neglected in the SOFC simulation. If we look closely, a kink along Γ is visible for the mass fractions. This is due to the jump in the diffusion coefficients across

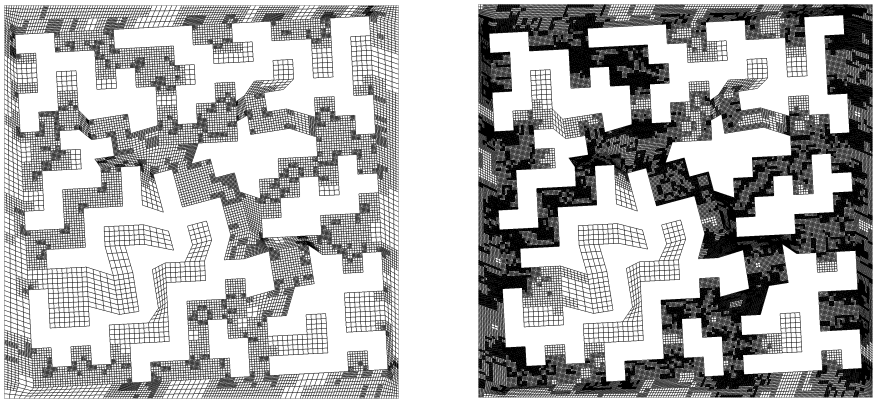

(a) Cell 1 **(b)** Cell 2

Figure 5.3.4.: Locally refined grids for the cell problems on the final refinement level (DIE).

this interface.

The flow configuration is pretty simple in this example, to the naked eye the flow is not distinguishable from Poiseulle flow. We see also that p_{hyd} is magnitudes smaller than p_{th}. The simplicity of the flow is one reason why J^{A} is so insensitive with respect to C_1^{bl}. This might change if the layout of the Fuel Cell is modelled more realistically. For instance, we neglect the (nickel)-mesh between the gas channel and the anode which transports the electrical current. An incorporation of this structure should make the flow more complex and consequently raise the importance of an exact flow simulation. Even though the exact value of C_1^{bl} is not so important in these examples, the coupling conditions (B.2.1p) and (B.2.1q) decouple the effective flow in Ω_{f} and Ω_{p}. This allows for dropping the effective flow in Ω_{p} and thus reduces the overall computational effort.

Influence on Overpotential

In this final section we examine the influence of I_{C} and $x_{\text{H}_2}^{\text{in}}$ on J^{A}. In we present Figure 5.3.5 the overpotentials computed for the configuration given in Table 5.3.4 for range of current density and hydrogen mole inlet fractions. We choose

$$x_{\text{H}_2}^{\text{in}} \in \{\, 0.15, 0.2, 0.3, 0.4, 0.5, 0.6, 0.7 \,\} \tag{5.3.8}$$

and

$$I_C \in \left\{ 5000\,\mathrm{A/m^2}, 10\,000\,\mathrm{A/m^2}, 15\,000\,\mathrm{A/m^2} \right\}. \tag{5.3.9}$$

$x^{\mathrm{in}}_{\mathrm{H_2O}}$ was chosen such that the ratio between hydrogen and steam is constant:

$$\frac{x^{\mathrm{in}}_{\mathrm{H_2}}}{x^{\mathrm{in}}_{\mathrm{H_2O}}} = 4. \tag{5.3.10}$$

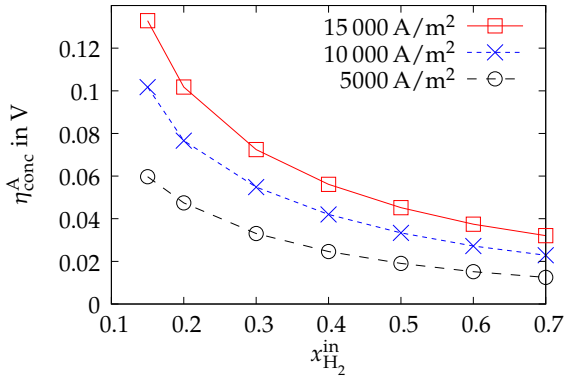

Figure 5.3.5.: Plot of $\eta^{\mathrm{A}}_{\mathrm{conc}}$ versus hydrogen mole fractions at the inlet for $I_C = 15\,000\,\mathrm{A/m^2}$, $I_C = 10\,000\,\mathrm{A/m^2}$ and $I_C = 5000\,\mathrm{A/m^2}$.

We see that the anodic overpotential increases with increasing I_C and decreasing $x^{\mathrm{in}}_{\mathrm{H_2}}$. This is expected: An increase in the current density is synonymous with a higher fuel demand at Γ_{el}. This means that more fuel needs to get to the anode/electrolyte interface. That increases $\eta^{\mathrm{A}}_{\mathrm{conc}}$. The decrease in $x^{\mathrm{in}}_{\mathrm{H_2}}$ corresponds to a higher fuel utilization, which results also in higher values of $\eta^{\mathrm{A}}_{\mathrm{conc}}$. In this scenario, the transport by diffusion is slower and thus closer to the hydrogen consumption rate at Γ_{el}. Note that the increase in the overpotential gets steeper with lower $x^{\mathrm{in}}_{\mathrm{H_2}}$.

The whole behaviour is qualitatively in agreement with the results of Tseronis et al. [131], Yakabe et al. [136] (as we have no information on the microstructure in their tests, it is unrealistic to expect more in this scenario) and shows that our model is able to grasp the relevant effects.

Remark 5.3.1 (Influence of Microstructure on Overpotential)**.** *Note that the anode overpotential of the DIE at* $x^{\mathrm{in}}_{\mathrm{H_2}} = 0.6$ *and* $I_C = 15\,000\,\mathrm{A/m^2}$ *is round about* $0.04\,\mathrm{V}$*, which is twice the value of the overpotential in the CIE and more than* 1.5 *times the value of the overpotential in the AIE.*

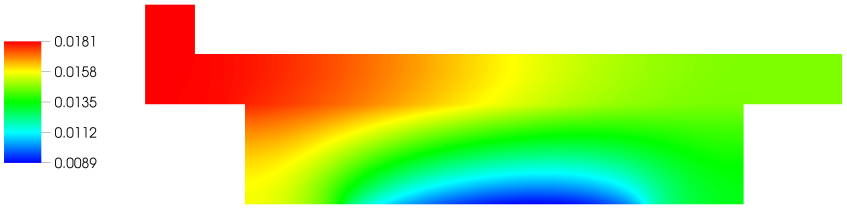

(a) y_{H_2}

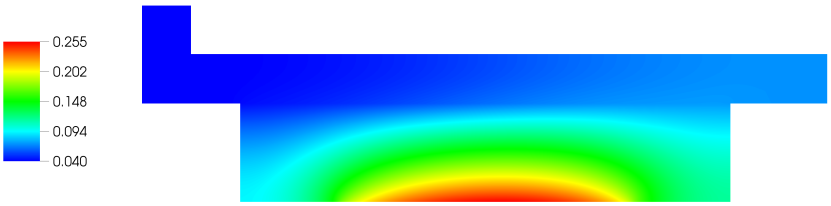

(b) y_{H_2O}

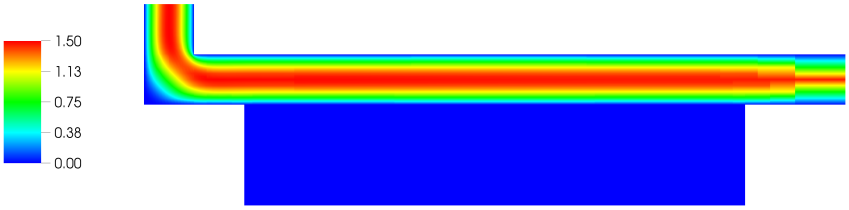

(c) $|\mathbf{v}|$

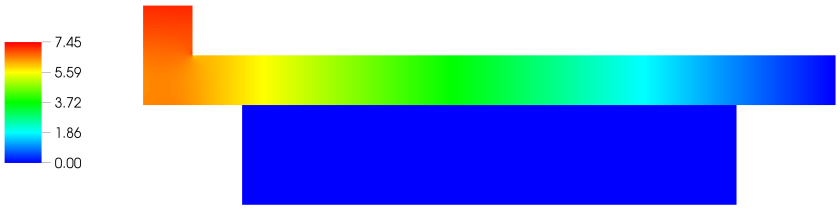

(d) p_{hyd}

Figure 5.3.6.: Mass fractions of hydrogen and steam, norm of the velocity and the pressure values in the fuel cell for the detailed microstructure example.

6. Conclusions and Outlook

This thesis is devoted to numerically simulate the anodic overpotential of a SOFC efficiently. The overpotential depends on the distribution of chemical species (hydrogen and oxygen) in the anode, which consists of a porous material.

6.1. Summary

We derived in Chapter 5 a stationary model of the momentum and species transport in the pore space of the anode and the overlying gas channel. A direct numerical approximation by continuous finite elements of this system is not feasible because the triangulation would need to resolve the porous microstructure, which is way too expensive computationally. We are thus interested in a homogenized version of the microscopic model in the gas channel and a "homogenized" version of the anode. Key features of the microscopic structure enter the equation through effective parameters, which depend on the solution of auxiliary problems.

We focused on the following three aspects in this thesis.

Stokes-Darcy Coupling Stokes equation is part of aforementioned microscopic model. The effective flow is described by Stokes equation in the gas channel and by Darcy equation in the anode. We have to specify how these two equations couple across the gas channel/anode interface on the macroscopic level. These coupling conditions have been a subject of controversy for some time. In Marciniak-Czochra and Mikelić [98] a set of coupling conditions have been analytically proven for the case of a main flow direction that is tangential to the interface, which is the situation we face in the fuel cell simulation. We have verified these conditions in Chapter 3 by numerical simulations of the flow on the microscopic level in a variety of configurations. The difficulty lay in the fact that we have to ensure that the discretization error lies below the homogenization error. We handled this by (goal-oriented) adaptive mesh refinement.

The same investigation was conducted for a main flow direction that is normal to the interface, where another set of coupling conditions hold true,

see Carraro et al. [37]. We were able to verify the conditions in this scenario too.

Error Estimator The discretization of the auxiliary problems influences the discretization of the macroscopic problem through the effective constants. We developed an algorithm based on the DWR-method of Becker and Rannacher [20] to estimate this coupling w.r.t. the discretization error in a quantity of interest in Chapter 4. We showed at the example of some characteristic homogenization problems that the algorithm is able to quantify the error contributions of the involved problems. The algorithm supplies further a set of error indicators to refine the triangulations of the macroscopic problem and the auxiliary problems locally. We showed that the balancing of the error contributions from the different sources together with the local mesh adaption allows for substantial savings in the computations compared to global mesh refinement.

Fuel Cell Simulation We derived under the assumption that the anode is a periodically perforated domain in 2-d formally an effective model that depends on three auxiliary equations. This effective model of the gas transport was verified for some test cases by comparison with direct numerical simulations on the microscopic level. The overpotential computed with the model shows qualitatively the same behaviour as given in the literature and depends heavily on the form of the microstructure. We showed with a representative example that the adaptive algorithm developed in Chapter 4 computes the anode overpotential with with substantial savings w.r.t. degrees of freedom as well as computational time compared to a global mesh refinement. We saw also that the boundary layer constant C_1^{bl} in the Beavers-Joseph-Saffman condition plays only a minor role in these simulations. Nevertheless, the new formulation allows for a decoupling of the effective flow, which also reduces the computational work, as the Darcy flow can be neglected.

6.2. Possibilities for Future Work

There are several directions that seem worthy exploring.

Coupling Conditions This is a very interesting topic that allows for a variety of directions to examine. How do the coupling conditions presented in Chapter 3 carry over to the 3-d case? What about the incorporation of different boundary conditions? What are the effects of considering Navier-Stokes (*NS*) instead of pure Stokes equation? The nonlinearity in the NS equations adds another nonsymmetrie effect that makes the coupling conditions

possibly more elaborate. Direct numerical simulations can give valuable insight in this situation (at least in 2-d).

Fuel Cell Simulations There is a broad range of interesting extensions possible. Apart from model extensions (consider the whole cell, take temperature variations into account, model the electrochemistry, use 3-d microstructures for the cell problems), a proper derivation of the effective equations is needed. For instance, how does the three-phase boundary behave under the upscaling process?

The long term goal would be to optimize the SOFC configuration (runtime parameters, form of the microstructure) with the help of optimization algorithms. The savings in runtime due to the adaptive algorithm presented in this thesis should help in cutting the computational costs so that this becomes feasible.

A. Effective Equation of Quasilinear Diffusion

We present the asymptotic expansion of a quasilinear Diffusion problem, i.e. a diffusion equation for u in which the diffusion tensor depends only on u, not on ∇u. This type of problem is interesting for us as the mass diffusion model we consider in Chapter 5 belongs to this category. Our goal is to derive (as done for linear diffusion coefficients in Section 2.2), a candidate for the homogenized equation. It is important that one needs only a small, a priori known number of cell problems to define the homogenized equation, as we want to employ the algorithm of Chapter 4.

Remark A.0.1. *Please keep in mind that asymptotic expansion is a purely formal method. This is the reason that we do not specify aspects like regularity of the right hand side or the coefficients. Note also that we present, for the sake of clarity, only the case of a scalar equation. We assume that all the presented PDEs are meaningful in the sense that they allow for a unique (weak) solution in the appropriate function spaces.*

A.1. Asymptotic Expansion

Let $\Omega^\varepsilon \subset \mathbb{R}^n$ be a periodically perforated domain with unit cell Y with an inclusion Y_s (see Definition 2.2.6). We call

$$\partial Y = \Gamma_{\text{per}} \text{ and } \partial Y_s = \Gamma_s. \tag{A.1.1}$$

We call Ω the domain Ω^ε without the inclusions and split the boundary into the parts

$$\partial\Omega = \Gamma_D \dot\cup \Gamma_N. \tag{A.1.2}$$

Let the (nonlinear) coefficient $a : \mathbb{R} \to \mathbb{R}^+$ and a right hand side f as well as some Neumann data f_N be given. We consider the following microscopic problem

Problem A.1.1 (Microscopic Problem)**.** *Let* $0 < \varepsilon \ll 1$ *be given. Find* u^ε *s.t.*

$$-\nabla \cdot \left(a(u^\varepsilon)\nabla u^\varepsilon\right) = f, \qquad \text{in } \Omega^\varepsilon, \tag{A.1.3a}$$
$$u^\varepsilon = 0, \qquad \text{on } \Gamma_{\mathrm{D}}, \tag{A.1.3b}$$
$$\mathbf{n} \cdot a(u^\varepsilon)\nabla u^\varepsilon = f_{\mathrm{N}}, \qquad \text{on } \Gamma_{\mathrm{N}}, \tag{A.1.3c}$$
$$\mathbf{n} \cdot a(u^\varepsilon)\nabla u^\varepsilon = 0 \qquad \text{on } \partial O^\varepsilon. \tag{A.1.3d}$$

We are interested in the (formal) limit

$$\lim_{\varepsilon \to 0} u^\varepsilon, \tag{A.1.4}$$

using the asymptotic expansion

$$u^\varepsilon(x) = \sum_{i=0}^{\infty} \varepsilon^i u_i(x, y), \qquad x \in \Omega^\varepsilon, \tag{A.1.5}$$

where the functions $u_i(x, y)$ are Y-periodic with respect to the variable $y = \frac{x}{\varepsilon}$ for all $x \in \Omega$. We assume $0 < \varepsilon \ll 1$ to so small that we can assume a separation of scales, i.e. treat x and y as independent variables.

We utilize the expansion (A.1.5) and get

$$a(u^\varepsilon) = a(\sum_{i=0}^{\infty} \varepsilon^i u_i) =: g(\varepsilon). \tag{A.1.6}$$

We assume that the function $g : \mathbb{R} \to C^3(\mathbb{R})$ allows for a Taylor-Expansion around 0 and conclude

$$g(\varepsilon) = g^{(0)}(0) + \varepsilon g^{(1)}(0) + \frac{\varepsilon^2}{2} g^{(2)}(0) + \mathcal{O}(\varepsilon^3), \tag{A.1.7}$$

which is short for

$$a(u^\varepsilon) = a(u_0) + \varepsilon a'(u_0)u_1 + \varepsilon^2 \left(\frac{1}{2}a'(u_0)u_2 + a''(u_0)u_1^2\right) + \mathcal{O}(\varepsilon^3). \tag{A.1.8}$$

Remark A.1.2. *We will drop the argument* (0) *from* g *to shorten the notation, i.e. we write* $g^{(i)}$ *for* $g^{(i)}(0)$ *etc..*

We insert the expansion into the microscopic problem. Let $\varphi^\varepsilon(x) := \varphi(x, y)$ with $y = {}^{x}/_{\varepsilon}$. Keeping in mind that it holds $\nabla\varphi^\varepsilon = \nabla_x\varphi + \frac{1}{\varepsilon}\nabla_y\varphi$ (see (2.2.26)), we

express the microscopic differential operator on Ω^ε

$$\mathcal{A}^\varepsilon(g)\varphi^\varepsilon := -\nabla\cdot(g(\varepsilon)\nabla\varphi^\varepsilon) \tag{A.1.9}$$

by

$$\mathcal{A}^\varepsilon\varphi^\varepsilon = \left(\varepsilon^{-2}\mathcal{A}_1 + \varepsilon^{-1}\mathcal{A}_2 + \varepsilon^0\mathcal{A}_3\right)\varphi \tag{A.1.10}$$

where

$$\mathcal{A}_1 = \mathcal{D}_1(g^{(0)}), \tag{A.1.11a}$$
$$\mathcal{A}_2 = \mathcal{D}_2(g^{(0)}) + \mathcal{D}_1(g^{(1)}), \tag{A.1.11b}$$
$$\mathcal{A}_3 = \mathcal{D}_3(g^{(0)}) + \mathcal{D}_2(g^{(1)}) + \tfrac{1}{2}\mathcal{D}_1(g^{(2)}) \tag{A.1.11c}$$

and

$$\mathcal{D}_1(g^{(i)}) = -\nabla_y\cdot\left(g^{(i)}\nabla_y\right), \tag{A.1.12a}$$
$$\mathcal{D}_2(g^{(i)}) = -\nabla_y\cdot\left(g^{(i)}\nabla_x\right) - \nabla_x\cdot\left(g^{(i)}\nabla_y\right), \tag{A.1.12b}$$
$$\mathcal{D}_3(g^{(i)}) = -\nabla_x\cdot\left(g^{(i)}\nabla_x\right). \tag{A.1.12c}$$

Keeping this splitting in mind when putting (A.1.5) into the microscopic equation (A.1.3a) leads to a whole bouquet of equations which we sort by powers of epsilon. Considering only the first three orders of ε leads to the following equations:

$$\mathcal{O}(\varepsilon^{-2}): \quad \mathcal{A}_1 u_0 = 0 \quad \text{in } \Omega\times Y_\mathrm{f}, \tag{A.1.13a}$$
$$\mathcal{O}(\varepsilon^{-1}): \quad \mathcal{A}_1 u_1 + \mathcal{A}_2 u_0 = 0 \quad \text{in } \Omega\times Y_\mathrm{f}, \tag{A.1.13b}$$
$$\mathcal{O}(\varepsilon^{0}): \quad \mathcal{A}_1 u_2 + \mathcal{A}_2 u_1 + \mathcal{A}_3 u_0 = f \quad \text{in } \Omega\times Y_\mathrm{f}. \tag{A.1.13c}$$

We conduct in the same way for the microscopic boundary operator (on ∂O^ε)

$$\mathcal{B}^\varepsilon(g)\varphi^\varepsilon := \mathbf{n}\cdot(g(\varepsilon)\nabla\varphi^\varepsilon), \tag{A.1.14}$$

the splitting

$$\mathcal{B}^\varepsilon\varphi^\varepsilon = \left(\varepsilon^{-1}\mathcal{B}_1 + \varepsilon^0\mathcal{B}_2 + \varepsilon^1\mathcal{B}_3\right)\varphi, \tag{A.1.15}$$

where

$$\mathcal{B}_1 = \mathcal{C}_y(g^{(0)}), \tag{A.1.16a}$$
$$\mathcal{B}_2 = \mathcal{C}_x(g^{(0)}) + \mathcal{C}_y(g^{(1)}), \tag{A.1.16b}$$
$$\mathcal{B}_3 = \mathcal{C}_x(g^{(1)}) + \tfrac{1}{2}\mathcal{C}_y(g^{(2)}) \tag{A.1.16c}$$

and

$$\mathcal{C}_y(g^{(i)}) = \mathbf{n} \cdot \left(g^{(i)} \nabla_y\right), \tag{A.1.17a}$$
$$\mathcal{C}_x(g^{(i)}) = \mathbf{n} \cdot \left(g^{(i)} \nabla_x\right). \tag{A.1.17b}$$

Analogously to (A.1.13) we obtain the following three equations on the boundary of the inclusions:

$$\mathcal{O}(\varepsilon^{-1}): \qquad \mathcal{B}_1 u_0 = 0 \qquad \text{on } \Omega \times \partial Y_s, \tag{A.1.18a}$$
$$\mathcal{O}(\varepsilon^{0}): \qquad \mathcal{B}_1 u_1 + \mathcal{B}_2 u_0 = 0 \qquad \text{on } \Omega \times \partial Y_s, \tag{A.1.18b}$$
$$\mathcal{O}(\varepsilon^{1}): \qquad \mathcal{B}_1 u_2 + \mathcal{B}_2 u_1 + \mathcal{B}_3 u_0 = 0 \qquad \text{on } \Omega \times \partial Y_s. \tag{A.1.18c}$$

Now, we try to destille an homogenized equation out of three equations (A.1.13) with the boundary conditions (A.1.18).

- For the smallest order terms (ε^{-2} in the interior and ε^{-1} on Γ_s), we obtain the equation

$$\mathcal{A}_1 u_0(x, \cdot) = 0 \qquad \text{in } Y_f, \tag{A.1.19a}$$
$$\mathcal{B}_1 u_0(x, \cdot) = 0 \qquad \text{on } \Gamma_s, \tag{A.1.19b}$$

  which is short for

$$-\nabla_y \cdot \left(g^{(0)} \nabla_y u_0(x, \cdot)\right) = 0 \qquad \text{in } Y_f, \tag{A.1.20a}$$
$$\mathbf{n} \cdot g^{(0)} \nabla_y u_0(x, \cdot) = 0 \qquad \text{on } \Gamma_s. \tag{A.1.20b}$$

  In this equation, $x \in \Omega^\varepsilon$ plays the role of a parameter. As $u_0 = u_0(x, y)$ is Y-periodic in y (and thus $g^{(0)}$ is also Y-periodic) and **assumed** that the equation is (modulo a constant) uniquely solvable, we obtain

$$u_0 = u_0(x), \tag{A.1.21}$$

and subsequently

$$\nabla_y u_0 = 0. \tag{A.1.22}$$

- The next order terms (ε^{-1} in the interior and ε^0 on Γ_s) lead us to

$$\mathcal{A}_1 u_1(x,\cdot) + \mathcal{A}_2 u_0(x) = 0 \qquad \text{in } Y_f, \tag{A.1.23a}$$
$$\mathcal{B}_1 u_1(x,\cdot) + \mathcal{B}_2 u_0(x) = 0 \qquad \text{on } \Gamma_s. \tag{A.1.23b}$$

Which is aequivalent to (remember $u_0 = u_0(x) \Rightarrow \nabla_y u_0 = 0$)

$$-\nabla_y \cdot g^{(0)} \nabla_y u_1(x,\cdot) = \nabla_y \cdot g^{(0)} \nabla_x u_0(x) \qquad \text{in } Y_f, \tag{A.1.24a}$$
$$\mathbf{n} \cdot g^{(0)} \nabla_y u_1(x,\cdot) = -\mathbf{n} \cdot g^{(0)} \nabla_x u_0(x) \qquad \text{on } \Gamma_s. \tag{A.1.24b}$$

We take the ansatz:

$$u_1(x,y) = \sum_{j=1}^{n} w_j(y) \partial_{x_j} u_0(x), \tag{A.1.25}$$

which leads to

$$\nabla_y u_1(x,y) = \sum_{j=1}^{n} \nabla_y w_j(y) \partial_{x_j} u_0(x). \tag{A.1.26}$$

The functions w_j ($j = 1, \dots n$) are solutions of the *cellequations*

$$-\nabla_y \cdot \nabla_y w_j = \nabla_y \cdot \mathbf{e}_j \qquad \text{in } Y_f, \tag{A.1.27a}$$
$$\mathbf{n} \cdot \nabla_y w_j = -\mathbf{n} \cdot \mathbf{e}_j \qquad \text{on } \Gamma_s. \tag{A.1.27b}$$

This choice of w_j serves us because the ansatz for u_1 fullfills equation (A.1.24). Be aware that it is a linear equation for u_1, and is thus, up to a constant depending on x, uniquely solvable, see e.g. Bensoussan et al. [22]. Note here that

$$\nabla_y g^{(0)} = a'(u_0) \nabla_y u_0 = 0. \tag{A.1.28}$$

Remark A.1.3. *Equation* (A.1.27a) *simplifies of course to* $-\Delta w_j = 0$. *We keep this structure as it clarifies what happens if the factor a in the microscopic equation depends on the fast variable* y.

- The term of order ε^0 in the interior and of order ε^1 on Γ_s yields:

$$\mathcal{A}_1 u_2(x,\cdot) + \mathcal{A}_2 u_1(x,\cdot) + \mathcal{A}_3 u_0(x) = f(x) \qquad \text{in } Y_f, \tag{A.1.29a}$$
$$\mathcal{B}_1 u_2(x,\cdot) + \mathcal{B}_2 u_1(x,\cdot) + \mathcal{B}_3 u_0(x) = 0 \qquad \text{on } \partial Y_s. \tag{A.1.29b}$$

Integration of (A.1.29a) over Y_f and (A.1.29b) over Γ_s leads to the following

$$\int_{Y_f} \mathcal{A}_1 u_2(x,y) + \mathcal{A}_2 u_1(x,y) + \mathcal{A}_3 u_0(x)\,\mathrm{d}y = |Y_f|\, f, \tag{A.1.30a}$$
$$\int_{\Gamma_s} \mathcal{B}_1 u_2(x,s) + \mathcal{B}_2 u_1(x,s) + \mathcal{B}_3 u_0(x)\,\mathrm{d}s = 0. \tag{A.1.30b}$$

We split equation (A.1.30a), considering (A.1.22), into three parts (and neglect the arguments in favour of readability)

$$\int_{Y_f} \overbrace{\nabla_x \cdot g^{(0)} \nabla_y u_1}^{II} \overbrace{+\nabla_x \cdot g^{(0)} \nabla_x u_0}^{III} + \underbrace{\nabla_y \cdot \left(g^{(0)} \nabla_y u_2 + (g^{(1)} \nabla_y + g^{(0)} \nabla_x) u_1 + g^{(1)} \nabla_x u_0 \right)}_{I} \mathrm{d}y \tag{A.1.31}$$

and consider them separately.

We use Stokes' theorem and gain for the integral over the part I:

$$I = \int_{\partial Y_f} \mathbf{n} \cdot \left(g^{(0)} \nabla_y u_2 + \left(g^{(1)} \nabla_y + g^{(0)} \nabla_x \right) u_1 + g^{(1)} \nabla_x u_0 \right) ds \tag{A.1.32}$$

As, by definition, the integrand is Y-periodic w.r.t. y, the part of the integral over ∂Y dissapears, and only the part over Γ_s remains. However, this part vanishes due to the boundary conditions (A.1.30b).

The integral over the second part in (A.1.30a) yields:

$$\int_{Y_f} \nabla_x \cdot g^{(0)} \nabla_y u_1 \,\mathrm{d}y = \int_{Y_f} \nabla_x \cdot g^{(0)} \sum_{j=1}^{N} \nabla_y w_j \partial_{x_j} u_0 \,\mathrm{d}y \tag{A.1.33}$$
$$= \sum_{j=1}^{N} \int_{Y_f} \nabla_x \cdot \left(g^{(0)} \nabla_y w_j \partial_{x_j} u_0 \right) \mathrm{d}y \tag{A.1.34}$$
$$= \sum_{j=1}^{N} \nabla_x \cdot \left(g^{(0)} \int_{Y_f} \sum_{i=1}^{N} \nabla_y w_j \cdot \mathbf{e}_i \, \partial_{x_j} u_0 \right) \mathrm{d}y \tag{A.1.35}$$

Using the abbreviation $\mathbf{A}^{\text{hom}} = (A_{ij}^{\text{hom}})_{i,j}$ with

$$\mathbf{A}_{ij}^{\text{hom}} := \int_{Y_{\text{f}}} \nabla_y w_j \cdot \mathbf{e}_i + \delta_{ij} \, \mathrm{d}y, \qquad 1 \leq i, j \leq n, \tag{A.1.36}$$

and taking into account that the integral I vanishes, we deduce from (A.1.30a) the homogenized problem:

Problem A.1.4 (Macroscopic problem)**.** *Let* $\mathbf{A}^{\text{hom}}$ *be given by* (A.1.36)*. Find* u_0 *s.t.*

$$-\nabla_x \cdot \left(g^{(0)} \mathbf{A}^{\text{hom}} \nabla u_0 \right) = |Y_{\text{f}}| \, f \qquad \text{in } \Omega, \tag{A.1.37a}$$

$$u_0 = 0 \qquad \text{on } \Gamma_{\text{D}}, \tag{A.1.37b}$$

$$\mathbf{n} \cdot \left(g^{(0)} \mathbf{A}^{\text{hom}} \nabla_x u_0 \right) = f_{\text{N}} \qquad \text{on } \Gamma_{\text{N}}. \tag{A.1.37c}$$

So Problem 4.2.2 is our homogenized equation, and to determine the auxiliary functions w_j, it is enough to solve n cellproblems, as in the linear case presented in Section 2.2.

B. (A)dimensional Formulations

B.1. Dimensional Formulation of Stokes-Darcy Coupling

We present the dimensional formulation of Problem 3.1.3 and the effective Problems 3.1.12 and 3.1.14. In this section, dimensional quantities are labeled by $\tilde{\cdot}$. We start with the flow on the microscopic level.

B.1.1. Microscopic Problem

Let the adimensional, periodically perforated domain Ω^ε be given. Consider the flow domain $\widetilde{\Omega^\varepsilon}$ defined by

$$\widetilde{\Omega^\varepsilon} := \left\{ \tilde{x} = L_c x \;\middle|\; x \in \Omega^\varepsilon \right\}, \tag{B.1.1}$$

with a *reference length* L_c. The domains and boundaries $\widetilde{\Gamma_{ns}^\varepsilon}$, $\widetilde{\Gamma_{ns}}$, $\widetilde{\Gamma}$, $\widetilde{\Omega_p}$ and $\widetilde{\Omega_f}$ are defined analoguosly. Let a dynamic viscosity μ and a body force $\tilde{\mathbf{f}}$ be given. A slow, stationary flow in $\widetilde{\Omega^\varepsilon}$ is modeled by the Stokes equations. Let $\widetilde{\Delta}$ and $\widetilde{\nabla}$ be differential operators w.r.t. $\tilde{x}$.

Problem B.1.1 (Dimensional Microscopic Problem)**.** *Find velocity $\tilde{\mathbf{v}}^\varepsilon$ and pressure $\tilde{p}^\varepsilon$, both $L_c L$-periodic w.r.t. to $\tilde{x}_1$, such that*

$$-\mu\widetilde{\Delta}\tilde{\mathbf{v}}^\varepsilon + \widetilde{\nabla}\tilde{p}^\varepsilon = \tilde{\mathbf{f}} \qquad \text{in } \widetilde{\Omega^\varepsilon} \tag{B.1.2a}$$

$$\widetilde{\nabla}\cdot\tilde{\mathbf{v}}^\varepsilon = 0 \qquad \text{in } \widetilde{\Omega^\varepsilon} \tag{B.1.2b}$$

$$\tilde{\mathbf{v}}^\varepsilon = 0 \qquad \text{on } \widetilde{\Gamma_{ns}^\varepsilon}, \tag{B.1.2c}$$

with $\int_f \tilde{p}^\varepsilon(x)\,\mathrm{d}x = 0$.

To proceed with the adimensionalization, we choose a *reference velocity* v_c as well as a *reference pressure* p_c and apply the normalization (let $x \in \Omega^\varepsilon$)

$$\mathbf{v}^\varepsilon(x) = \frac{1}{v_c}\tilde{\mathbf{v}}^\varepsilon(xL_c), \quad p^\varepsilon(x) = \frac{1}{p_c}\tilde{p}^\varepsilon(xL_c), \quad \mathbf{f}(x) = \frac{1}{f_c}\tilde{\mathbf{f}}(xL_c) \tag{B.1.3}$$

to the equation (B.1.2). We set

$$f_c := \frac{\mu v_c}{L_c^2}. \tag{B.1.4}$$

We obtain the following dimensionless form of the stationary incompressible Stokes equations

$$-\frac{\mu v_c}{L_c^2}\Delta \mathbf{v}^\varepsilon + \frac{p_c}{L_c}\nabla p^\varepsilon = f_c \mathbf{f} \qquad \text{in } \Omega^\varepsilon, \tag{B.1.5}$$

$$\nabla \cdot \mathbf{v}^\varepsilon = 0 \qquad \text{in } \Omega^\varepsilon. \tag{B.1.6}$$

Consequently, we choose $p_c = \mu v_c / L_c$ so that (B.1.5) becomes

$$-\Delta \mathbf{v}^\varepsilon + \nabla p^\varepsilon = \mathbf{f} \qquad \text{in } \Omega^\varepsilon, \tag{B.1.7}$$

which es exactly the form of the equation in Problem 3.1.3.

B.1.2. Effective Flow and Darcy's Law

In the following we give the dimensional formulation of the effective equations using the adimensionalization of the previous section. Let ℓ be the characteristic pore size in $\widetilde{\Omega^\varepsilon}$, i.e. $\varepsilon L_c = \ell$. The dimensional form of Problem 3.1.12 is

Problem B.1.2 (Dimensional Effective Flow in Ω_f)**.** *Find a velocity field $\tilde{\mathbf{v}}_f$and a pressure field $\tilde{p}_f$, both L_cL-periodic in $\tilde{x}_1$-direction, such that there holds*

$$-\widetilde{\Delta}\tilde{\mathbf{v}}_f + \widetilde{\nabla}\tilde{p}_f = \tilde{\mathbf{f}} \qquad \text{in } \widetilde{\Omega_f} \tag{B.1.8a}$$

$$\widetilde{\nabla} \cdot \tilde{\mathbf{v}}_f = 0 \qquad \text{in } \widetilde{\Omega_f}, \tag{B.1.8b}$$

together with the boundary conditions

$$\tilde{\mathbf{v}}_f = 0 \qquad \text{on } \widetilde{\Gamma_{ns}}, \tag{B.1.8c}$$

$$\tilde{v}_{f,2} = 0 \qquad \text{on } \widetilde{\Gamma}, \tag{B.1.8d}$$

$$\tilde{v}_{f,1} + \ell C_1^{bl} \tfrac{\partial \tilde{v}_{f,1}}{\partial \tilde{x}_2} = 0 \qquad \text{on } \widetilde{\Gamma} \tag{B.1.8e}$$

and the normalization condition $\int_{\widetilde{\Omega_f}} \tilde{p}_f(x)\,\mathrm{d}x = 0$. The constant C_1^{bl} is given by (3.1.51)*.*

The dimensional form of Problem 3.1.14 reads

Problem B.1.3 (Dimensional Darcy's Law)**.** *Find $\tilde{p}_\mathrm{p}$, $L_\mathrm{c}L$-periodic with respect to $\tilde{x}_1$, such that*

$$-\widetilde{\nabla}\cdot\left(\tilde{\mathbf{K}}(\tilde{\mathbf{f}}-\widetilde{\nabla}\tilde{p}_\mathrm{p})\right)=0 \qquad \text{in } \widetilde{\Omega_\mathrm{p}}, \tag{B.1.9a}$$

$$\tilde{\mathbf{K}}(\tilde{\mathbf{f}}-\widetilde{\nabla}\tilde{p}_\mathrm{p})\cdot\mathbf{e}^2=0 \qquad \text{on } \widetilde{\Gamma_\mathrm{ns}}, \tag{B.1.9b}$$

$$\tilde{p}_\mathrm{p}=\tilde{p}_\mathrm{f}+\mu C_\omega^\mathrm{bl}\tfrac{\partial\tilde{v}_{\mathrm{f},1}}{\partial x_2} \qquad \text{on } \widetilde{\Gamma}. \tag{B.1.9c}$$

The physical permeability tensor $\tilde{\mathbf{K}}$ is given by Definition B.1.4, the interface constant C_ω^bl by (3.1.52)*.*

In the given context, we define the physical permeability $\tilde{\mathbf{K}}$.

Definition B.1.4 (Physical Permeability)**.** *Let the permeability tensor $\mathbf{K}$ be given by Definition 3.1.20. The physical permeability is defined by*

$$\tilde{\mathbf{K}}=(\varepsilon L_\mathrm{c})^2\mathbf{K}=\ell^2\mathbf{K}. \tag{B.1.10}$$

The *Darcy velocity* $\tilde{\mathbf{v}}_\mathrm{p}$ is given by

$$\tilde{\mathbf{v}}_\mathrm{p}=\frac{\tilde{\mathbf{K}}}{\mu}\left(\tilde{\mathbf{f}}-\widetilde{\nabla}\tilde{p}_\mathrm{p}\right). \tag{B.1.11}$$

Remark B.1.5. *Note that ε in this section is dimensionless.*

B.2. Adimensional Formulation of the Effective SOFC Model

We present the dimensional formulation of Problem 5.2.13. We choose the same characteristic quantities as given in Table 5.2.2 and apply the scaling as given in (5.2.54).

Problem B.2.1. *Let inflow velocity $\mathbf{v}^\mathrm{in}$, inflow mass fractions y_k^in, molar masses m_k and viscosities μ_k for $k\in\{\mathrm{H}_2,\mathrm{H}_2\mathrm{O},\mathrm{N}_2\}$ as well as the current density I_C and the thermodynamic pressure p_th be given.*

*Find **velocity field** $\mathbf{v}$, the **pressure** p_hyd and the **species mass fractions** y_i^ε s.t. for*

$i \in \{ \mathrm{H}_2, \mathrm{H}_2\mathrm{O} \}$ it holds in Ω^ε

$$-\nabla \cdot (\mu \nabla \mathbf{v}) + \nabla p_{\mathrm{hyd}} = 0, \qquad \text{in } \Omega_{\mathrm{f}} \tag{B.2.1a}$$
$$\nabla \cdot (\rho \mathbf{v}) = 0, \qquad \text{in } \Omega_{\mathrm{f}} \tag{B.2.1b}$$
$$\nabla \cdot (\rho y_i \mathbf{v}) + \nabla \cdot \mathfrak{F}_i = 0, \qquad \text{in } \Omega_{\mathrm{f}}, \tag{B.2.1c}$$
$$\nabla \cdot (\mathbf{A}^{\mathrm{hom}} \mathfrak{F}_i) = 0, \qquad \text{in } \Omega_{\mathrm{p}}. \tag{B.2.1d}$$

On the boundaries, it holds

$$\mathbf{v} = \mathbf{v}^{\mathrm{in}}, \qquad \text{on } \Gamma_{\mathrm{in}}, \tag{B.2.1e}$$
$$\mathbf{v} = 0, \qquad \text{on } \Gamma_{\mathrm{f,ns}}, \tag{B.2.1f}$$
$$\mathbf{n} \cdot (\mu \nabla \mathbf{v} - p_{\mathrm{hyd}}\, \mathrm{id}) \cdot \mathbf{n} = 0, \qquad \text{on } \Gamma_{\mathrm{out}}, \tag{B.2.1g}$$

and

$$y_i = y_i^{\mathrm{in}}, \qquad \text{on } \Gamma_{\mathrm{in}}, \tag{B.2.1h}$$
$$\mathfrak{F}_i \cdot \mathbf{n} = 0, \qquad \text{on } \Gamma_{\mathrm{out}}, \tag{B.2.1i}$$
$$\mathfrak{N}_i \cdot \mathbf{n} = 0, \qquad \text{on } \Gamma_{\mathrm{f,ns}}, \tag{B.2.1j}$$
$$\mathbf{A}^{\mathrm{hom}} \mathfrak{F}_i \cdot \mathbf{n} = 0, \qquad \text{on } \Gamma_{\mathrm{p,ns}}, \tag{B.2.1k}$$
$$\mathbf{A}^{\mathrm{hom}} \mathfrak{F}_{\mathrm{H}_2} \cdot \mathbf{n} = -I_{\mathrm{C}} \frac{m_{\mathrm{H}_2}}{2}, \qquad \text{on } \Gamma_{\mathrm{el}}, \tag{B.2.1l}$$
$$\mathbf{A}^{\mathrm{hom}} \mathfrak{F}_{\mathrm{H}_2\mathrm{O}} \cdot \mathbf{n} = I_{\mathrm{C}} \frac{m_{\mathrm{H}_2\mathrm{O}}}{2}, \qquad \text{on } \Gamma_{\mathrm{el}}. \tag{B.2.1m}$$

On the interface, the following coupling conditions hold true

$$[y_i] = 0, \qquad \text{on } \Gamma, \tag{B.2.1n}$$
$$[\mathfrak{F}_i^{\mathrm{hom}} \cdot \mathbf{n}] = 0 \qquad \text{on } \Gamma, \tag{B.2.1o}$$
$$v_2 = 0, \qquad \text{on } \Gamma \tag{B.2.1p}$$
$$v_1 + \varepsilon C_1^{\mathrm{bl}} \frac{\partial v_1}{\partial x_2} = 0 \qquad \text{on } \Gamma. \tag{B.2.1q}$$

$\mathfrak{F}^{\mathrm{hom}}$ is defined analoguosly to (5.2.58)*.*

Remark B.2.2. *Note that ε in this section has the dimension* m *and is defined as $\varepsilon = L_{\mathrm{c}} \varepsilon^*$.*

Bibliography

[1] A. ABDULLE. *A priori and a posteriori error analysis for numerical homogenization: a unified framework*, volume 16 of *Series in Contemporary Applied Mathematics*, pages 280–305. World Scientific Publishing, 2011. 86

[2] A. ABDULLE and A. NONNENMACHER. A posteriori error analysis of the heterogeneous multiscale method for homogenization problems. *Comptes Rendus Mathematique*, 347(17–18):1081–1086, 2009. 87

[3] A. ABDULLE and A. NONNENMACHER. Adaptive finite element heterogeneous multiscale method for homogenization problems. *Computer Methods in Applied Mechanics and Engineering*, 200(37–40):2710–2726, 2011. Special Issue on Modeling Error Estimation and Adaptive Modeling. 87

[4] A. ABDULLE and A. NONNENMACHER. A posteriori error estimates in quantities of interest for the finite element heterogeneous multiscale method. *Numerical Methods for Partial Differential Equations*, 29(5):1629–1656, 2013. 87, 88, 92

[5] A. ABDULLE, W. E, B. ENGQUIST, and E. VANDEN-EIJNDEN. The heterogeneous multiscale method. *Acta Numerica*, 21:1–87, Apr. 2012. 86

[6] R. ADAMS and J. FOURNIER. *Sobolev Spaces*. Pure and Applied Mathematics. Elsevier Science, 2003. 12

[7] A. ALEXANDERIAN, M. RATHINAM, and R. ROSTAMIAN. Homogenization, symmetry, and periodization in diffusive random media. *Acta Mathematica Scientia*, 32(1):129–154, 2012. 122

[8] G. ALLAIRE. Homogenization and two-scale convergence. *SIAM Journal on Mathematical Analysis*, 23(6):1482–1518, 1992. 27, 85, 87

[9] G. ALLAIRE. *One-phase Newtonian flow*, chapter 3, pages 45–68. Springer-Verlag New York, Inc., 1997. 35, 39, 41

[10] T. ALOUI and K. HALOUANI. Analytical modeling of polarizations in a solid oxide fuel cell using biomass syngas product as fuel. *Applied Thermal Engineering*, 27(4):731–737, 2007. Energy: Production, Distribution and Conservation. 120

[11] M. ANDERSSON, J. YUAN, and B. SUNDÉN. Review on modeling development for multiscale chemical reactions coupled transport phenomena in solid oxide fuel cells. *Applied Energy*, 87:1461–1476, 2010. 120

[12] J. ANDÚJAR and F. SEGURA. Fuel cells: History and updating. a walk along two centuries. *Renewable and Sustainable Energy Reviews*, 13:2309–2322, 2009. 3, 117

[13] N. BAKHVALOV and G. PANASENKO. *Homogenisation: Averaging Processes in Periodic Media: Mathematical Problems in the Mechanics of Composite Materials*. Mathematics and its Applications. Springer, 1989. 23

[14] W. BANGERTH and R. RANNACHER. *Adaptive Finite Element Methods for Differential Equations*. Birkhäuser Verlag, 2003. 99

[15] W. BANGERTH, R. HARTMANN, and G. KANSCHAT. deal.II – a general purpose object oriented finite element library. *ACM Transactions on Mathematical Software*, 33(4):24/1–24/27, 2007. 46, 78, 102, 139

[16] W. BANGERTH, T. HEISTER, L. HELTAI, G. KANSCHAT, M. KRONBICHLER, M. MAIER, B. TURCKSIN, and T. D. YOUNG. The `deal.ii` library, version 8.1. *arXiv preprint*, `http://arxiv.org/abs/1312.2266v4`, 2013. 46, 78, 102, 139

[17] M. L. BARS and M. G. WORSTER. Interfacial conditions between a pure fluid and a porous medium: implications for binary alloy solidification. *Journal of Fluid Mechanics*, 550:149–173, 2006. 35

[18] W. L. BARTH and G. F. CAREY. On a boundary condition for pressure-driven laminar flow of incompressible fluids. *International Journal for Numerical Methods in Fluids*, 54(11):1313–1325, 2007. 130

[19] G. S. BEAVERS and D. D. JOSEPH. Boundary conditions at a naturally permeable wall. *Journal of Fluid Mechanics*, 30(1):197–207, 1967. 29, 35, 36, 67, 111

[20] R. BECKER and R. RANNACHER. An optimal control approach to a posteriori error estimation in finite element methods. *Acta Numerica*, 10:1–102, 2001. 6, 8, 9, 51, 52, 72, 87, 95, 97, 98, 99, 102, 152

[21] R. BECKER, M. BRAACK, D. MEIDNER, R. RANNACHER, and B. VEXLER. Adaptive finite element methods for pde-constrained optimal control problems. In W. JÄGER, R. RANNACHER, and J. WARNATZ, editors, *Reactive Flows, Diffusion and Transport*, pages 177–205. Springer Berlin Heidelberg, 2007. 99

[22] A. BENSOUSSAN, J.-L. LIONS, and G. PAPANICOLAOU. *Asymptotic analysis for periodic structures*. Studies in mathematics and its applications. North-Holland Pub. Co. New York, Amsterdam, New York, 1978. 16, 23, 24, 26, 85, 92, 159

[23] C. BERNARDI, F. HECHT, and O. PIRONNEAU. Coupling Darcy and Stokes equations for porous media with cracks. *ESAIM: Mathematical Modelling and Numerical Analysis*, 39:7–35, 1 2005. 36

[24] A. BERTEI, A. THOREL, W. BESSLER, and C. NICOLELLA. Mathematical modeling of mas and charge transport and reaction in a solid oxide fuel cell with mixed ionic conduction. *Chemical Engineering Science*, 68:606–610, Feb. 2012. 120

[25] U. BOSSEL. Does a hydrogen economy make sense? *Proceedings of the IEEE*, 94(10):1826 – 1837, 2006. 3

[26] A. BOURGEAT and A. PIATNITSKI. Approximations of effective coefficients in stochastic homogenization. *Annales de l'Institut Henri Poincare (B) Probability and Statistics*, 40(2):153 – 165, 2004. 122

[27] R. BOVE and S. UBERTINI. Modeling solid oxide fuel cell operation: Approaches, techniques and results. *Journal of Power Sources*, 159(1):543–559, 2006. 118, 120, 121, 125, 130

[28] M. BRAACK and T. RICHTER. Solving multidimensional reactive flow problems with adaptive finite elements. In W. JÄGER, R. RANNACHER, and J. WARNATZ, editors, *Reactive Flows, Diffusion and Transport*. Springer, Berlin, 2005. 125, 126

[29] M. BRAACK and T. RICHTER. Solutions of 3D Navier–Stokes benchmark problems with adaptive finite elements. *Computers & fluids*, 35(4):372–392, 2006. 52

[30] S. C. BRENNER and L. SCOTT. *The mathematical theory of finite element methods*. Texts in Applied Mathematics. Springer-Verlag, second edition, 2002. 45, 93

[31] F. BREZZI and M. FORTIN. *Mixed and hybrid finite elements methods*. Springer series in computational mathematics. Springer-Verlag, 1991. 47

[32] H. BRINKMAN. A calculation of the viscous force exerted by a flowing fluid on a dense swarm of particles. *Applied Scientific Research*, 1(1):27–34, 1949. 35

[33] Y. CAO, M. GUNZBURGER, F. HUA, and X. WANG. Coupled Stokes-Darcy model with Beavers-Joseph interface boundary condition. *Communications in Mathematical Sciences*, 8(1):1–25, 2010. 29, 35

[34] Y. CAO, Y. CHU, X. HE, and M. WEI. Decoupling the stationary Navier-Stokes-Darcy system with the Beavers-Joseph-Saffman interface condition. *Abstract and Applied Analysis*, 2013:10, 2013. 35

[35] T. CARRARO, J. JOOS, B. RÜGER, A. WEBER, and E. IVERS-TIFFÉE. 3d finite element model reconstructed mixed-conducting cathodes: I. performance quantication. *Electrochimca Acta*, 77(0):315 – 323, 2012. 88

[36] T. CARRARO, C. GOLL, A. MARCINIAK-CZOCHRA, and A. MIKELIČ. Pressure jump interface law for the Stokes-Darcy coupling: confirmation by direct numerical simulations. *Journal of Fluid Mechanics*, 732:510–536, 2013. 30, 34, 38, 89, 90, 112

[37] T. CARRARO, C. GOLL, A. MARCINIAK-CZOCHRA, and A. MIKELIĆ. Effective interface conditions for the forced infiltration of a viscous fluid into a porous medium using homogenization. submitted to Computer Methods in Applied Mechanics and Engineering, 2014. 30, 70, 72, 74, 76, 152

[38] C. CARSTENSEN and R. VERFURTH. Edge residuals dominate a posteriori error estimates for low order finite element methods. *SIAM Journal on Numerical Analysis*, 36(5):pp. 1571–1587, 1999. 100

[39] F. N. CAYAN, S. R. PAKALAPATI, F. ELIZALDE-BLANCAS, and I. CELIK. On modeling multi-component diffusion inside the porous anode of solid oxide fuel cells using Fick's model. *Journal of Power Sources*, 192(2):467–474, 2009. 120

[40] S. CHAN, K. KHOR, and Z. XIA. A complete polarization model of a solid oxide fuel cell and its sensitivity to the change of cell component thickness. *Journal of Power Sources*, 93(1–2):130 – 140, 2001. 119

[41] P. G. CIARLET. *Finite Element Method for Elliptic Problems*. Society for Industrial and Applied Mathematics, Philadelphia, PA, USA, 2002. 45, 93

[42] F. CIMOLIN and M. DISCACCIATI. Navier-Stokes/Forchheimer models for filtration through porous media. Technical report, Dipartimento di Matematica - Politecnico di Torino, 2010. 35

[43] D. CIORANESCU and P. DONATO. *An introduction to homogenization*. Number 17 in Oxford lecture series in mathematics and its applications ; 17 ; Oxford lecture series in mathematics and its applications. Oxford Univ. Press, Oxford [u.a.], 1999. 6, 16, 85

[44] D. CIORANESCU and J. PAULIN. *Homogenization of Reticulated Structures*. Number Bd. 136 in Applied Mathematical Sciences. SPRINGER VERLAG GMBH, 1999. 14, 25, 26

[45] D. CIORANESCU, A. DAMLAMIAN, and G. GRISO. Periodic unfolding and homogenization. *Comptes Rendus Mathematique*, 335(1):99–104, 2002. 27

[46] D. CIORANESCU, P. DONATO, and R. ZAKI. The periodic unfolding method in perforated domains. *Portugaliae Mathematica. Nova Série*, 63(4):467–496, 2006. 27

[47] B. COOK. Introduction to fuel cells and hydrogen technology. *Engineering Science & Education Journal*, 11:205–216(11), Dec. 2002. 2, 3, 117, 118

[48] P. M. COX, R. A. BETTS, C. D. JONES, S. A. SPALL, and I. J. TOTTERDELL. Acceleration of global warming due to carbon cycle feedbacks in a coupled climate model. *Nature*, 408:184–187, 2000. 2

[49] C. D'ANGELO and P. ZUNINO. Robust numerical approximation of coupled Stokes' and Darcy's flows applied to vascular hemodynamics and biochemical transport. *ESAIM: Mathematical Modelling and Numerical Analysis*, 45:447–476, May 2011. 29

[50] T. A. DAVIS. Algorithm 832: Umfpack v4.3—an unsymmetric-pattern multifrontal method. *ACM Transactions on Mathematical Software*, 30(2): 196–199, June 2004. 104, 139

[51] S. C. DECALUWE, H. ZHU, R. J. KEE, and G. S. JACKSONA. Importance of anode microstructure in modeling solid oxide fuel cells. *Journal of The Electrochemical Society*, 155:B538–B546, 2008. 118

[52] M. DISCACCIATI and A. QUARTERONI. Navier-Stokes/Darcy Coupling: Modeling, analysis and numerical approximation. *Revista Matemática Complutense*, 22(2):315–426, 2009. 35, 37, 72

[53] M. DISCACCIATI, E. MIGLIO, and A. QUARTERONI. Mathematical and numerical models for coupling surface and groundwater flows. *Applied Numerical Mathematics*, 43(1–2):57–74, 2002. 19th Dundee Biennial Conference on Numerical Analysis. 29, 71

[54] W. E. *Principles of multiscale modeling*. Cambridge university press, Cambridge, New York, 2011. 16

[55] W. E and B. ENGQUIST. The heterogeneous multi-scale methods. *Communications in Mathematical Sciences*, 1:87–132, 2002. 86

[56] W. E, P. MING, and P. ZHANG. Analysis of the heterogeneous multiscale method for elliptic homogenization problems. *Journal of the American Mathematical Society*, 18(1):121–156, 2005. 86

[57] M. ENDER, J. JOOS, T. CARRARO, and E. IVERS-TIFFÉE. Quantitative characterization of lifepo4 cathodes reconstructed by fib/sem tomography. *Journal of the electrochemical society*, 159(7):A972–A980, 2012. 88

[58] H. ENE and E. SÁNCHEZ-PALENCIA. Equations et phénomènes de surface pour l'écoulement dans un modèle de milieu poreux. *Journal de Mécanique*, 14:73–108, 1975. 35, 36

[59] T. FATIMA, A. MUNTEAN, and M. PTASHNYK. Unfolding-based corrector estimates for a reaction–diffusion system predicting concrete corrosion. *Applicable Analysis*, 91(6):1129–1154, 2012. 86

[60] A. FICK. Über Diffusion. *Annalen der Physik*, 170(1):59–86, 1855. 127

[61] FUEL CELL TODAY. The fuel cell industry review 2013, 2013. 3

[62] R. S. GEMMEN and C. D. JOHNSON. Effect of load transients on SOFC operation—current reversal on loss of load. *Journal of Power Sources*, 144(1): 152–164, 2005. 121

[63] V. GIOVANGIGLI. *Multicomponent flow modeling*. Modeling and simulation in science, engineering and technology. Birkhäuser, Boston ; Basel ; Berlin [u.a.], 1999. 127

[64] V. GIRAULT and P. RAVIART. *Finite element methods for Navier-Stokes equations: theory and algorithms*. Springer series in computational mathematics. Springer-Verlag, 1986. 47

[65] C. GOLL, T. WICK, and W. WOLLNER. DOpElib: Differential equations and optimization environment; a goal oriented software library for solving pdes and optimization problems with pdes. *preprint*, `www.dopelib.net`, 2013. 46, 78, 102, 139

[66] C. GOLL, R. RANNACHER, and W. WOLLNER. On the adjoint to the damped Crank-Nicolson time marching scheme: Applications to goal-oriented mesh adaptation for the Black-Scholes equation. to appear, 2014. 99

[67] B. GOYEAU, D. LHUILLIER, D. GOBIN, and M. VELARDE. Momentum transport at a fluid–porous interface. *International Journal of Heat and Mass Transfer*, 46(21):4071–4081, 2003. 35

[68] B. HABERMAN and J. YOUNG. Three-dimensional simulation of chemically reacting gas flows in the porous support structure of an integrated-planar solid oxide fuel cell. *International Journal of Heat and Mass Transfer*, 47(17–18): 3617–3629, 2004. 120, 126

[69] N. HANSPAL, A. WAGHODE, V. NASSEHI, and R. WAKEMAN. Development of a predictive mathematical model for coupled stokes/darcy flows in cross-flow membrane filtration. *Chemical Engineering Journal*, 149(1–3): 132 – 142, 2009. 29

[70] N. S. HANSPAL, A. N. WAGHODE, V. NASSEHI, and R. J. WAKEMAN. Numerical analysis of coupled Stokes/Darcy flows in industrial filtrations. *Transport in Porous Media*, 64:73–101, 2006. 71

[71] J. G. HEYWOOD, R. RANNACHER, and S. TUREK. Artificial boundaries and flux and pressure conditions for the incompressible Navier-Stokes equations. *International Journal of Numerical Methods in Fluids*, 22(5):325–352, 1996. 130

[72] J. HIRSCHFELDER and C. CURTISS. Theory of propagation of flames. part i: General equations. *Symposium on Combustion and Flame, and Explosion Phenomena*, 3(1):121–127, 1948. Third Symposium on Combustion and Flame and Explosion Phenomena. 128

[73] U. HORNUNG. *Homogenization and Porous Media*. Interdisciplinary Applied Mathematics. Springer New York, 1997. 6

[74] T. Y. HOU and X.-H. WU. A multiscale finite element method for elliptic problems in composite materials and porous media. *Journal of Computational Physics*, 134(1):169–189, 1997. 86

[75] T. J. HUGHES, G. R. FEIJÓO, L. MAZZEI, and J.-B. QUINCY. The variational multiscale method – a paradigm for computational mechanics. *Comput. Methods Appl. Mech. Eng.*, 166(1-2):3–24, 1998. 86

[76] O. ILIEV and V. LAPTEV. On numerical simulation of flow through oil filters. *Computing and Visualization in Science*, 6:139–146, 2004. 71

[77] W. JÄGER and A. MIKELIĆ. On the interface boundary condition of Beavers, Joseph, and Saffman. *SIAM Journal on Applied Mathematics*, 60(4):1111–1127, Mar. 2000. 29, 35, 36, 37, 42, 111

[78] W. JÄGER and A. MIKELIĆ. On the boundary conditions at the contact interface between a porous medium and a free fluid. *Annali della Scuola Normale Superiore di Pisa - Classe di Scienze*, 23(3):403–465, 1996. 35, 44, 72, 75

[79] W. JÄGER, O. OLEINIK, and A. SHAMAEV. On a homogenization problem for the Laplace operator in a partially perforated domain with the Neumann condition on holes. *preprint ICTP no. SMR.719/3, Second Workshop on Composite Media and Homogenization, Trieste*, 1993. 137

[80] W. JÄGER, A. MIKELIĆ, and N. NEUSS. Asymptotic analysis of the laminar viscous flow over a porous bed. *SIAM Journal on Scientific Computing*, 22(6): 2006–2028, 2000. 29, 35, 37, 42, 44, 48, 49, 58, 68

[81] J. JOOS, M. ENDER, T. CARRARO, A. WEBER, and E. IVERS-TIFFÉE. Representative volume element size for accurate solid oxide fuel cell cathode reconstructions from focused ion beam tomography data. *Electrochimica Acta*, 82(0):268–276, 2012. 88

[82] S. KAKAÇ, A. PRAMUANJAROENKIJ, and X. Y. ZHOU. A review of numerical modeling of solid oxide fuel cells. *International Journal of Hydrogen Energy*, 32(7):761–786, 2007. Fuel Cells. 120

[83] C. M. KALAMARAS and A. M. EFSTATHIOU. Hydrogen production technologies: Current state and future developments. *Conference Papers in Energy*, 2013, 2013. 2

[84] G. KANSCHAT and B. RIVIÈRE. A strongly conservative finite element method for the coupling of Stokes and Darcy flow. *Journal of Computational Physics*, 229(17):5933–5943, Aug. 2010. 35

[85] M. KAVIANY. *Principles of Heat Transfer in Porous Media*. Mechanical Engineering Series. Springer-Verlag New York Inc., 1995. 58

[86] A. KIRUBAKARAN, S. JAIN, and R. NEMA. A review on fuel cell technologies and power electronic interface. *Renewable and Sustainable Energy Reviews*, 13:2430–2440, 2009. 3, 117

[87] M. KORNELY, A. LEONIDE, A. WEBER, and E. IVERS-TIFFÉE. Performance limiting factors in anode-supported cells originating from metallic interconnector design. *Journal of Power Sources*, 196(17):7209–7216, 2011. Proceedings of 2010 European Solid Oxide Fuel Cell Forum. 3, 118

[88] M. KORNELY, A. NEUMANN, N. H. MENZLER, A. LEONIDE, A. WEBER, and E. IVERS-TIFFÉE. Degradation of anode supported cell (asc) performance by cr-poisoning. *Journal of Power Sources*, 196(17):7203–7208, 2011. Proceedings of 2010 European Solid Oxide Fuel Cell Forum. 3

[89] R. KRISHNA and J. WESSELINGH. The Maxwell-Stefan approach to mass transfer. *Chemical Engineering Science*, 52(6):861 – 911, 1997. 127

[90] J. LARMINIE and A. DICKS. *Fuel Cell Systems Explained*. J. Wiley, 2003. 117

[91] R. E. LARSON and J. J. L. HIGDON. Microscopic flow near the surface of two-dimensional porous media. part 1. axial flow. *Journal of Fluid Mechanics*, 166(1):449–472, 1986. 58

[92] R. E. LARSON and J. J. L. HIGDON. Microscopic flow near the surface of two-dimensional porous media. part 2. tranverse flow. *Journal of Fluid Mechanics*, 178(1):119–136, 1987. 58

[93] W. J. LAYTON, F. SCHIEWECK, and I. YOTOV. Coupling fluid flow with porous media flow. *SIAM Journal on Numerical Analysis*, 40:2003, 2003. 35, 37, 72

[94] T. LEVY and E. SÁNCHEZ-PALENCIA. On boundary conditions for fluid flow in porous media. *International Journal of Engineering Science*, 13(11):923 – 940, 1975. 35, 71

[95] P.-W. LI and M. K. CHYU. Simulation of the chemical/electrochemical reactions and heat/mass transfer for a tubular SOFC in a stack. *Journal of Power Sources*, 124(2):487 – 498, 2003. 120

[96] R. LIPTON and M. AVELLANEDA. Darcy's law for slow viscous flow past a stationary array of bubbles. *Proceedings of the Royal Society of Edinburgh: Section A Mathematics*, 114:71–79, Jan. 1990. 39

[97] U. LUCIA. Overview on fuel cells. *Renewable and Sustainable Energy Reviews*, 30(0):164–169, 2014. 2, 118

[98] A. MARCINIAK-CZOCHRA and A. MIKELIĆ. Effective pressure interface law for transport phenomena between an unconfined fluid and a porous medium using homogenization. *Multiscale Modeling & Simulation*, 10(2): 285–305, 2012. 7, 9, 29, 31, 35, 36, 37, 38, 40, 58, 86, 89, 151

[99] E. MASON and A. MALINAUSKAS. *Porous Media: The Dusty-Gas Model*. Elsevier, 1983. 127, 128

[100] J. C. MAXWELL. On the dynamical theory of gases. *Philosophical Transactions of the Royal Society of London*, 157:pp. 49–88, 1867. 127

[101] P. MING and P. ZHANG. Analysis of the heterogeneous multiscale method for parabolic homogenization problems. *Mathematics of Computation*, 76 (257):153–177, 2007. 86

[102] F. MURAT and L. TARTAR. H-convergence. In A. CHERKAEV and R. KOHN, editors, *Topics in the Mathematical Modelling of Composite Materials*, volume 31 of *Progress in Nonlinear Differential Equations and Their Applications*, pages 21–43. Birkhäuser Boston, 1997. 27

[103] V. NASSEHI, N. HANSPAL, A. WAGHODE, W. RUZIWA, and R. WAKEMAN. Finite-element modelling of combined free/porous flow regimes: simulation of flow through pleated cartridge filters. *Chemical Engineering Science*, 60:995–1006, 2005. 71

[104] G. NEALE and W. NADER. Practical significance of Brinkman's extension of Darcy's law: Coupled parallel flows within a channel and a bounding porous medium. *The Canadian Journal of Chemical Engineering*, 52(4):475–478, 1974. 35

[105] G. NGUETSENG. A general convergence result for a functional related to the theory of homogenization. *SIAM Journal on Mathematical Analysis*, 20 (3):608–623, May 1989. 27

[106] D. NIELD. The Beavers–Joseph boundary condition and related matters: A historical and critical note. *Transport in Porous Media*, 78(3):537–540, 2009. 35, 72

[107] J. OCHOA-TAPIA and S. WHITAKER. Momentum transfer at the boundary between a porous medium and a homogeneous fluid–i. theoretical development. *International Journal of Heat and Mass Transfer*, 38(14):2635–2646, 1995. 35, 71

[108] J. A. OCHOA-TAPIA and S. WHITAKER. Momentum transfer at the boundary between a porous medium and a homogeneous fluid—ii. comparison with experiment. *International Journal of Heat and Mass Transfer*, 38(14): 2647–2655, 1995. 35

[109] J. T. ODEN, S. PRUDHOMME, A. ROMKES, and P. BAUMAN. Multiscale modeling of physical phenomena: Adaptive control of models. *SIAM Journal on Scientific Computing*, 28(6):2359–2389, 2006. 92

[110] M. OHLBERGER. A posteriori error estimates for the heterogeneous multiscale finite element method for elliptic homogenization problems. *Multiscale Modeling & Simulation*, 4(1):88–114, 2005. 86, 87, 92

[111] R. RANNACHER. Adaptive galerkin finite element methods for partial differential equations. *Journal of Computational and Applied Mathematics*, 128: 205–233, 1999. 52

[112] R. RANNACHER. Adaptive fe eigenvalue computation with applications to hydrodynamic stability. In R. RANNACHER and A. SEQUEIRA, editors, *Advances in Mathematical Fluid Mechanics*, pages 425–450. Springer Berlin Heidelberg, 2010. 52

[113] W. C. RHEINBOLDT and C. K. MESZTENYI. On a data structure for adaptive finite element mesh refinements. *ACM Transactions on Mathematical Software*, 6(2):166–187, June 1980. 94

[114] T. RICHTER. *Parallel Multigrid Method for Adaptive Finite Elements with Application to 3D Flow Problems*. PhD thesis, Mathematisch-Naturwissenschaftliche Gesamtfakultät, Universität Heidelberg, 2005. 102

[115] B. RIVIÈRE and I. YOTOV. Locally conservative coupling of Stokes and Darcy flows. *SIAM Journal on Numerical Analysis*, 42(5):1959–1977, 2005. 35, 37, 72

[116] K. SAB and B. NEDJAR. Periodization of random media and representative volume element size for linear composites. *Comptes Rendus Mécanique*, 333 (2):187–195, 2005. 122

[117] P. G. SAFFMAN. On the boundary condition at the interface of a porous medium. *Studies in Applied Mathematics*, 1:93–101, 1971. 29, 36, 111

[118] M. SAHRAOUI and M. KAVIANY. Slip and no-slip velocity boundary conditions at interface of porous, plain media. *International Journal of Heat and Mass Transfer*, 35(4):927 – 943, 1992. 58

[119] E. SÁNCHEZ-PALENCIA. *Non-homogeneous media and vibration theory*. Lecture notes in physics. Springer-Verlag, 1980. 23

[120] M. SCHÄFER and J. TUREK. *Benchmark computations of laminar flow around a cylinder*. Vieweg, Braunschweig, January 1996. 112

[121] Y. SHI, N. CAI, C. LI, C. BAO, E. CROISET, J. QIAN, Q. HU, and S. WANG. Modeling of an anode-supported Ni–YSZ | Ni–ScSZ | ScSZ | LSM–ScSZ multiple layers SOFC cell: Part I. experiments, model development and validation. *Journal of Power Sources*, 172(1):235 – 245, 2007. {ACS} San Francisco 2006 Fuel and Cell Symposium. American Chemical Society National Meeting. San Francisco, {CA} Sept 10-14 2006. 120

[122] A. STAMBOULI and E. TRAVERSA. Solid oxide fuel cells (SOFCs): a review of an environmentally clean and efficient source of energy. *Renewable and Sustainable Energy Reviews*, 6(5):433–455, 2002. 117

[123] A. B. STAMBOULI and E. TRAVERSA. Fuel cells, an alternative to standard sources of energy. *Renewable and Sustainable Energy Reviews*, 6:297–306, 2002. 3

[124] J. STEFAN. Über das Gleichgewicht und Bewegung, insbesondere die Diffusion von Gemischen. *Sitzungsberichte der Kaiserlichen Akademie der Wissenschaften Wien, 2te Abteilung a*, 63:63–124, 1871. 127

[125] R. SUWANWARANGKUL, E. CROISET, M. FOWLER, P. DOUGLAS, E. ENTCHEV, and M. DOUGLAS. Performance comparison of Fick's, Dusty-Gas and Stefan–Maxwell models to predict the concentration overpotential of a SOFC anode. *Journal of Power Sources*, 122(1):9–18, 2003. 118, 121, 127, 128, 132

[126] L. TARTAR. Quelques remarques sur l'homogénéisation. In *Functional Analysis and numerical Analysis*, Japan-France Seminar 1976, pages 469–482. M. Fujita Society for the Promotion of Science, 1978. 27

[127] L. TARTAR. *The general theory of homogenization. A personalized introduction.* Berlin: Springer, 2009. 6, 16, 27, 85

[128] C. TAYLOR and P. HOOD. A numerical solution of the Navier-Stokes equations using the finite element technique. *Computers & Fluids*, 1(1):73 – 100, 1973. 47

[129] R. TEMAM. *Navier-Stokes equations*. AMS Chelsea Publ., Providence, RI, reprinted with corr. edition, 2001. AMS Chelsea ed.:Reproduction of the 3. rev. ed. 1984, + Appendix III (new material). 31

[130] S. TLUPOVA and R. CORTEZ. Boundary integral solutions of coupled Stokes and Darcy flows. *Journal of Computational Physics*, 228(1):158 – 179, 2009. 37

[131] K. TSERONIS, I. KOOKOS, and C. THEODOROPOULOS. Modelling mass transport in solid oxide fuel cell anodes: a case for a multidimensional dusty gas-based model. *Chemical Engineering Science*, 63:5626–5638, 2008. 6, 120, 121, 128, 129, 132, 143, 148

[132] J. URQUIZAA, D. N'DRI, A. GARON, and M. DELFOUR. Coupling Stokes and Darcy equations. *Applied Numerical Mathematics*, 58:525 – 538, 2008. 35, 37

[133] J. VELDSINK, R. VAN DAMME, G. VERSTEEG, and W. VAN SWAAIJ. The use of the dusty-gas model for the description of mass transport with chemical reaction in porous media. *The Chemical Engineering Journal*, 57:115–125, 1995. 120, 127

[134] K. WANG, D. HISSEL, M. PÉRA, N. STEINER, D. MARRA, M. SORRENTINO, C. PIANESE, M. MONTEVERDE, P. CARDONE, and J. SAARINEN. A review on solid oxide fuel cell models. *International Journal of Hydrogen Energy*, 36 (12):7212–7228, 2011. 4, 120

[135] J. WLOKA. *Partielle Differentialgleichungen*. Mathematische Leitfäden. Teubner, Stuttgart, 1982. 12

[136] H. YAKABE, M. HISHINUMA, M. URATANI, Y. MATSUZAKI, and I. YASUDA. Evaluation and modeling of performance of anode-supported solid oxide fuel cell. *Journal of Power Sources*, 86(1–2):423 – 431, 2000. 119, 121, 132, 137, 148

[137] S. YANG, T. CHEN, Y. WANG, Z. PENG, and W. G. WANG. Electrochemical analysis of an anode-supported SOFC. *International Journal of Electrochemical Science*, 8(2):2330–2344, 2013. 3, 118

[138] P. YU, T.S.LEE, Y.ZENG, and H. T. LOW. A numerical method for flows in porous and homogenous fluid domains coupled at the interface by stress jump. *International Journal for Numerical Methods in Fluids*, 53:1755–1775, 2007. 71

[139] V. ZHIKOV, S. KOZLOV, and O. OLEINIK. *Homogenization of differential operators and integral functionals*. Springer-Verlag, 1994. 16, 17, 21, 85

[140] H. ZHU, R. J. KEE, V. M. JANARDHANAN, O. DEUTSCHMANN, and D. G. GOODWIN. Modeling elementary heterogeneous chemistry and electrochemistry in solid-oxide fuel cells. *Journal of the electrochemical society*, 152 (12):A2427–A2440, 2005. 6, 130

Acknowledgments

An dieser Stelle möchte ich all jenen danken, die mich bei der Durchführung dieser Arbeit unterstützt haben. Herrn Prof. Rolf Rannacher danke ich für die Möglichkeit, an diesem spannenden Thema zu arbeiten, seine zielgerichteten Kommentare sowie seine allzeitige Unterstützung bei Konferenzbesuchen und Anträgen.

I would also like to thank Prof. Béatrice Rivière for her interest in my work and insightful comments about it. Many thanks go also to Prof. Anna Marciniak-Czochra and Prof. Andro Mikelić for the opportunity to work with them and for sharing their huge knowledge about homogenization with me.

Zu großem Dank bin ich Dr. Thomas Carraro verpflichtet, der mich vom ersten bis zum letzten Tag mit Rat und Tat begleitet hat. Ebenso bedanke ich mich bei Jun.-Prof. Winnifried Wollner und Dr. Thomas Wick für die Möglichkeit, Teil des spannenden `DOpElib` Projektes zu sein. Zudem möchte ich meinem langjährigen Büronachbarn Daniel für ungezählte Diskussionen danken. Und was wäre eine Woche ohne Kuchen? Vielen Dank an die gesamte AG Numerik für allzeit offene Türen und Ohren, insbesondere möchte ich hierbei Matthias M. und Jun.-Prof. Thomas Richter erwähnen.

Mein Promotionsvorhaben an der Fakultät für Mathematik und Informatik der Universität Heidelberg wurde finanziell unterstützt von der HGS Mathcomp, dem IWE am KIT sowie der Landesgraduierenförderung.

Den aufmerksamen Augen von Sara, Julian, Christoph, Matthias und Melanie entging kaum ein Fehler, vielen Dank dafür. Was wäre Heidelberg ohne die Taktik-Künstler der Los Duderinos, Meister der Herzen? Danke für die gelegentliche Ablenkung.

Mein besonderer Dank gilt meiner Familie, insbesondere meiner Frau Silke, für die liebevolle Unterstützung und Bestärkung in den ganzen Jahren.